2014

Time-resolved and steady-state studies of biologically and chemically relevant systems using laser, absorption, and fluorescence spectroscopy

Charles Ashley Barnes
Iowa State University

Recommended Citation

Barnes, Charles Ashley, "Time-resolved and steady-state studies of biologically and chemically relevant systems using laser, absorption, and fluorescence spectroscopy" (2014). *Graduate Theses and Dissertations*. 13978.
https://lib.dr.iastate.edu/etd/13978

Time-resolved and steady-state studies of biologically and chemically relevant systems using laser, absorption, and fluorescence spectroscopy

by

Charles Ashley Barnes

A dissertation submitted to the graduate faculty

in partial fulfillment of the requirements for the degree of

DOCTOR OF PHILOSOPHY

Major: Physical Chemistry (Chemical Instrumentation)

Program of Study Committee:
Jacob W. Petrich, Major Professor
Theresa Windus
Emily Smith
Xeuyu Song
Ning Fang

Iowa State University

Ames, Iowa

2014

I dedicate this thesis to my close family and friends. I would not be in this position today without their strong love and support.

TABLE OF CONTENTS

ACKNOWLEDGEMENTS

I would like to thank my advisor Jacob W. Petrich for welcoming me into his group and providing the resources necessary for me to start and complete my graduate career. I would also like to thank my program of study committee specifically Emily Smith, Theresa Windus, Mark Gordan, Xeuyu Song, and Ning Fang for their helpful discussions and insights in our annual meetings.

I thank everyone in the Petrich group who have come and gone during my time at ISU. Specifically, I would like to thank Ramkrishna Adhikary for taking the time to teach me about our laser instrumentation. His knowledge in these areas was vast and helpful. Also I would like to thank Sayantan Bose for his help in understanding theories concerning solvation dynamics. I thank Philip J. Carlson for his friendship and helpful dissucusions from our time entering graduate school and the Petrich group together. Also I would like to thank Ujjal, Kalyan, and Priyanka.

I would also like to thank Marilu Perez for her friendship, helpful advice, and the times we had together. I thank Tak W. Kee at the University of Adelaide in Australia for his help and collaboration with regards to the cyclocurcumin project. I thank Mark Rassmussen for his help in supplying fecal samples for the efflux pump inhibitor project. I thank Mark Hargrove and his group for allowing me to come into their lab and relearn and expand my knowledge of protein expression and purification as well as additional biochemical methods of analysis.

Importantly, I would like to thank my parents and especially my younger sister, Tiffini, for their love and support. Finally I would like to take some time to especially thank Harold and Jennifer Goldston for their love and support. They are family to me and I would

not be in this position today without them. I consider Jennifer to be my best sister and friend and all of our times together are forever cherished. Her wisdom and advice has been awesome and I hope she realizes how much of a difference she has made in my life. I consider Harold as my older brother and friend. Sunday afternoons watching our favorite NFL team will remain some of my best memories. He has also provided essential advice, great humor, and wisdom. There honestly are not enough words in this limited space to truly express my gratitude and love for the both of them.

ABSTRACT

In Chapter 2 several experimental and data analysis methods used in this thesis are described. In Chapter 3 steady-state fluorescence spectroscopy was used to determine the concentration of the efflux pump inhibitors (EPIs), pheophorbide *a* and pyropheophorbide *a*, in the feces of animals and it was found that their levels far exceed those reported to be inhibitory to efflux pumps. In Chapter 4 the solvation dynamics of 6-Propionyl-2-(N,N-dimethyl) aminonaphthalene (PRODAN) was studied in reverse micelles. The two fluorescent states of PRODAN solvate on different time scales and as such care must be exercised in solvation dynamic studies involving it and its analogs. In Chapter 5 we studied the experimental and theoretical solvation dynamics of coumarin 153 (C153) in wild-type (WT) and modified myoglobins. Based on the nuclear magnetic resonance (NMR) spectroscopy and time-resolved fluorescence studies, we have concluded that it is important to thoroughly characterize the structure of a protein and probe system before comparing the theoretical and experimental results. In Chapter 6 the photophysical and spectral properties of a derivative of the medically relevant compound curcumin called cyclocurcumin was studied. Based on NMR, fluorescence, and absorption studies, the ground- and excited-states of cyclocurcumin are complicated by the existence of multiple structural isomers. In Chapter 7 the hydrolysis of cellulose by a pure form of cellulase in an ionic liquid, HEMA, and its aqueous mixtures at various temperatures were studied with the goal of increasing the cellulose to glucose conversion for biofuel production. It was found that HEMA imparts an additional stability to cellulase and can allow for faster conversion of cellulose to glucose using a pre-treatment step in comparison to only buffer.

CHAPTER 1: GENERAL INTRODUCTION

Optical Spectroscopy

Optical spectroscopy involves methods to study physical matter based on its interactions with light. In general there are three main methods, those being light absorption, emission (fluorescence and phosphorescence), and scattering. It is these types of interactions that have allowed matter to be "visible" by the human eye as well as analysis of molecular and atomic species in various types of environments. The field of optical spectroscopy is important in a number of fields, including chemistry, biochemistry, physics, biophysics, molecular biology, and astronomy. Initially, optical techniques were reserved for understanding the wavelength dependent nature of a sample's absorption, emission, and/or scattering processes. However, it has grown and expanded to wide-ranging and complex analysis. With the advent of pulsed lasers, time-resolved optical techniques have evolved to aid in understanding dynamics and kinetics with time scales as short as a few femtoseconds.[1-3] This combined with the technological advances in the sensitivity and speeds of optical detectors have now made it possible to study individual molecules and the motions of atoms and nuclei within them. One of the main advantages of optical techniques is the noninvasive and nondestructive analysis of samples with minimal interference of the properties under study.[2-5] Thereby optical spectroscopy can be thought of as an indiscrete camera of the "action". In effect optical spectroscopy has now provided essential properties and analysis of matter that are not possible by any other technique. Of the three main methods the absorption and emission, specifically fluorescence, of light by molecules will be the focus throughout this thesis. In order to have a general understanding of the research topics presented it is important to briefly define light and the fates of its photons upon and following interactions with molecules in the absorption and fluorescence process.

Light itself is not continuous in energy values. Based on quantum theory, each frequency of light only corresponds to photons of certain discrete energy values

$$E = h\upsilon \tag{1.1}$$

where ν is the frequency in inverse seconds and h is Planck’s constant. This is often referred to as Planck’s equation and the discrete energy is said to be quantized. In the case of energy levels among molecules, these are also quantized. The absorption and emission of a photon can only happen if the photon energy matches the energy difference between two participating energy levels. In this case Planck’s relationship is rewritten as

$$\Delta E_{mn} = E_m - E_n = h\upsilon_{mn} \tag{1.2}$$

in which E_m and E_n are the energy of the final (m) and initial state (n) respectively.[1-5] When the frequency of light matches this requirement the transition between energy levels is defined as being in resonance with the light. The energy levels involved could be electronic, vibrational, and rotational. The population and probability of a molecule being in a particular level can be defined through the Boltzman distribution as[5,6]

$$P_i = \frac{g_i}{Z}\, e^{-E_i/kT} \tag{1.3}$$

where E_j is the energy of the jth level (or state), k is Boltzman’s constant, T is the temperature, g_i is the degeneracy, and Z is the partition function defined as $= \sum_i^\infty g_i e^{-E_i/kT}$. In optical transitions, one is normally interested in the populations between two different levels. In this case the distribution can be reformulated as[5,6]

$$\frac{N_n}{N_m} = e^{-\frac{(E_m - E_n)}{kT}} \tag{1.4}$$

The N is the number of molecules (or atoms) in each level. In normal ambient conditions molecules can undergo vibrational and rotational transitions between levels. In terms of the electronic transitions which will be most important in subsequent chapters, the thermal surroundings are not enough to populate the upper electronic levels to any appreciable degree with >99% existing in the ground (lowest level) electronic state. To induce these transitions by non-optical means such as temperature increases is not particularly viable for most organic molecules due to structural stability concerns.[2,5,6] One of the least invasive ways is by using low intensity light with frequencies that match the energy difference between the electronic energy levels. The electronic absorption of resonant light by a molecule from E_n to E_m will place the molecule in the electronic excited state. The molecule will not stay in this excited state indefinitely but will undergo various transitions in the release of this energy to come back to the ground state level. In general these downward transitions can be classified into two different groups, radiational and nonradiational (or raditionless) transitions. The Jablonski diagram of a typical organic molecule can help to further explain these processes and define the general rate constants involved in each transition.

In the Jablonski diagram presented in Figure 1.1, the S_0 and $S_{n>0}$ represent the singlet electronic energy manifolds of the ground and excited state respectively with n as a whole number integer and higher numbers equaling higher energies. Vibrational transitions are normally closely coupled with electronic transitions and these are depicted as the smaller lines within S_0 and S_1. Nonradiative transitions are represented by wavy and dashed lines while radiative are solid lines. At room temperature several of the low lying vibrational levels of S_0 are appreciably populated so that transitions to the S_1 state can occur from any of these levels. Absorption of light takes place on a time scale of 10^{-15}s which according to the Franck-Condon principle occurs much too fast in comparison to motions of the nuclei.[2,5] Thus the nuclei can be thought of as effectively “frozen” during these transitions. Depending on the energy and molecule the absorption could excite the molecule to the S_1, S_2 or even higher. However, once in this state, vibrational and nonradiative thermal transitions will quickly occur to the lowest vibrational level of S_1. The nonradiative transitions from different singlet electronic states (e.g. $S_1 \rightarrow S_0$) are termed internal conversion and have rate constants of k_{IC}. Based on the molecule and its environment, transitions back to S_0 may be preferentially nonradiative or radiative. If radiative then the molecule would give off a photon when returning to the ground state, S_0. This is fluorescence and it occurs with a rate constant of k_F. Also some molecules can nonradiatively transition from S_1 to an excited state triplet state (T_1), in a process called intersystem crossing with a rate constant of k_{ISC}. The T_1 is a state of different spin multiplicity and as such transitions between S_1 to T_1 are spin-forbidden and typically much slower in comparison to those of S_1 to S_0. Radiative transitions from T_1 to S_0 are called phosphorescence with a rate constant of k_p. Other intermolecular (external) nonradiative transitions can occur as well such as energy transfer, collisional quenching, etc. with a rate constant of $k_{nr_{ex}}$.

From experiment, each of the aforementioned rate constants can be determined if appropriate techniques and analysis of results are utilized. Of particular importance for time-resolved fluorescence experiments is the molecules fluorescence lifetime from which the rate constants of the radiative and nonradiative processes can be extracted.

$$\tau_F = \frac{1}{k_F + k_{IC} + k_{ISC} + k_{TS} + k_P + k_{nr_{ex}}} \tag{1.5}$$

This constant is also directly proportional to the molecules fluorescence quantum yield by

$$\Phi_F = k_F \tau_F. \tag{1.6}$$

Thus the fluorescent lifetime of a fluorophore is particularly useful in obtaining information about not only the molecule itself but also of its environmental surroundings. Many of the studies in this thesis work to understand the fundamental photophysical and chemical processes occurring in molecular assemblies in biological and chemical systems by analyzing changes presented in a fluorophores fluorescent lifetime.

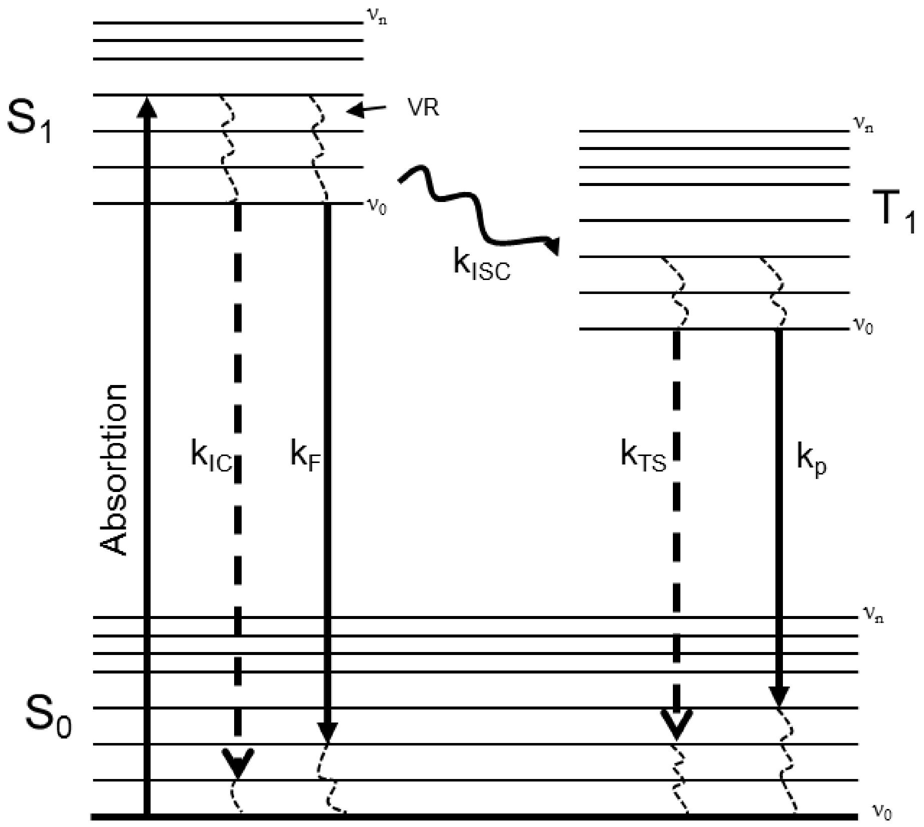

Figure 1.1. Jablonski diagram illustrating the different internal rate processes involved in the deactivation of the excited state of a molecule following light absorption. Different vibrational levels are indicated by ν. For clarity higher singlet ($S_{n>1}$) and triplet ($T_{n>1}$) states as well as other external nonradiative processes ($k_{nr_{ex}}$) are omitted. VR – vibrational relaxation.

Protein Dynamics

Based on the earliest obtained X-ray crystal structures, proteins were originally thought to have well defined (unique) and rigid structures. In effect, they were assumed to be static entities in organisms. But it was the pioneering work performed by Dr. Gregorio Weber in the early 1960s that helped challenge this mode of thinking. His work revealed that proteins are not “lifeless” but in his words actually “kicking and screaming stochastic models” which are involved in a rich array of important dynamical processes.[7] These types of processes could be as simple as local vibrational fluctuations to facilitate a chemical reaction or large-scale conformational changes in order to perform their inherent functions.

The field of protein dynamics is based on elucidating the kinetics and thermodynamics involved in transitional state changes of proteins in order to develop an energy landscape that will serve to understand their biological functions.[8] Many experimental techniques such as time-resolved fluorescence, three-photon echo peak shift (3PEPS), nuclear magnetic resonance (NMR), and Raman spectroscopy have helped to elucidate these motions on a time scale of a few femtoseconds to several seconds and in order to develop a full dynamical model a concerted effort among not only experimental but theoretical techniques will be required. In the case of ultrafast dynamics, which is the focus here, time-resolved fluorescence techniques are well suited to explore the fast dynamical processes proteins undergo in regulating various reactions and in performing their biological functions.

Heme proteins are metalloproteins that have an iron-containing prosthetic group (heme). The heme is composed of an iron atom placed at the center of a tetrapyrrole ring which is bound to the rest of the protein through covalent bonds. This group often serves as a cofactor that plays a significant role in carrying out the proteins' primary functions such as cell signaling, catalysis and/or gaseous ligand transportation.[9] Two particularly interesting heme proteins are myoglobin and hemoglobin. Hemoglobins are tetrameric globular proteins often associated with red blood cells and the transport of oxygen throughout the circulatory systems of mammals. The distinctive bright red color of these cells and mammalian blood is due to hemoglobins. In contrast myoglobin is a monomeric form of hemoglobin found in the muscles of living organisms. These proteins' hemes can bind not only oxygen but other gaseous ligands such as hydrogen sulfide, nitric oxide, and carbon monoxide. Most are familiar with the term carbon monoxide poisoning and it is the binding of CO to hemoglobin and myoglobin that is responsible.

Hemoglobin and myoglobin have routinely been used as model proteins in attempting to understand the relationship between structure and biological function. With the function and structure of these proteins better resolved, their underlying dynamics can be more easily understood. Between these two heme proteins, it is easier to theoretically and experimentally study the protein dynamics of myoglobin due to its smaller size and number of amino acid residues (154). Although myoglobin is monomeric it is generally believed that its dynamics can be globally applied to other larger proteins.[8]

Proteins can undergo ultrafast processes on the femtosecond to picosecond time regime. Often this time scale is overlooked in trying to formulate ideas on how certain dynamical exchanges are connected to functions. Fleming and coworkers, however, demonstrated the importace of this time scale using photon echo spectroscopy to show that ~70% of the dynamical response was complete within ~20 fs using eosin in lysozyme.[10] In studying ultrafast protein dynamics we use experimental and theoretical solvation dynamics within apomyoglobinin to further understand the structure and functional relationships of proteins.

Solvation Dynamics

Many important chemical and biochemical processes occur in solutions which consist of two components, solute and solvent. The solvent-solute system could be something as simple as water-salt or a much more complex system of protein-ligand. The question of whether or how effectivly a process can proceed is often dependent on the role the solvent plays in moderating the potential energy of the participating solute molecules.[10-15] For example in liquid-phase chemical reactions the solvent plays a critical role in the rates of various charge transfer processes such as electron, proton, and energy transfers between species. Before a reaction starts the surrounding solvent and solute species are in equilibrium. However, once the reaction is triggered, newly-charged reactants (or solute) are instantaneously formed thereby placing the system in a nonequilibrium condition. The solvent is much too slow to adjust to this redistribution of charge and it is essentially “frozen” in place. The solvent must then readjust around the solute molecules in such a way as to minimize the energy of the system. If the solvent is unable to accommodate the transition states then the products being produced may recross the reaction free energy barrier, thereby causing a reduction in the reaction rate.[16] Thus the solvent is not merely a spectator in the events, but an actual participant. It is the reorganization of the solvent around the solute species with time that is termed solvation dynamics.

Experimentally, various time-resolved optical techniques can be utilized to study solvation dynamics. But one of the most effective ways is time-resolved fluorescence in which changes in the fluorescence signal of a probe molecule (solute) with time are used to report on the solvation process.[2,16-21] A general scheme of this method using a fluorescence molecule is presented in Figure 1.2. Using a short pulse of light, a molecule is excited from the S_0 state to S_1. As mentioned before this absorption event is very fast (10^{-15} s according to the Franck Condon principle) and is too fast in comparison to molecular motions of the solvent. The excited-state dipole moment of the molecule in S_1 is much different than it was in the S_0 state and as a consequence creates charge redistribution. At this point the solute-solvent system is in a highly nonequilibrium state. Assuming a polar solvent (which is a prerequisite for studying solvation), its molecules with the dipoles will then begin to reorganize around the solute to lower the free energy of the system. As this occurs, the S_1 excited state potential energy of the probe molecule decreases and its emission spectrum shifts to lower energies (longer wavelengths). This is commonly referred to as the dynamic stokes shift (DSS).[17] Since the fluorescence lifetime of the probe molecule is generally slower than solvation, its fluorescence with time can be used to resolve important solvation characteristics such as solvation time and reorganization energies. It is important to note that the solvation response to this perturbation is analogous to the perturbation imposed by chemical/biochemical reactions. Thus the experimental solvation events can be directly extrapolated to actual chemical and biochemical processes in solution.

For solvation dynamic studies it is important to use an inert probe molecule that will report on the solvation event but not actually contribute to it. One of the most commonly used probes is coumarin 153 (C153). It is structurally rigid, has a high fluorescence quantum yield, and undergoes a substantial change in its dipole moment upon excitation to S_1.[18] Furthermore, C153 only has one singlet excited state that fluoresces and does not participate in multiple intramolecular charge transfer processes which could change its excited-state properties during solvation.[18] This is important in order to prevent the probe from introducing artifacts into the solvation dynamics. The consequences of using probes that have multiple fluorescent states in solvation dynamic studies is discussed in the PRODAN section below and in Chapter 4.

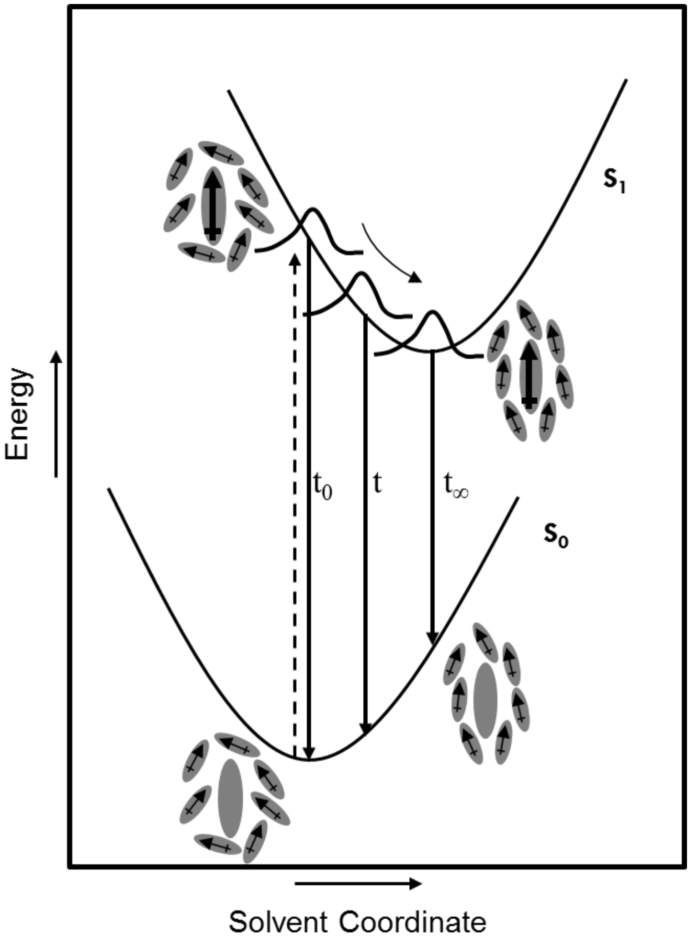

Figure 1.2. Schematic representation of solvation dynamics.

Antibiotic Resistance: Efflux Pump Proteins and Inhibitors

Treatment of bacterial infections typically involves the administration of various types of antibiotics, but the success in curing an infection is dictated by the effectiveness of the antibiotic in reaching its intended destination. An unfortunate byproduct of antibiotic use is the growth of antibiotic resistance among bacterial strains which poses a serious health threat to humans and animals.[19,20] The development of multidrug resistance (MDR) is due to membrane transport proteins called multidrug resistant efflux pumps which have the ability to reduce intracellular concentrations of the toxic drugs. For example the growth of antibiotic resistant *Staphylococcus aureus* has increased through the expression of the QacA efflux pump that allows resistance to various clinically important cationic quaternary ammonium compounds (QACs).[19,20] Analysis of MDR proteins have provided clues to the mechanism by which drug binding sites interact with several drugs, but a full understanding is inhibited by the lack of structural information available for these large proteins.[20] Although working to develop a better picture of their activity is important over the long term, the inhibition of their activity with better types of drugs or compounds is of more clinical or immediate significance.

Evidence has been presented which suggests that efflux pumps are inhibited by several types of compounds thereby causing them to lose their ability to remove antibiotics from the intracellular environment. Even though artificial inhibitors such as synthetic drugs are generally of focus with respect to clinical applications, natural inhibitors from plants have been a recent area of interest as some can be acquired through dietary means and have been proven to be effective efflux pump inhibitors. The first such inhibitory compounds acquired from plants were reported by Stermitz and Lewis.[21,22] In their work they used a NorA efflux pump assay to identify flavolignan (5'-methoxyhydnocarpin) acquired from extracts of *Berberis trifoliolata* and pheoborbide *a*, a cholorophyll metabolite as effective inhibitors. Between the two, pheophorbide *a* was found to be much more potent.

Unlike the aerobic metabolism of chlorophyll in leaf tissue which oxidatively degrades its porphyrin ring to a linear tetrapyrolle, anerobic metabolism in the gut of animals follows a different mechanism that leaves this ring intact (Figure 1.3).[23] This results in the production of various metabolites, the most predominant being pheophorbide *a* and pyropheophorbide *a*. Therefore in the gut of animals there is a substantial amount of pheophorbide *a* present. In comparison to the parent compound, chlorophyll, pheophorbide *a* is highly fluorescent.[24,25] Previous work has been able to utilize this signal for the detection of fecal material on meat carcasses.[24] In the work presented in Chapter 3 this fluorescent marker is also used to determine the diet-dependent concentrations of pheophorbide *a* in the feces of animals.

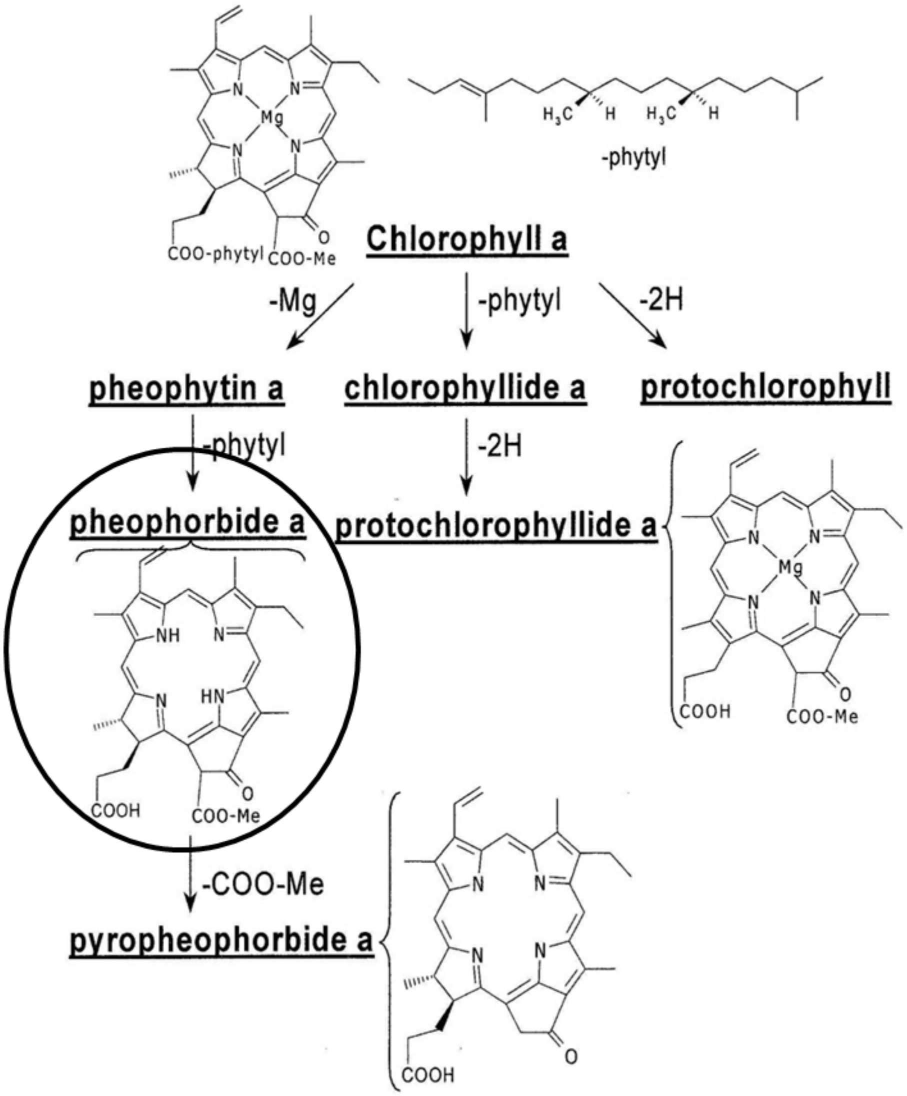

Figure 1.3. Anerobic metabolism of chlorophyll in the gut of animals to various metabolites with pheophorbide a being one of the most prominent.

PRODAN

6-Propionyl-2-(*N*,*N*-dimethylamino) naphthalene (PRODAN) is a highly fluorescent molecule first synthesized in 1979 by Weber and Ferris.[26] Following photoexcitation there is a drastic change in PRODAN's excited-state dipole moment due to charge transfer between its electron-donating dimethylamino group and electron-withdrawing propionyl groups connected to the aromatic ring (Figure 1.4). This effect causes the absorption and fluorescent spectra to be highly sensitive to the polarity of the environment which is demonstrated by a large solvochromatic shift on going from heptane to water (~130 nm). As a result, PRODAN has routinely been utilized as an optical probe in various biological and liquid based environments such as proteins, membranes, polar liquids, ionic liquids, and supercritical fluids.[27-34] However, its excited-state kinetics are complicated by the existence of at least two different emissive states according to the environment and the origin of its solvochramitic shift has been scrutinized.[35-41]

According to various studies there is an agreement that nonpolar and polar environments produce emission from a locally excited state (LE) and charge transfer state (CT) respectively.[42] Furthermore the excited state properties of these two states are significantly different. Obviously the existence of a different excited state according to the polarity of the environment could be problematic in characterizing the photophysical properties of a heterogeneous environment such as proteins. Several research groups have used analogues of PRODAN to probe protein dynamics and have reported some unusual results which were difficult for them to explain.[43-45] In Chapter 3, we explore the use of PRODAN within reverse micelles to create an analogous environment to that of proteins. We then discuss the consequences of using this probe in these type of environments and offer an alternative explanation to the results reported by these groups.

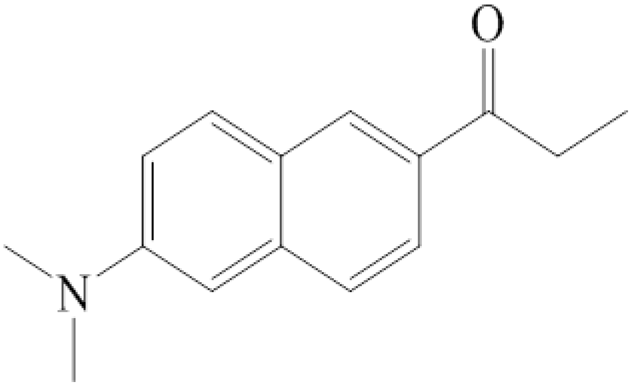

Figure 1.4. 6-Propionyl-2-(N,N-dimethyl)aminonaphthalene (PRODAN).

Cyclocurcumin

Tumeric is a yellowish pigment routinely used as a spice and food coloring agent in Asian countries.[46] The component originates from the plant *Curcuma longa* and has for decades been cited as providing antioxidant, anticancer, and anti-inflammatory benefits. Close analysis of this spice has revealed that its yellowish color is mainly caused by a group of structurally similar polyphenols called curcumanoids, mostly composed of curcumin (77%), and two of its closely related analogues, methoxycurcumin (17%) and bismethoxycurcumin (3%).[47] More recently there was the isolation of another curcumanoid called cyclocurcumin.[48] Since their isolation from turmeric, several studies have been performed to derive and understand the curcumanoids and their roles in these reported health benefits.[48,49] In one study the three major components exhibited significant inhibitory effects on the growth of MCF-7 tumor cancer cells while cyclocurcumin was found to be much less inhibitory.[49] Based on this finding the difference in antiproliferative properties may result from the structural differences between cyclocurcumin and the other curcumanoids. Cyclocurcumin lacks a diketo/keto-enol moiety group (Figure 1.5). Furthermore, previous studies on curcumin have indicated that this ketol-enol group undergoes excited-state intramolecular hydrogen atom transfer (ESIHT) which may play a role in its medicinal effects.[50-52] Based on these observations we have studied the photophysical properties of cyclocurcumin for the first time and compared them to that of curcumin in Chapter 6 in order to understand more about its excited state properties.

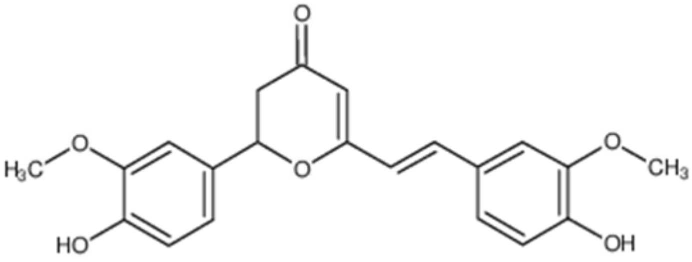

Figure 1.5. Cyclocurcumin

Biofuels: Cellulose, Cellulase and Ionic Liquids

The search for suitable biofuels has been an intense industrial focus for a number of years due to the increased need to replace fossil fuels. In this regards, a promising avenue is the conversion of biomass into ethanol. Cellulose is the main component of biomass and is the most biorenewable resource available today. Over the past several decades there has been increased research into developing an efficient means to hydrolyze cellulose into glucose that can then be subsequently converted into ethanol at price that is competitive with fossil fuel production.[53-59] Unfortunately, however, the critical hydrolysis step is often problematic as it requires a soluble substrate. Cellulose is a linear polymer of multiple D-glucose units (>500-10000) connected by β(1→4) linkages (Figure 1.6).[58] With an extended mesh of hydrogen bonding between chains, its structure is rigidly composed and as such has limited solubility in water and other organic solvents. This has led to the search for solvents that increase the dissolution of cellulose. Although the few that have been found are expensive, toxic, and unrecyclable.[60-62] Recently, however, the use of room-temperature ionic liquids has been reported to dissolve significant amounts of cellulose.[61,63-67]

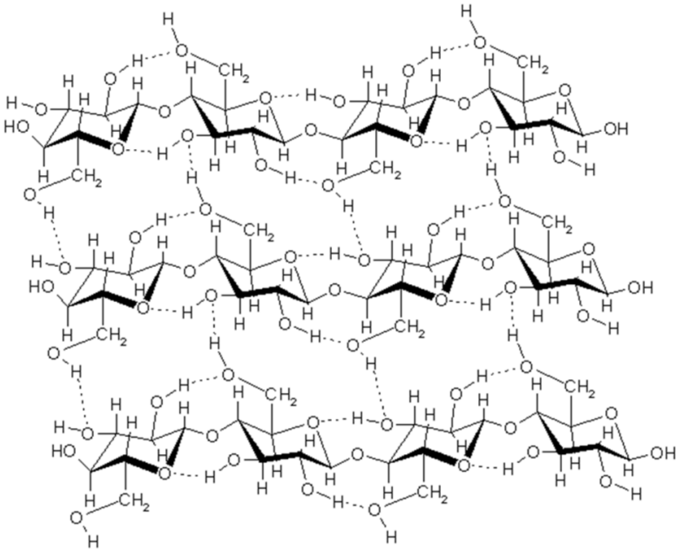

Figure 1.6. Structure of cellulose.

Room-temperature ionic liquids (RTILs) are defined as ionic liquids (IL's) with melting points less than or equal to ambient temperatures. Most ionic liquids are composed of large asymmetric organic cations such as imidazolium, N-methyl-N-alkylpyrrolidinium and 1-alkylpyridinium. The anionic portion is either organic or inorganic in nature and contains among others, nitrates, halides, toyslate, and triflate. Due to their environmentally friendly applications as replacements for hazardous organic solvents in organic synthesis, these liquids have often been referred to as the "green" solvents.[68-70] The interest in RTIL's can be attributed to their unique physiochemical properties. Generally, RTIL's have high thermal stability and very low vapor pressures.[68-70] In addition, based on the anionic and cationic combination, these properties can be altered (or tuned) to suite the application of interest. Because of this control, synthetic RTIL's have found their way into chemical research.[68-70]

The most extensive preliminary work on dissolving cellulose in ionic liquids was performed by Rogers and coworkers.[61,63,71] Out of the several ILs tested, 1-butyl-3-methylimidazolium chloride (BMIM Cl) was reported to provide the best results. This was explained as being due to the extensive hydrogen bonding between the hydroxyl groups of cellulose with the chloride ions. Reportedly the 1-allyl-3-methylimidazolium chloride (AMIM CL) has also proven capable of dissolving significant amounts of cellulose as well.[72] Aside from the "green" nature of ILs, two additional major benefits are realized. First the cellulose can be recovered (or regenerated) following dissolution in ILs.[73] Secondly these ILs appear to alter the cellulose structure in such a way as to allow for more efficient hydrolysis in water following regeneration.[73] This pretreatment step could provide another means to use ILs with other methods already in place within industry and academia.

Of the many methods to hydrolyze the glycosidic bonds of cellulose, the use of an enzyme called cellulase has been found to be one of the most economical.[74] Cellulase is produced by several different species. In order to use cellulase in ILs for hydrolysis of cellulose an important point to consider is preventing the enzyme's denaturation. The most studied enzyme in ionic liquids is *Candida antarctica* lipase B (Cal B) which is used for transesterification reactions.[75-78] A recent report demonstrated that cellulases can also dissolve in ILs and retain their activity.[79] Using this along with the aforementioned cellulose dissolvability in ILs, Bose et al examined the hydrolysis of cellulose by cellulase in eight different ILs.[80] It was found that only the methylimidazolium chloride (mim Cl) and tris-(2-hydroxyethyl)methylammonium methylsulfate (HEMA) were suitable solvents for this reaction, with HEMA being the most efficient. To this end, we further investigate the stability of cellulase in HEMA and the effect of its pretreatment on cellulose before subsequent hydrolysis. The results of this study are discussed in Chapter 7.

Organization of Thesis

Chapter 1 provides a general overview of the research area and topics presented in the later chapters.

Chapter 2 discusses the relavant instrumental and data analysis techniques that were used for the various studies throughout the thesis.

Chapter 3 uses fluorescence spectroscopy to determine the concentration of an efflux pump inhibitor in the feces of animals

Chapter 4 presents the solvation dynamics of the two emissive states of PRODAN in reverse micelles and discusses the consequences of using probes with complicated excited-state intramolecular processes in solvation dynamic studies of heterogenous enviroments such as proteins.

Chapter 5 discusses the experimental and theoretical solvation dynamics of C153 in wild type and modified proteins.

Chapter 6 studies the photophysical and spectral properties of a derivative of the medically relevant compound curcumin called cyclocurcumin in order to gain insight into the parent compound.

Chapter 7 examines cellulose hydrolysis by a pure form of cellulase in an ionic liquid and aqueous mixtures at various temperatures with the goal of increasing cellulose conversion to glucose for biofuel production.

Chapter 8 summarizes the work presented in this thesis with a general overview of the results and conclusions in chapters 3-7.

References

(1) Abramczyk, H. *Introduction to Laser Spectroscopy*; Elsevier: Amsterdam & Boston, 2005.

(2) Lakowicz, J. R. *Principles of Fluorescence Spectroscopy*; Springer: New York, 2006.

(3) Tkachenko, N. V. *Optical Spectroscopy: Methods and Instrumentation*; Elsevier: Amsterdam: Boston, 2006.

(4) Parson, W. W. *Modern Optical Spectroscopy*; Springer-Verlag Berlin Heidelberg: New York, 2007.

(5) Ingle, J. D.; Crouch, S. R. *Spectrochemical Analysis*; Prentice Hall: Englewood Cliffs, N. J., 1988.

(6) McQuarrie, D. A.; Simon, J. D. *Physical Chemistry: A Molecular Approach*; University Science Books: Sausalito, Calif., 1997.

(7) Weber, G. In *Adv. Protein Chem.*; Anfinsen, C. B., Ed.; Academic Press, Inc: New York, 1975; Vol. 29.

(8) Frauenfelder, H.; Sligar, S.; Wolynes, P. *Science* **1991**, *254*, 1598.

(9) Lin, Y.-W.; Wang, J. *Journal of Inorganic Biochemistry* **2013**, *129*, 162.

(10) Jordanides, X. J.; Lang, M. J.; Song, X.; Fleming, G. R. *The Journal of Physical Chemistry B* **1999**, *103*, 7995.

(11) Barbara, P. F.; Jarzeba, W. *Accounts of Chemical Research* **1988**, *21*, 195.

(12) Barbara, P. F.; Jarzeba, W. In *Advances in Photochemistry*; John Wiley & Sons, Inc.: 2007, p 1.

(13) Fleming, G. R.; Wolynes, P. *Phys. Today* **1990**, *43*.

(14) Hynes, J. T. *Annual Review of Physical Chemistry* **1985**, *36*, 573.

(15) Kahlow, M. A.; Jarzęba, W. o.; Kang, T. J.; Barbara, P. F. *The Journal of Chemical Physics* **1989**, *90*, 151.

(16) Jimenez, R.; Fleming, G. R.; Kumar, P. V.; Maroncelli, M. *Nature* **1994**, *369*.

(17) Maroncelli, M. *Journal of Molecular Liquids* **1993**, *57*, 1.

(18) Maroncelli, M.; Fleming, G. R. *J. Chem. Phys.* **1987**, *86*.

(19) Schumacher, M. A.; Miller, M. C.; Grkovic, S.; Brown, M. H.; Skurray, R. A.; Brennan, R. G. *Science* **2001**, *294*, 2158.

(20) Grkovic, S.; Hardie, K. M.; Brown, M. H.; Skurray, R. A. *Biochemistry* **2003**, *42*, 15226.

(21) Stermitz, F. R.; Lorenz, P.; Tawara, J. N.; Zenewicz, L. A.; Lewis, K. *Proceedings of the National Academy of Sciences* **2000**, *97*, 1433.

(22) Stermitz, F. R.; Tawara-Matsuda, J.; Lorenz, P.; Mueller, P.; Zenewicz, L.; Lewis, K. *Journal of Natural Products* **2000**, *63*, 1146.

(23) Ma, L.; Dolphin, D. *Phytochemistry* **1999**, *50*, 195.

(24) Ashby, K. D.; Wen, J.; Chowdhury, P.; Casey, T. A.; Rasmussen, M. A.; Petrich, J. W. *Journal of Agricultural and Food Chemistry* **2003**, *51*, 3502.

(25) Lee, M. R. F.; Theobald, V. J.; Ougham, H. J.; Dahl, A. V.; Lundby, F.; Scollan, N. D.; Wold, J. P. *Meat Science* **2010**, *86*, 966.

(26) Weber, G.; Farris, F. J. *Biochemistry* **1979**, *18*, 3075.

(27) Bondar, O. P.; Rowe, E. S. *Biophysical Journal* **1996**, *71*, 1440.

(28) Bondar, O. P.; Rowe, E. S. *Biophysical Journal* **1999**, *76*, 956.

(29) Krasnowska, E. K.; Gratton, E.; Parasassi, T. *Biophysical Journal* **1998**, *74*, 1984.

(30) Lasagna, M.; Vargas, V.; Jameson, D. M.; Brunet, J. E. *Biochemistry* **1996**, *35*, 973.

(31) Moreno, F.; Cortijo, M.; Gonzalez-Jimenez, J. *Photochemistry and Photobiology* **1999**, *69*, 8.

(32) Rottenberg, H. *Biochemistry* **1992**, *31*, 9473.

(33) Sommer, A.; Paltauf, F.; Hermetter, A. *Biochemistry* **1990**, *29*, 11134.

(34) Zeng, J. W.; Chong, P. L. *Biochemistry* **1991**, *30*, 9485.

(35) Balter, A.; Nowak, W.; Pawelkiewicz, W.; Kowalczyk, A. *Chem. Phys. Lett.* **1988**, *143*, 565.

(36) Catalan, J.; Perez, P.; Laynez, J.; Garcia Blanco, F. *Journal of Fluorescence* **1991**, *1*, 215.

(37) Marks, D.; Prosposito, P.; Zhang, H.; Glasbeek, M. *Chem. Phys. Lett.* **1998**, *289*, 535.

(38) Nowak, W.; Adamczak, P.; Balter, A.; Sygula, A. *J. Mol. Struct. THEOCHEM* **1986**, *32*, 13.

(39) Parusel, A. *Journal of the Chemical Society, Faraday Transactions* **1998**, *94*, 2923.

(40) Parusel, A. B. J.; Nowak, W.; Grimme, S.; Koehler, G. *Journal of Physical Chemistry A* **1998**, *102*, 7149.

(41) Parusel, A. B. J.; Schneider, F. W.; Kohler, G. *J. Mol. Struct. THEOCHEM* **1997**, *398-399*, 341.

(42) Rollinson, A. M.; Drickamer, H. G. *Journal of Chemical Physics* **1980**, *73*, 5981.

(43) Abbyad, P.; Shi, X.; Childs, W.; McAnaney, T. B.; Cohen, B. E.; Boxer, S. G. *J. Phys. Chem. B* **2007**, *111*, 8269.

(44) Bashkin, J. S.; McLendon, G.; Mukamel, S.; Marohn, J. *The Journal of Physical Chemistry* **1990**, *94*, 4757.

(45) Cohen, B. E.; McAnaney, T. B.; Park, E. S.; Jan, Y. N.; Boxer, S. G.; Jan, L. Y. *Science* **2002**, *296*, 1700.

(46) Goel, A.; Kunnumakkara, A. B.; Aggarwal, B. B. *Biochemical Pharmacology* **2008**, *75*, 787.

(47) Anand, P.; Thomas, S. G.; Kunnumakkara, A. B.; Sundaram, C.; Harikumar, K. B.; Sung, B.; Tharakan, S. T.; Misra, K.; Priyadarsini, I. K.; Rajasekharan, K. N.; Aggarwal, B. B. *Biochemical Pharmacology* **2008**, *76*, 1590.

(48) Kiuchi, F.; Goto, Y.; Sugimoto, N.; Akao, N.; Kondo, K.; Tsuda, Y. *Chemical & pharmaceutical bulletin* **1993**, *41*, 1640.

(49) Simon, A.; Allais, D. P.; Duroux, J. L.; Basly, J. P.; Durand-Fontanier, S.; Delage, C. *Cancer Letters* **1998**, *129*, 111.

(50) Adhikary, R.; Carlson, P. J.; Kee, T. W.; Petrich, J. W. *J. Phys. Chem. B* **2010**, *114*, 2997.

(51) Adhikary, R.; Mukherjee, P.; Kee, T. W.; Petrich, J. W. *J. Phys. Chem. B* **2009**, *113*, 5255.

(52) Kee, T. W.; Adhikary, R.; Carlson, P. J.; Mukherjee, P.; Petrich, J. W. *Aust. J. Chem.* **2011**, *64*, 23.

(53) Dadi, A. P.; Varanasi, S.; Schall, C. A. *Biotechnol. Bioeng.* **2006**, *95*, 904.

(54) Ladisch, M. R.; Ladisch, C. M.; Tsao, G. T. *Science (Washington, DC, United States)* **1978**, *201*, 743.

(55) Lynd, L. R.; Cushman, J. H.; Nichols, R. J.; Wyman, C. E. *Science (Washington, DC, United States)* **1991**, *251*, 1318.

(56) Su, Y.; Brown, H. M.; Huang, X.; Zhou, X.-d.; Amonette, J. E.; Zhang, Z. C. *Appl. Catalysis A* **2009**, *361*, 117.

(57) Xiang, Q.; Lee, Y. Y.; Pettersson, P. O.; Torget, R. W. *Appl. Biochem. Biotechnol.* **2003**, *107*, 505.

(58) Zhang, Y.-H. P.; Lynd, L. R. *Biotechnol. Bioeng.* **2004**, *88*, 797.

(59) Zhao, H.; Holladay, J. E.; Brown, H.; Zhang, Z. C. *Science (Washington, DC, United States)* **2007**, *316*, 1597.

(60) Suganuma, S.; Nakajima, K.; Kitano, M.; Yamaguchi, D.; Kato, H.; Hayashi, S.; Hara, M. *Journal of the American Chemical Society* **2008**, *130*, 12787.

(61) Swatloski, R. P.; Spear, S. K.; Holbrey, J. D.; Rogers, R. D. *J. Am. Chem. Soc.* **2002**, *124*, 4974.

(62) Zhang, H.; Wu, J.; Zhang, J.; He, J. *Macromol.* **2005**, *38*, 8272.

(63) Fort, D. A.; Remsing, R. C.; Swatloski, R. P.; Moyna, P.; Moyna, G.; Rogers, R. D. *Green Chem.* **2007**, *9*, 63.

(64) Liu, Q.; Janssen, M. H. A.; van Rantwijk, F.; Sheldon, R. A. *Green Chemistry* **2005**, *7*, 39.

(65) Phillips, D. M.; Drummy, L. F.; Conrady, D. G.; Fox, D. M.; Naik, R. R.; Stone, M. O.; Trulove, P. C.; De Long, H. C.; Mantz, R. A. *Journal of the American Chemical Society* **2004**, *126*, 14350.

(66) Zhao, H.; Jones, C. L.; Baker, G. A.; Xia, S.; Olubajo, O.; Person, V. N. *J. Biotechnol.* **2009**, *139*, 47.

(67) Zhu, S.; Wu, Y.; Chen, Q.; Yu, Z.; Wang, C.; Jin, S.; Ding, Y.; Wu, G. *Green Chemistry* **2006**, *8*, 325.

(68) Earle Martyn, J.; Seddon Kenneth, R. In *Clean Solvents*; American Chemical Society: 2002; Vol. 819, p 10.

(69) Freemantle, M. *Chemical & Engineering News Archive* **1998**, *76*, 32.

(70) Welton, T. *Chemical Reviews* **1999**, *99*, 2071.

(71) Remsing, R. C.; Swatloski, R. P.; Rogers, R. D.; Moyna, G. *Chem. Commun.* **2006**, 1271.

(72) Doherty, T. V.; Mora-Pale, M.; Foley, S. E.; Linhardt, R. J.; Dordick, J. S. *Green Chem.* **2010**, *12*, 1967.

(73) Hendriks, A. T. W. M.; Zeeman, G. *Bioresource Technology* **2009**, *100*, 10.

(74) Beldman, G.; Searle-Van Leeuwen, M. F.; Rombouts, F. M.; Voragen, F. G. J. *European Journal of Biochemistry* **1985**, *146*, 301.

(75) Lau, R. M.; Rantwijk, F. v.; Seddon, K. R.; Sheldon, R. A. *Org. Lett.* **2000**, *2*, 4189.

(76) Lau, R. M.; Sorgedrager, M. J.; Carrea, G.; Rantwijk, F. v.; Secundo, F.; Sheldon, R. A. *Green Chem.* **2004**, *6*, 483.

(77) Park, S.; Kazlauskas, R. J. *Curr. Opin. Biotechnol.* **2003**, *14*, 432.

(78) Sheldon, R. A.; Lau, R. M.; Sorgedrager, M. J.; Rantwijk, F. v.; Seddon, K. R. *Green Chem.* **2002**, *4*, 147.

(79) Wang, Y.; Radosevich, M.; Hayes, D.; Labbé, N. *Biotechnol. Bioeng.* **2010**, *108*, 1042.

(80) Bose, S.; Armstrong, D. W.; Petrich, J. W. *J. Phys. Chem. B* **2010**, *114*, 8221.

CHAPTER 2: EXPERIMENTAL METHODS AND DATA ANALYSIS

Fluorescence Spectrometer

The workhorse for steady state (or equilibrium) fluorescence/emission experiments is the fluorometer (fluorescence spectrophotometer). The design used in our lab is presented in Figure 1.[1,2] The main components are a light source, two wavelength selectors, a detector, and a computer. The light source is a Xe arc lamp with continuous emission in the ultraviolet and visible regions. Two monochromators referred to as excitation and emission, based on their location with respect to the excitation and emission beams, are used to select the desirable wavelength. There are entrance and exit slits on the monochromators that control the intensity and bandwidth of the light. The detector is a photomultiplier tube (PMT) that converts the fluorescence signal into a voltage reading which can be analyzed through a computer. The working principle is as follows. An elliptical mirror collects Xe lamp illumination and directs it into the entrance slit of the excitation monochromator. Within the monochromator the light is collimated by parabolic mirror 1 and sent to the diffraction grating. The grating can effectively disperse light into a range of wavelengths from 200-900 nm. This diffracted light is then refocused by parabolic mirror 2 and sent to the exit slit which serves to select a narrow band pass of the wavelengths coming from the grating. The selected wavelength(s) are then sent into the sample compartment and sample cell from which some of the light is absorbed. A portion of the emission from the sample is collected at a 90 degree angle with respect to the excitation beam by the emission monochromator. The 90 degree angle is preferred to reduce scattered excitation light from interfering with the analysis and damaging the detector if not prevented by the emission monochromator. The selected wavelengths from the emission monochromator are then sent into the PMT and computer for conversion and analysis.

A fluorescence spectrum is obtained by variation of the emission monochromator wavelength at a fixed excitation wavelength. The excitation spectrum is recorded in a similar but reverse manner – excitation wavelength varied at a constant emission wavelength. Due to the lamp intensity fluctuations with wavelength, the intensity needs to be continuously monitored and compared with a reference to prevent instrumental induced spectral anomalies. This is corrected by the placement of beam splitter at a point between the Xe arc lamp and sample cell. The beam splitter directs ~8% of the arc lamp light to a photodiode (PD). Next the instrument takes the ratio of fluorescence to reference signal which prevents lamp-induced spectral changes from interfering with the measurement. Furthermore, the grating transmission and PMT efficiencies vary with wavelength. As a result, a correction factor is needed to correct for these response characteristics. The wavelength dependent correction factor (γ) and fluorescence intensity (I_{exp}) of the sample are multiplied together to produce the instrument independent fluorescence spectrum as[3]

$$I_{corr}(\lambda) = \gamma(\lambda) I_{exp}(\lambda) \tag{2.1}$$

Due to instrumental drift or variations with time, calibration of the monochromators should be checked and performed routinely before performing experiments. This is done by examining the spectra of the Xe arc lamp and water raman with appropriate parameters.

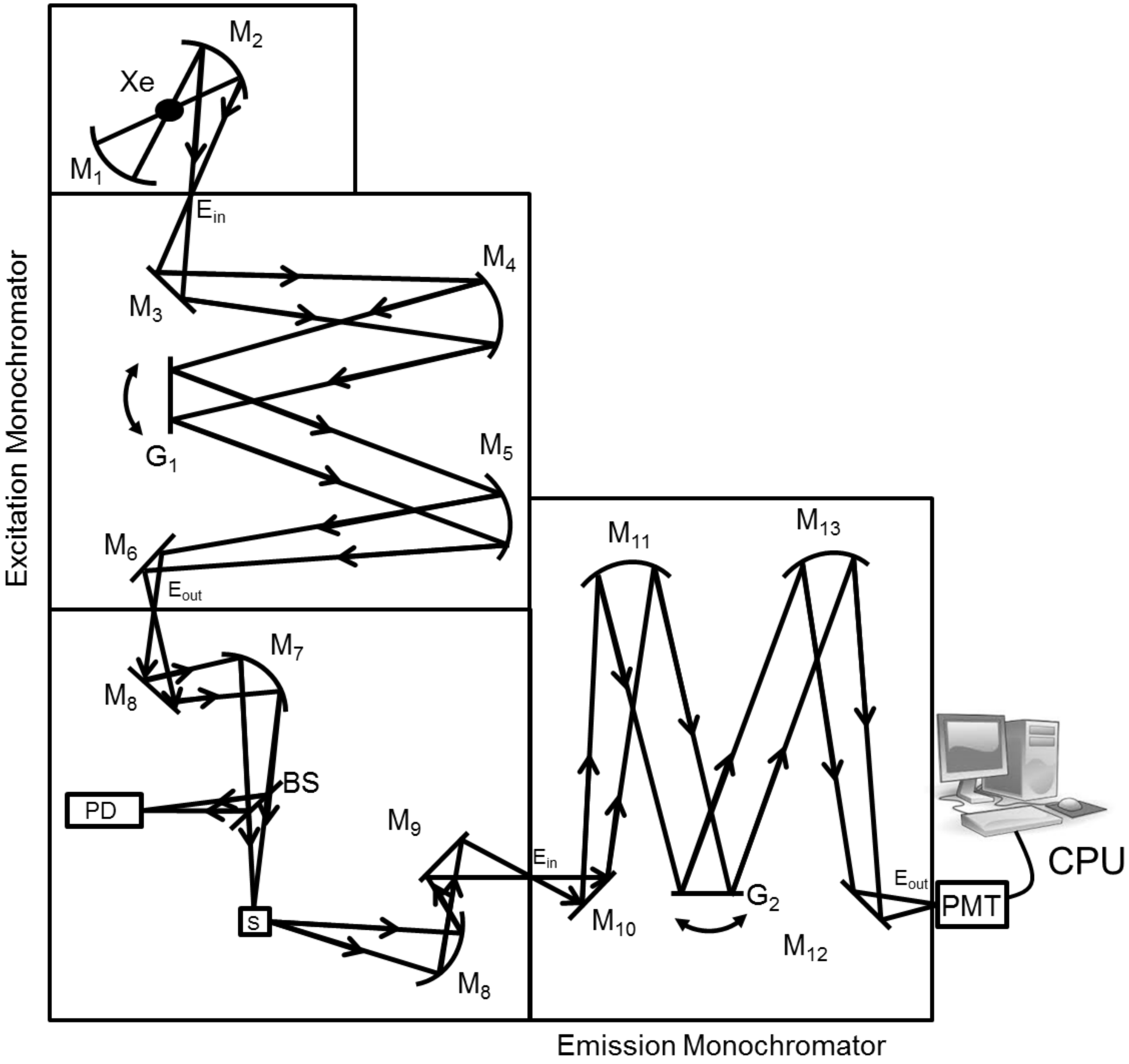

Figure 2.1. Schematic and working principles of the fluorescence spectrophotomter. Xe – Xenon Arc Lamp, $E_{in/out}$ – entrance/exit slits, M – Mirror, G – Grating, BS – Beam Splitter, PD – Photodiode, S – Sample Holder, PMT – Photomultiplier Tube, CPU – Computer.[1,2]

Solid State Lasers: Nd:YAG and Ti:Sapphire

Solid state lasers consists of mediums in which the active lasing ions have been added as an impurity in an otherwise optically transparent solid crystalline or glass host.[4-12] Most commonly the impurity or dopant comes from the rare earth or transition metal ions. Since their inception, many types of solid state lasers have been invented and they can generally be classed into two groups, tunable and nontunable, based on their wavelength availability.

One of the most commonly used nontunable solid state lasers is the Nd:YAG.[4-12] The dopant is the rare earth neodymium (III) ion (Nd $^{3+}$) and its placement within an yttrium-aluminum garnet (YAG) host supplies the active medium of this laser. A detailed investigation into the electronic structure of Nd $^{3+}$ provides information concerning the reasons for its effective use as a lasing ion. The Nd^{3+} ion's ground state, E_0 leaves three unpaired electrons in the 4f shell. The 4f shell is where electronic transitions responsible for lasing action occur. This shell is effectively shielded by the filled subshells, $5s^2$ and $5p^6$. As such, this prevents significant alterations from occurring to its electronic structure by its inclusion within a glass or crystalline matrix such as YAG.[4,6-8,12] But the small interaction that does occur with the crystal field of the host effectively allows the 4f shell to be split into 2J+1 levels, thereby making it a four-level laser.[12]

Typically the Nd:YAG is optically pumped by a flash lamp which excites the Nd^{3+} from the ground, E_0, to the excited, E_4, energy level. The excited state ions in E_4 quickly undergo a transition to E_3. The lifetime of the excited Nd^{3+} ions in E_3 is ~100-230 μs.[8,12] Subsequent relaxation to E_2 results in the emission of a photon with a wavelength of ~1064 nm. [4-12] The necessary condition of population inversion then occurs between E_3 and E_2. From E_2, fast relaxation back to E_0 resupplies the ground state with neodymium ions. This laser can be used as a continuous or pulsed light source. If Q-switching is involved, then pulses as short as a few nanoseconds can be emitted.[12] In addition, this type of laser has high gain even with low excitation powers.[12,13] The bandwidth around the ~1064 nm wavelength is small, but the high efficiency and thus low threshold pump powers required outweigh these types of disadvantages. Since this laser is restricted to one wavelength, nonlinear optics allowing for 2nd, 3rd, and 4th harmonic generation are usually required to give wavelengths of 532, 355, and 266 nm, respectively. The Nd:YAG is a very robust and reliable laser. It was used as a pump source of the Ti:Sapphire laser used in subsequent chapters.

Tunable lasers are desirable commodities for applications in not only ultrafast time resolved laboratories but also in other fields such as medicine and industry.[12] Initially the ability to change wavelengths was restricted to the use of fluorescent dyes as the laser gain medium.[8-10,12] Changing the dye allowed access to other wavelengths. However, laser dyes are often problematic due to various issues such as toxicity risks (from dye and/or solvent) to the operator, photobleaching after short-term operation (~100 hrs), and costly pumping sources. The inception of the solid state tunable Ti:Sapphire lasers in 1986 solved many of these issues and brought with them other desirable features such as ease of construction and simplified short pulse operations inaccessible in other types of lasers.[14] As a result, the Ti:Sapphire laser has quickly risen to become the most utilized tunable laser in use today.

The Ti:Sapphire medium is composed of a ~0.1-0.5% dopant of titanium in a host matrix of sapphire (Al_2O_3).[9,14] Small amounts of Ti^{3+} replace Al^{3+} at octahedral symmetry sites within the crystal lattice. The Ti^{3+} ion has a single free electron in the 3d subshell. This five-fold degenerate energy shell (neglecting spin) is then split into a doubly degenerate excited state ^2E and a triply degenerate ground state $^2T_2$ by perturbation from the surrounding sapphire crystal field. Lasing action happens between these two states (Figure 2.2). There are no energy levels greater than ^2E which eliminates possibilities for excited-state absorption. This is an important feature for its efficient lasing and tuning capabilities. As was the case for Nd:YAG, Ti:Sapphire is also a four-level laser. What makes this laser tunable and different than the Nd:YAG is the broad range of energy levels available in its transitions. The Nd:YAG has only two single band states, while for Ti:Sapphire the two states (^2E and $^2T_2$) are broadened by strong coupling with the electrons and vibrational levels of the sapphire crystal. Ti:Sapphire and other similar tunable solid state lasers are sometimes termed vibronic lasers due to this phenomenon.[9,10,12] This creates access to several vibrational levels in the upper and lower state, thereby allowing a wide range of wavelength tunability (~680-1100 nm). According to the uncertainty principle, broad wavelength bands can produce short pulse widths in time. Ti:Sapphire lasers have a broad emission band of ~400 nm and reportedly have the capability to produce pulses as short as 2-3 fs.[10] The broad absorption band of these lasers with a center ~500 nm allows optical pumping with a variety of laser sources such as Argon, Nd:YLF, or the aforementioned Nd:YAG. In our lab we use a frequency-doubled Nd:YAG from Spectraphysics with output powers of up to 5.5 W. Ti:Sapphire lasers have the ability to undergo passive modelocking to produce short pulses.

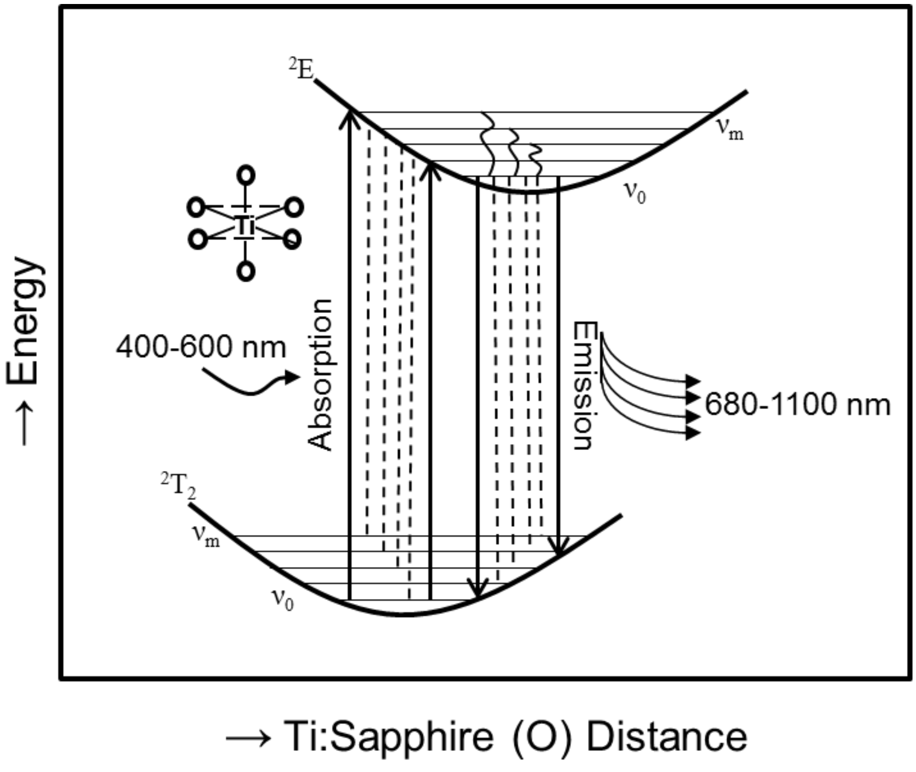

Figure 2.2. Diagram of the titanium (Ti) energy levels in an octahedral configuration within the sapphire crystal lattice. The wavy lines in ^2E represent nonradiative/vibrational relaxations to ν_0.

Ultrashort Pulses - Modelocking

An essential element of many ultrafast time-resolved spectroscopy techniques is the interrogation of a system by a very short delta pulse(s), much shorter than the process under study, which will disturb the system just enough to form a new state that can be followed with time to gain information about the process. In order to do this though, ultrashort pulses need to be created. Various methods have been developed through the years. During the early years of ultrafast spectroscopy two of the most common methods were Q-switching and cavity dumping. However, these methods produced at best pulse widths of a few nanosceconds. It wasn't until the early 1960s when modelocking was developed that ultrafast spectroscopy took an enormous leap with studies on the femtosecond time scale.[12] This progress was made possible by the development of the modelocking technique. To understand modelocking, there at first needs be some background given pertaining to the theory.

A laser cavity can operate over a bandwidth of frequencies depending on the medium. This is called the gain bandwidth. For example the Ti:Sapphire can produce gain bandwidths ~100 THz while that of the Nd:YAG is ~100 GHz.[7,8,12] In traveling back and forth between the end mirrors of the cavity, the frequencies of this bandwidth will constructively and deconstructively interfere with one another to produce a certain number of standing waves. These standing waves are termed longitudal modes. The number of modes supported by the cavity is dependent on the length (L) between the cavity mirrors

$$N = \frac{2L}{\lambda} \tag{2.2}$$

where N is the number of modes and λ being the wavelength of light the laser operates. Normally the L is fairly large. For a Ti:Sapphire cavity of 30 cm this would correspond to 250000 modes. Normally these modes oscillate independent of one another without a fixed phase relationship. Assuming that each mode can be represented as a planar wave $E(t) = E_0e^{i\omega t}$ with an angular frequency of ω_0 and that there are $2n+1 = N$ modes, then the total electric field of light can be expressed as[12,15]

$$E(t) = E_0e^{i\omega_0 t}\frac{\sin\frac{N(\Delta\omega_0 t + \Delta\varphi_n)}{2}}{\sin\frac{(\Delta\omega_0 t + \Delta\varphi_n)}{2}} \tag{2.3}$$

in which $\Delta\varphi_n$ and $\Delta\omega_n$ are the difference in phase and frequency between modes, respectively. It can be seen from this equation that if the phase difference varies with time then so does the electric field of light. The output of the laser is random and noisy (Figure 2.3). This is the continuous wave (CW) condition of the laser. If the phase becomes fixed the I(t) becomes[12,15]

$$I(t) = E(t)^2 = E_0^2\frac{\sin^2\frac{N(\Delta\omega_0 t + \Delta\varphi_n)}{2}}{\sin^2\frac{(\Delta\omega_0 t + \Delta\varphi_n)}{2}} \tag{2.4}$$

Based on diffraction theory the maxima occur when the terms in parentheses equal zero. From this the I(t) is shown to be periodic in time with repetitive pulses of light. The time between pulses, T, can be inferred from successive maxima which is found to be 2π. Thus mode locked pulses have a time of

$$T = \frac{2\pi}{\Delta\omega_n} = \frac{2\pi}{2\pi\Delta\nu_n} = \frac{2L}{c} \tag{2.5}$$

between them where $\Delta\nu_n$ is the difference in frequency between adjacent modes. The temporal width of each pulse is found in a similar way but with the minima of 2.4. This occurs when the numerator is zero and therefore gives a pulse duration of

$$t_p = \frac{2\pi}{N\Delta\omega_n} = \frac{2L}{Nc}. \tag{2.6}$$

This shows that an essential goal with mode-locking is to bring as many of these N modes as possible, in fixed phase with one another to produce the shortest possible pulses.

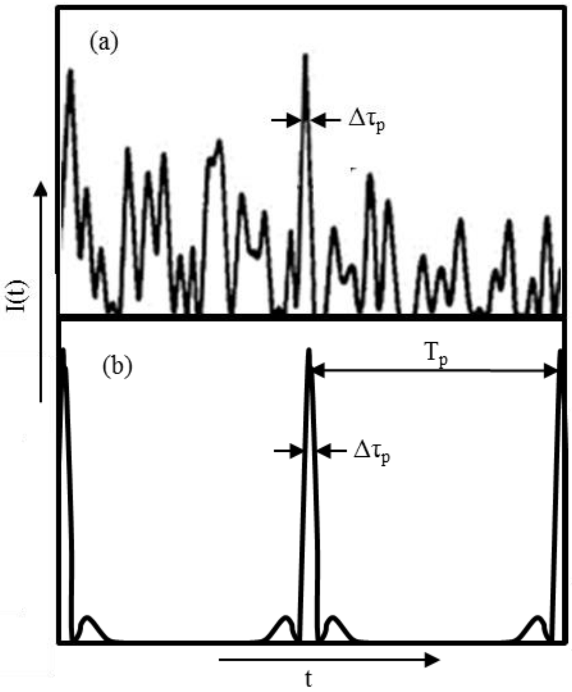

Figure 2.3. The intensity versus time output from an un-mode-locked (a) and mode-locked laser (b). The intensity in (a) is random in nature with occasional intense burst of light. In (b) the intense bursts are favored and amplified with phases fixed between modes.

Passive Mode-locking

The two types of general modelocking mechanisms are called passive and active. Active modelocking is based on the use of some external electrical signal for pulse generation in the oscillator. While passive modelocking ultilizes the light itself to induce a change in an optical component within the oscillator which will favor pulses of light. Passive modelocking is generally preferred for ultrafast pulses since the temporal pulse width achieved can be in the femtosecond regime.[16] The work presented in this thesis was based on the use of this mechanism for ultrafast pulses. Therefore this section will be focused on the passive modelocking technique.

A saturable absorber is a material that displays some intensity-dependent transmission of light. This absorber will saturate at low intensities of light while allowing high intensities of light to transmit.[12,17-19] Usually the absorber is a dye, but it could also be a semiconductor. Considering the former, a cell holding the dye is typically placed close to and in front of the rear mirror of the laser cavity. At the onset of laser medium pumping, the dye will absorb enough light to prevent the gain in the laser cavity from overcoming the losses. In addition, the longitudal modes are out of phase and the output intensity of the laser is random in time (Figure 2.3a). As amplification increases eventually the dye becomes saturated and its ground state population depleted. At this point the dye suddenly becomes transparent thereby allowing highly amplified light to pass. It will then reflect off the rear mirror, go back through the now transparent dye cell into the medium and cause complete depletion of the population inversion, thus resulting in an intense pulse of light. The decay or recovery time of the dye is typically on the order of a few ps.[12] Following this time frame it will repeatedly complete the absorption and transmit cycle again, resulting in a train of pulses will result from this to produce a modelocked laser. A drawback of this technique is the difficulty in maintaining long-term stability. Often frequent adjustment of dye concentration and proper maintenance of resonator alignment conditions are needed to ensure its stability.[12]

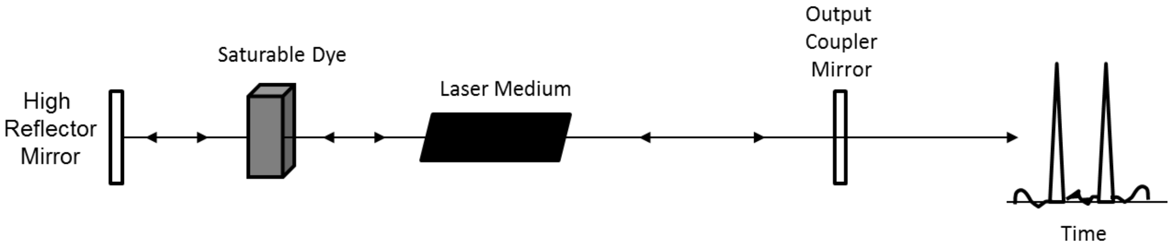

Figure 2.4. General scheme of passive modelocking with a saturable absorber dye.

Kerr lens modelocking is based on the Kerr lens effect. The Kerr lens effect is an intensity-dependent index of refraction change that results when an intense beam of light with

Guassian intensity distribution is directed and passed through a bifringent nonlinear material.[8,9] The basic principles of this type of modelocking are presented in Figure 2.5. The intensity profile of the laser causes the index of refraction of the material to increase at the center of the beam and to decrease as the intensity decreases away from the center. The intense section is refracted more towards the center than the less intense portion. In effect the beam becomes "self-focused" by the development of a transient lens with a positive focal length within the material.[20] As the beam travels through the media the beam will become smaller. Introduction of an aperture some distance from the Kerr lens media can take advantage of this self-focusing effect to favor the pulsed mode. This occurs because in a continuous wave or unmodelocked laser, random fluctuations of the pulse intensity occur with time and the various modes propagating in the cavity are out of phase. With the aperture the lower intensity parts of the beam are blocked by divergence and lack of focusing while the more intense parts are allowed to pass. The intense parts experience low loss and begin to become more amplified during each round trip in the cavity. After several of these low loss-amplification cycles, intense pulses of light are produced resulting in a mode-locked train of pulses. Tighter focusing and shrinking of the beam width will produce shorter pulses in time. Often a telescope is incorporated in the cavity around the Kerr lens medium to enhance the self-focusing effect. However, Kerr lens mode-locking is not automatic. A perturbation is often needed to initiate locking of the phases together to induce a pulsed mode. This could be done by a tap or vibration on one of the optical components within the oscillator.

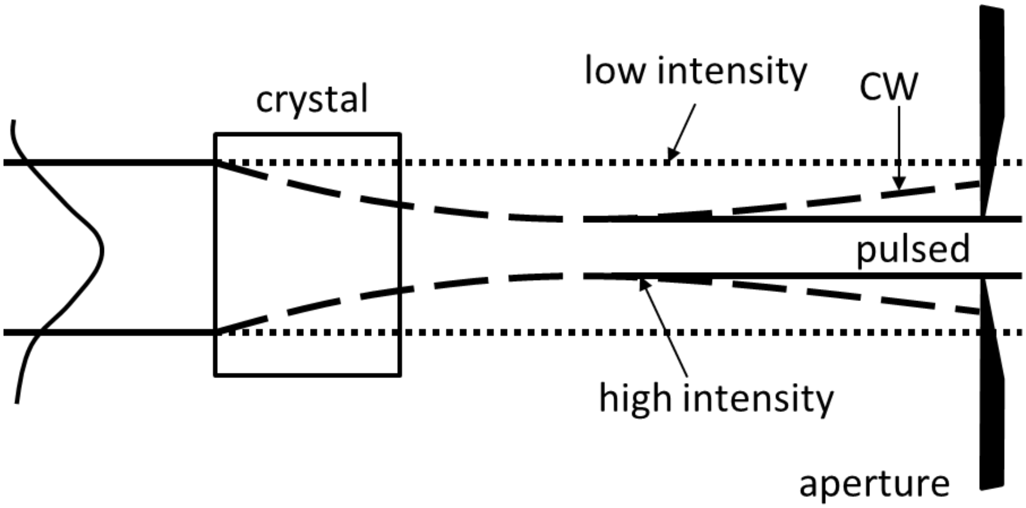

Figure 2.5. General scheme of Kerr lens modelocking with an aperture. CW – continuous wave.

Ti:Sapphire Oscillator

The Ti:Sapphire laser in our lab is based on the design developed by Kapteyn and Murnane in 1993.[21] The setup in our lab is presented in Figure 2.6. The pump is a Nd:YAG SpectraPhysics laser generating the second harmonic 532 nm with a pumping power of 5W. The cavity contains two spherical mirrors (M1 & M2), three flat mirrors (M3, M4, and OC), a Ti:Sapphire rod cut at the Brewster angel, and two prisms (P1 and P2). With this design the laser can operate in pulsed mode by means of self modelocking. The two spherical mirrors act as a telescope to increase the Kerr Lens effect. The two prisms compensate for wavelength-dependent dispersion by the optics in the cavity. The optics in the laser cavity, specifically the Ti:Sapphire rod causes the pulse to broaden due to positive group velocity dispersion (GVD). This type of dispersion widens the temporal pulse as a result of the shorter (bluer) wavelengths traveling slower than the longer (redder) wavelengths on passage through the cavity. The prism pair minimizes this effect by introducing negative GVD. The P1 prism disperses the beam with shorter wavelengths refracting more than the faster moving longer wavelengths. Upon entrance to P2 the longer wavelengths must transverse more glass. Subsequent reflection from the high reflector M4 and back through the prism pair into the cavity completes the process needed to cancel the GVD from the rod. Laser light leaves the cavity through the OC which transmits at ~10%. The output power is ~600-800 mW in CW mode with a repetition rate of ~88 MHz. The bandwidth is between 680-1100 nm with the best stability at ~800 nm. Tuning to different wavelengths is achieved by using a slit in front of the high reflector. Careful adjustments of the prisms (more glass or less) can also provide tunability. To mode-lock the laser, we first optimize the power and alignment. M1 or M2 is then tapped to add the perturbation needed to trigger mode-locking. The pulse train is monitored through oscilloscopes to check stability, repetition rate, and wavelength.

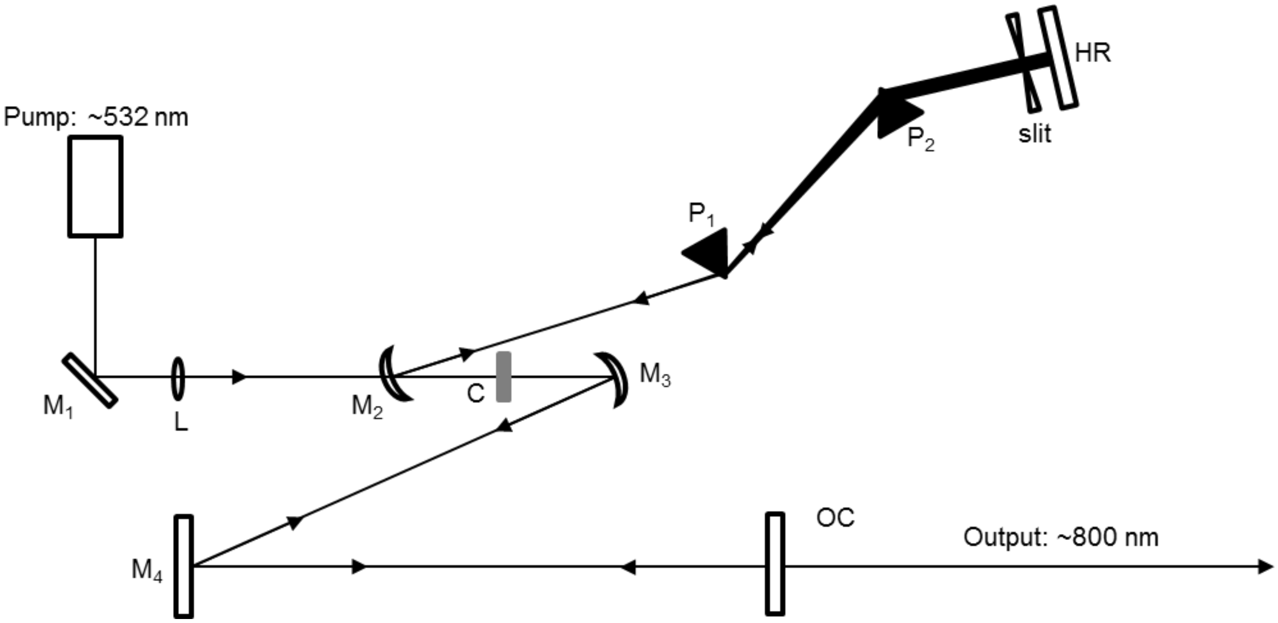

Figure 2.6. Schematic of the home-built Ti:Sapphire Oscillator. M_1 and M_4 are plane mirrors, while M_2 and M_3 are curved mirrors. P: Prism, HR: high reflector, OC: output coupler.

Second Harmonic and Sum Frequency Mixing Generation

Many relevant chemical and biochemical systems require absorption wavelengths in the visible and near UV regions of the spectrum to induce fluorescence. The tunability of the Ti:Sapphire laser is not enough to gain access to these wavelengths. Thus there is a need to create these wavelengths by some other means. If cost is not an issue, then buying multiple lasers is an option. However, this would likely be instrumentally cumbersome and quite expensive. Harmonic generation is a more affordable option allowing access to wavelengths from the ultraviolet to visible and IR.

When light propogates through a dielectric material, the electrons of the atoms in the material are displaced from equilibrium positions and induced to oscillate by the electric field component of the light. This type of oscillation is termed induced polarization. The magnitude of this polarization, P, will depend on the electric field strength, E, and can be written as[8]

$$\boldsymbol{P} = \varepsilon_0 \chi \boldsymbol{E} \tag{2.7}$$

where the bolded text indicates that these variables are vectors, ε_0 is the permittivity of free space and χ is the medium susceptibility. At low light intensities this equation holds and the induced polarization responds in a linear fashion (i.e. as the light intensity increases so does the polarization). However as the intensity increases this equation breaks down and can no longer adequately describe the polarization. At high intensities the above equation must be expanded into a power series to account for the observed phenomena as[8]

$$P = \varepsilon_0(\chi^{(1)}E^1 + \chi^{(2)}E^2 + \chi^{(3)}E^3 + \ldots\ldots\ldots + \chi^{(n)}E^n) \tag{2.8}$$

where for simplicity it is assumed that P and χ are scalar quantities. The (1), (2), (3),…..(n) are the 1st, 2nd, 3rd,….nth orders of the susceptibility. The linear, first-order term, is most dominant with low powers of light, and the electric field of light is linear with respect to polarization. When the incident power of light becomes very significant (eg. from pulsed lasers) the second and third polarization orders can contribute enough to result in a nonlinear relationship between the electric field and induced polarization of the medium. It is useful to examine these terms separately. The second order term is significant here as it contains information required to account for second harmonic as well as sum and difference frequency mixing generation of light.

If we consider an oscillating electric field interaction with the medium then the total electric field can be written as[8]

$$E(t) = E_0^* e^{-i\omega t} + E_0 e^{i\omega t} \tag{2.9}$$

in which the first term is the complex conjugate of the field. Now the second order term will be

$$P^{(2)} = \varepsilon_0 \chi^{(2)} E^2 = \varepsilon_0 \chi^{(2)} [E^* E + E E^* + E^2 e^{-i2\omega t} + E^2 e^{+i2\omega t}] \tag{2.10}$$

The last 2ω terms are responsible for second harmonic generation and become significant under intense light. Considering two photons of light with different frequencies ω_1 and ω_2 propagating through the medium, the total electric field in Equation 2.9 will have an additional term with ω_2 added and the second order polarization term will be recast as[8]

$$\begin{aligned} P^{(2)} &= \varepsilon_0 \chi^{(2)} E^2 \\ &= \varepsilon_0 \chi^{(2)} [(E_1^2) e^{-i2\omega t} + (E_1^{*2}) e^{-i2\omega t} + (E_2^2) e^{-i2\omega t} + (E_2^{*2}) e^{-i2\omega t} \\ &\quad + 2E_1 E_1^* + 2E_2 E_2^* + 2E_1 E_2 e^{-i(\omega_1+\omega_2)t} \\ &\quad + 2E_1^* E_2^* e^{-i(\omega_1+\omega_2)t} + 2E_1 E_2^* e^{-i(\omega_1-\omega_2)t} \\ &\quad + 2E_1^* E_2 e^{-i(\omega_1-\omega_2)t}]. \end{aligned} \tag{2.11}$$

The sum and difference frequency terms are apparent by the plus and minus signs in the exponential. Note if the material is symmetrical then the polarization term will be reduced to odd terms since the even terms such as $E_2 = -E_2$ and $P_2 = -P_2$, which can only be true if E = P = 0). Thus the even terms will cancel leaving the third, fifth, seventh, etc polarization terms to account for frequency generations.

Phase Matching

The above discussion could lead to the assumption that with sufficient intensity several different frequencies are transmitted when passing two pulses of different frequencies (e.g. ω_1 and ω_2) through a nonlinear crystal and that the desired frequency could be obtained by filtering of the others. However, this is not generally the case. In order to enhance the sum, difference, or harmonic generation outputs an important criterion must be met. The phase of the interacting pulses must constructively interfere with one another to produce the "new frequency". This criterion is known as the phase matching condition which is generally written as[8,10,12]

$$k_3(\omega_3) = k_1(\omega_1) + k_2(\omega_2) \qquad (2.12)$$

Where the wave vector k_3 at frequency ω_3 is the generated wave output from mixing incident photons of $k_1(\omega_1)$ and $k_2(\omega_2)$. For second harmonic generation the right side would require the summation of two equal wave vectors (e.g. $2k_1(\omega_1)$). Equation 2.12 can also be rewritten as

$$\Delta k = k_3(\omega_3) - k_1(\omega_1) - k_2(\omega_2) = 0 \qquad (2.13)$$

in which Δk represents the phase mismatch. To be phased matched $\Delta k = 0$. But the phase velocity and wave vector of any wave passing through an optically transparent medium is dependent on the refractive index of the crystal as $v_p = \omega/k = c/n(\omega)$. As such, different frequencies will have different velocities and phases. This dispersion means that it is not possible to generate nonlinear output frequencies from just any medium since the index of refraction is linearly dependent on the frequency of light (ie $n_3(\omega_3) > n_2(\omega_3) > n_1(\omega_1)$). To overcome this it is best to use nonlinear birefringent crystals.

In a birefringent crystal the refractive index is dependent on both the frequency and orientation of the polarization vector of light in reference to the crystal's optical axis.[8,10,12,22-24] Although there are crystals with dual optical axis (biaxial), the most common for nonlinear frequency generations are uniaxial. In this type of crystal there are two different indices of refraction called the ordinary and extraordinary. When a linearly polarized beam of light passes through a uniaxial birefringent medium it is split into two orthogonal rays called the ordinary (o-ray) and extraordinary (e-ray) beams. Due to differences in the index of refraction these two beams will have different phase velocities. The o-ray beam is polarized perpendicular to the crystal's optical axis, and experiences a constant index of refraction (n_o) and phase velocity regardless of its propagation direction. In contrast the extraordinary beam has a phase velocity that can change according to its propagation of direction through the crystal. More specifically, the e-ray experiences an index of refraction (n_e) that is dependent on the angle of the e-ray's direction of propagation with respect to the optical axis of the crystal as[12]

$$n_e(\theta) = \frac{n_o n_e}{[(n_o)^2 sin^2\theta + (n_e)^2 cos^2\theta]^{1/2}} \tag{2.14}$$

The necessary phase matching condition can then be described through examination of Figure 2.7a. The trace of the crystal's n_o is a sphere that is perpendicular to its optical axis (-z) in the x-y plane. As can be seen it does not change regardless of the incident beam's propagation. The trace of n_e is represented by an ellipse that rotates about the optical axis in the y-z plane. At different angles the n_e will bisect the n_o. The index of refraction of n_e is a minimum when θ=0 (ie $n_e = n_o$). The value is a maximum at $\theta = 90^0$. Considering second harmonic generation using a negative uniaxial ($n_e<n_o$) crystal, the ordinary and extraordinary rays would be the fundamental, ω_1, and SHG, $2\omega_1$, frequencies, respectively, in order to compensate for the dispersion of the higher frequency SHG using the birefringence of the crystal.[22] The angle when $n_e(2\omega_1, \theta) = n_o(\omega_1)$ would be the phase matching angle (2.7b). This angle can be determined from equation 2.14 using $1 - sin^2\theta$ in place of $cos^2\theta$. Solving for $sin^2\theta$ gives[22]

$$sin^2\theta = \frac{\frac{1}{n_o(\omega)^2} - \frac{1}{n_o(2\omega)^2}}{\frac{1}{n_e(2\omega)^2} - \frac{1}{n_o(2\omega)^2}} \tag{2.15}$$

From this, the angle that produces maximum SHG can be obtained. In practice this usually means adjusting or rotating the crystal's angle with respect to the incident beam of light. This is called the angle tuning technique.[8]

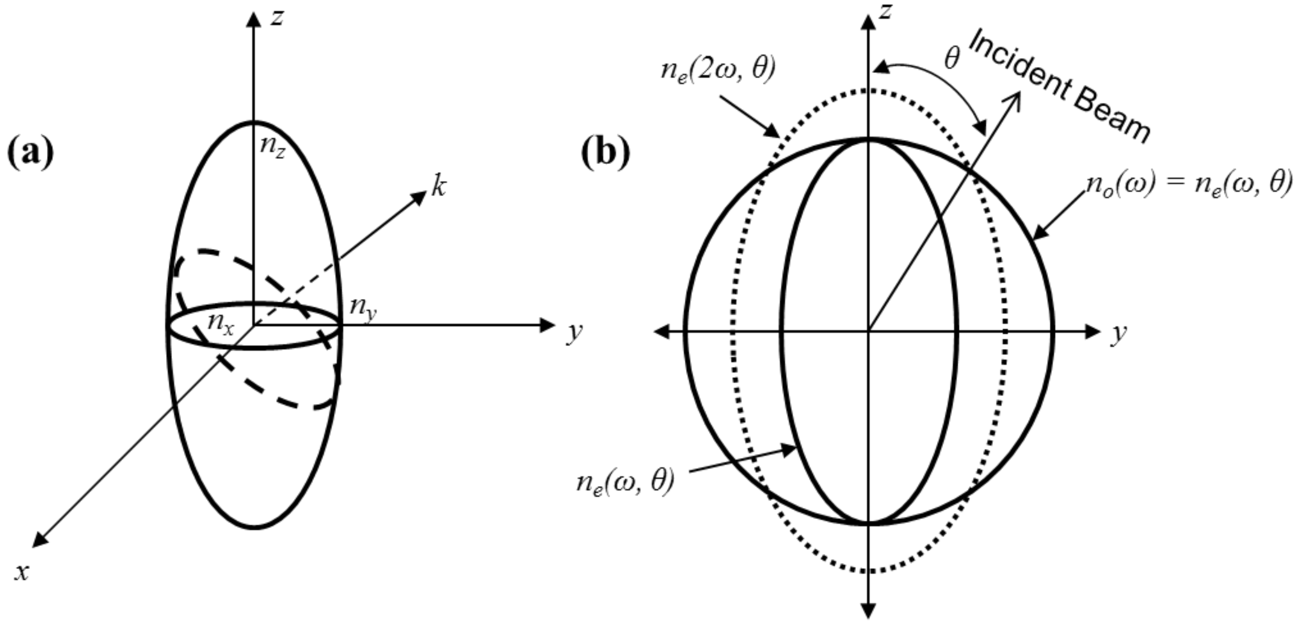

Figure 2.7. General diagram of a uniaxial crystal's index ellipsoid (a) and second harmonic generation in a negative uniaxial crystal (b) as described by equations 2.14 and 2.15.

Time-Correlated Single Photon Counting (TCSPC)

One of the most widely utilized time-resolved fluorescence techniques to study various photophysical processes on a short time scale (ps to ns) is time-correlated single photon counting (TCSPC). A brief introduction will be presented here but if the reader is interested in more information, several books and reviews have been published on this topic.[10,15,25-27] To understand the working principle of TCSPC, consider a population of fluorophores initially in the electronic ground state, $[S_o]$. Excitation of these species by a short delta pulse with energy greater than or equal to the energy gap between the ground and excited state produces a population of species in $[S_1]$. Now after some time, t, this population in S_1 will return to S_0 by radiative (r) and/or nonradiative (nr) means as mentioned in Chapter 1. The rate of return (or decay) to S_0 can be modeled by the first order differential equation:

$$\frac{d[S_1]}{dt} = -k[S_1] \qquad (2.16)$$

where k is the rate constant which takes into account the deactivation pathways according to k $=k_r + k_{nr}$. Subsequent integration of (X) will then yield:

$$[S_1]_t = [S_1]_0 e^{-kt} \tag{2.17}$$

where the intensity of fluorescence at time t and t_0 is $[S]_t$ and $[S]_0$, respectively. And the fluorescent lifetime is defined as

$$\tau = \frac{1}{k} \tag{2.18}$$

To accurately determine τ the intensity or number of photons at each time, t, would need to be measured. However, this $[S_1]_t$ is difficult to acquire by normal electronic recording systems due to the very short excited-state lifetimes (ns to ps) of typical organic compounds. Futhermore the time of photon emission is random in nature and unpredictable. Statistically speaking, it can be proved that the probability of photon emission from a single fluorophore after some time, t, following excitation is directly proportional to its intensity at some delay time Δt following excitation[28]

$$P(t) \sim e^{-\frac{\Delta t}{\tau}} \tag{2.19}$$

TCSPC is based on this probability distribution concept and measures one photon at a time. This means that by measuring a large number of individual time-resolved emission events from a population of fluorophores, a reproduction of its excited-state decay can be produced from the acquired probability histogram.

In a typical experiment, the excitation beam is split in two by a beam splitter. One beam is used to excite the sample, while the other is sent to a fast photodiode (PD) that serves as a timing reference for the beginning of the experiment. Trigging of this PD allows the signal to pass to a constant fraction discriminator (CFD). The CFD is needed to eliminate timing jitters resulting from electrical pulse height variations. The signal from the CFD is then sent to the time to amplitude converter (TAC) which begins charging a capacitor and increasing voltage in a linear fashion. This is the START of the experiment. (The TAC can be thought of as an electronic timing gate or stop watch.) In the meantime, the excited sample emits photons that impinge on the cathode of a multichannel plate PMT (MCP-PMT) which is sensitive enough to only collect a single photon. The MCP-PMT will then produce an electrical output pulse that is also sent through a CFD into the TAC which subsequently STOPS collection of data and charging of the capacitor. The voltage increase from START to STOP is equivalent to the time delay between reference and sample induced pulses. This time delay is then recorded by a multichannel analyzer (MCA) which incorporates the delay into an appropriate bin of a multichannel array. One cycle of START to STOP of this kind will not produce a representative probability distribution and decay. Many cycles are collected, analyzed by the MCA, and put into a histogram in the acquisition of a sample's fluorescent decay profile.

One problem that can arise in a TCSPC experiment, if not accounted for appropriately, is pulse pile up.[10,25,27,29] This occurs when the MCP-PMT is overwhelmed with too many photons which will prevent the measurement of a single photon. In this case the START-STOP cycle would be disrupted and data skewed towards faster decay profiles regardless of sample. As such it is generally recommended to decrease the photon counting rate to between 1-5% of the excitation rate. In addition, maintaining the energy per pulse (< 1 nJ) and concentration of fluorophore low is helpful.

The limiting factor in the time resolution of a typical TCSPC experiment is the transit time spread (TTS) of the MCP-PMT. The TTS is the time delay between the absorption of a photon at the photocathode and subsequent pulse output at the anode. With MCP-PMT, timing resolutions of ~30-50 ps can be achieved.[10,25,27,29]

The fluorescence decay profile, f(t), acquired from a TCSPC experiment is a convolution of the instrument response i(t) and fluorescence signal from the sample g(t). Mathematically this can be represented by[15]

$$f(t) = \int_0^\infty i(t - t')g(t')dt'. \tag{2.20}$$

To obtain the desired g(t), i(t) needs to be deconvoluted from f(t). Further analysis and least-squares fitting of g(t) with a sum of exponentials will then yield the time constant (s) of the fluorescence decay. In order to obtain accurate fits of the decay it is usually good practice to use a goodness of fit parameter. In our lab, we use the reduced chi square parameter with values closest to one representing the better fit.[30]

TCSPC Set Up

The general layout of the TCSPC system used for the experiments in this thesis is presented in Figure 2.8. Laser pulses tunable from ~780-880 nm were produced from a homebuilt 82-MHz mode-locked Ti:sapphire oscillator pumped by a 5-W Nd:VO_4 laser (Millennia, Spectra Physics). The resulting pulses were tuned to ~814 nm and this fundamental wavelength was modulated by a Pockels cell (Model 350-160, Conoptics Inc.) to reduce the repetition rate to ~8.8 MHz. The frequency-doubling or -tripling of this laser source by a harmonic generator (Model TP-2000B, U-Oplaz Technologies) provided the excitation wavelength at ~407 nm or ~266 nm, respectively. A half-wave plate and polarizer before the sample chamber is used to ensure vertically polarized excitation. Emission is collected in a perpendicular geometry (with respect to the excitation beam) and passed through a polarizer set at the magic angle (54.7^0) in reference to the excitation polarization. This magic angle is used for lifetime measurements to prevent rotational motion and anisotropy effects of fluorophores from altering the acquired decay profile. In anisotropy experiments this polarizer's is set at perpendicular and parallel angles with respect the excitation polarization. The placement of appropriate filters and/or a monochromator before the microchannel plate, MCP (Hamamatsu, R3809U-50), eliminates the excitation light and allows selection of emission from the sample. The signal from the MCP-PMT is passed into a Becker & Heckl SPC-module that contains the CFD, TAC, MCA, and an analog to digital converter (ADC). Each data point is added to a large histogram which is converted by the SPC software into a decay profile on the CPU screen. The full-width at half-maximum (FWHM) of the instrument response function is ~37-40 ps. All measurements are usually made with 1024-4096 channels. Up to a total of 65530 counts can be collected at the peak channel for each measurement.

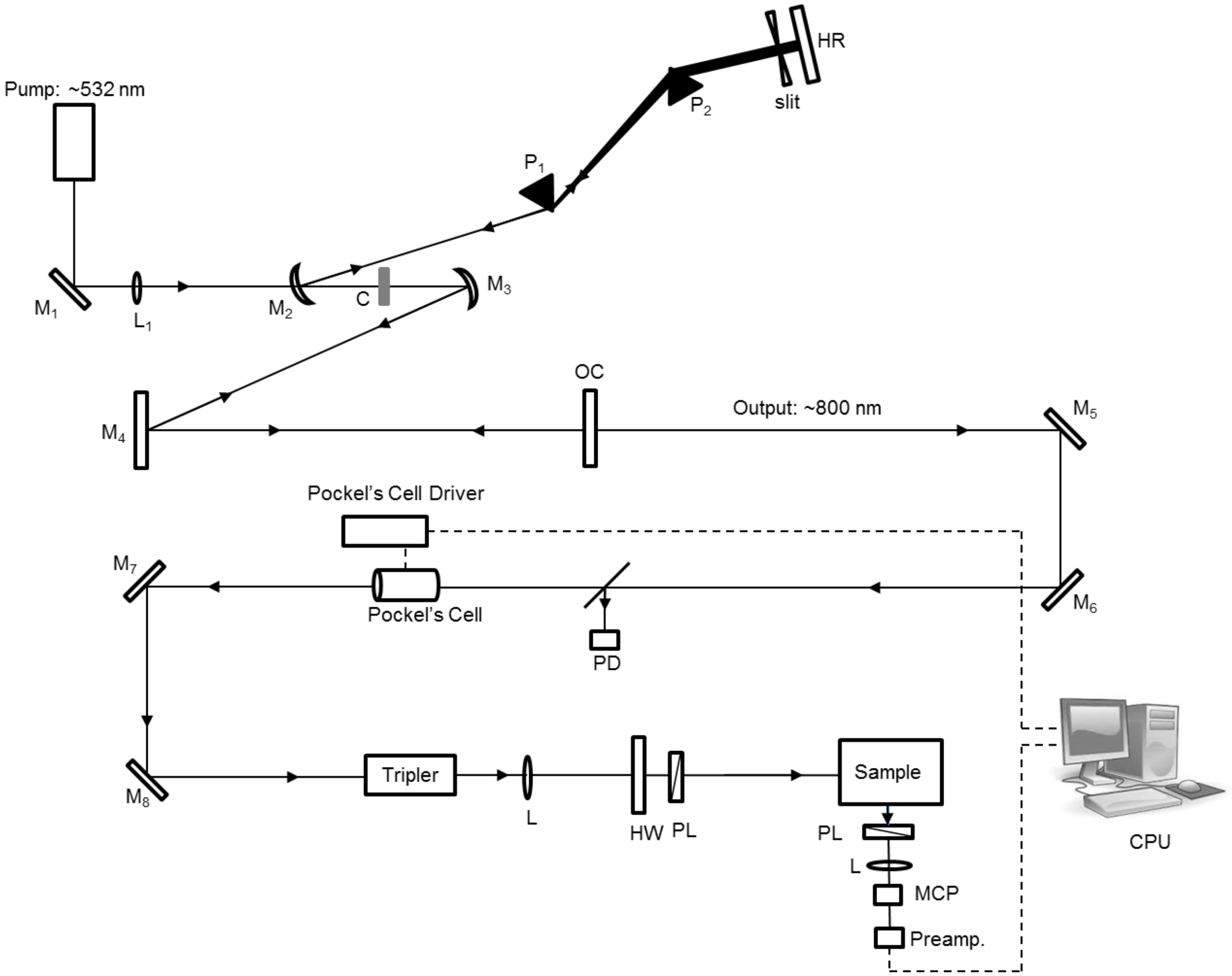

Figure 2.8. Time Correlated Single Photon Counting (TCSPC) setup. C – Ti:Sapphire Crystal, HR – High Refelctor Mirror, MCP – Multichannel Plate PMT, PL – Polarizer, HW – Half-Wave Plate, M-Mirror, OC – Output Coupler, PD – Photodiode, CPU – Computer.

Fluorescence Upconversion

In ultrafast spectroscopy, an essential goal is to capture the fastest occurring phenomena on as short a time scale as possible. Although TCSPC is a good method for many fundamental ultrafast processes, it lacks the necessary time resolution for important events which happen on faster time scales than the limited TTS in the detector allows (see above). In order to break this time barrier, one can use optical gating.[10,15,28] The idea with optical gating is to use very short pulses (shorter than the photophysical process under study) to act as a gate of the samples signal at various time delays from exitation across its decay profile. In this way the limits imposed by the detection system are removed. One of the most popular methods with regards to emission is fluorescence upconversion.

Fluorescence upconversion is based on using the nonlinear effect within a nonlinear bifringent crystal for sum frequency mixing of femtosecond excitation pulses with fluorescence signals at several times along its decay profile (Figure 2.9). Normally, the excitation beam is split into two with one serving to excite the sample while the other is used as the optical gate. The fluorescence (v_f) and optical gate pulse (v_g) are then focused on a nonlinear crystal. Within the crystal the electric fields of v_s and v_g interact with the electric field of the crystal to produce a signal $v_s = v_f + v_g$ that is shifted to a higher frequency than either signal or gate.[2] Hence the name flourescence upconversion. But in order for this upconverted signal to be produced the gate and fluorescence pulse need to be overlapped in time and space (phase matched) within the crystal. Otherwise, the sum frequency signal will not result. To collect signal across the time profile of the fluorescence, either the fluorescence or gate is incrementally delayed by a motorized stage while the other is fixed (ie gate delayed, fluorescence fixed or vice versa).

Assuming the fluorescence decay is slower in time than the gate and excitation pulse widths, the time resolution of upconversion is only limited by the width of these pulses.[10,15,28] Thus it is important to prevent broadening of the pulse by the optical components ultilized in the system. It is best to use highly efficient optics and optical components in the system.[2]

The sum frequency intensity, I_s, is the product of the intensities of the gate, I_g, and fluorescence intensities, I_f. This can be expressed as[15,31]

$$I_s(t') = \int_0^{t'} I_f(t - t') I_g(t)\,dt \tag{2.21}$$

From this equation it can be seen that when the fluorescence and/or gate signal decreases in intensity so does the upconversion signal. Furthermore, it expresses the requirement of gate and fluorescence overlap in order for there to be a sum frequency signal.

As in the case of TCSPC, the true fluorescence signal is convoluted with the instrument response function. The instrument response function can be obtained from of a cross correlation function.[15,31] This function is acquired by overlapping the gate pulse with the excitation pulse in the nonlinear crystal, using the same setup (optics, sample cell, etc) used for the sample.

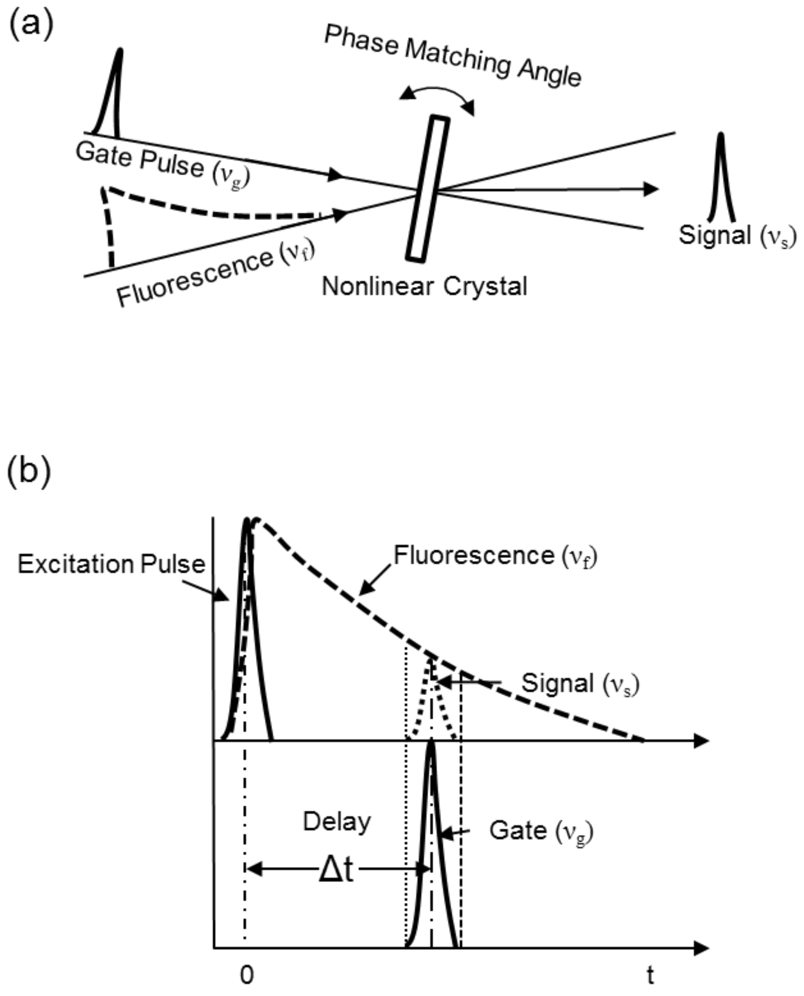

Figure 2.9. Basic principles of fluorescence upconversion. In (a) the fluorescence and gate pulse are mixed within a nonlinear crystal, at the phase matching angle to produce a sum frequency signal. In (b) the arrival of both fluorescence and gate at the same time produces a

signal that is the product of both intensities. Collecting this signal at various time delays from the excitation pulse results in a representative time-resolved decay from the sample.

Fluorescence Upconversion Setup

The fluorescence upconversion schematic used in this thesis is presented in Figure 2.10. A Ti:Sapphire oscillator supplies the fundamental output with a wavelength and frequency of 814 nm and 88 MHz, respectively . The output is then focused onto a type-1 LBO crystal (2 mm) and frequency-doubled (407 nm). This frequency-doubled pulse is then separated from the remaining 814 nm fundamental by a dichroic mirror for use as the excitation pulse. The residual of the fundamental following frequency-doubling is then used as the gate pulse of the fluorescence signal. Removal of the frequency doubled light from the fundamental is achieved with an appropriate filter. The gate pulses are passed through a $\lambda/2$ plate with 90^0 orientations with respect to the normal of the laser table while the excitation pulses pass through a $\lambda/2$ plate that is adjusted to the magic angle (54.7^0) in reference to the gate pulse polarization. In our system, the excitation pulse is sent to a motorized delay stage while the gate pulse is fixed. Translation of this stage by small increments allows acquisition of the fluorescence decay profile.

Sample solution is placed in a glass rotating cell of pathlength 1 nm and mounted perpendicularly to the exciting beam. This cell spins about an axis that is parallel to the excitation beam. To acquire the upconverted signal, the ~407 nm pulses are focused on the sample cell and the subsequent fluorescence signal is collected using a 10x objective lens. Output fluorescence from this lens is then focused along with the gate pulse, onto a 0.4 mm type-I BBO crystal. The generated sum frequency signal is passed through a monochromator to separate it from the fluorescence and gate pulses. As the upconverted signal is typically low in illumination and often buried in noise, an optical light chopper is placed in the excitation beam path. A chopping frequency of 1 kHz is used. The lock-in amplifier is connected to the PMT and set at the same frequency as the chopper. Using this scheme the cross correlation function is acquired from mixing the frequency doubled and fundamental beams. The full-width-at-half-maximum (FWHM) of the instrument response function is 300 fs.

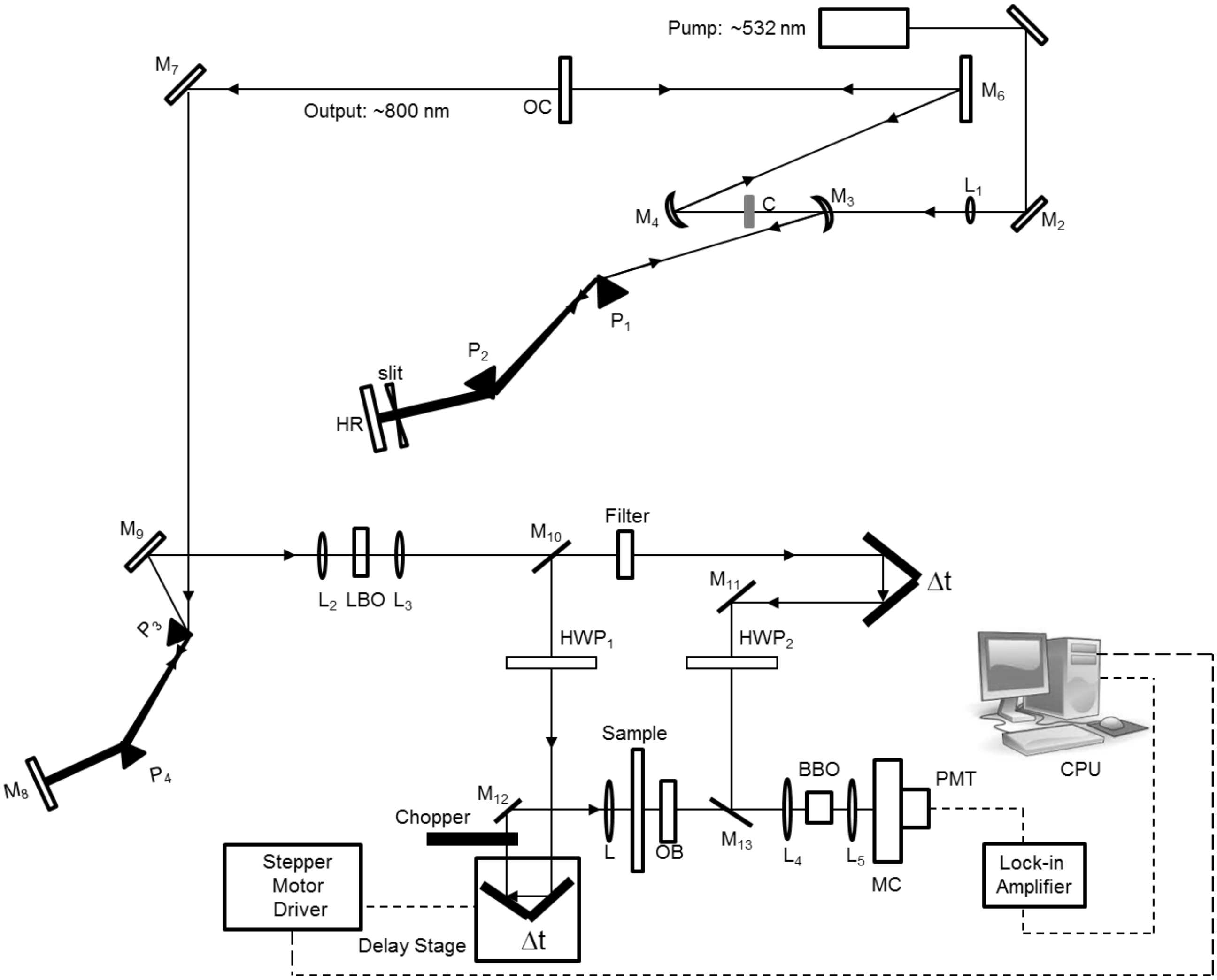

Figure 2.10. Fluorescence upconversion diagram. M-mirror, HR – high reflector mirror, C-Ti:Sapphire crystal, HWP – half-wave plate, OB – objective, L – lens, MC – monochromator, PMT – photomultiplier tube, P – prism.

Time-Resolved Emission Spectra (TRES)

Steady-state emission spectra of a molecule in condensed phase represent the equilibrium that exists between solvent and solute. In order to find out more about the kinetics and rates of the process that led to equilibrium an analysis of the emission spectra with time following excitation is needed. Time-resolved emission spectra (TRES) allow acquisition of this information. The TRES is particularly useful in solvation dynamics studies. Although it is possible to directly follow the changes in emission spectra with time in the acquisition of TRES, the inability to separate the instrument response from the solvation process imposes serious limitations on the accuracy of this method.[26,33] To overcome this issue, the TRES can be constructed indirectly by using the wavelength-dependent time-resolved fluorescence decays acquired during the process of solvation.

In a polar and/or viscous environment the emission spectra of a solvachromatic fluorophore will shift to lower energies and longer wavelength with time.[26,33] The wavelength-dependent decays across the steady-state spectrum of the fluorophore can provide an effective snapshot of these changes. These decays will be shorter in time at the blue, shorter wavelengths while longer with a rising component at red, longer wavelengths. The decays are shorter at lower wavelengths because the population of fluorophores are decaying by both emission and relaxation during the process.[26] While at longer observation wavelengths the decays are longer with a rising component because the emitting population takes time to populate the relaxed state. The intensity of the wavelength resolved decays are usually expressed as a sum of exponentials[26]

$$I(\lambda, t) = \sum_{i}^{\infty} \alpha_i(\lambda) e^{-\frac{t}{\tau_i}} \tag{2.27}$$

In which the decays have an intensity of I(λ, t), with pre-exponential factors $\alpha_i(\lambda)$ and time constants τ(λ) at the observation wavelength, λ. The D(λ, t) are collected across the steady state emission spectrum at varying incremental wavelengths. For each decay, the $\alpha_i(\lambda)$(s) sum to 1. No physical significance is given to the amount of each component in the decay. The main idea is to get the best fit possible in order to accurately construct the TRES.

To construct the TRES each I(λ, t) is normalized to the intensity of the steady-state by[26]

$$I(\lambda,t) = I^{SS}(\lambda)\frac{I(\lambda,t)}{\int_0^\infty I(\lambda,t)} \tag{2.28}$$

where I(λ, t) is the normalized time and wavelength dependent intensity and $I^{SS}(\lambda)$ is the steady-state intensity at the same wavelength. The value of the I(λ, t) or sum of exponentials is the average lifetime obtained from the fits.

For solvation studies each TRES acquired at a particular time is fit to a log normal function using[33]

$$I(\nu,t) = h\{\exp[-ln2\langle\ln(1+\alpha)\,/\gamma\rangle^2]\} \tag{2.29}$$

From the fits of the TRES, the peak maxima are extracted and used for construction of the solvation correlation function to describe the rate of solvation.

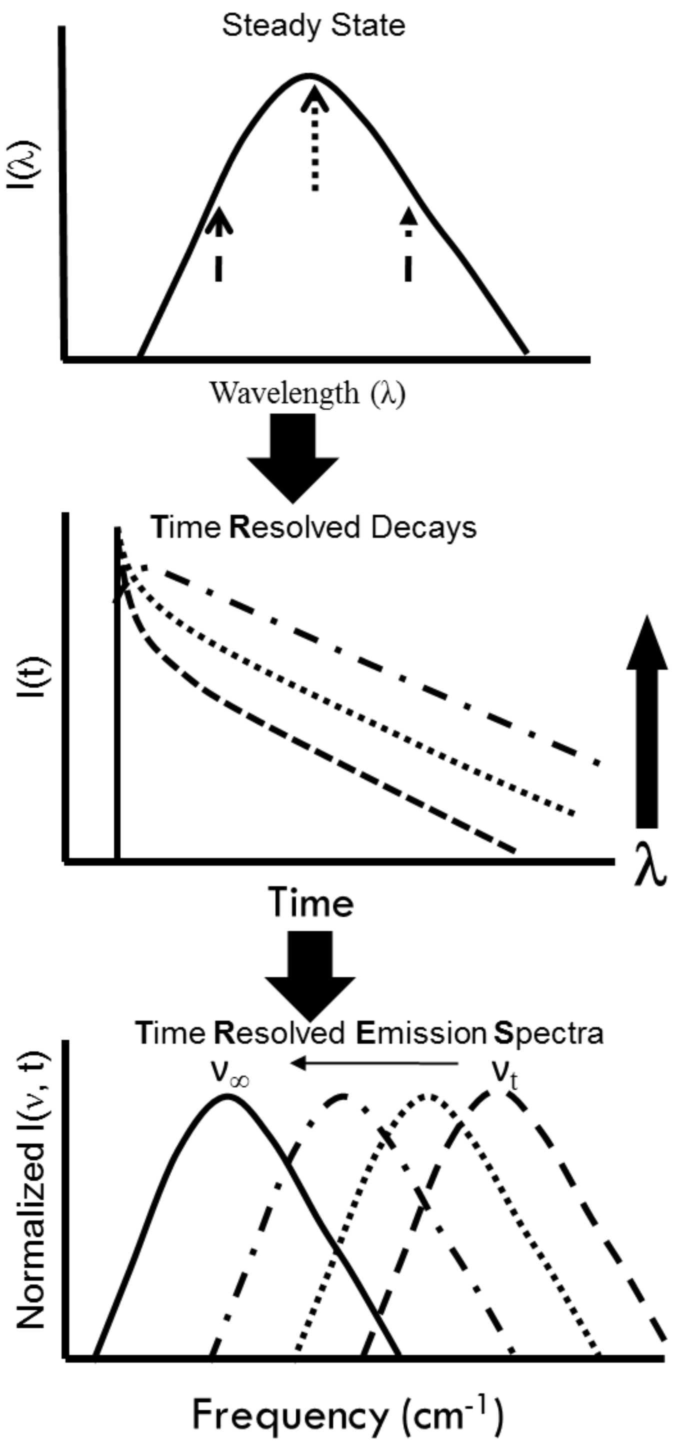

Figure 2.13. General diagram of the process used to acquire the time resolved emission spectra from the time resolved decays. The wavelengths of each are collected across the steady state spectrum.

Solvation Correlation Function

Solvation dynamics is best described and analyzed in terms of the normalized solvation correlation function[34]

$$C(t) = \frac{\nu(t) - \nu(\infty)}{\nu(\text{"0"}) - \nu(\infty)} \tag{2.30}$$

where the ν = “0”, ν = ∞, and ν = t represent the peak maxima in frequency units at time zero, infinity, and t. The time zero spectrum is obtained by the method reported by Fee and Maroncelli.[35] The ν = ∞ is typically taken as the maximum of the steady emission spectrum if the solvation process is completed within the lifetime of the fluorescence probe (the steady-state emission spectrum is limited by the lifetime of the probe). And ν = t is acquired from the constructed TRES with time as mentioned in Eq 2.29 above. Assuming that only solvation is contributing to the spectral shifts in the TRES with time, the C(t) is usually best fit to a sum of exponentials. Since the emission spectra containing the peak frequency values are normally very broad, each peak frequency value acquired carries uncertainty in its position on the frequency axis. Based on the signal-to-noise ratio and widths of the spectra (time zero, steady-state, and TRES), we have determined the following errors for each: ± 100 cm^{-1} (time zero and infinity/steady state), ±200 cm^{-1} (time = t, TRES). Using these computed uncertainties, error bars are added to the C(t). The fraction of solvation, f_t, can be calculated from $f_t = 1 - C(t)$ at various times along the solvation coorelation function.

Time-Resolved Fluorescence Anisotropy

Following absorption of polarized light by a fluorophore, the subsequent emission is also polarized in the same direction as the exciting light.[26,36,37] The degree to which this emission is polarized is defined as the fluorescence anisotropy. This means that the emission is directionally dependent. The origin of this phenomenon occurs as a result of the interaction of the absorption transition dipole moments of the sample with that of the electric field oscillations in the exciting light. In solution these dipole moments are randomly oriented. But when polarized light interacts with the sample, those dipoles that are parallel with respect to the electric field vector of polarization in the light are preferably excited.[26,36,37]

It is not necessary for a particular fluorophore's transition dipole moment to be perfectly aligned with that of the polarized light. The probability of absorption of light of a particular orientation is found to be directly proportional to $\cos^2 \theta$ with θ indicating the angle of the sample's transition moment with reference to the electric vector of the polarized light.[26] The maximum probability occurs under conditions of perfect alignment with respect to the excitation electric vector. Thus the dipole moments of a population can be selectively orientated along a particular direction by choice of an excitation source with a defined polarization. This is commonly referred to as photoselection.[36] In mathematical terms the fluorescence anisotropy is defined as[24,35,36]

$$r = \frac{I_{\perp} + I_{\parallel}}{2I_{\perp} + I_{\parallel}} \tag{2.31}$$

where $I_{\parallel}$ and $I_{\perp}$ are the vertically and horizontally polarized fluorescence intensities with respect to that of the electric vector of the exciting light. The $2I_{\perp}$ comes from the fact that there are two intensity vectors in the x and y planes versus one in the z plane (3 dimensional space). In terms of time-resolved studies of anisotropy which are the type presented in this thesis, the same equation is used but with a time component added to each variable.[26]

$$r(t) = \frac{I_{\perp}(t) + I_{\parallel}(t)}{2I_{\perp}(t) + I_{\parallel}(t)} \tag{2.32}$$

Assuming that the absorption and emission dipoles are collinear, the anisotropy at t=0 can be shown to be related to θ by[26,27]

$$r_0 = \frac{1}{5}\left(\frac{3\langle cos^2\theta\rangle - 1}{2}\right) \tag{2.33}$$

The maximum positive and negative anisotropies for which there are no depolarizing processes is 0.4 and -0.2, respectively (at θ = 0 and 90^0). At an angle, referred to as the magic angle, of 54.7^0 there is a complete loss of anisotropy. (Note this angle is used to prevent directional dependence from interfering in the analysis of studies for which the goal is to separate this affect from the desired variable (eg lifetime, τ)). The 0.4 is much less than perfect alignment. If a value greater than 0.4 is obtained, it is possible that another source such as scattered light (r =1) could be contributing to the anisotropy value.[26]

For depolarization by rotational diffusion which is presented in subsequent chapters, the time resolved anisotropy can be related to the rotational correlation time, τ_r, and r_0 by[26]

$$r(t) = r_0 e^{-\frac{t}{\tau_r}} \tag{2.34}$$

The τ_r can give information about the rigidity and/or viscosity of the fluorophore's environment. Utilizing the concept of a perfect rigid rotor for a molecule in solution, an estimate of τ_r can be inferred from the Stokes-Einstein-Debye relation[26,38]

$$\tau_r = \frac{\eta V}{k_B T} \tag{2.35}$$

where the solvent viscosity is η, the molecular volume is V, T is the temperature, and k_B is the Boltzman constant. If the r(t) never decays to zero within the fluorescence lifetime, then the above equation needs to be modified as[39]

$$r(t) = (r_0 - r_\infty)e^{-\frac{t}{\tau_r}} + r_\infty \tag{2.36}$$

In which the r_∞ is the amount of anisotropy not observed. This can occur for fluorophores attached to rigid structures such as proteins. Furthermore if there are multiple and/or complex types of motions, or nonspherical molecules involved then the time resolved anisotropy is described as a sum of exponential terms[26]

$$r(t) = \sum_{i}^{\infty} r_i e^{-\frac{t}{\tau_{r_i}}} \tag{2.37}$$

The depolarization of a photoselected population can happen by means of rotational diffusion, energy transfer, ligand binding, etc. Fluorescence anisotropy can provide insight into the interactions of molecules with their environment. It can help describe complex motions that are unobservable by other experimental means. In biological studies it has found great utility since the motions and rotations result in rotational correlation time scales that are much less than the lifetime of the fluorophore.[26]

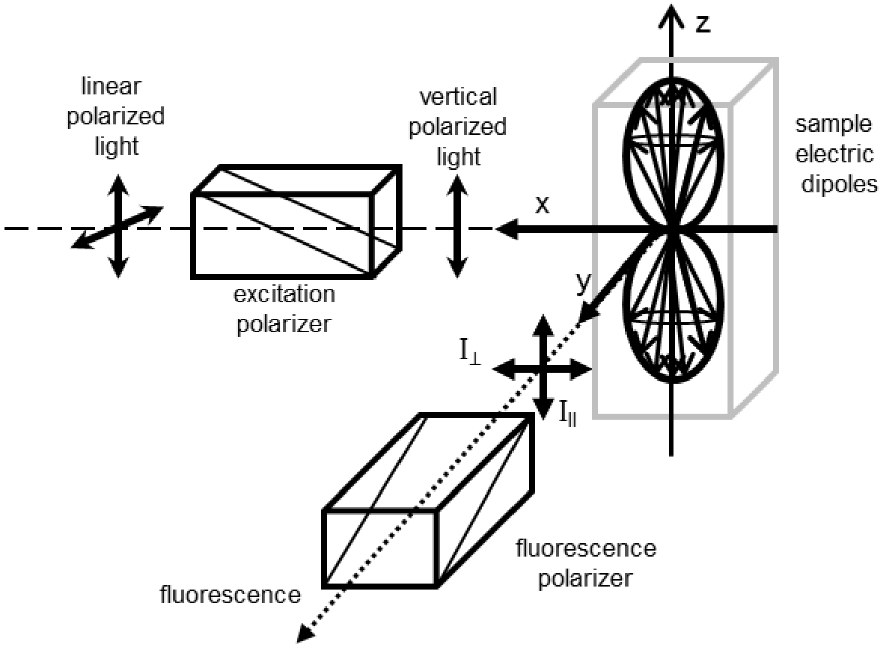

Figure 2.14. General principles of a fluorescence anisotropy experiment. Excitation of the sample by vertical polarized light produces a preferential population of its electric dipoles randomly distributed around the z-axis. Proper orientation of the emission polarizer along the z and x-axes allows measurement of $I_\parallel$ and $I_\perp$ for determining the sample's anisotropy.[26]

Forster Resonance Energy Transfer (FRET)

Two molecules in close proximity, with their transition dipoles in resonance may have the possibility to transfer energy between them in a process known as resonance energy transfer (RET).[26,40,41] Resonance energy transfer is a nonradiative process in which a molecule in the excited state transfers energy to another molecule in the ground state. The molecule releasing the energy to the other is called the donor (D) while the molecule accepting is referred to as the acceptor (A). Using classical physics this means that when the excited D molecule with its oscillating dipole comes in close distance to the A molecule, then A can have its dipole induced to oscillate as well.[26] When these two begin to oscillate at the same frequency energy is passed from the D to the A, thereby resulting in the donor returning to the ground state while the acceptor goes to the excited state (Figure 2.15). Hence, the term "resonance" energy transfer in its description. If D is fluorescent, then this process may be called fluorescence resonance energy transfer (FRET).[26,41] But it is important to note that it does not actually involve the emission and absorption of a photon from the D to A, respectively.

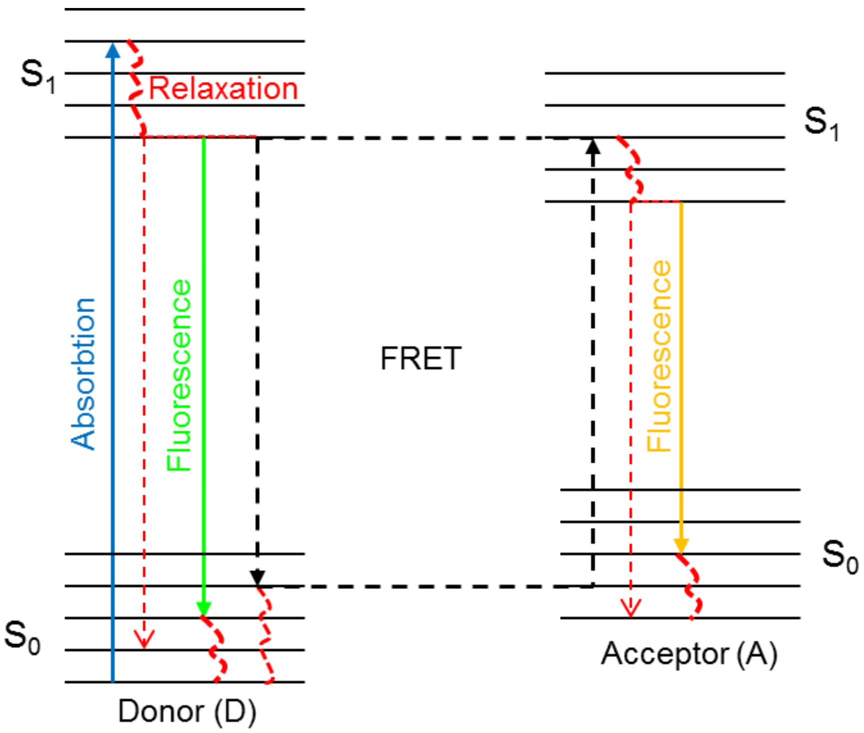

Figure 2.15. General electronic energy level diagram of a donor (D) and acceptor (A) molecule coupled by FRET. Both excited donor and acceptor can relax radiatively by fluorescence. But energy transfer from D to A occurs nonradiatively. Other nonradiative relaxation processes are indicated in red.

Based on Forster's theory occurrence of RET needs several conditions to be met in order to be of significance.[41] One the D emission and A absorption spectra must overlap. Two, the D and A need to be within a distance of 10-100 Å. Three, orientation between the D and A should be appropriate to allow energy transfer or at least one of the pair (D or A) should have significant rotational degrees of freedom. And lastly the quantum yield of the D must be high. Forster was able express to the dependence of the rate of energy transfer on these criteria as[26,41]

$$k_T = \frac{9000\kappa^2(ln10)\phi_D c^4}{128\pi^5 n^4 N\tau_D R^6}\int_0^\infty f_D(\tilde{\nu})\varepsilon_A(\tilde{\nu})\frac{d\tilde{\nu}}{\tilde{\nu}^4} \qquad (2.38)$$

where ϕ is the quantum yield of the donor, τ_D is the fluorescent lifetime of the donor, ε_A the absorption coefficient of the acceptor, the integral quantifies the amount of spectral overlap between donor and acceptor, R is the distance between D and A, and R_0 is the critical distance at which energy transfer is 50% efficient, and κ is the orientation factor that is defined using the angles between the interacting dipoles of D and A (as represented in Figure 2.17) by[26]

$$\begin{aligned}\kappa^2 &= [\boldsymbol{D}\cdot\boldsymbol{A} - 3(\boldsymbol{D}\cdot\boldsymbol{A})(\boldsymbol{A}\cdot\boldsymbol{R})]^{\mathbf{2}}\\ &= [cos\theta_T - 3cos\theta_D cos\theta_A]^2 \\ &= [sin\theta_D \cdot sin\theta_A \cdot cos\phi - 2cos\theta_D cos\theta_A]^2\end{aligned} \tag{2.39}$$

where θ_T is the angle between the transition dipole moments of the donor and acceptor, θ_A and θ_D are the angles of the acceptor and donor with respect to the vector R that pairs the two together, and ϕ is the angle between the planes of the interacting dipoles. This value ranges between 0-4. If the orientation between D and A dipoles becomes randomly orientated (eg due to significant rotational degrees of freedom) within the lifetime of the donor, τ_D , then the value becomes 2/3. Typically this value has been used without much thought for molecules known to have random orientation. However, this has recently been called into question.[41]

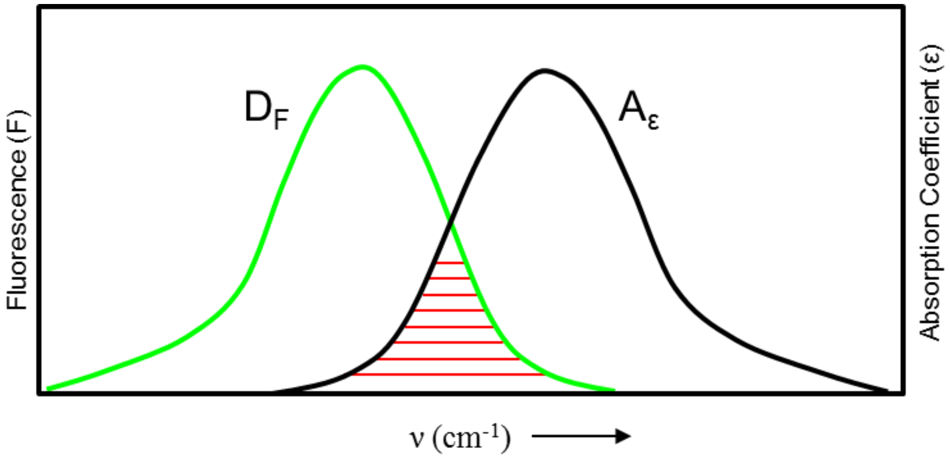

Figure 2.16. Donor fluorescence and acceptor absorption spectra. The overlap integral is displayed as the shaded area in red.

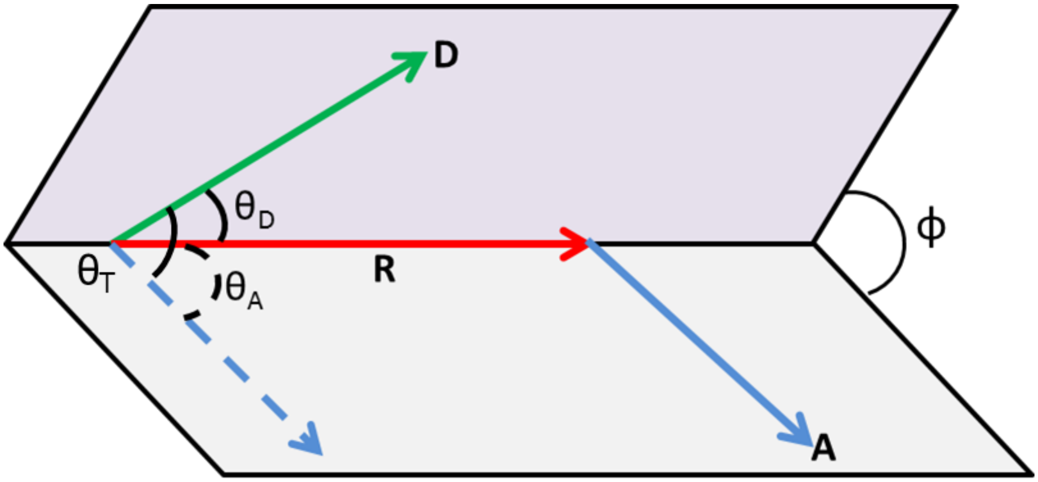

Figure 2.17. Depiction of the orientation between D and A in the derivation of the orientation factor (κ^2).[26]

The Fȍrster distance is explicitly shown to be[26,40,41]

$$R_0^6 = \frac{9000\kappa^2(ln10)\phi_D c^4}{128\pi^5 n^4 N}\int_0^\infty f_D(\tilde{v})\varepsilon_A(\tilde{v})\frac{d\tilde{v}}{\tilde{v}^4} \tag{2.40}$$

Using this, the rate of energy transfer is commonly written in a more condensed form as

$$k_{ET} = \frac{1}{\tau_D}\left(\frac{R_0}{R}\right)^6 \tag{2.41}$$

As can be seen the inverse of the distance is directly proportional to the rate of energy transfer. The energy transfer efficiency can be written in terms of the Forster distance or rate of energy transfer[26,41]

$$E = \frac{k_T}{k_T + 1/\tau_D} = \frac{R_0^6}{R_0^6 + R^6} \tag{2.42}$$

RET is most commonly used as a "spectroscopic ruler" to measure distances between two sites in a molecular assembly that fall between 10-100 Å.[26,41] It has found wide utility in biological studies that work to understand the interplay between structure and function of many biomolecules such as proteins and membranes. Also if a pair of molecules can be found with spectral properties that allow energy transfer, it will not be affected significantly by inclusion of the D-A within a biological environment.[26] The method itself is relatively noninvasive and allows analysis in *in vivo* conditions.

References

(1) *Fluoromax Spectrophotometer: Operation and Maintence*; SPEX Industries: Edison, N.J., 1990.

(2) Adhikary, R., Iowa State University, 2011.

(3) Bigger, S. W.; Ghiggino, K. P.; Meilak, G. A.; Verity, B. *Journal of Chemical Education* **1992**, *69*, 675.

(4) Demtroder, W. *Laser Spectroscopy: Basic Concepts and Instrumentation* 3rd ed.; Springer: Berlin: New York, 2003.

(5) Ingle, J. D.; Crouch, S. R. *Spectrochemical Analysis*; Prentice Hall: Englewood Cliffs, N. J., 1988.

(6) Milonni, P. W.; Eberly, J. H. *Laser Physics*; John Wiley & Sons Inc., 2010.

(7) Siegman, A. E. *Lasers*; University Science Books: Mill Valley, CA, 1986.

(8) Silfvast, W. T. *Laser Fundamentals*; 2nd ed.; Cambridge University Press: New York, 2005.

(9) Svelto, O. *Principles of Lasers*; 5th ed.; Springer: New York, 2010.

(10) Tkachenko, N. V. *Optical Spectroscopy: Methods and Instrumentation*; Elsevier: Amsterdam: Boston, 2006.

(11) Wilson, J.; Hawkes, J. F. B. *Lasers, Principles, and Applications*; Prentice Hall: New York, 1987.

(12) Abramczyk, H. *Introduction to Laser Spectroscopy*; Elsevier: Amsterdam & Boston, 2005.

(13) Hecht, J. *Understanding Lasers: An Entry-Level Guide*; 3rd ed.; John Wiley & Sons, Inc: Piscataway, NJ, 2008.

(14) Moulton, P. F. *J. Opt. Soc. Am. B* **1986**, *3*, 125.

(15) Fleming, G. R. *Chemical Applications of Ultrafast Spectroscpy*; University Press: London, 1986.

(16) Paschotta, R. *Field Guide to Laser Pulse Generation*; SPIE: Bellingham, Wash., 2008.

(17) Haus, H. A. *J. Appl. Phys.* **1975**, *46*, 3049.

(18) In *Springer Handbook of Lasers and Optics*; Träger, F., Ed.; Springer: New York, 2007.

(19) Keller, U. *Nature* **2003**, *424*, 831.

(20) English, D. S., Iowa State University, 1998.

(21) Asaki, M. T.; Haung, C.-P.; Garvery, D.; Zhou, J.; Kapteyn, H. C.; Murnane, M. M. *Optics Lett.* **1993**, *18*, 977.

(22) Boyd, R. W. *Nonlinear Optics*; Academic Press, Inc.: Boston, 1992.

(23) Dmitriev, V. G. *Handbook of Nonlinear Optical Crystals*; 3rd ed.; Springer: Berlin, 1991.

(24) Hecht, E. *Optics*; Addison-Wesley: Ready, Massachusetts, 2002.

(25) Becker, W. *Advanced Time-Correlated Single Photon Counting Techniques*; Springer: New York, 2005.

(26) Lakowicz, J. R. *Principles of Fluorescence Spectroscopy*; Springer: New York, 2006.

(27) O'Connor, D. V.; Philips, D. *Time-Correlated Single Photon Counting*; Academic Press: Orlando, Florida, 1984.

(28) Tkachenko, N. V.; Lemmetyinen, H. *Springer Ser. Fluoresc.* **2008**, *5*, 195.

(29) Becker, W. *TCSPC Handbook*; 4th ed.; Becker & Hickl GmbH: Berlin, Germany, 2010.

(30) Bevington, P. R.; Robinson, D. K. *Data Reduction and Error Analysis for Physical Sciences* 3rd ed.; McGraw-Hill: New York, 2003.

(31) Kahlow, M. A.; Jarzęba, W. o.; Kang, T. J.; Barbara, P. F. *The Journal of Chemical Physics* **1989**, *90*, 151.

(32) Lakowicz, J. R.; Gratton, E.; Cherek, H.; Maliwal, B. P.; Laczko, G. *Journal of Biological Chemistry* **1984**, *259*, 10967.

(33) Maroncelli, M. *Journal of Molecular Liquids* **1993**, *57*, 1.

(34) Fee, R. S.; Maroncelli, M. *Chemical Physics* **1994**, *183*, 235.

(35) Jameson, D. M.; Seifried, S. E. *Methods* **1999**, *19*, 222.

(36) Mann, T. L.; Krull, U. J. *Analyst* **2003**, *128*, 313.

(37) Van Holde, K. E.; Johnson, W. C.; Ho, P. S. *Principles of Physical Biochemistry*; Prentice Hall: New Jersey, 2005.

(38) Schröder, G. F.; Alexiev, U.; Grubmüller, H. *Biophysical journal* **2005**, *89*, 3757.

(39) Clegg, R. M. *Fluorescence Resonance Energy Transfer*; John Wiley and Sons: New York, 1996.

(40) Medintz, I.; Hildebrandt, N. *FRET - Forster Resonance Energy Transfer*; Wiley-VCH: Weinheim, Germany, 2014.

CHAPTER 3: DETERMINATION OF THE CONCENTRATION OF THE EFFLUX PUMP INHIBITOR, PHEOPHORBIDE *a*, IN THE FECES OF ANIMALS

A paper published in the *Journal of Agricultural and Food Chemistry*

[1]CA Barnes, [2]SL Rasmussen, [1]JW Petrich, and [2]MA Rasmussen*

Abstract

Efflux pumps are vital bacterial components, and research has demonstrated that some plant compounds such as pheophorbide a (php) possess efflux pump inhibitor (EPI) activity. This study determined the quantity of php present in feces as an indicator of EPI activity. Feces were collected from different species of animals fed a variety of feeds. The chlorophyll metabolites, php and pyropheophorbide *a* (pyp) were determined using fluorescent spectroscopy. The average concentration of pyp/php in feces were: guinea pig, 180 µg/g DM (dry matter) feces; goat, 150; rabbit, 150; dairy cow, 120; feedlot cattle, 60; rat, <1; pig, <1; chicken, <1. These data indicate that animals consuming "green" diets will excrete feces with concentrations of php/pyp that exceed levels demonstrated to be inhibitory to bacterial efflux pumps (0.5 µg/mL).

Reprinted with permission from *Journal of Agricultural and Food Chemistry* 2012, 60 (42), pp 10456–10460. Copyright (2012) American Chemical Society. [1]Department of Chemistry, Iowa State University, Ames, Iowa 50011 and [2]Center for Veterinary Medicine, FDA, Laurel, Maryland 20708, United States

The natural presence EPIs in the gastrointestinal tract may modulate the activity of microbial efflux pumps and exert selection pressure upon resident microbial populations.

Introduction

Since their discovery in the early 1980s, bacterial multidrugresistance (MDR) efflux pumps have been extensively investigated in regard to antimicrobial resistance.[1] MDR efflux pumps appear to be involved in bacterial resistance to a wide range of antibiotics, and transport capabilities have been reported for many classes of efflux pumps.[2] Evidence exists suggesting that these pumps may be ubiquitous and possess other functions important to microbial metabolism.[3,4] Although their description is incomplete, it is clear that these pumps are an important mechanism of antimicrobial resistance.[5] All require energy to function, with some types using ATP directly and others depending upon proton or sodium gradients.[6] Some of the best described pumps for bacteria include the AcrABTolC pump in Escherichia coli, MexABOprM in Pseudomonasaeruginosa, and FloR in Salmonella enterica serovar Typhimurium.

Research concerning the activity of these pumps indicates that they can be inhibited by a variety of compounds that render them nonfunctional in terms of antibiotic efflux.[7] Therefore, by denying a microbe the means to remove accumulated antibiotics from within the cell, these inhibitors are seen as potential adjuvants to reverse antimicrobial resistance in a manner similar to the role played by clavulanic acid as a β-lactamase inhibitor.[7,8] Whereas the search for inhibitors is primarily an effort focused on clinical applications,[9] the role of food and diet is also of interest, and some secondary compounds from plants are reported to have efflux pump inhibiting activity.[10-12]

Some of the first evidence that natural plant compounds are inhibitors of efflux pumps was reported by the Stermitz and Lewis group in 2000.[13,14] In this work, they identified and isolated a flavolignan (5’-methoxyhydnocarpin) from extracts of *Berberis trifoliolata* and demonstrated its inhibition of the NorA efflux pump of *Staphylococcus aureus*. They subsequently identified pheophorbide *a*, a chlorophyll metabolite, as an even more potent efflux pump inhibitor using the same NorA assay.[15] In later work, they screened the inhibitory activity of plant extracts against several bacteria including *Bacillus megaterium, E. coli, S. enterica*, and *P. aeruginosa*. The most potent inhibitors lowered the MICs (minimum inhibitory concentration) for several of the antibiotics tested 10- to 100- fold.[11] From an evolutionary perspective, these authors concluded that plant derived efflux pump inhibitors allowed antimicrobials within the plant, which when alone do not show strong antimicrobial activity, to be more effective against bacterial pathogens. Additionally, the pump inhibiting activity of some plant compounds could be considered to be part of a complex mechanism of defense against microbial pathogens. One example highlighted by Tegos et al. was that of rhein, an anthraquinone from rhubarb.[11] This compound alone had essentially no activity against *Pseudomonas* (MIC > 500 µg/ml) but when assayed with one of several efflux pump inhibitors, the MIC of rhein was reduced 100-fold (5 µg/ml). Similarly, Musumeci et al. reported large MIC reductions when pheophorbide was used to block the pumps responsible for ciprofloxacin efflux in resistant strains of *S. aureus*.[16]

The activity of pheophorbide *a* as an efflux pump inhibitor is one of particular interest in our investigations. Degradation of chlorophyll in the anaerobic environment of the gut follows a mechanism dissimilar to the aerobic metabolism within leaf tissue. Chlorophyll turnover in plants occurs when the porphyrin ring is oxidatively degraded into a linear tetrapyrrole.[17,18] In contrast, anaerobic metabolism in the gut leaves the porphyrin ring intact (**Figure 1**). As a result of these differences, chlorophyll degradation in the gut produce large quantities of pheophorbide *a* which may have significant inhibitory activity on efflux pumps of enteric bacteria. On the basis of this background information, the work presented here was designed to dertermine the concentration of chlorophyll metabolites in the feces of animals.

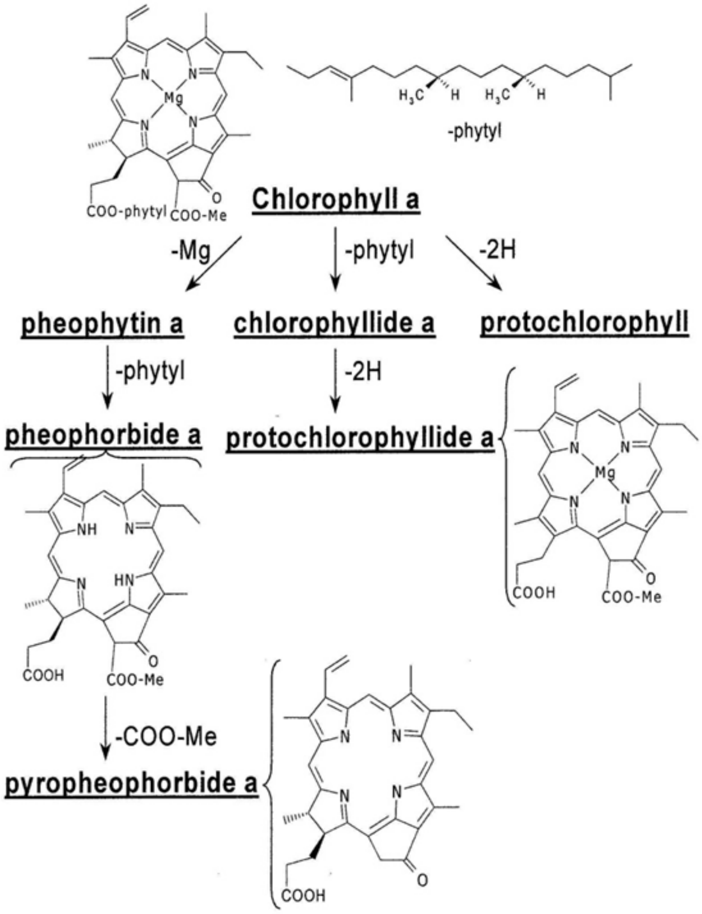

Figure 1. Metabolism of chlorophyll into various metabolites in the GI tract. Reproduced with permission from reference 21, copyright 2003, American Chemical Society.

Materials and Methods

Freshly voided feces were collected from several individuals (n>3) of different species of laboratory and farm animals being fed a wide variety of animal feeds (**Table 1**). Samples were dried at 60°C in the dark. Fifty milligrams of dried fecal material was finely ground and added to 5.0 ml of 2-propanol (Sigma-Aldrich, > 99.9%). Overnight extraction and sedimentation at 4°C was allowed before fluorescence measurements were collected. Preliminary experiments indicated that overnight extraction resulted in extraction coefficients exceeding 95%. Fluorescence spectra were obtained on a SPEX Fluoromax-4 spectrofluorometer (ISA Jobin-Yvon/SPEX, Edison, NJ, USA) with a 1-nm band-pass and corrected for lamp spectral intensity and detector response. Fecal extracts were excited at λ_{ex} = 420 nm with an interference filter on the excitation side and emission was collected at $\lambda_{em} \geq 430$ nm using a cutoff filter before the detector to eliminate scattered light. A calibration curve was generated with equal quantities of authentic standards of pheophorbide *a* and pyropheophorbide *a* (Frontier Scientific, Logan, Utah, USA) in 2-propanol using peak emission at λ_{em} = 673 nm. Measurements on samples from each individual animal within a species were performed in triplicate.

Table 1. Animal Diet Composition.

Animal Type	**Primary Feed Ingredients**	**Relative Chlorophyll Content of Diet**
Goat	alfalfa hay, other grass hay	High
Dairy Cow	fresh orchard grass, corn grain	High
Pig	corn grain, soybean meal	Low
Guinea Pig	alfalfa meal	High
Rabbit	alfalfa meal	High
Chicken	corn, other grain, soybean meal	Low
Rat	corn, wheat, soybean meal	Low
Feedlot Cattle	corn grain, corn silage	Medium

Results and Discussion

The intact chlorophyll present in the chloroplasts of plants is weakly fluorescent as 98-99% of the light energy absorbed is efficiently transferred to other molecules during the normal process of photosynthesis.[19] However, in the gastrointestinal (GI) tract, chlorophyll is degraded into various metabolites.[20] As a result, the chlorophyll metabolites become much more fluorescent. Although other metabolites may also reside in the feces of animals, previous work has demonstrated that pheophorbide *a* and pyropheophorbide *a* are the two predominant compounds.[20-22] Thus, the feces of animals whose diets are chlorophyll rich give a strong fluorescence signal corresponding to php and pyp. Previously these optical properties have used to develop instrumentation for the sensitive detection of fecal material on the meat of carcasses.[21] In the current work we ultilize these optical characterisitcs to determine the amount of php and pyp in the feces of various species of animals on diets that vary the amount of chlorophyll-containing components.

The fluorescence spectra obtained when 1 μM solutions of php and pyp where excited at λ_{ex} = 420 nm are very similar and both compounds having a maximum emission peak at λ_{em} = 673 nm. The pyp/php spectral ratio of ~1.3 (**Figure 2**). Because it is not possible to resolve these two based on their fluorescence spectra, we assumed a 50/50 mix of these two in the feces of animals, for which a calibration curve was generated using an authentic standard composed of equal concentrations of php and pyp in 2-propanol. The fluorescence intensity at λ_{em} = 673 was used to generate a calibration curve (**Figure 3**).

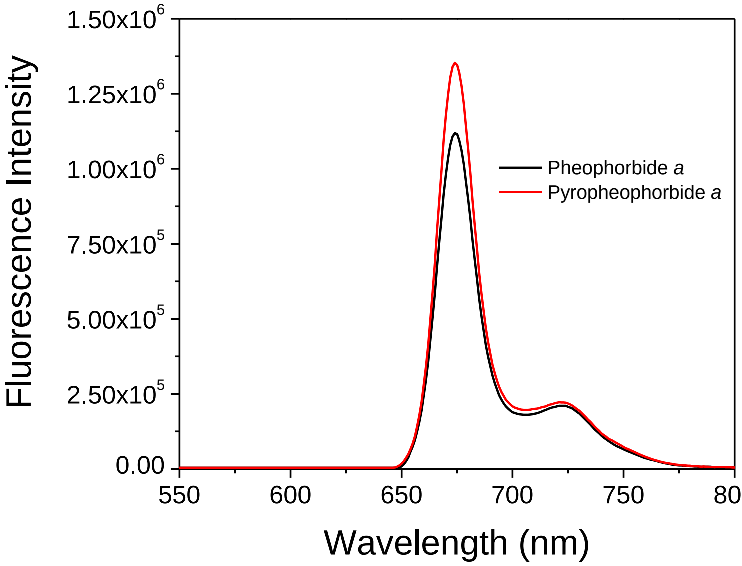

Figure 2. Fluorescence spectra of pheophorbide *a* (1 uM) and pyropheophorbide *a* (1 uM) in 2-propanol (λ_{ex} = 420 nm). The ratio was ~ 1.3 pyp/php.

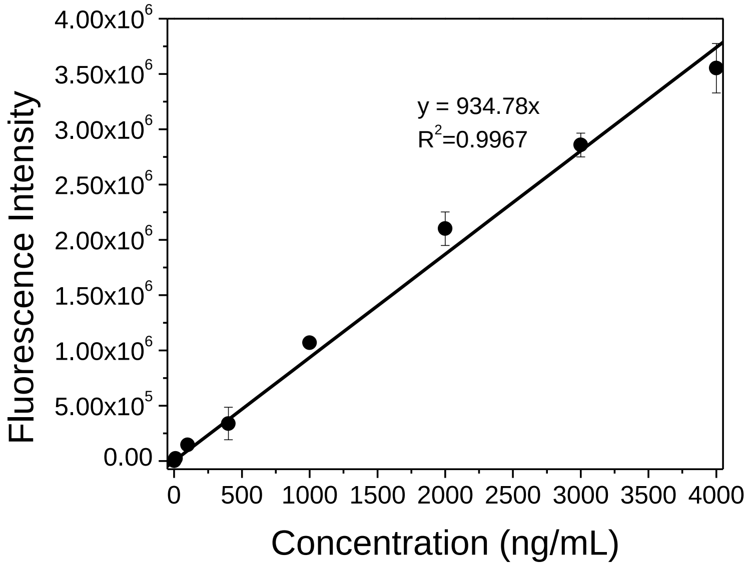

Figure 3. Fluorescence calibration curve of pyp/php (1:1) in 2-propanol (λ_{ex} = 420 nm). The peak maximum of 673 nm was used for calibration.

The fluorescence spectra of fecal samples from feedlot cattle, dairy cows, and pigs are presented in **Figures 4-6**. The feedlot cattle and dairy cow samples give intense peak maxima characteristic of php and pyp. Similarly the spectra of goats, rabbits, and guinea pigs also produced intense peak maxima at 673 nm (spectral graphs not shown). In contrast, the fluorescence spectra of pigs produced two peak maxima at ~500 nm and 673 nm. The broad 500 nm peak, ranging from 450-550 nm, results from other unknown fluorescence compounds and is of greater intensity than the 673 nm. It is important to note that this broad 500 nm peak is also produced in the other species of animals, but of negligible fluorescence intensity in comparison to the peak at 673 nm. The spectra of rat and chicken samples also produced peak maxima at 673 nm, but of much lesser intensity in comparison to the feedlot cattle, dairy cows, guinea pigs and goats. The average concentration of pyp/php in all animal feces are presented in **Table 2**.

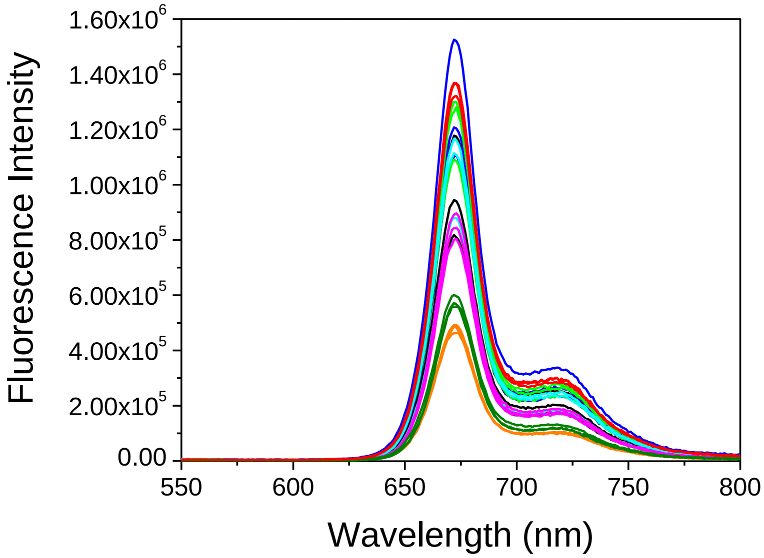

Figure 4. Fluorescence spectra of several samples of feedlot cattle feces in 2-propanol (λ_{ex} = 420 nm).

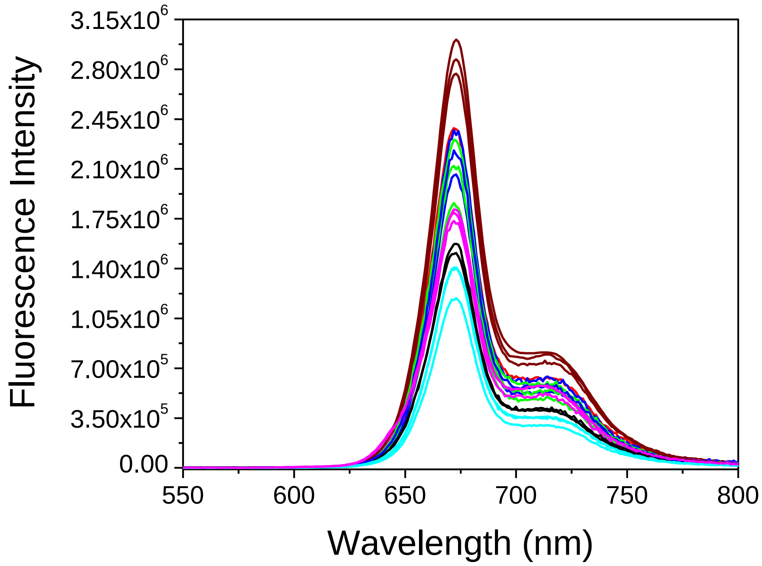

Figure 5. Fluorescence spectra of several samples of dairy cow feces in 2-propanol (λ_{ex} = 420nm).

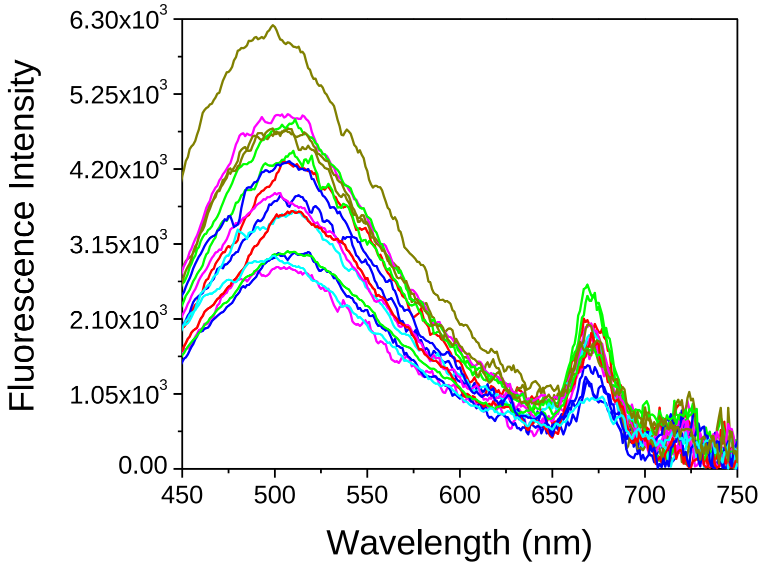

Figure 6. Fluorescence spectra of several samples of pig feces in 2-propanol (λ_{ex} = 420 nm).

Table 2. Average Concentration of pyp/php in Feces of Several Species of Animals.

Species	**Mean Fluorescence of Maximum Intensity (λ_{em} = 673)**	**Pyp/php µg/g DM feces**	**Standard Deviation µg/g**
Guinea Pig	3.05×10^{6}	180	± 10
Goat	2.55×10^{6}	150	± 40
Rabbit	2.48×10^{6}	150	± 13
Dairy Cow	2.01×10^{6}	120	± 29
Rat	4.14×10^{4}	<1	± 1
Pig	1.77×10^{3}	<1	±3
Feedlot Cattle	9.73×10^{5}	60	±20
Chicken	5.49×10^{3}	<1	± 0.12

Concentrations were, as anticipated, diet dependent, and low-chlorophyll-containing diets produced correspondingly low levels of php and pyp in feces. The diets of feedlot cattle, dairy cows, guinea pigs, goats, and rabbits had significant quantities of chlorophyll as a result of the feed ingredients, namely: alfalfa meal, alfalfa/grass hay, and fresh pasture **(Table 1)**. The high-level, chlorophyll-fed animals possessed greater variability in fecal levels of pyp/php. In contrast, pigs had low levels of pyp/php present in their feces. They received a diet consisting primarily of corn and soybean meal, and this diet contained very little green plant material. Rats and chickens also had low levels of pyp/php present in their feces. They consumed commercially available rodent- and chicken-feed diets, which contained minimal levels of chlorophyll-containing feed ingredients.

These results indicate that animals consuming diets with substantial levels of green plant material will excrete feces with concentrations of pheophorbide *a* (php) that greatly exceed (by 10- to 30-fold) levels demonstrated to be inhibitory to bacterial efflux pumps (0.5 μg/ml).[11,13-15] Although the EPI activity of pyp is not currently known, the natural abundance of php and its properties as an EPI may exert selection pressure upon microbial populations dependent upon efflux pump activity. Inhibitors are known to stimulate synthesis of additional efflux pump capacity as a means of metabolic compensation. This may place an energy burden upon the bacterial cell and this cost can serve as an environmental factor that selects against antimicrobial resistant phenotypes, which depend upon efflux pumps as a defense mechanism to counter antimibrobial activity. As a result, it is possible that the EPI activity of php may influence the level of antimicrobial resistance expressed in the GI tract environment. In contrast to the antimicrobial resistance displayed in the isolated conditions of pure culture, antimicrobial resistance in the gut may be substantially altered in the presence of plant derived inhibitors such as php. Given these data, further research is warranted to determine if other EPIs exist and if feed components can modulate the antimicrobial resistance of bacteria in the gut.

Acknowledgements

We thank Jim Wells (USMARC/ARS/USDA, Clay Center NE) for providing the feedlot cattle samples; Jennifer Patro (CFSAN/FDA, Laurel MD) for the rabbit, guinea pig, and rat samples; and Joe Kawalek (OR/FDA) for the chicken samples.

References

(1) Van Bambeke, F.; Glupczynski, Y.; Plésiat, P.; Pechère, J. C.; Tulkens, P. M. Antibiotic efflux pumps in prokaryotic cells: occurrence, impact on resistance and strategies for the future of antimicrobial therapy. *J. Antimicrob. Chemother.* **2003**, *51*, 1055-1065.

(2) Piddock, L. J. V. Clinically Relevant Chromosomally Encoded Multidrug Resistance Efflux Pumps in Bacteria. *Clin. Micro. Rev.* **2006**, *19*, 382-402.

(3) Piddock, L. J. V. Multidrug-resistance efflux pumps - not just for resistance. *Nat. Rev. Micro.* **2006**, *4*, 629-636.

(4) Martinez, J. L.; Sánchez, M. B.; Martínez-Solano, L.; Hernandez, A.; Garmendia, L.; Fajardo, A.; Alvarez-Ortega, C. Functional role of bacterial multidrug efflux pumps in microbial natural ecosystems. *FEMS Microbiol. Rev.* **2009**, *33*, 430-449.

(5) Van Bambeke, F.; Balzi, E.; Tulkens, P. M. Antibiotic efflux pumps. *Biochem. Pharmacol.* **2000**, *60*, 457-470.

(6) Béatrice, M. Bacterial efflux systems and efflux pumps inhibitors. *Biochimie* **2005**, *87*, 1137-1147.

(7) Kristiansen, J. E.; Hendricks, O.; Delvin, T.; Butterworth, T. S.; Aagaard, L.; Christensen, J. B.; Flores, V. C.; Keyzer, H. Reversal of resistance in microorganisms by help of non-antibiotics. *J. Antimicrob. Chemother.* **2007**, *59*, 1271-1279.

(8) Pagès, J.-M.; Amaral, L. Mechanisms of drug efflux and strategies to combat them: Challenging the efflux pump of Gram-negative bacteria. *Biochim. Biophys. Acta, Proteins Proteomics* **2009**, *1794*, 826-833.

(9) Okandeji, B. O.; Greenwald, D. M.; Wroten, J.; Sello, J. K. Synthesis and evaluation of inhibitors of bacterial drug efflux pumps of the major facilitator superfamily. *Bioorg. Med. Chem.* **2011**, *19*, 7679-7689.

(10) Lewis, K. In search of natural substrates and inhibitors of MDR pumps. *Mol. Microbiol. Biotechnol.* **2001**, *3*, 247-254.

(11) Tegos, G.; Stermitz, F. R.; Lomovskaya, O.; Lewis, K. Multidrug Pump Inhibitors Uncover Remarkable Activity of Plant Antimicrobials. *Antimicrob. Agents Chemother.* **2002**, *46*, 3133-3141.

(12) Garvey, M. I. R., M.M.; Gibbons, S.; Piddock, L.J.V. Medicinal plant extracts with efflux inhibitory activity against Gram-negative bacteria. *Int. J. Antimicrob. Agents* **2011**, *37*, 45-51.

(13) Stermitz, F. R.; Lorenz, P.; Tawara, J. N.; Zenewicz, L. A.; Lewis, K. Synergy in a medicinal plant: Antimicrobial action of berberine potentiated by 5′-methoxyhydnocarpin, a multidrug pump inhibitor. *Proc. Natl. Acad. Sci. U. S. A.* **2000**, *97*, 1433-1437.

(14) Stermitz, F. R.; Tawara-Matsuda, J.; Lorenz, P.; Mueller, P.; Zenewicz, L.; Lewis, K. 5‘-Methoxyhydnocarpin-D and Pheophorbide A: Berberis Species Components that Potentiate Berberine Growth Inhibition of Resistant Staphylococcus aureus. *J. Nat. Prod.* **2000**, *63*, 1146-1149.

(15) Stermitz, F. R.; Beeson, T. D.; Mueller, P. J.; Hsiang, J.-F.; Lewis, K. Staphylococcus aureus MDR efflux pump inhibitors from a Berberis and a Mahonia (sensu strictu) species. *Biochem. Syst. Ecol.* **2001**, *29*, 793-798.

(16) Musumeci, R.; Speciale, A.; Costanzo, R.; Annino, A.; Ragusa, S.; Rapisarda, A.; Pappalardo, M. S.; Iauk, L. Berberis aetnensis C. Presl. extracts: antimicrobial properties and interaction with ciprofloxacin. *Int. J. Antimicrob. Agents* **2003**, *22*, 48-53.

(17) Hörtensteiner, S.; Wüthrich, K. L.; Matile, P.; Ongania, K.-H.; Kräutler, B. The Key Step in Chlorophyll Breakdown in Higher Plants. *J. Biol. Chem.* **1998**, *273*, 15335-15339.

(18) Schelbert, S.; Aubry, S.; Burla, B.; Agne, B.; Kessler, F.; Krupinska, K.; Hörtensteiner, S. Pheophytin Pheophorbide Hydrolase (Pheophytinase) Is Involved in Chlorophyll Breakdown during Leaf Senescence in Arabidopsis. *The Plant Cell Online* **2009**, *21*, 767-785.

(19) Aronoff, S. In *The Chlorophylls*; Vernon, L. P., Seely, G. R. , Ed.; Academic Press: New York, 1966, p 6-18.

(20) Ma, L.; Dolphin, D. The metabolites of dietary chlorophylls. *Phytochemistry* **1999**, *50*, 195-202.

(21) Ashby, K. D.; Wen, J.; Chowdhury, P.; Casey, T. A.; Rasmussen, M. A.; Petrich, J. W. Fluorescence of Dietary Porphyrins as a Basis for Real-Time Detection of Fecal Contamination on Meat. *J. of Agric. Food Chem.* **2003**, *51*, 3502-3507.

(22) Lee, M. R. F.; Theobald, V. J.; Ougham, H. J.; Dahl, A. V.; Lundby, F.; Scollan, N. D.; Wold, J. P. Natural faecal fluorophores and the potential of chlorophyll based markers to optimise fluorescence as a real-time solution for the detection of faecal contamination on carcasses. *Meat Science* **2010**, *86*, 966-975.

CHAPTER 4: SOLVATION DYNAMICS OF THE FLUORESCENT PROBE, PRODAN, IN HETEROGENEOUS ENVIRONMENTS: CONTRIBUTIONS FROM THE LOCALLY EXCITED AND CHARGE-TRANSFERRED STATES

A paper published in *The Journal of Physical Chemistry B*

R. Adhikary, CA Barnes, and JW Petrich*

Abstract

The coexistence of different excited states with different properties of the same chromophores could have significant consequences for the accurate characterization of solvation dynamics in a heterogeneous environment, such as a protein. The purpose of this work is to study the contributions of the locally-excited (LE) and charge-transferred (CT) states of the fluorescent probe molecule, 6-propionyl-2-(N,N-dimethylamino)naphthalene (PRODAN), PRODAN to its solvation dynamics in the heterogeneous environment provided by reverse micelles formed by sodium 1,4-bis-(2-ethylhexyl) sulfosuccinate (AOT)/nheptane/water. We have found that the LE and CT states of PRODAN solvate on different time scales in reverse micelles (2 and ~0.4 ns, respectively), consistent with results suggested in the literature, and have concluded that PRODAN's use as a probe of heterogeneous

---

Reprinted with permission from *The Journal Physical Chemistry B* 2009, 113(35), 11999-12004. Copyright (2009) American Chemical Society. Department of Chemistry, Iowa State University, Ames, Iowa 50011.

Introduction

Fluorescent molecules sensitive to environmental polarities have been used extensively as probes in the studies of physicochemical properties of solvents, surfaces, proteins, membranes, cells etc.[1-5] It is critical to understand the photophysical properties of the fluorescent probe molecule, especially if it can emit from more than one state. 6-Propionyl-2-(N,N-dimethylamino)naphthalene (PRODAN) (**Figure 4.1**) is a highly fluorescent, hydrophobic molecule, first synthesized and characterized by Weber and Farris in 1979.[6] Its absorption and emission spectra are strongly dependent upon the polarity of its environment [6], and it has a long history of use in probing biological systems.[7-14] It has been used as an optical probe of the function and dynamics of proteins and membranes.[7-14] Recently it has also been used to study solvation dynamics in polar liquids, ionic liquids, and supercritical fluids.[15-19]

PRODAN is a push-pull, charge-transfer chromophore that produces a substantial change in its excited-state dipole moment upon photoexcitation owing to the presence of an electron-donating dimethylamino group and electron-withdrawing propionyl group connected to the aromatic spacer by a single bond. The excited-state kinetics of PRODAN are complex, and the origins of its solvatochromatic nature have been debated.[20-26] Theoretical calculations suggest a planar structure in the ground state. But the geometry of its charge-transferred emissive state has not yet been confirmed.[20,27] Several theoretical studies have been performed to determine the possible conformational changes in its excited-state geometry: for example, whether the emissive state is twisted intramolecular charge transfer (TICT) or planar intramolecular charge transfer (PICT).[20,23-35]

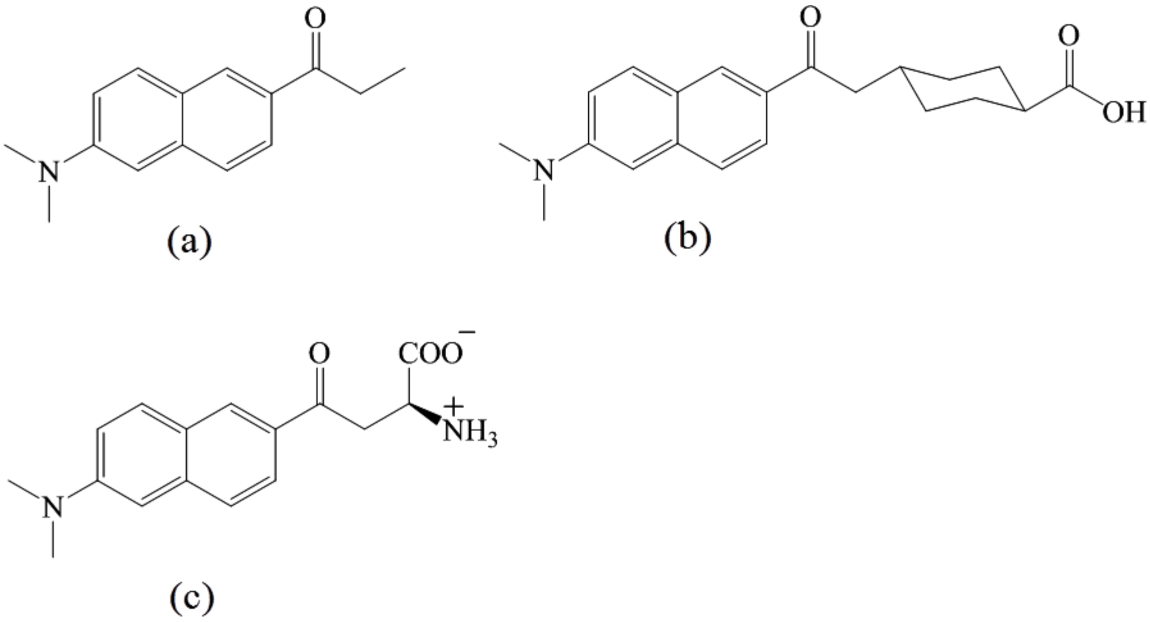

Figure 4.1. Structure of (a) 6-Propionyl-2-(N,N-dimethylamino)naphthalene (PRODAN), (b) 2′-(N,N-dimethylamino)-6-naphthoyl-4-trans-cyclohexanoic acid (DANCA) and (c) Aladan.

Lakowicz and Balter [36,37] studied PRODAN in n-butanol and suggested that its spectral relaxation requires at least two steps. Later Heisel et al. [28] explained the time-resolved fluorescence experimental results of PRODAN in n-butanol in terms of a nonradiative intramolecular reaction from a locally-excited state to an energetically lower charge-transferred state and to solute-solvent interactions. Chapman et al. [15] and Chapman and Maroncelli [16] discussed the spectral relaxation of PRODAN in terms of a continuous solvation process. It is generally agreed that, PRODAN undergoes excited-state intramolecular charge-transfer following excitation from the ground state. The charge-trasferred state, CT, is formed from an initially excited state referred to as the locally-excited state (LE).[38] In nonpolar environments, emission is from the LE state, while in polar environments the emission is from the CT state (**Figure 4.2**).[38]

PRODAN has a single broad emission spectrum with a dramatic solvatochromatic shift (~130 nm) of its maximum, ranging from 401 nm in cyclohexane to 531 nm in water.[6] Weber and Farris [6] first reported a change in dipole moment, Δμ ~ 20 D, upon excitation, and concluded that this was responsible for its large Stokes shift. Balter et al. modified this value to 10 D and suggested that solvent-specific interactions (e.g., hydrogen bonding) may cause a large Stokes shift in polar protic solvents.[29] Recently Samanta et al. [32] have suggested this value to be 4.4-5.0 D based on transient dielectric loss measurements. Recently ground and excited Frank-Condon state dipole moment of PRODAN was also reported from electrooptical absorption measurements.[39]

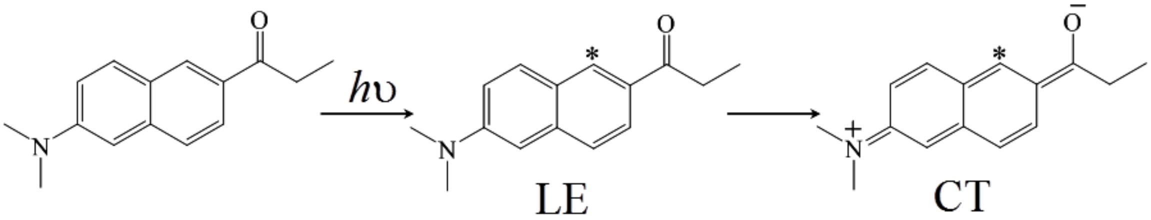

Figure 4.2. The charge-transferred (CT) state is created via the locally-excited (LE) state in polar environments.

PRODAN has a single-exponential fluorescence lifetime decay in nonpolar solvents (e.g., cyclohexane: ~ 0.2 ns; heptane: ~ 0.14 ns) and in polar aprotic solvents (e.g., acetonitrile: ~3.3 ns).[22,40] However, it exhibits a biexoponential lifetime in polar protic solvents such as methanol and water. The reported lifetime components in methanol are ~2.0 ns (75%) and 3.4 ns (25%).[22] The fluorescence behavior is more complex in water than in other solvents: Balter et al. [22] observed an additional, weak emission band around 430 nm. They also reported a biexponential fluorescence lifetime (τ_1~0.5 ns and τ_2~1.9 ns) with an additional small contribution from a long-lived component of ~ 13 ns at the blue edge of emission spectrum, exciting at 337 nm. The faster lifetime component in protic solvent was interpreted in terms of a solute-solvent complex formation via hydrogen bonding. Later, Bunker et al. [29] noticed a stronger blue emission band exciting at 280 nm, and they suspected that the blue emission was the consequence of water-soluble impurities present in commercial PRODAN. Sun and coworkers [41] resolved this ambiguity. They showed that the extra blue-edge shoulder and the small contribution from the additional long-lived component (~ 13 ns) in fluorescence decay were the result of PRODAN-PRODAN intermolecular interactions in a supersaturated solution of PRODAN in water.

Our work here is motivated by previous studies using PRODAN to study the environments of reverse micelle.[40,42-48] While most of these studies attributed PRODAN fluorescence to only the LE state and rationalized the observed emission to partitioning of the fluorophore in different regions of the reverse micelle [42-47], Novaira et al. [40,48] have reported dual fluorescence from both LE and CT in reverse micelles arising from both the LE and CT states by using time-resolved area normalized emission spectroscopies.

The coexistence of different excited states with different properties of the same chromophores could have significant consequences for the accurate characterization of solvation dynamics in a heterogeneous environment, such as a protein. Therefore, the purpose of this work is to study the contributions of LE and CT states of PRODAN to its solvation dynamics, in particular, in reverse micelles formed by sodium 1,4-bis-(2-ethylhexyl) sulfosuccinate (AOT)/n-heptane/water (**Figure 4.3**). We have found that the LE and CT states of PRODAN solvate on different time scales and concluded that PRODAN's use as a probe of heterogeneous environments must be used with caution.

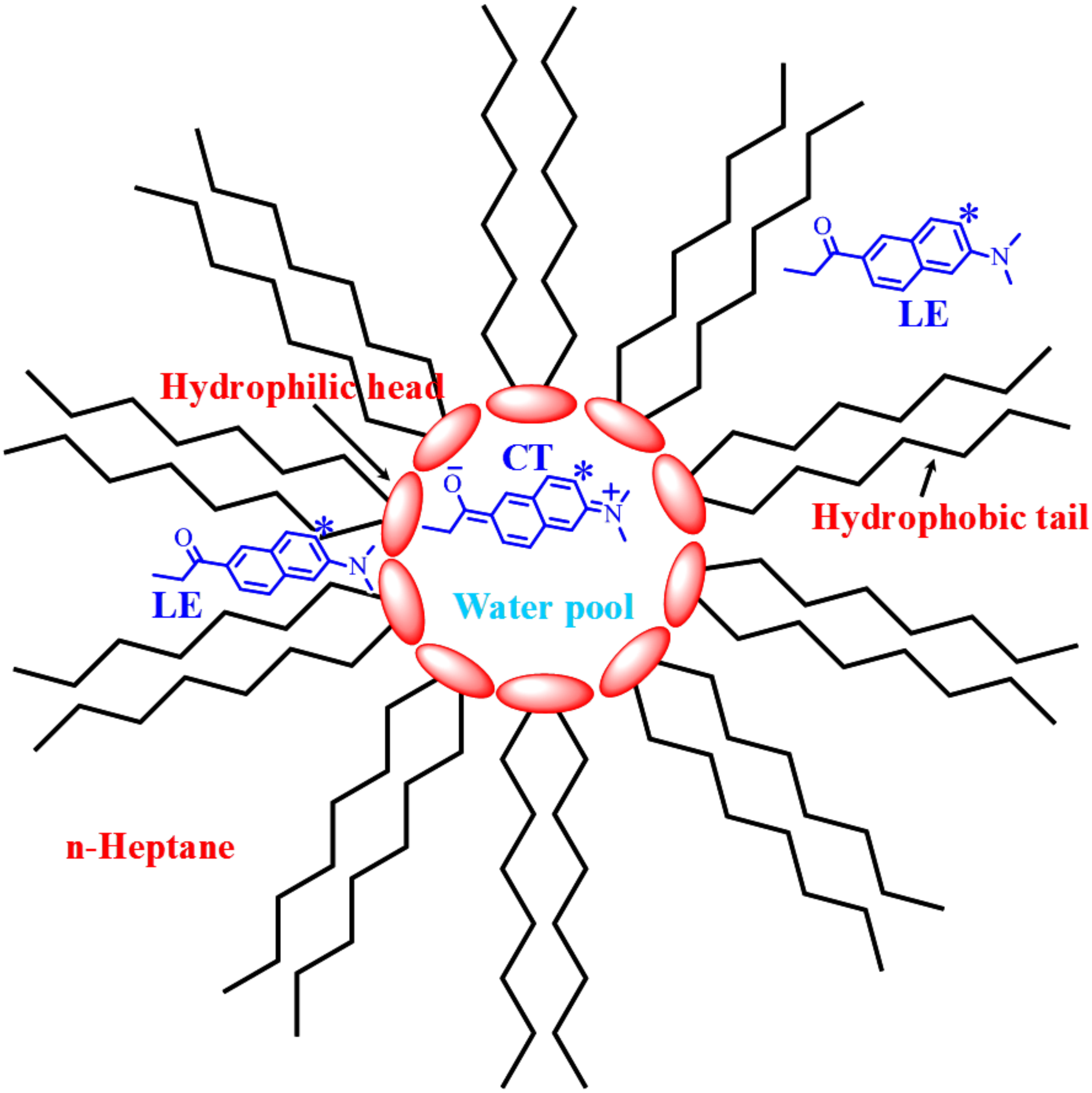

Figure 4.3. PRODAN in the 1,4-bis-(2-ethylhexyl) sulfosuccinate (AOT)/n-heptane/water reverse micellar environment. LE and CT are the locally-excited and charge-transferred emissive states of PRODAN, respectively.

Experimental Section

Materials. 6-Propionyl-2-(N,N-dimethylamino)naphthalene (PRODAN) (purity ≥ 98%) and sodium 1,4-bis-(2-ethylhexyl) sulfosuccinate (AOT) (purity > 99%) were obtained from Sigma-Aldrich and used as received. n-Heptane was obtained from Acros, Spectragrade. Methanol and acetonitrile (purity 99.9%) were purchased from Fisher Scientific and used without further purification.

Sample Preparation. Stock solutions of PRODAN (0.05 M) in acetonitrile and AOT (0.8 M) in n-heptane were prepared. The reverse micelle system was prepared through volumetric dilution from the stock solutions. The final AOT concentration was 0.2 M. The concentrated PRODAN in acetonitrile solution was used to introduce the probe into the system. The final concentration of PRODAN was 5×10^{-5} M with an organic content of < 0.1%. An appropriate amount of nanopure water was then added to obtain w = 20 ($w = [H_2O]/[AOT]$). All samples were allowed to equilibrate for 24 hrs before subsequent steady-state and time-resolved measurements. To prepare a PRODAN/water solution, 45μL of a solution of 1×10^{-3} M PRODAN in methanol (Fisher Scientific, HPLC) was added to 5 mL of water: i.e., 9×10^{-6} M PRODAN/water was prepared with an organic content < 0.9%. This freshly prepared solution was then used for the steady-state and time-resolved measurements.

Steady-State Measurements. Steady-state absorption spectra were obtained on a Hewlett Packard 8453 UV-visible spectrophotometer with 1-nm resolution. Steady-state emission spectra were obtained on a Spex Fluoromax-4 with a 3- or 4-nm bandpass and corrected for lamp spectral intensity and detector response. For absorption and emission measurements, 5-mm and 1-cm path-length quartz cuvettes were used, respectively. All experiments were done at room temperature.

Time-Resolved Measurements. Measurements of excited-state lifetimes were performed with the time-correlated single-photon counting (TCSPC) technique. The apparatus for time-correlated single-photon counting is described elsewhere.[49] The fundamental from a home-made mode-locked Ti-sapphire oscillator was modulated by a Pockels cell (Model 350-160, Conoptics Inc) to reduce the repetition rate to 8.8 MHz. All experiments were performed using either the 407-nm or 266-nm excitation obtained from the 814 nm fundamental by means of a U-Oplaz Technologies (Model TP-2000B) doubler/tripler. Recent modifications in the experimental setup include the replacement of NIM-style electronics by a Becker & Hickl photon counting module (Model SPC-630). With this modified system, the full-width at half-maximum of the instrument-response function is ~40 – 50 ps. A cuvette of 5-mm or 1-cm path length was used for the time resolved measurement depending upon the system.

To construct the time-resolved spectra, a series of decays were collected typically from 370 nm to 560 nm at 10 nm intervals. Transients were fit to sums of exponentials, and time-dependent spectra were reconstructed from these fits by normalizing to the steady-state spectra:

$$S(\lambda,t) = D(\lambda,t)\frac{S_0(\lambda)}{\int_0^\infty D(\lambda,t)} \qquad (4.1)$$

$D(\lambda,t)$ is the wavelength-resolved fluorescence decay, and $S_0(\lambda)$ is the steady-state emission intensity at a given wavelength. We have employed the traditional approach of fitting the time-resolved spectra to a log-normal function, from which we extract the peak frequency, $\nu(t)$, as a function of time.

Results and Discussion

The absorption and emission spectra of PRODAN in AOT/n-heptane/water (w = 20) are shown in **Figure 4.4**. The emission spectrum of PRODAN in AOT/n-heptane/water exciting at 266 nm consists of two bands. This result is consistent with the dual emission obtained previously exciting at 330 nm in AOT/n-heptane/water reverse micelles [40] from a locally-excited state (LE) at $\lambda^{em}{}_{max}$ = 411 nm and from a charge-transferred state (CT) at $\lambda^{em}{}_{max}$ = 507 nm. Upon excitation at 407 nm, only one emission band was obtained, with $\lambda^{em}{}_{max}$ = 508 nm. This indicates that only PRODAN molecules in the polar environment of AOT/n-heptane/water reverse micelle are excited at red edge excitation. Thus, it is possible to observe PRODAN emission from both the LE and CT states in the same sample; and its emission can be tuned with excitation energy.

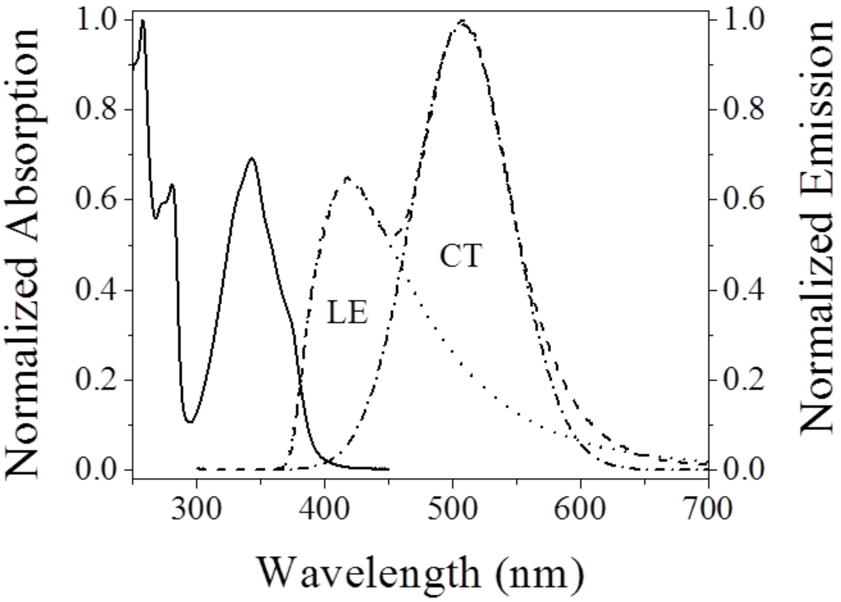

Figure 4.4. Normalized absorption (solid line) and emission spectra (dashed line) of PRODAN in AOT/n-heptane/water (w = 20). The emission spectrum was fit with two log-normal equations to obtain individual emission spectra for the CT (dashed-dotted line) and LE states (dotted line). The sample was excited at 266 nm and emission was collected using a 345 nm long-pass filter.

Fluorescence lifetime decays of PRODAN in water, n-heptane and AOT/n-heptane/water (w = 20) at different excitation wavelengths are displayed in **Figure 4.5**. **Figure 4.5A** presents the decay traces of PRODAN in n-heptane and water exciting at 266 nm. The lifetime parameters are given in **Table 4.1**. PRODAN has a single-exponential lifetime with a time constant of 0.15 ns in n-heptane. The decay of PRODAN in water is well described by a biexponential function with time constants of 0.70 ns (60%) and 2.0 ns (40%). There is a significant change in the decay kinetics of PRODAN in AOT/n-heptane/water (w = 20) depending on whether the excitation wavelength is 266 or 407 nm **(Figure 4.5B)**. The trace obtained with 266 nm excitation was best fit with a biexponential function with time constants of

0.16 ns (70%) and 2.3 ns (30%). The trace obtained with 407 nm, however, was best fit by a single exponential with a time constant of 2.6 ns. The absence of a rise time of the CT emission band (**Table 3.1**, **Figure 4.5B**) suggests that in such a polar environment the LE→CT reaction rate of PRODAN is too fast to be resolved under the present experimental conditions. 4-*N*,*N*-dimethylaminobenzonitrile (DMABN) is a well studied molecule which emits from both LE and CT states and shows dual emission bands in polar solvents.[50,51] It is important to note that DMABN also leads to complete cutoff of LE emission band and shows only CT emission band upon red edge excitation of its absorption spectrum in polar solvent.[52] The charge-transferred time found for DMABN in a polar acetonotrile solution was ~ 4-6 ps. [53,54]

To investigate the solvation of the LE and CT states, wavelength-resolved lifetime measurements were carried out at 20 different wavelengths from 370 to 560 nm for PRODAN in AOT/n-heptane/water (w = 20) and were fit to a sum of two decaying exponentials. Representative wavelength-resolved fluorescence decay traces are displayed in **Figure 4.6.** To evaluate the spectra and dynamics of the LE and CT states separately, the emission spectrum in **Figure 4.4** was decomposed into two bands using log-normal functions. Time-resolved emission spectra were constructed according to eq 1 for each using the fitting parameters for the 20 wavelength-resolved decay traces. Representative time-resolved emission spectra for the LE and the CT states are given in **Figure 4.7**. Plots of peak frequencies as a function of time are given in **Figure 4.8** for the LE and CT states. The peak shift was fit to a single exponential of time constant 2.0 ns for LE and to two exponentials with time constants of 0.40 ns (91%) and 4.0 ns (9%) for CT.

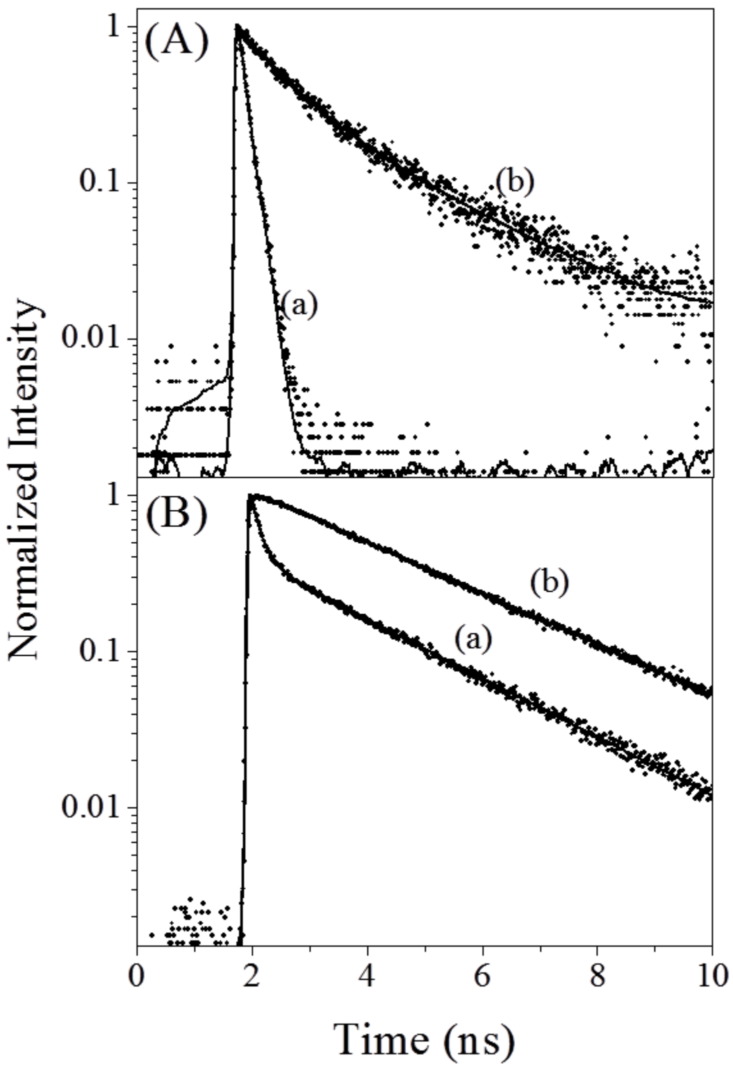

Figure 4.5. (A) Fluorescence decay traces of PRODAN in (a) n-heptane and (b) water, exciting at 266 nm. (B) Fluorescence decay traces of PRODAN in AOT/n-heptane/water (w = 20) exciting at (a) 266 nm and (b) 407 nm.

Table 4.1

Lifetime Parameters of PRODAN in Different Environments

System	a_1	τ_1 (ns)	a_2	τ_2 (ns)
[a] n-heptane	1.0	0.15	----	----
[a] water	0.60	0.70	0.40	2.0
[a] AOT/n-heptane/water (w = 20)	0.70	0.16	0.30	2.3
[b] AOT/n-heptane/water (w = 20)	1.0	2.6	----	----

[a] $\lambda_{ex} = 266$ nm, $\lambda_{em} \geq 300$ nm
[b] $\lambda_{ex} = 407$ nm, $\lambda_{em} \geq 425$ nm

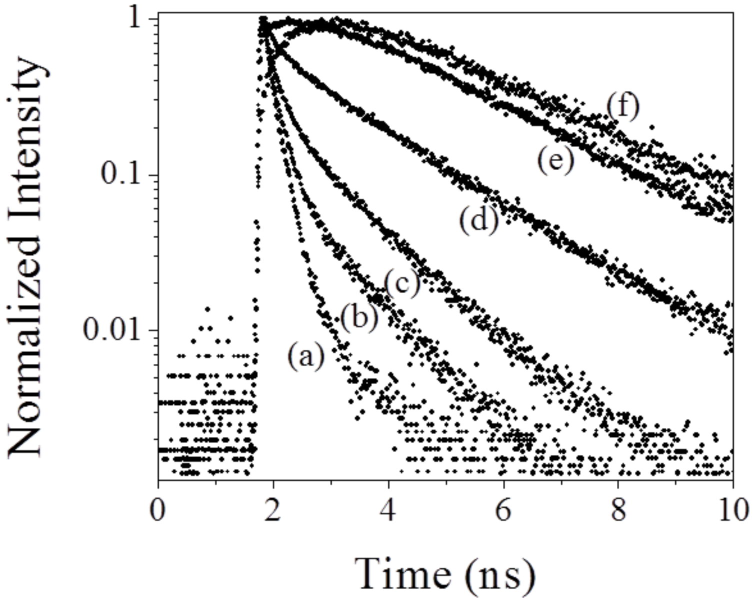

Figure 4.6. Representative wavelength-resolved decay traces of PRODAN in AOT/n-heptane/water (w = 20) at (a) 370 nm, (b) 400 nm, (c) 430 nm, (d) 460 nm, (e) 490 nm, and (f) 560 nm, exciting at 266 nm.

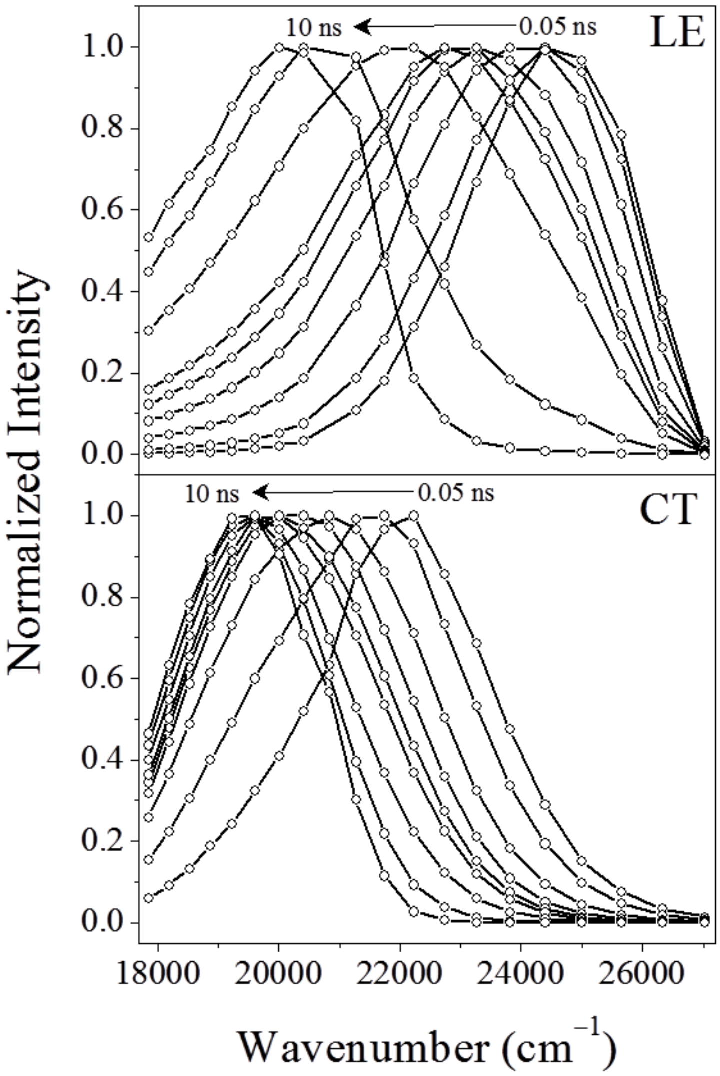

Figure 4.7. Representative normalized time-resolved emission spectra of (A) the locally-excited state (LE) and (B) the charged-transferred state (CT) at 0.05, 0.2, 0.4, 0.6, 0.8, 1.0, 2.0, 5.0, and 10.0 ns.

These results clearly demonstrate that the solvatochromic probe, PRODAN, can emit from different states in a heterogeneous environment and that, owing to the different natures of these states (i.e., charge-transferred or not), their solvation dynamics can occur on different time scales and they can have significantly different Stokes shifts. This, consequently, introduces another level of complication into the interpretation of the data when fluorescence is observed from chromophores capable of emitting from more than one excited state. If the properties of each state are known, it is possible to take them into account. We have recently discussed and compared two methods of performing such an analysis.[55]

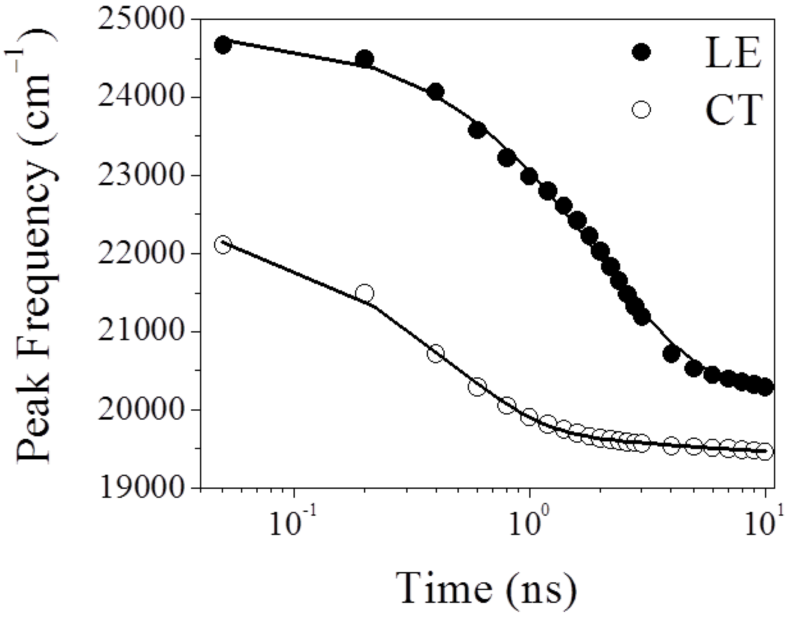

Figure 4.8. Plots of the maxima of the time-resolved emission spectra for the locally-excited (LE) state (solid circles) and the charge-transferred (CT) state (empty circles). Peak frequencies were obtained by fitting the time-resolved emission spectra to log-normal functions. The peak shift was fit to a single exponential of time constant 2.0 ns for LE and to two exponentials with time constants of 0.40 ns (91%) and 4.0 ns (9%) for CT.

There are other factors, however, that are more difficult to account for, namely the effects of slow conformational changes or aggregation, which is possible at the high concentrations (~ 1 mM) [56,57] at which some of these experiments are performed. We now refer to a few examples. As illustrated in **Figure 4.1**, more elaborate fluorescent probes of biological systems are based upon the PRODAN chromophore, namely, DANCA [58] and, more recently, a nonnatural amino acid analog, Aladan [59]. Boxer and coworkers [56] have incorporated the latter at different buried and exposed sites of the immunoglobin binding domain, B1, of protein G (GB1) and measured the time-dependent Stokes shift. All the sites showed a bimodal relaxation with an inertial ultrafast response of ~80-140 fs followed by a much slower relaxation on the timescale of several picoseconds to several nanoseconds, depending upon the location of the probe. This experimental work forms the basis for a good comparison with simulations performed by Golosov and Karplus.[60] In the context of their study, an interesting observation was that the time-resolved emission spectra of Aladan at fully and partially exposed sites of the protein showed a blue shift at long times (> 1 ns). The authors suggested that this blue shift could be attributed either to different chromophore populations having different lifetimes and solvation dynamics or to aggregation effects.

Based on our above results for the PRODAN photophysics and solvation dynamics, we suggest a model that can produce a blue shift of time-resolved spectra at long times. In this model we assume that the LE state is formed from CT states. *In particular, we assume a slow ground-state conformational change or aggregation that perturbs the environment of the chromophore in such a manner that CT states are no longer predominantly favored and thus increases the population of LE states.* As LE is gradually formed in this manner, it will undergo its characteristic solvation dynamics, which must be convoluted with the LE formation and decay in order to obtain the complete spectral response of this newly formed species. The spectrum at any given time will then have contributions from both CT and LE.

Thus, the time course of production and decay of LE, $L(t)$ is given by

$$L(t) = I_0(e^{-\frac{t}{\tau_f}} - e^{-\frac{t}{\tau_{LE}}}) \qquad (4.2)$$

where I_0 is fraction of the protein population that undergoes the conformational change discriminating against the formation of CT and instead favoring the production of LE. In our simulation, we took $I_0 = 0.1$ (~20% of the CT population, as given by the spectral decomposition of eq 1). The time of formation, τ_f, of LE from CT was chosen as 5.0 ns. The fluorescence lifetime of LE, τ_{LE}, was found experimentally to be 0.15 ns. The evolution of time-resolved spectra of LE is

$$I(\lambda,t) = Ae^{-\frac{1}{2}\frac{(\lambda-\lambda_m(t))^2}{\sigma^2}} e^{-\frac{t}{\tau_{LE}}} \qquad (4.3)$$

where A = 2.4 and was obtained by spectral decomposition using eq 1 and σ = 1280 cm^{-1} , as obtained from the time-resolved emission spectrum at the instrumental time-zero. The peak frequency of the time-resolved spectra is given by $\lambda_m = (\lambda_0 - \lambda_\infty)e^{-\frac{t}{\tau_{sol}}} + \lambda_\infty$, where λ_0 and λ_∞ were taken from the experimental data as 24675 cm^{-1} and 20292 cm^{-1}, respectively. The solvation time, τ_{sol}, of LE is 2.0 ns **(Figure 4.8)**. The convolution of *L(t)* with *I(λ, t)* is

$$LE(\lambda,t) = \int_0^t L(t')I(\lambda,t-t')dt' \qquad (4.4)$$

and yields the time-resolved emission spectrum induced by the slow conformational change or aggregation postulated above (**Figure 4.9**). The time-resolved spectra for LE and CT were then summed to generate the total time-resolved spectra. Those at t = 0, 1.0, and 10.0 ns are shown in **Figure 4.10**. At t = 0 ns, there is virtually no contribution from LE in the total time-resolved spectrum; but with increasing time, LE contributes significantly to the total time-resolved spectrum. Other variations of this model are clearly possible.

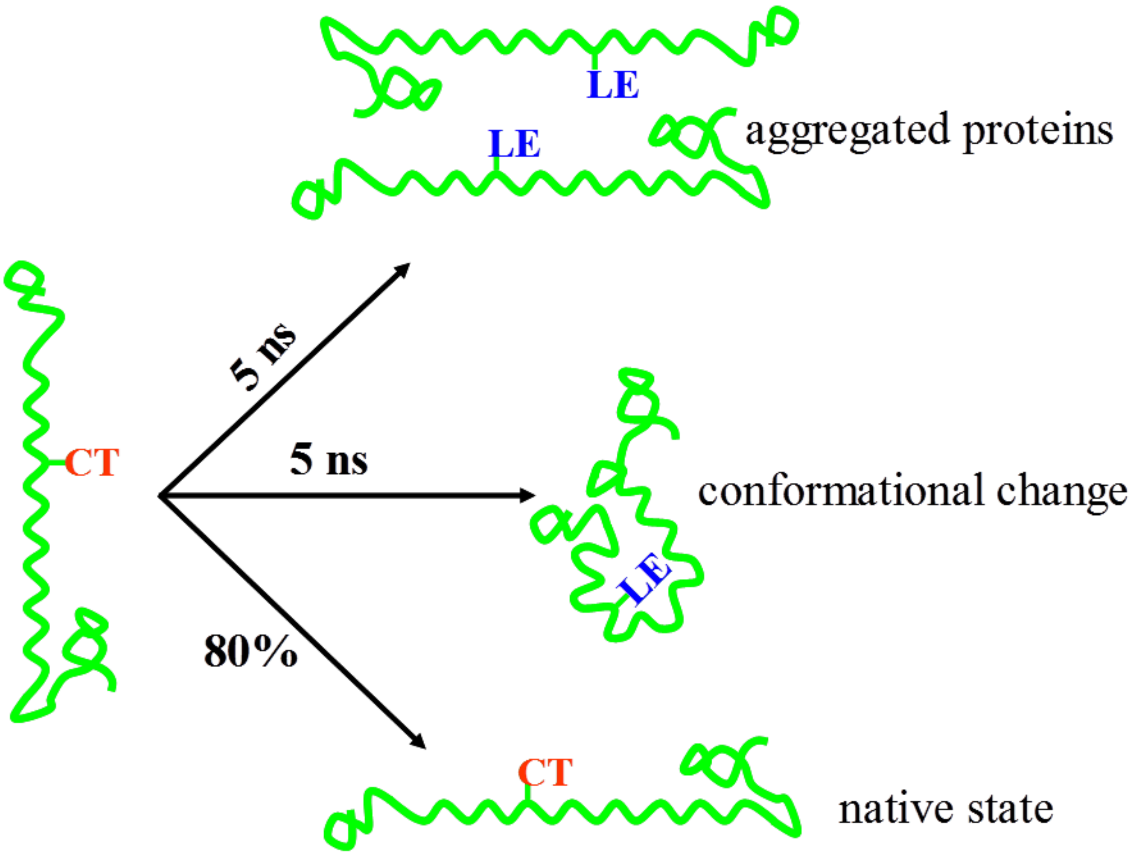

Figure 4.9. Schematic diagram illustrating the assumptions underlying the simulation described in the text. As noted in the Introduction and in the caption to Figure 2, it is generally agreed that in all cases, regardless of solvent or environment, the LE state is formed immediately upon excitation and that whether the LE state decays into the CT state does, however, depend on environment. The purpose of the simulation, whose results are illustrated in Figure 10, is to suggest a mechanism by which blue shifts in the dynamic Stokes shift may be observed at long times. We propose that they may arise from a system that emits completely from an ensemble of CT states initially, but that after several nanoseconds, for example, a small but nonnegligible population of protein assumes conformations where LE, not CT, is the emissive state. It must be noted that in the time required for the conformational change or aggregation to occur, the same protein sample is being used for the experiment (~ 2 hours for single wavelength decay measurement). We do not suggest that the slow ground-state changes are triggered by photoexcitation. Furthermore, it is not being suggested that the lifetime of CT is 5 ns, nor that there is an excited-state pathway converting CT to LE on this time scale.

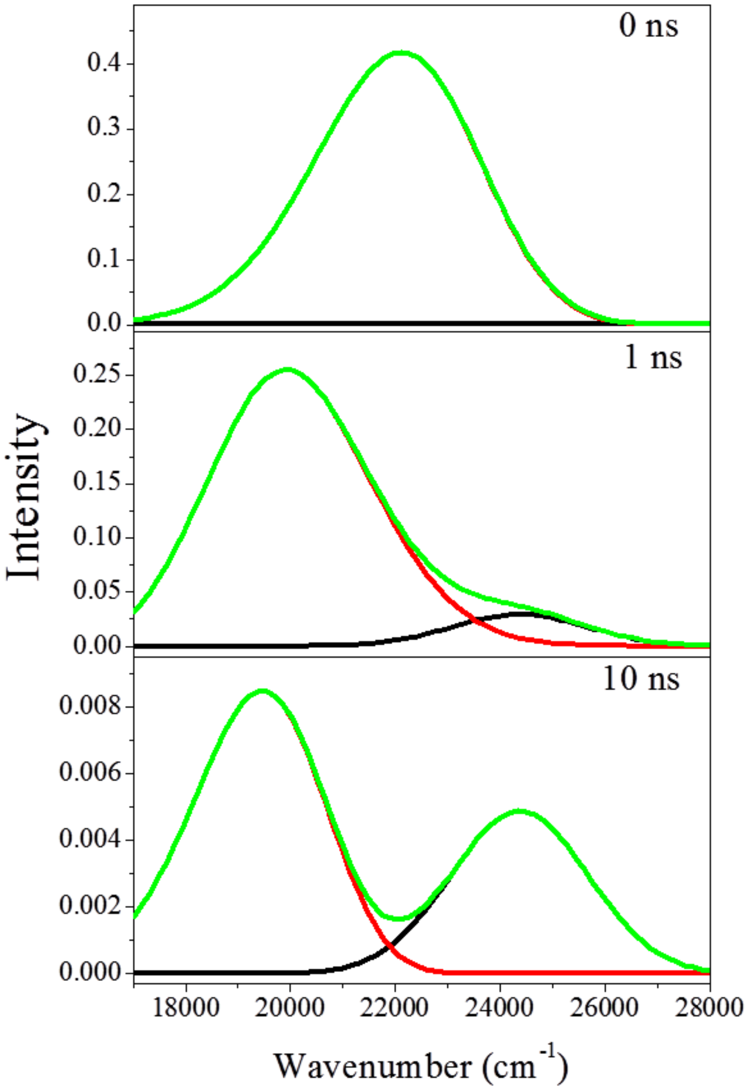

Figure 4.10. Simulation of the total time-resolved emission spectra at 0, 1, and 10 ns as described in the text. The black line is the time-resolved emission spectrum for LE; the red line, for CT. The sum of the two time-resolved spectra is shown in green. Note that the scale of the ordinate changes with time.

Given, however, that the LE state was not accessed with 400 nm excitation (**Table 4.1**), the excitation wavelength used by Boxer and coworkers, and that their steady-state spectra showed no evidence of the LE state, the blue shift they observed is likely to have other origins. On the other hand, it is useful to consider three different investigations carried out to study the solvation response of myoglobin using various chromophores to replace the heme. These chromophores are: the PRODAN derivative, DANCA [58]; another charge-transfer molecule capable of emitting from dual states, aniline-2-aminonaphthalene-6-dimethylsulfonamide (ANSDMA) [61], and coumarin 153 [57]. Each probe of solvation dynamics exhibited a different response. DANCA yielded a complicated solvation response with significant contributions into the nanosecond regime. ANSDMA provided a single-exponential response of ~ 9 ns (although rapid components might have been neglected because of the time resolution of the experiment). Using coumarin 153, it was found that almost 60 % of the solvation is complete within the time resolution of the experiment (300 fs) and that this initial response is followed by a slower one. Most importantly, there was excellent agreement between the solvation correlation function, $C(t)$, from fluorescence upconversion experiments and those obtained from molecular dynamics simulations. While some of these differences may be attributed to how [55] or whether a solvation correlation function was actually constructed, it is legitimate to inquire whether some of the discrepancy might not also be attributed to the nature of the fluorescent probes employed. While DANCA and ANSDMA are both capable of charge transfer in the excited state, coumarin 153 is exquisitely inert, which is one of the reasons it has been so extensively employed as a probe of salvation.[57,62-73] (The DANCA experiments used an excitation wavelength of 345 nm. Novaira et al. have observed that both LE and CT emission can be observed in reverse micelles at 330 nm. While the DANCA work [58] does not mention a blue-shift at long times, it is feasible that some of the long-time dynamics observed are a result of the possible behavior we have suggested above.)

Conclusions

Stimulated by the work of Novaira et al. [40,48], we have studied the solvation dynamics of PRODAN in a heterogeneous environment (reverse micelles) that permits a distribution of the chromophores to emit from both the LE and the CT states. We have studied the solvation dynamics of both states and found them to be very different, as suggested by the work of Novaria et al. This result consequently leads to the question of whether PRODAN-based chromophores or, more generally, any chromophore capable of undergoing excited-state photochemistry, can induce artifacts into the interpretation of solvation dynamics in heterogeneous environments—in particular, those provided by biological systems such as proteins. Considerable care in choosing and characterizing the system is required in order to analyze the results fully.

References

(1) Demchenko, A. P. *Luminescence and Dynamics of Protein Structure*; Nauka Dumka: Kiev, 1988.

(2) Silvius, J. R. *Annu. Rev. Biophys. Biomol. Struct.* **1992**, *21*, 323.

(3) Dobrestov, G. E. *Fluorescence Probes in Investigations of Cells, Membranes and Lipoproteins*; Nauka: Moscow, 1989.

(4) Parasassi, T.; De Stasio, G.; Ravagnan, G.; Rusch, R. M.; Gratton, E. *Biophys. J.* **1991**, *60*, 179.

(5) Viard, M.; Gallay, J.; Vincent, M.; Meyer, O.; Robert, B.; Paternostre, M. *Biophys. J.* **1997**, *73*, 2221.

(6) Weber, G.; Farris, F. J. *Biochemistry* **1979**, *18*, 3075.

(7) Moreno, F.; Cortijo, M.; Gonzalez-Jimenez, J. *Photochem. Photobiol.* **1999**, *69*, 8.

(8) Lasagna, M.; Vargas, V.; Jameson, D. M.; Brunet, J. E. *Biochemistry* **1996**, *35*, 973.

(9) Rottenberg, H. *Biochemistry* **1992**, *31*, 9473.

(10) Bondar, O. P.; Rowe, E. S. *Biophys. J.* **1999**, *76*, 956.

(11) Bondar, O. P.; Rowe, E. S. *Biophys. J.* **1996**, *71*, 1440.

(12) Sommer, A.; Paltauf, F.; Hermetter, A. *Biochemistry* **1990**, *29*, 11134.

(13) Krasnowska, E. K.; Gratton, E.; Parasassi, T. *Biophys. J.* **1998**, *74*, 1984.

(14) Zeng, J. W.; Chong, P. L. *Biochemistry* **1991**, *30*, 9485.

(15) Chapman, C. F.; Fee, R. S.; Maroncelli, M. *J. Phys. Chem.* **1990**, *94*, 4929.

(16) Chapman, C. F.; Maroncelli, M. *J. Phys. Chem.* **1991**, *95*, 9095.

(17) Betts, T. A.; Zagrobelny, J.; Bright, F. V. *J. Supercrit. Fluids* **1992**, *5*, 48.

(18) Karmakar, R.; Samanta, A. *J. Phys. Chem. A* **2002**, *106*, 6670.

(19) Betts, T. A.; Zagrobelny, J.; Bright, F. V. *J. Am. Chem. Soc.* **1992**, *114*, 8163.

(20) Nowak, W.; Adamczak, P.; Balter, A.; Sygula, A. *J. Mol. Struct. THEOCHEM* **1986**, *32*, 13.

(21) Marks, D.; Prosposito, P.; Zhang, H.; Glasbeek, M. *Chem. Phys. Lett.* **1998**, *289*, 535.

(22) Balter, A.; Nowak, W.; Pawelkiewicz, W.; Kowalczyk, A. *Chem. Phys. Lett.* **1988**, *143*, 565.

(23) Catalan, J.; Perez, P.; Laynez, J.; Garcia Blanco, F. *J. Fluoresc.* **1991**, *1*, 215.

(24) Parusel, A. B. J.; Schneider, F. W.; Kohler, G. *J. Mol. Struct. THEOCHEM* **1997**, *398-399*, 341.

(25) Parusel, A. B. J.; Nowak, W.; Grimme, S.; Koehler, G. *J. Phys. Chem. A* **1998**, *102*, 7149.

(26) Parusel, A. *J. Chem. Soc., Faraday Trans.* **1998**, *94*, 2923.

(27) Ilich, P.; Prendergast, F. G. *J. Phys. Chem.* **1989**, *93*, 4441.

(28) Heisel, F.; Miehe, J. A.; Szemik, A. W. *Chem. Phys. Lett.* **1987**, *138*, 321.

(29) Bunker, C. E.; Bowen, T. L.; Sun, Y. P. *Photochem. Photobiol.* **1993**, *58*, 499.

(30) Pal, S. K.; Mandal, D.; Bhattacharyya, K. *J. Phys. Chem. B* **1998**, *102*, 11017.

(31) Lobo, B. C.; Abelt, C. J. *J. Phys. Chem. A* **2003**, *107*, 10938.

(32) Samanta, A.; Fessenden, R. W. *J. Phys. Chem. A* **2000**, *104*, 8972.

(33) Davis, B. N.; Abelt, C. J. *J. Phys. Chem. A* **2005**, *109*, 1295.

(34) Mennucci, B.; Caricato, M.; Ingrosso, F.; Cappelli, C.; Cammi, R.; Tomasi, J.; Scalmani, G.; Frisch, M. J. *J. Phys. Chem. B* **2008**, *112*, 414.

(35) Bakalova, S. M.; Kaneti, J. *Spectrochim. Acta Part A, Mol. Biomol. Spectrosc.* **2009**, *72*, 36.

(36) Lakowicz, J. R.; Balter, A. *Biophys.Chem.* **1982**, *16*, 117.

(37) Lakowicz, J. R.; Balter, A. *Biophys. Chem.* **1982**, *16*, 223.

(38) Rollinson, A. M.; Drickamer, H. G. *J. Chem. Phys.* **1980**, *73*, 5981.

(39) Nemkovich, N. A.; Baumann, W. *J. Photochem. Photobiol., A* **2007**, *185*, 26.

(40) Novaira, M.; Biasutti, M. A.; Silber, J. J.; Correa, N. M. *J. Phys. Chem. B* **2007**, *111*, 748.

(41) Sun, S.; Heitz, M. P.; Perez, S. A.; Colon, L. A.; Bruckenstein, S.; Bright, F. V. *Appl. Spectrosc.* **1997**, *51*, 1316.

(42) Sengupta, B.; Guharay, J.; Sengupta, P. K. *Spectrochim. Acta, Part A* **2000**, *56A*, 1433.

(43) Karukstis, K. K.; Frazier, A. A.; Martula, D. S.; Whiles, J. A. *J. Phys. Chem.* **1996**, *100*, 11133.

(44) Karukstis, K. K.; Frazier, A. A.; Loftus, C. T.; Tuan, A. S. *J. Phys. Chem. B* **1998**, *102*, 8163.

(45) Lissi, E. A.; Abuin, E. B.; Rubio, M. A.; Ceron, A. *Langmuir* **2000**, *16*, 178.

(46) Karukstis, K. K.; Zieleniuk, C. A.; Fox, M. J. *Langmuir* **2003**, *19*, 10054.

(47) Karukstis, K. K.; Suljak, S. W.; Waller, P. J.; Whiles, J. A.; Thompson, E. H. Z. *J. Phys. Chem.* **1996**, *100*, 11125.

(48) Novaira, M.; Moyano, F.; Biasutti, M. A.; Silber, J. J.; Correa, N. M. *Langmuir* **2008**, *24*, 4637.

(49) Chowdhury, P. K.; Halder, M.; Sanders, L.; Calhoun, T.; Anderson, J. L.; Armstrong, D. W.; Song, X.; Petrich, J. W. *J. Phys. Chem. B* **2004**, *108*, 10245.

(50) Lippert, E.; Lueder, W.; Moll, F.; Naegele, W.; Boos, H.; Prigge, H.; Seibold-Blankenstein, I. *Angew. Chem.* **1961**, *73*, 695.

(51) Lippert, E.; Lueder, W.; Boos, H. *Advances in Molecular Spectroscopy*; Pergamon Press: Oxford, U.K., 1962;p443.

(52) Tomin, V. I.; Hubisz, K.; Kwiek, P. *Opt. Spectrosc.* **2005**, *99*, 43.

(53) Changenet, P.; Plaza, P.; Martin, M. M.; Meyer, Y. H. *J. Phys. Chem. A* **1997**, *101*, 8186.

(54) Druzhinin, S. I.; Ernsting, N. P.; Kovalenko, S. A.; Lustres, L. P.; Senyushkina, T. A.; Zachariasse, K. A. *J. Phys. Chem. A* **2006**, *110*, 2955.

(55) Bose, S.; Adhikary, R.; Mukherjee, P.; Song, X.; Petrich, J. W. *J. Phys. Chem. B* **2008**, *in press*.

(56) Abbyad, P.; Shi, X.; Childs, W.; McAnaney, T. B.; Cohen, B. E.; Boxer, S. G. *J. Phys. Chem. B* **2007**, *111*, 8269.

(57) Halder, M.; Mukherjee, P.; Bose, S.; Hargrove, M. S.; Song, X.; Petrich, J. W. *J. Chem. Phys.* **2007**, *127*, 055101/1.

(58) Pierce, D. W.; Boxer, S. G. *J. Phys. Chem.* **1992**, *96*, 5560.

(59) Cohen, B. E.; McAnaney, T. B.; Park, E. S.; Jan, Y. N.; Boxer, S. G.; Jan, L. Y. *Science* **2002**, *296*, 1700.

(60) Golosov, A. A.; Karplus, M. *J. Phys. Chem. B* **2007**, *111*, 1482.

(61) Bashkin, J. S.; Mclendon, G.; Mukamel, S.; Marohn, J. *J. Phys. Chem.* **1990**, *94*, 4757.

(62) Changenet-Barret, P.; Choma, C. T.; Gooding, E. F.; DeGrado, W. F.; Hochstrasser, R. M. *J. Phys. Chem. B* **2000**, *104*, 9322.

(63) Maroncelli, M.; Fleming, G. R. *J. Chem. Phys.* **1987**, *86*, 6221.

(64) Horng, M. L.; Gardecki, J. A.; Papazyan, A.; Maroncelli, M. *J. Phys. Chem.* **1995**, *99*, 17311.

(65) Lewis, J. E.; Maroncelli, M. *Chem. Phys. Lett.* **1998**, *282*, 197.

(66) Muhlpfordt, A.; Schanz, R.; Ernsting, N. P.; Farztdinov, V.; Grimme, S. *Phys. Chem. Chem. Phys.* **1999**, *1*, 3209.

(67) Jiang, Y.; McCarthy, P. K.; Blanchard, D. J. *Chem. Phys.* **1994**, *183*, 249.

(68) Flory, W. C.; Blanchard, D. J. *Appl. Spectrosc.* **1998**, *52*, 82.

(69) Palmer, P. M.; Chen, Y.; Topp, M. R. *Chem. Phys. Lett.* **2000**, *318*, 440.

(70) Chen, Y.; Palmer, P. M.; Topp, M. R. *Int. J. Mass Spectrom* **2002**, *220*, 231.

(71) Agmon, N. *J. Phys. Chem.* **1990**, *94*, 2959.

(72) Chowdhury, P. K.; Halder, M.; Sanders, L.; Arnold, R. A.; Liu, Y.; Armstrong, D. W.; Kundu, S.; Hargrove, M. S.; Song, X.; Petrich, J. W. *Photochem. Photobiol.* **2004**, *79*, 440.

(73) Mukherjee, P.; Halder, M.; Hargrove, M.; Petrich, J. W. *Photochem. Photobiol.* **2006**, *82*, 1586.

CHAPTER 5: COMPARISON OF THE DIELECTRIC RESPONSE OBTAINED FROM FLUORESCENCE UPCONVERSION MEASURMENTS AND MOLECULAR DYNAMICS SIMULATIONS FOR COUMARIN 153−APOMYOGLOBIN COMPLEXES AND STRUCTURAL ANALYSIS OF THE COMPLEXES BY NMR AND FLUORESCENCE METHODS

A paper published in the *Journal of Physical Chemistry B*

S. Bose[1], R. Adhikary[1], CA Barnes[1], B. Fulton[2], MS Hargrove[2], X. Song[1], and JW Petrich[1],*

Abstract

We present a comparison of the dielectric response obtained from fluorescence upconversion experiments and from molecular dynamics simulations of the complexes of coumarin 153 with five apomyoglobins (apoMbs): wild-type horse heart (HH-WT) and those of wild-type sperm whale (SW-WT); its two triple mutants, L29F/H64Q/V68F and H64L/V68F/P88A; and its double mutant, L29F/V68L. Comparisons between experimental and simulated solvation relaxation functions, *C*(*t*)s, for the wild-type proteins range from very good to excellent. For the three mutants we investigated, however, agreement between experiment

---

Reproduced with permission from Journal of Physical Chemistry B, 2010, in press. Copyright (2010) American Chemical Society. Departments of Chemistry[1] and Biochemistry, Biophysics, and Molecular Biology[2] Iowa State University; Ames, Iowa 50011 USA.

* Author to whom all correspondence should be addressed

and simulation was considerably inferior. Thus, an NMR study of the complex of the HH-WT complex apoMb; and fluorescence energy transfer and anisotropy studies of the five complexes were performed to investigate the structures upon which the simulations were based. The NMR measurements confirm our earlier conclusions that the C153 lies in the heme pocket of the HH-WT apoMb. For the wild-type complexes, fluorescence energy transfer measurements provide two rise times, suggesting a definite spatial relationship between the two Trp donors and the C153 acceptor. These results confirm the structural integrity of the wild-type complexes and validate the initial structures used for the molecular dynamics simulations. On other hand, the three mutants provided single exponential rise times for the energy transfer, suggesting that the position of the C153 used in the simulations may have been in error or that the C153 is mobile on the time scale of the energy transfer experiment. Fluorescence anisotropy studies also suggest that the double mutant was not structurally intact. Furthermore, examination of these systems demonstrates the sensitivity of C153 to its environment and permits the observation of differences in the heme pockets. These results point to the importance of structural characterization of modified proteins used in studies of the dielectric response and suggest strategies for performing molecular dynamics simulations of modified proteins.

Introduction

The study of solvation dynamics is a powerful tool for understanding the dielectric relaxation of solvating media. For homogeneous dielectric fluids, solvation dynamics can be described by linear response theory. [1-12] A simple dielectric continuum theory[13-15] adequately describes their dielectric response, which led to several successful comparisons between theory and experiments. [11,12,16,17] However, for inhomogeneous dielectric materials, such as proteins, dielectric fluctuations are severely restricted due to the inherent constraints of the materials. The delicate balance in the electrostatic interactions play important role to control structure, function and dynamics in proteins.[18-22] The nature of the interactions is heterogeneous because the charged and polar groups in protein can interact over long distances with each other and surrounding solvent molecules. A large protein can have its dielectric response vary from place to place. [23-29] A sudden change in the charge distribution for many elementary processes such as electron and energy transfer in a protein causes dielectric relaxation due to the adjustment of its structure in response to the new charge distribution. Traditional dielectric continuum theory assumes that there is only one intrinsic microscopic length scale. Hence, such theory is questionable when applied to inhomogeneous dielectric materials. As a result understanding the dielectric response in proteins is very challenging due to the existence of different length scales of relaxation.

In a series of papers, [30-33] we have discussed the extensive literature on this topic and have suggested the utility of using the fluorescent probe, coumarin 153 (C153), to study the dielectric response of monomeric hemoglobins, such as myoglobin. The choice of C153 was in large part inspired by the work of Cocco and Lecomte who characterized the complex of the fluorescent dye ANS (**Figure 5.1a**) with apomyoglobin (apoMb) using nuclear magnetic resonance (NMR) spectroscopy and proved that ANS resides in the distal side of the heme pocket.[34] Using 2D- DQF-COSY and NOESY experiments, they showed that the H_a and H_b protons of ANS have cross peaks with heme pocket residues such as His64, Val67, Val68, and Ala71.

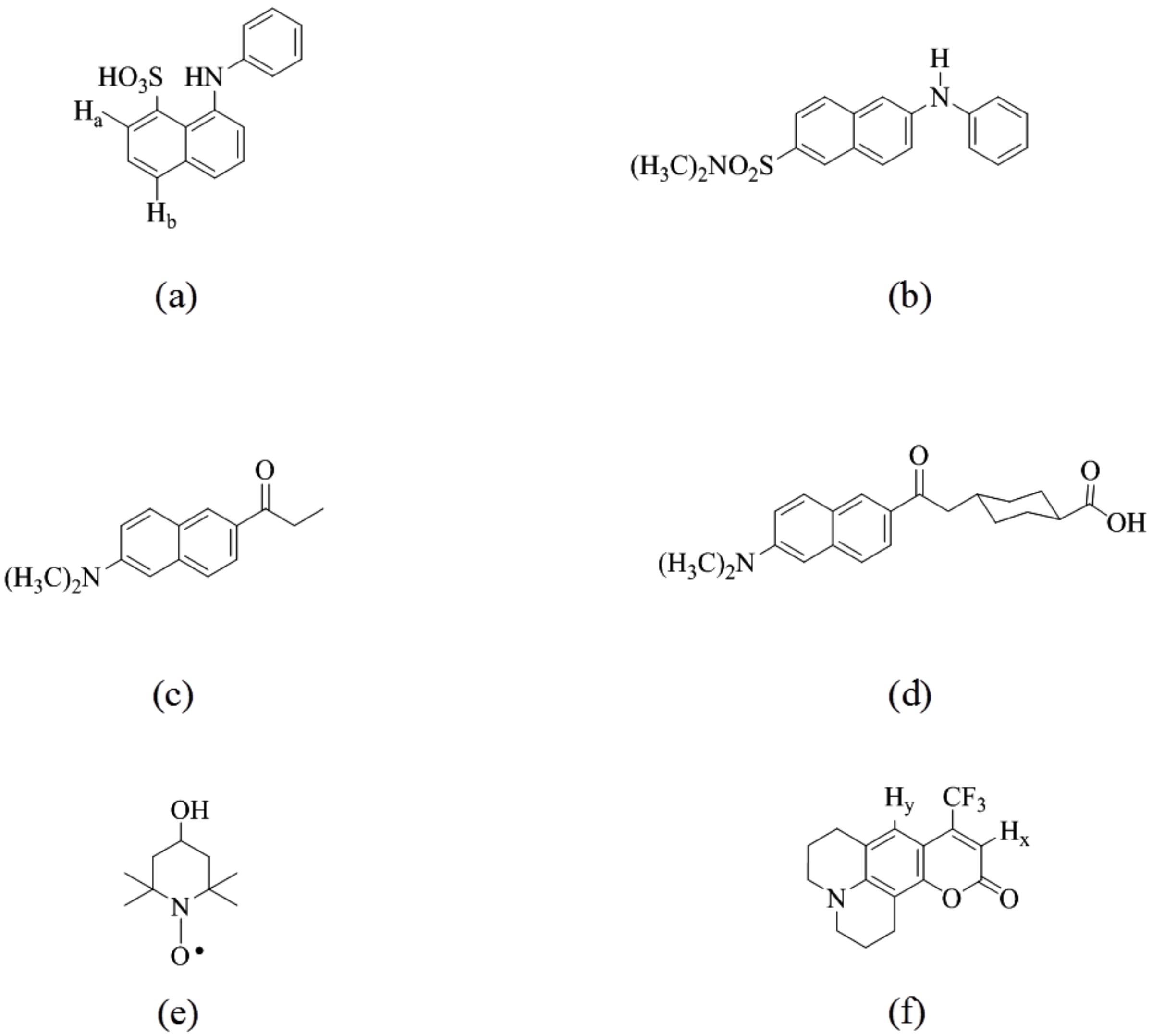

(a) (b) (c) (d) (e) (f)

Figure 5.1. Structures of different probes discussed here. (a) 8-anilino-1-naphthalenesulfonic acid (ANS), (b) 2-anilino-6-N,N-dimethylnaphthalenesulfonamide (ANSDMA), (c) 6-Propionyl-2-(N,N-dimethylamino)naphthalene (PRODAN), (d) 2′-(N,N-dimethylamino)-6-naphthoyl-4-trans-cyclohexanoic acid (DANCA), (e) 4-hydroxy-2,2,6,6-tetramethylpiperidine 1-oxy (TEMPOL) and (f) Coumarin 153 (C153).

We thus initially considered the probe ANS, [34] for which there is a structure of its complex with apoMb. This probe is not, however, ideal because its absorption spectrum is complicated by overlapping electronic states.[35] Even if internal conversion from higher-lying states to the lower fluorescent state is faster than solvation dynamics, as has been suggested to be the case in Trp,[36-39] an accurate determination of the reorganization energy[40,41] based on the steady-state spectra becomes very difficult. In addition, while ANS[34,42] as well as other chromophores such as PRODAN[43], DANCA,[44] and ANSDMA[45] (**Figure 5.1b-d**) may bind to the heme pocket of apoMb, they are also capable of charge transfer in the excited state, which could complicate the interpretation of the fluorescence upconversion results. [46]

On the other hand, C153 is exquisitely inert, structurally rigid, and also associated with a large change of dipole moment upon optical excitation. This is why it is has been so extensively employed as a probe of solvation dynamics.[30-33,47-59] We consequently opted for C153 as a probe for studying the dielectric response of proteins. Elsewhere, we have shown using Job's plot experiments that C153 binds to apoMb with a 1:1 stoichiometry with $K_D \cong 6\text{x}10^{-6}$ M.[30,31] The ANS-apoMb complex is reported to have $K_D \cong 3\text{x}10^{-6}$ M.[42] The anisotropy decay time (τ_{rot}) of C153 when bound to apoMb is 9.2 ns,[30] which is consistent with the slow rotational correlation time of apoMb,[60] whereas free C153 exhibits a very fast depolarization time of ~100 ps in bulk solvent.[30] More significantly, the anisotropy decay of bound C153 was single-exponential, which supports rigid binding of coumarin in the heme pocket; because single-exponential decay would not be expected for a surface bound chromophore.[61,62]

These findings, suggesting that a 1:1, well-defined complex of C153 and apoMb could be formed, authorized us to perform a comparison of the solvation correlation functions (dielectric responses) obtained from fluorescence upconversion experiments and molecular dynamics simulations[32] of C153 with wild-type horse heart (HH-WT) apoMb and with apoleghemoglobin (apoLba). This comparison provided excellent agreement between experiment and theory and emboldened us to perform the similar set of comparisons presented here for the complexes of C153 with four apoMbs: those of wild-type sperm whale (SW-WT); its two triple mutants, L29F/H64Q/V68F and H64L/V68F/P88A; and its double mutant, L29F/V68L. All of these mutant proteins do bind heme and fold to form stable holoproteins. Mutations at each position have various effects on the oxygen binding properties of the holoprotein, and have various effects on the stability of the apoprotein. For example, mutations of HisE7 to an apolar side chain lower oxygen affinity in the holoprotein, and increase stability to denaturation. The effects of mutations at other positions are generally milder. In general, when a polar side chain is introduced into the heme pocket, the resulting mutant apoprotein is less stable.

The intent of this comparison is to initiate a detailed study of the effects of individual amino acids on the dielectric response with the ultimate goal of developing a new type of model for the response.[63] The basic philosophy behind such a model is to account for the dielectric inhomogeneity of a protein without full atomistic details. Our previous results have indicated that a model based on the polarizabilities at the residue level can offer a universal description for proteins' dielectric response.

Despite the encouraging, initial success on this path obtained with the horse heart system, the results for the sperm whale system revealed themselves to be more complicated. Although the agreement between experiment and theory was excellent for the SW-WT, the agreement varied for the mutants. Our previous work suggests no reason to attribute such disagreement to the force fields used in the simulation but rather to question the structure of the complex used as the starting point for the simulation. Thus, *un esprit critique* requires that painstaking attention be paid to structural details when comparisons are being made between theory and experiment for different proteins and, in particular, the same proteins with slight modifications.

Our work presents, in outline:

1. a comparison of the dielectric response obtained from fluorescence upconversion experiments and from molecular dynamics simulations of the complexes of coumarin 153 with five apoMbs (apoMbs): wild-type horse heart (HH-WT) and those of wild-type

sperm whale (SW-WT); its two triple mutants, L29F/H64Q/V68F and H64L/V68F/P88A; and its double mutant, L29F/V68L;

2. an NMR study of the complex of C153 with HH-WT apoMb (we have used equine myoglobin, because it contains more resolved lines (especially from histidines) compared to the SW-WT [64]);
3. fluorescence energy transfer and anisotropy studies of the five complexes to complement the NMR studies.

We believe that this is the most thorough structural characterization to date of any system, whether it be based on nonnatural fluorescence probes or mutants, employed for the investigation of the dielectric response of proteins.

Materials and Methods

Coumarin 153 (C153) was purchased from Exciton Inc. (Dayton, OH) and used without further purification. 4-hydroxy-2,2,6,6- tetramethylpiperidinyl-1-oxy (TEMPOL) (**Figure 5.1e**), deuterated water (D_2O), dimethylsulfoxide (DMSO-d_6) and methanol (HPLC grade) from Aldrich was used without further purification. Equine myoglobin (Mb) was purchased from Sigma. Recombinant sperm whale myoglobins and its mutants were constructed, expressed, and purified as described elsewhere.[65,66]

Sample Preparation for NMR experiments Apoproteins were prepared using a method described elsewhere.[32,67] Protein concentrations were kept between ~ 1.5–2.0 mM for the NMR experiments. Because C153 is sparingly soluble in water, a stock solution of 40 mM was prepared in DMSO-d_6 and then added to the apoMb, keeping the stoichiometry 1:1. The solution was shaken for an hour and then dialyzed against 5 L pH 7.0 buffer overnight at 4°C. The solution was then centrifuged and concentrated using Centricon-3 (Amicon) to 0.5 mL, and the process was repeated four times by adding D_2O for deuterium exchange. The protein samples were stored at –20^{o}C without lyophilization. A 0.05 M TEMPOL solution was prepared in D_2O and the appropriate microliter volume was added to a 500 μL protein solution and was equilibrated overnight at 4°C before doing the NMR experiments.

Sample preparation for Fluorescence Measurements. Concentrations of 1:1 C153/apoMb complexes were maintained from 5.0 to 80×10^{-6} M by adding microliter amounts of 20×10^{-3} M C153/MeOH to pH 7.0 buffer, keeping the organic content < 0.3 % (v/v) in the final sample for all the steady-state and lifetime measurements. The resulting solution was sonicated. For fluorescence upconversion experiments a stock solution of C153/MeOH was added to 1.2 ml of ~ 1.0×10^{-3} M apoprotein solution, keeping the organic content < 3 % (v/v) in the final solution with 1:1 protein to C153 ratio. The concentrations of the apoproteins were determined spectrophotometrically using an extinction coefficient of 15.2 $mM^{-1}cm^{-1}$ at 280 nm.[30] All samples were equilibrated overnight at 4°C before making the steady-state or time-resolved measurements.

NMR Experiments. NMR spectra were recorded at a sample temperature of 25 °C using a Bruker Avance 700 spectrometer operating at a ^{1}H frequency of 700.13 MHz and equipped with a 5-mm H/C/N cryoprobe. Experiments were done in pure deuterated solvents in standard 5 mm NMR tubes (Wilmad). 1D ^{1}H and 2D ^{1}H-^{1}H NOESY spectra were acquired using standard experimental protocols. Very weak solvent saturation (B_1 power of 5 Hz) was used during recycling delays and the NOESY mixing time to suppress the residual HOD signal. For 1D spectra, 8 scans were accumulated with a sweep width of 25252 Hz (36 ppm). For NOESY spectra 400 time increments each consisting of 80 scans were acquired with a sweep width in both dimensions of 9803 Hz (14 ppm). The NOESY mixing time was 150 ms.

Steady-state Measurements. Steady-state absorption spectra were obtained on a Hewlett-Packard 8453 UV-visible spectrophotometer with 1-nm resolution. Steady-state fluorescence spectra were obtained on a Spex Fluoromax-4 with a 2-nm bandpass and corrected for lamp spectral intensity and detector response. For absorption and fluorescence measurements, a 3-mm path-length quartz cuvette was used. The steady-state spectra can be used to compute the reorganization energy, λ[68]

$$\lambda = \hbar \frac{\int_0^\infty d\nu[\sigma_a(\nu) - \sigma_f(\nu)]\nu}{\int_0^\infty d\nu[\sigma_a(\nu) + \sigma_f(\nu)]} \qquad (5.1)$$

The $\sigma_{a,f}$ are the absorption (or excitation) and emission spectral line-shapes, respectively. λ(∞) represents the total stokes-shift, which is calculated using the steady-state excitation, ν_{ex}, and emission, ν(∞), spectra. On the other hand, λ(“0”), which is the measure of intramolecular contribution and not solvent relaxation, is computed using steady-state excitation (ν_{ex}) and calculated “zero-time” spectra, ν(“0”). These values are collated in **Table 5.3**.

Time-resolved Measurements. Lifetime measurements were made using the time-correlated single-photon counting (TCSPC) apparatus described elsewhere.[33,41] The data were acquired in 1024 channels with a time window of 3.33 ns. The instrument response function had a full width at half-maximum (FWHM) of ~40 ps. A 3-mm path-length quartz cuvette was used for all the time-resolved measurements. Fluorescence decays were collected at the magic angle (polarization of 54.7^{o}) with respect to the vertical excitation light at 266 nm, with ~ 40,000 counts in the peak channel. To obtain the rotational dynamics of C153, samples were excited at 407 nm and emission was collected parallel and perpendicular to the polarization of the excitation light. Anisotropy data were aquired in 1024 channels with a time window of 22 ns collecting 65,530 counts in the peak channel. The fluorescence upconversion measurements were done with the apparatus described elsewhere. [41] The instrument response function had a full width at half-maximum (FWHM) of 300 fs. A rotating sample cell was used. To construct the time-resolved spectra from upconversion measurements, a series of decays were collected, typically from 480 nm to 560 nm at 10-nm intervals, in a time window of 10 ps. The wavelength-resolved fluorescence transients were fit to sums of exponentials (typically 2 or 3, as necessary to fit the data), and time-resolved emission spectra (TRES) were reconstructed as described elsewhere. [33,41]

We have employed the traditional approach of fitting the time-resolved emission spectra to a log-normal function [41,47,69], from which we extract the peak frequency $\nu(t)$ as a function of time. We describe the solvation dynamics by the following normalized correlation function:

$$C(t) = \frac{\nu(t) - \nu(\infty)}{\nu(\text{"0"}) - \nu(\infty)} \quad . \tag{5.2}$$

Because *C(t)* is a *normalized* function, the accurate determination of *C(t)* depends upon accurate values for ν(“0”) and ν(∞). ν(“0”) is the frequency at zero-time, estimated using the method of Fee and Maroncelli [70], who have described a robust, model independent, and simple procedure for generating this “zero-time” spectrum, ν(“0”). We have checked its validity using a different method for estimating the “zero-time” reorganization energy[68]. ν(∞) is (usually[71,72]) the frequency at infinite time, obtained from the maximum of the steady state spectrum. (This is not, however, true in the case of very slowly relaxing solvents, as has been demonstrated in the case of certain ionic liquids [71-73]: where the emission spectrum at ~3 times the fluorescence lifetime of the probe is *red-shifted* to that of the equilibrium spectrum.) The ν(t)s are determined from the maxima of the log-normal fits of the TRES. In most of the cases, however, the spectra are broad, so there is some uncertainty in the exact position of the emission maxima. Thus, we have considered the range of the raw data points in the neighborhood of the maximum to estimate an error for the maximum obtained from the log-normal fit. Depending on the width of the spectrum (i.e., “zero-time”, steady-state, or time-resolved emission spectrum), we have determined the typical uncertainties as follows: “zero-time” ~ steady-state (~ ± 100 cm^{-1}) < time-resolved emission (~ ± 200 cm^{-1}). We use these uncertainties to compute error bars for the $C(t)$. Finally, in generating the $C(t)$, the first point was obtained from the “zero-time” spectrum. The second point was taken at the maximum of the instrument response function. Fractional solvation at 300 fs is given by $f_{300fs} = 1 - C\ (t = 300\ fs)$.

Recently, we provided an analysis [33] of various methods of constructing $C(t)$ and reviewed selected examples from the literature.[36-38,74-79] We demonstrated that it is possible to exaggerate the amplitudes of slower solvation phenomenon that may be attributed to “biological water”, water-protein interactions, or the protein itself.

Molecular Dynamics Simulations. The starting configurations of sperm whale myoglobin (SW-WT) are from the protein DATA BANK (PDB id 1VXD) and with TIP3P water models. To have a reasonable starting point for the C153-protein complex the heme is replaced by C153 and then energy minimization is used to obtain the starting configuration of the C153/apoMb complex. Standard constant pressure-temperature MD was performed using the ORAC package[80] with the Amber force field. [81] In all simulations, short-range non-bonded interactions were calculated up to a 10 Å cutoff, whereas long-range electrostatic interactions were treated by the SPME method using a very fine grid, 128 points per axis, with periodic boundary conditions, and Ewald convergence parameter of 0.43 $Å^{-1}$. Three different Nosé-Hoover thermostats were coupled to solute, solvent, and total center of mass. An external pressure of 0.1 MPa was applied all along the trajectory. A five time-step rRESPA [37] algorithm with times of 0.5-1.0-2.0-4.0-12.0 fs was used with bond constraints on hydrogen covalent bonds handled by a Shake-Rattle-like algorithm. The final system was first equilibrated with velocity rescaling for 60 ps at 50 K and

80 ps at 300 K. Following this initial equilibration, we ran the system for one additional nanosecond at constant temperature (T = 300 K) and pressure (P = 0.1 MPa). To achieve full relaxation, the simulation box was entirely flexible for the first 300 ps, whereas for the remainder of the run, only isotropic changes of the box were allowed. [35] Finally, the system was simulated for an additional 10 ns. As we have demonstrated in our previous work, [30] an equilibrium configuration for C153 in the heme pocket of the protein can be found and experimental measurements seem to support our interpretation. Using the equilibrated configuration, additional 12-ns trajectories are generated and are used for the calculation of solvation correlations functions for horse heart apoMb complexes; and 30-ns trajectories are used for the corresponding calculations for the sperm whale apoMb complexes.

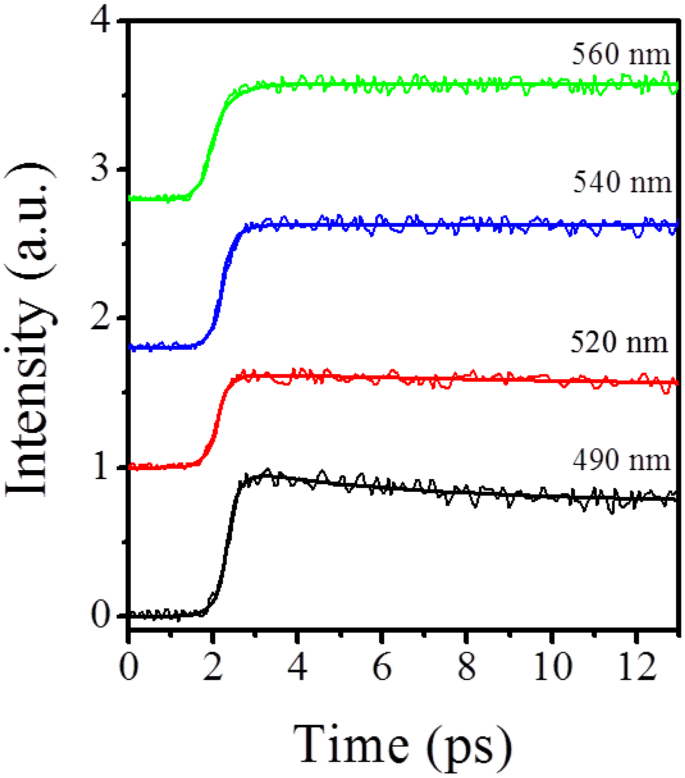

Figure 5.2. Representative fluorescence upconversion traces obtained for C153 in H64L/V68F/P88A apoMb mutant at the indicated wavelengths. The decay at blue end of the spectrum decays faster than that of at the red end of the spectrum. The decay at the red end of the spectrum shows a growing component. The decays used to construct the time-resolved emission spectra were typically collected over a range of wavelengths from 480 to 560 nm at 10-nm intervals, a total of nine decays were used to generate the time-resolved emission spectra, from which the *C*(*t*) values were calculated.

Using the charges of C153 in the ground and excited states,[12] the solvation correlation function can be obtained within the linear response theory[82] as

$$C(t) = \frac{<\delta\Delta E(t)\delta\Delta E(0)>}{<\delta\Delta E(0)\delta\Delta E(0)>} \tag{5.3}$$

where $\delta\Delta E(t) = \Delta E(t) - <\Delta E(t)>$ and $\Delta E(t)$ is the interaction energy difference between C153 in its excited state and ground state with surrounding protein and water molecules at time t. The symbol <···> denotes the ensemble average in the simulation. The reorganization energy λ is calculated using $\lambda = <(\delta\Delta E)^2> /2k_BT$. For the simulations of the mutants, the residues of the equilibrated WT-apoMb/C153 complex are mutated to the desired amino acids starting from the equilibrated wild type and C153 complex structure. Then, an energy minimization and 1-ns equilibration run is performed. Using the equilibrated configuration, additional 30-ns trajectories are generated and are used for the calculation of solvation correlations functions and the reorganization energies.

Results and Discussions

Dielectric Relaxation of the ApoMb Complexes

Representative wavelength-resolved decay traces of C153/apoMb complexes are presented in **Figure 5.2**. The solvation correlation function, *C*(*t*), obtained from spectral reconstruction from fluorescence unpconversion traces and from molecular dynamics simulations for C153 in HH-WT and SW-WT apoMbs and its mutants using eq 2 and 3 are given in **Figure 5.3 and 5.4**. There is remarkable agreement between the *C*(*t*)s from fluorescence upconversion experiments and those obtained from molecular dynamics simulations in the SW-WT apoMb, but deviations were observed in the mutants. The time constants for the dielectric relaxation in all the systems are collated in **Table 5.1**. For all the apoMb complexes studied here, the experimentally obtained solvation response was best fit to two decaying exponentials, with a significant (~60%) (**Table 5.2**) response being completed within the time resolution of our experimental apparatus (~300fs) succeeded by a slower response, which is also consistent with the MD results. This ultrafast relaxation suggests that water is playing a dominant role, which is consistent with the report by Fleming and coworkers [40] that solvation in the lysozyme/eosin system is dominated by water. (Solvation in bulk water is characterized largely by an ~30-fs component and is complete in ~15 ps. [17,83]) The remainder of the solvation can be attributed to motions of the protein matrix or coupled protein-water [84] motions. The protein's contribution to solvation should not be neglected. For example, Nilsson and Halle have simulated the Stokes shift in the protein monellin [85] and have discussed how to separate the relative contributions of protein and water. They find a significant protein component, at least 25%. Li et al. [84] find that the relative protein and water contributions can vary substantially with the conformational substate of myoglobin: sometimes the protein contribution can even be larger than water. Both Nilsson and Halle [85] and Li et al. [84] find that the protein contribution also has an ultrafast component. In general, there will always be some slow relaxation due to the conformational motions of proteins. In our case, the structures of C153/wild type complexes obtained from NMR and FRET measurements are consistent with those obtained from simulations. For the mutants, the structures of the C153 complexes used in the simulations are not that certain, as indicated by the comparison with the experimental evidence. This may be the reason for less satisfactory agreements between the *C(t)*s.

TABLE 5.1

C(t) parameters obtained from upconversion experiments and MD simulations [a]

System		f_{300fs}	**a_1**	**τ_1 (ps)**	**a_2**	**τ_2 (ps)**	**a_3**	**τ_3 (ps)**	**$<\tau_{solv}>$ (ps)**
HH-WT	Expt.	0.64	0.59	0.02	0.41	3.4			1.4
	Simul.		0.73	0.14	0.27	9.3			2.6
SW-WT	Expt.	0.61	0.69	0.14	0.31	15.2			4.8
	Simul.		0.53	0.07	0.18	1.16	0.29	15.0	4.7
L29F/H64Q/V68F	Expt.	0.56	0.61	0.12	0.39	15.4			6.1
	Simul.		0.47	0.07	0.17	1.6	0.34	28.0	10.3
H64L/V68F/P88A	Expt.	0.64	0.68	0.12	0.32	5.5			1.8
	Simul.		0.43	0.06	0.18	1.0	0.39	40.0	15.8
L29F/V68L	Expt.	0.60	0.60	0.10	0.40	3.8			1.6
	Simul.		0.38	0.06	0.16	1.1	0.46	52.0	23.2

[a] Results from experiments and simulations are fit to a sum of exponentials. That three exponentials are used to fit the results from simulations and only two, those from experiments, is a consequence of the error bars for the experimental results being larger than those for the data points resulting from the simulations.

Another example of agreement between experiment and theory that is emerging in the study of solvation dynamics of proteins is the recent work by Boxer and coworkers [86] and by Golosov and Karplus .[87] In our previous reports[32] on solvation dynamics in HH-WT apoMb and apoLba (where the heme pockets differs significantly[88,89]), we have also found excellent agreement between the *C*(*t*) obtained from both experiments and molecular dynamics simulations. It is significant that the only difference between the heme pockets of the two WT Mbs is that Val67 in HH is replaced by Thr in SW. A close comparison of the *C*(*t*)s for these two systems indicates small but significant differences that must arise from this single amino acid substitution **(Figure 5.3)**.

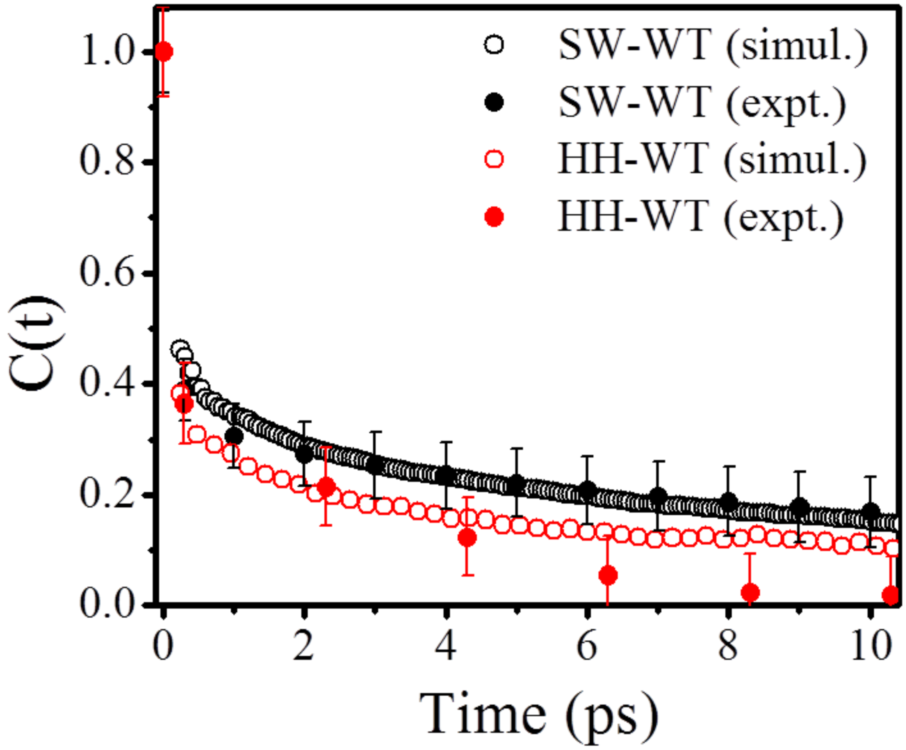

Figure 5.3. Comparison of *C*(*t*) for C153 in wild type sperm whale and horse heart apoMb obtained from fluorescence upconversion experiments with those from molecular dynamics simulations. In both proteins, the initial fast component occurs within the time resolution of our instrument. There is a remarkable agreement between experiment and theory for both the wild type apoproteins. There is only one change between the heme pockets of the horse heart and sperm whale myoglobins: Val67 in HH is replaced by Thr in SW.

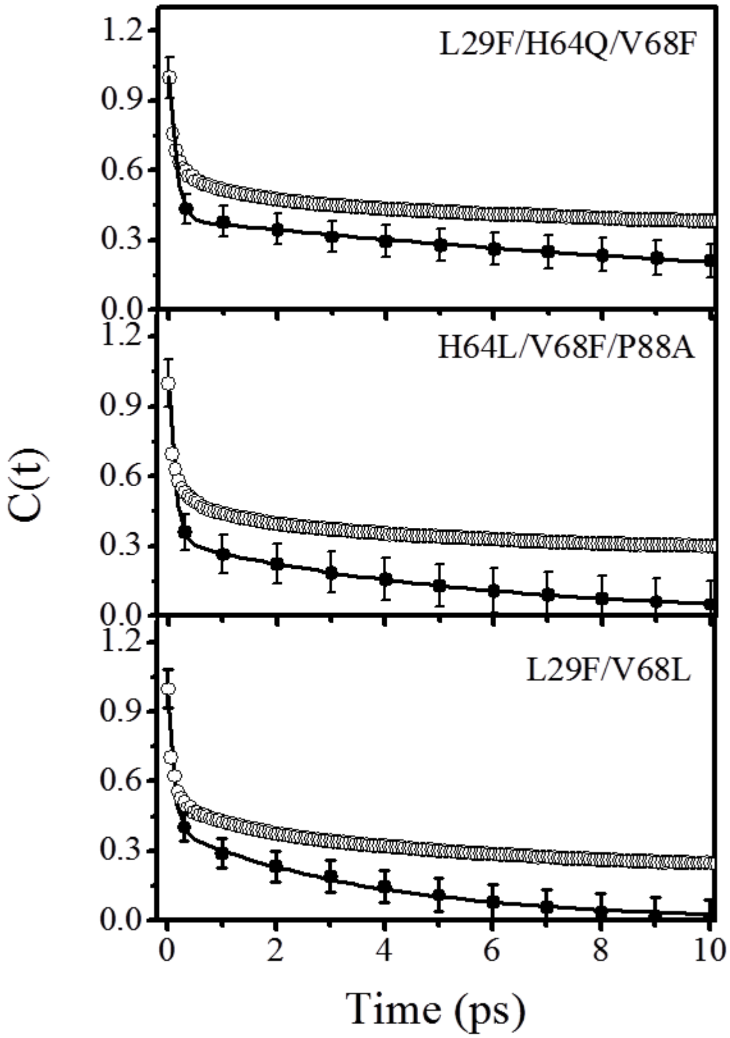

Figure 5.4. Comparison of solvation correlation functions, *C*(*t*) for C153 in sperm whale apoMb mutants obtained from fluorescence upconversion experiments (closed circles) with those obtained from molecular dynamics simulations (open circles). *C*(*t*)s from experiments and simulations were calculated using eqs 2 and 3 respectively, and were fitted with a sum of two and three exponentials respectively.

The sensitivity of C153 to its local environment is also reflected by the reorganization energies for each of the C153/apoMb complexes. The reorganization energies differed not only between the WT and its mutants, but also between the two WT apoMbs (sperm whale and horse heart, **Table 5.3**). The solvation response is thus critically dependent on the environment that the probe (C153) experiences inside the heme pocket.

While there is very good agreement between experiment and simulation for the wild-types proteins, the agreement for the mutant proteins is much less satisfactory. The origin of this discrepancy for the mutants may be found by means of the structural studies of the complexes that we now discuss.

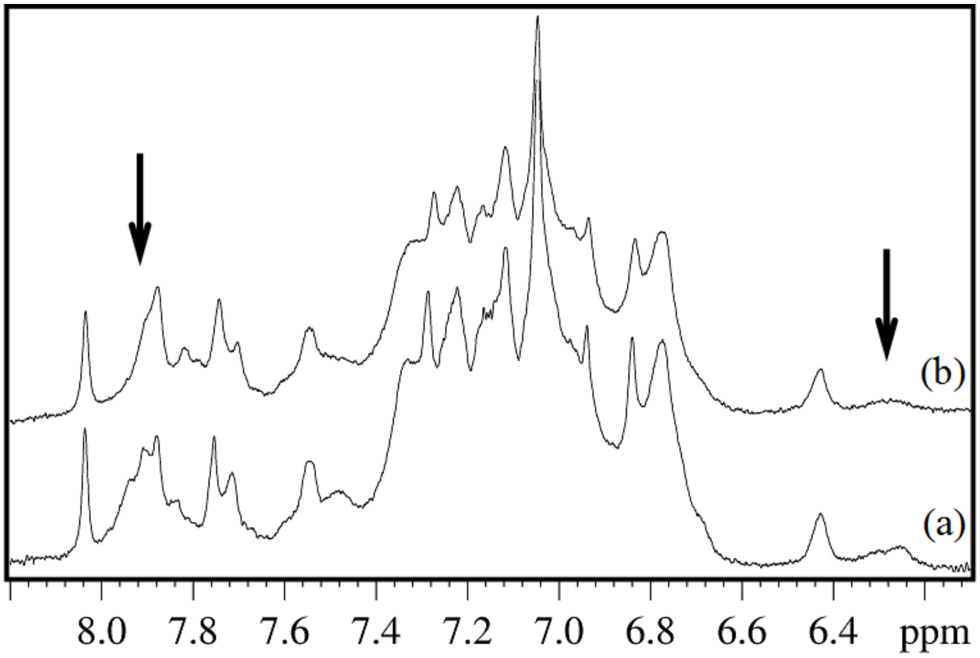

Figure 5.5. Representative 1D, ^{1}H-NMR spectra of (a) equine apoMb and (b) its complex with 2 equivalents of TEMPOL in D_2O at 298 K and pH 7.0. Addition of TEMPOL selectively broadens signals (indicated by arrows) from C^{ε} H of His64 and C^{ζ} H of Phe33 in the heme pocket, which confirms that the paramagnetic dye binds to the distal side of the pocket.

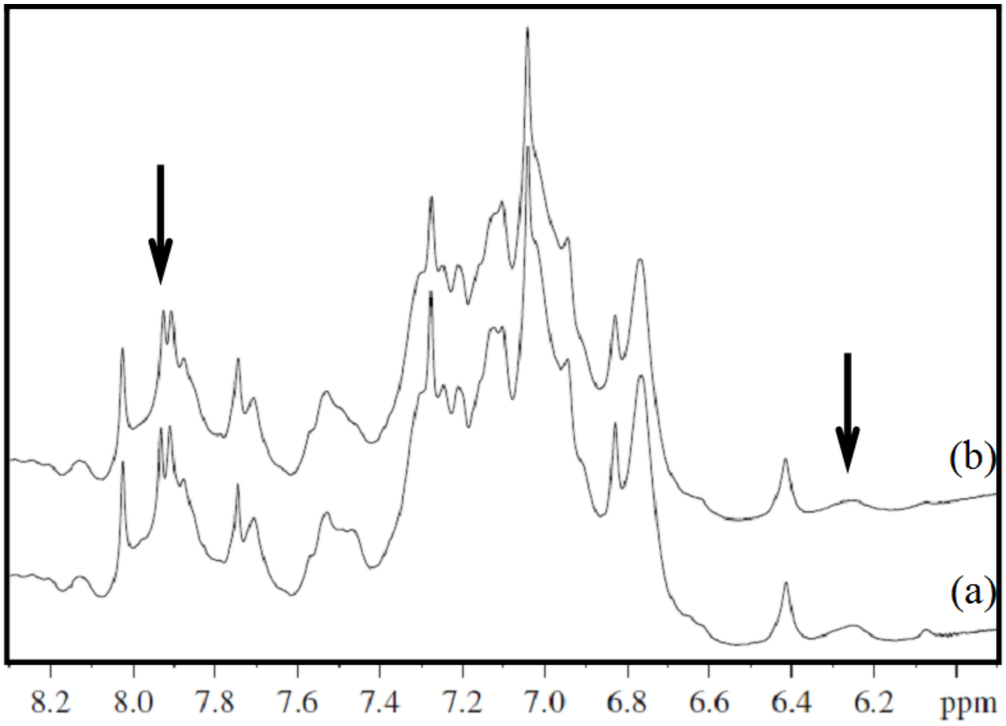

Figure 5.6. Representative 1D ^{1}H-NMR spectra of (a) the 1:1 complex of C153/equine apoMb. A new peak at 6.04 ppm arises due to the proton (H_x, **Figure 5.1f**) adjacent to the carbonyl carbon in C153; (b) the complex of C153/equine apoMb with two equivalents of TEMPOL in D_2O at 298 K and pH 7.0. There is no perturbation in either the His64 or the Phe33 signals (indicated by arrows) as was seen in Figure 5. The two spectra 'a' and 'b' are almost identical, which indicates that coumarin occupies the heme pocket and prohibits the entry of TEMPOL.

Structural Characterization of the Complex of C153 and HH – WT ApoMb by NMR

One-dimensional ^{1}H-NMR spectra of HH-WT apoMb and of the complex of two equivalents of the paramagnetic dye, TEMPOL (**Figure 5.1e**), with one equivalent of apoMb in D_2O are shown in **Figure 5.5**. Although the overall spectral characteristics remain similar, specific signals are perturbed upon addition of TEMPOL. In particular, the peak at 7.91 ppm arising from C^{ε} H of His64 in the E7-helix is broadened upon insertion of TEMPOL. Also the peak due to C^{ζ} H of Phe33 is broadened, which is consistent with the reports of Cocco and Lecomte.[34] Excess addition of TEMPOL, beyond two equivalents, was avoided to prevent attenuation of other signals by through-space relaxation.

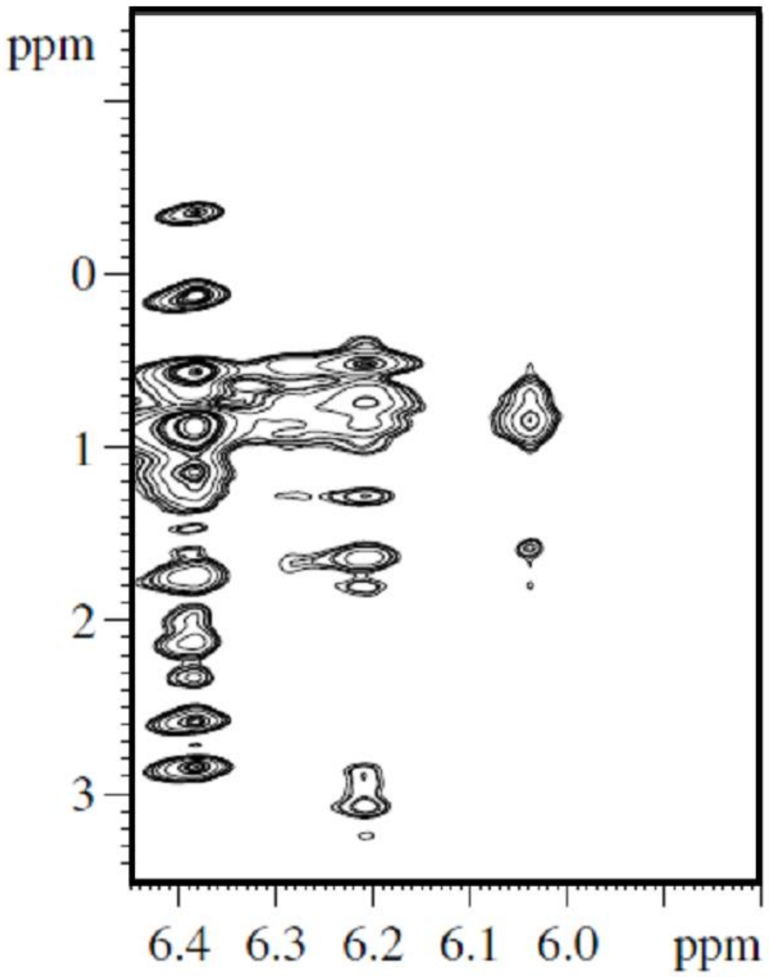

Figure 5.7. NOESY spectrum of C153/apoMb complex in D_2O at 298 K and pH 7.0. The resonance at 6.04 ppm arises from H_x C153, and the cross peaks arise from Val67 and Ala 71. Other weaker cross peaks are unidentified. The assigned cross peaks show that C153 is in the distal side of the heme pocket, constituted by Leu29, His64, Val67, Val68, and Ala71.

When, however, C153 is added to apoMb, several signals are seen to have sharpened and shifted as seen in **Figure 5.6a**, which indicates a decreased rate of backbone amide exchange and a change in the population of various conformers. A new peak at 6.04 ppm arises in the C153-apoMb spectrum due to the proton (H_x, **Figure 5.1f**) adjacent to the carbonyl carbon in C153. Other signals from coumarin could not be resolved due to their overlap with other signals from the apoprotein residues.

When TEMPOL was added to the C153/apoMb complex, no changes in the signals from pocket residues, such as His64 and Phe33 were observed as was the case when adding TEMPOL to apoMb (**Figure 5.6b**). The peak at 7.45 ppm is considerably broadened on addition of TEMPOL in both cases (with and without C153) showing that it arises from a solvent exposed residue. These observations collectively suggest that C153 provides certain rigidity to the flexible structure of the apoprotein and thus prevents TEMPOL from diffusing inside the heme pocket. This is consistent with our circular dichroism results reported elsewhere[30] that addition of C153 helps to regain some of the secondary structure present in the native holo form of myoglobin.

Based on the assignments of Lecomte[34,64,90-95] and coworkers, we have assigned selected NOEs from the heme pocket residues in the 2D NMR spectra. Comparing the spectra of apoMb with that of the C153/apoMb complex, new cross peaks can be interpreted as follows (**Figure 5.7**). The resonance at 6.04 ppm arises from the proton (H_x, **Figure 5.1f**) adjacent to the carbonyl carbon in C153, which has cross peaks with methyl protons of Val67 and also with those of Ala71. The peak at 7.93 ppm from C^{ε} H of His64 is sharpened and slightly shifted downfield on addition of C153. His64 shows strong NOEs with methyl protons of Val67 and Leu29 at 0.89 and 1.70 ppm, respectively. C153 selectively perturbed the residues on the distal side of the heme pocket. A complete characterization of the apoMb structure is very difficult owing to its large size, partial unfolding, and exchange among different conformations. Chemical shifts, internuclear distances, NOEs, and dihedral angles are inadequate to provide correlation between various motions and interchanging conformations, because although the global unfolding of the apoprotein is cooperative, the local motions, like folding-unfolding processes occurs independently.[64,94,95] Moreover chemical shift degeneracy of various protons hinder the assignments of peaks in the NMR spectra.

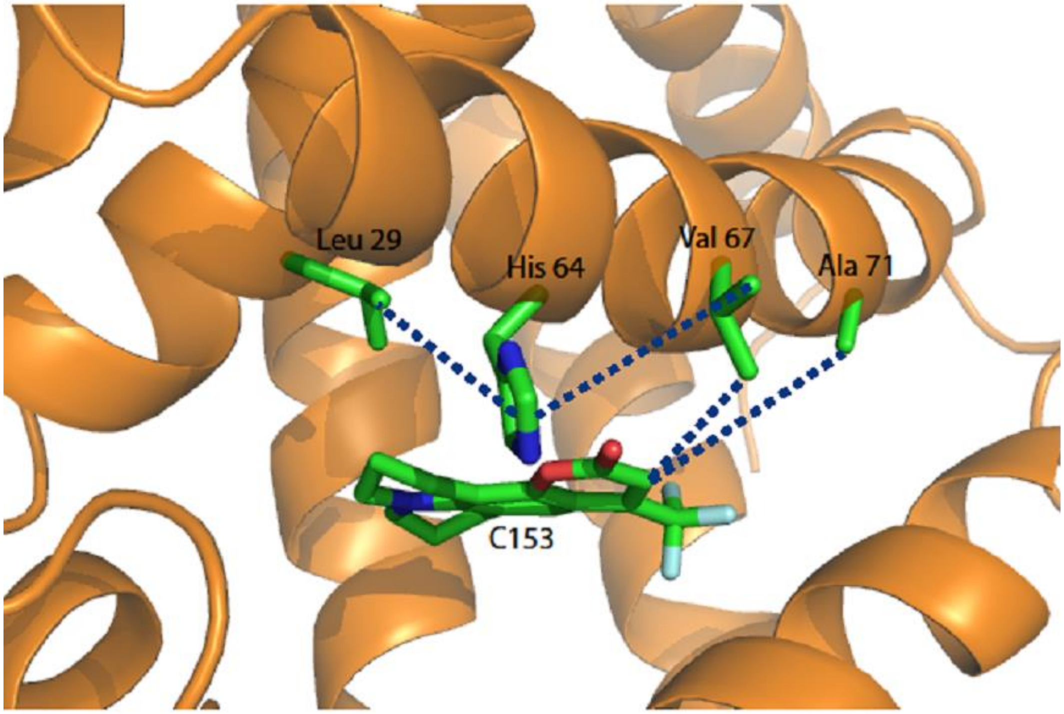

Figure 5.8. Representative diagram of apoMb, constructed by the removal of the heme from wild-type equine holo myoglobin (1WLA.pdb), showing the interactions of C153 proton with Val67 and Ala71, along with other selective interactions among the distal residues such as His64–Leu29 and His64–Val67 as obtained from NMR studies.

Based on the above 1D- and 2D-NMR results, a tentative location of C153 can be obtained. Considering the NOEs of coumarin with the pocket residues and inter-residue interactions, it can be confirmed that the fluorescent dye (C153) occupies the distal side of the heme pocket, similar to the case of ANS, as shown in **Figure 5.8**, which illustrates the approximate distances and location of C153 with respect to the distal heme pocket residues. The H_x proton of C153 is < 5 Å from the methyl residues of Val67 and Ala71. Accurate determination of inter-proton distances using the NOE cross peak intensity is unreliable[95] because of the rapid to intermediate time scales of exchange among the related conformations within the apoprotein.

TABLE 5.2

Summary of Results for C153/apoMbs

	Anisotropy[a]		**Lifetime**[b,c]						**Solvation**
System	r(0)	τ_{rot} (ns)	a_1	τ_1 (ns)	a_2	τ_2 (ns)	a_3	τ_3 (ns)	f_{300fs}
HH WT	0.29	9.2	1.0	5.1	-0.13	0.2	-0.23	0.5	0.64
SW WT	0.32	10.5	1.0	5.0	-0.18	0.42	-0.22	0.1	0.61
L29F/H64Q/V68F	0.32	10.2	1.0	5.0	-0.18	0.25			0.56
H64L/V68F/P88A	0.28	10.0	1.0	7.3	-0.33	0.17			0.64
L29F/V68L	0.18	>20.0	0.84	5.5	0.16	0.84	-0.27	0.25	0.60

All experiments were repeated at least three times.

[a] Error bars for r(0) and τ_{rot} are within 3-5%. The fluorescence anisotropy is measured by probing the C153: $\lambda_{ex} = 407$ nm; $\lambda_{em} \geq 500$ nm.

[b] Lifetime experiments were done at $\lambda_{ex} = 266$ nm, $\lambda_{em} \geq 500$ nm and components varied within a range of 10%.

[c] Components with negative amplitude refer to the growth in the fluorescence decay traces of C153 observed at 266 nm excitation in all the apoMb complexes, which was completely absent using 407 nm excitation. The rise time can come only from the acceptor (C153) emission and indicates energy transfer from Trp to C153. The decay time constants are associated with positive amplitudes.

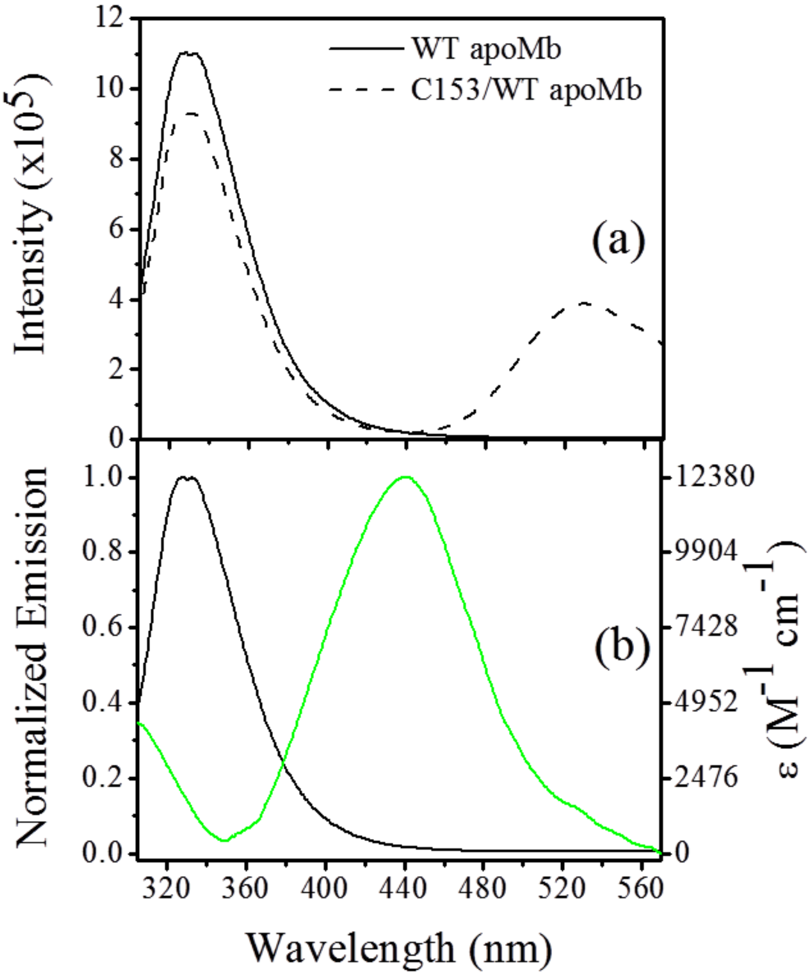

Figure 5.9. (a) Steady-state fluorescence spectra (λ_{ex} = 266 nm) of WT horse–heart apoMb with (- - -) and without C153 (——). The peak maxima at 330 and 530 nm are due to Trps and C153. Addition of C153 into the heme pocket quenches the Trp fluorescence in apoMb, indicating energy transfer from Trp to C153. (b) Spectral overlap of C153 molar extinction coeffient (ε) (green) and tryptophan emission (black) in the 1:1 WT equine apoMb/C153 complex. The calculated R_0 is 25.5 and 27 Å for Trp14 and Trp7. The distances, R, between Trp14 and Trp7 from C153 are 17.3 and 20.1 Å, respectively.

Characterization of the Complexes of C153 and ApoMbs by Fluorescence Energy Transfer and Fluorescence Anisotropy

Fluorescence Energy Transfer. In order to characterize the C153/apoMb complexes further, we performed steady-state and time-resolved fluorescence energy transfer experiments. **Figure 5.9a** presents quenching of the donor (D), Trp, fluorescence from apoMb ($\Phi_{Trp}^{ApoMb} = 0.11$) after insertion of the acceptor (A), C153, into the heme pocket ($\Phi_{Trp}^{C153/ApoMb} = 0.09$). The fluorescence quantum yield of Trp (Φ_{Trp}) in apoMb was calculated using Trp in buffer (pH 7.0) as a standard.[62,96,97] There is significant overlap of the Trp emission and C153 absorption spectra (**Figure 5.9b**), which is a critical factor in energy transfer between D and A. When excited at 266 nm, a shortening of the Trp lifetime was observed in all the C153/apoMb complexes (τ = 2.0 ns), compared to the lifetime in the free apoproteins (τ = 2.3 ns). The fluorescence lifetime of C153 in the apoMb complexes was also monitored exciting at λ_{ex} = 266 and 407 nm and $\lambda_{em} \geq$ 505 nm. Excitation at 407 nm only excites the acceptor (see **Figure 5.9**) resulting in its prompt fluorescence since no energy transfer can occur. **Figure 5.10** presents the time-resolved fluorescence decays of C153/apoMb complexes when Trp and C153 are selectively excited. The sets of decays are clearly different when excited at 266 and 407 nm. Upon exciting at 266 nm, significant growth in the fluorescence decay traces of C153 was observed in all the apoMb complexes, which was absent completely at 407 nm excitation. The rise time can thus come only from the acceptor (C153) emission and indicates energy transfer from Trp to C153.

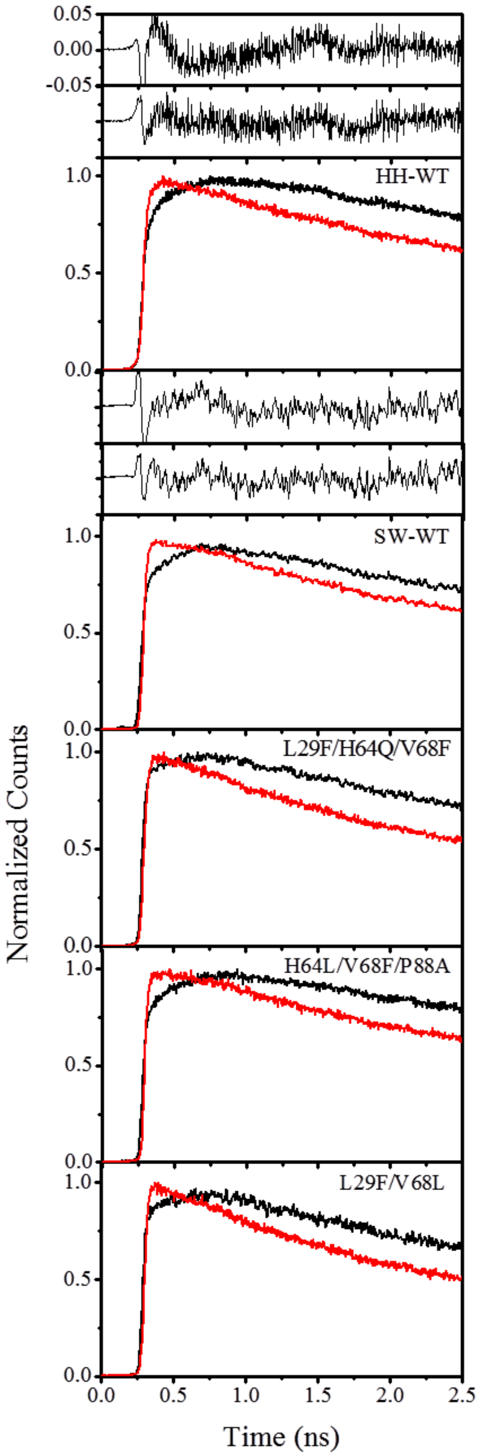

Figure 5.10. Fluorescence decay traces of complexes of C153 with HH-WT and SW-WT apoMbs, and the mutants of the latter. λ_{ex} = 266 nm (black) or λ_{ex} = 407 nm (red). $\lambda_{em} \geq 500$ nm. Upon exciting at 266 nm, a rise in the fluorescence decay traces of C153 was observed in

(**Figure 5.10 cont**) all of the apoMb complexes. This rise was absent for $\lambda_{ex} = 407$ nm. All the measurements were repeated three times. Data for the HH samples were acquired in 4096 channels, whereas the rest were taken in 1024 channels. The residuals from the fits for wild type HH and SW are shown. In each pair, the residuals in the upper panel and in lower panel are obtained from single ($\chi^2 > 2.5$) and bi-exponential fits ($\chi^2 \sim 1.3$), respectively. Decays for all of the mutants are best fit with a single exponential ($\chi^2 \leq 1.3$). The results are collated in **Table 5.2.**

A crucial result in helping us to characterize the C153/apoMb complexes is that for the wild-type complexes *two exponentials were required to fit the rise times adequately* (**Table 5.2** and **Figure 5.10**). It is reasonable to observe two rise times for the energy transfer since the apoMbs have two Trps (Trp7 and Trp14) and energy transfer from two Trps at different distances from C153 can lead to two different rise times (**Table 5.2**). But more importantly for purposes of the structural characterization, this result also implies that C153 is rigidly bound inside the heme pocket at a fixed orientation and that it is immobile within the time-scale of the experiment. On the other hand, the three mutants all provided single exponential rise times for the energy transfer. Such a result can be interpreted in at least three ways: 1) R^6/κ^2 is the same for C153 and each of the two Trps (assuming a fixed dipole moment for C153); 2) the position and orientation of C153 only favors energy transfer from a single Trp residue; 3) the mutants proteins are not correctly folded and there are multiple C153 binding sites or the C153 is mobile on the time scale of the energy transfer giving rise to a averaged time constant.

Quantitative structural details can be gleaned from the energy transfer data by computing the critical distance, R_0, between the Trps and C153:

$$k_{ET} = \frac{1}{\tau_D}\left(\frac{R_0}{R}\right)^6 \qquad (5.4)$$

$$R_0^6 = \frac{9000(\ln 10)\Phi_D}{128\pi^5 n^4 N}\kappa^2\left(\frac{\int_0^\infty F_D(\bar{\nu})\varepsilon_A \bar{\nu}^{-4} d\bar{\nu}}{\int_0^\infty F_D(\bar{\nu}) d\bar{\nu}}\right) \tag{5.5}$$

where k_{ET} is the rate of energy transfer, τ_D is the average fluorescence lifetime of the donor, R is the distance between donor and acceptor, κ^2 is the orientation factor, n is the refractive index of the medium (considered as 1.33), N is Avogadro's number, Φ_D is the fluorescence quantum yield of the donor, F_D is the emission spectrum of the donor on a wavenumber scale, and ε_A is the molar extinction coefficient of the acceptor ($M^{-1}cm^{-1}$).

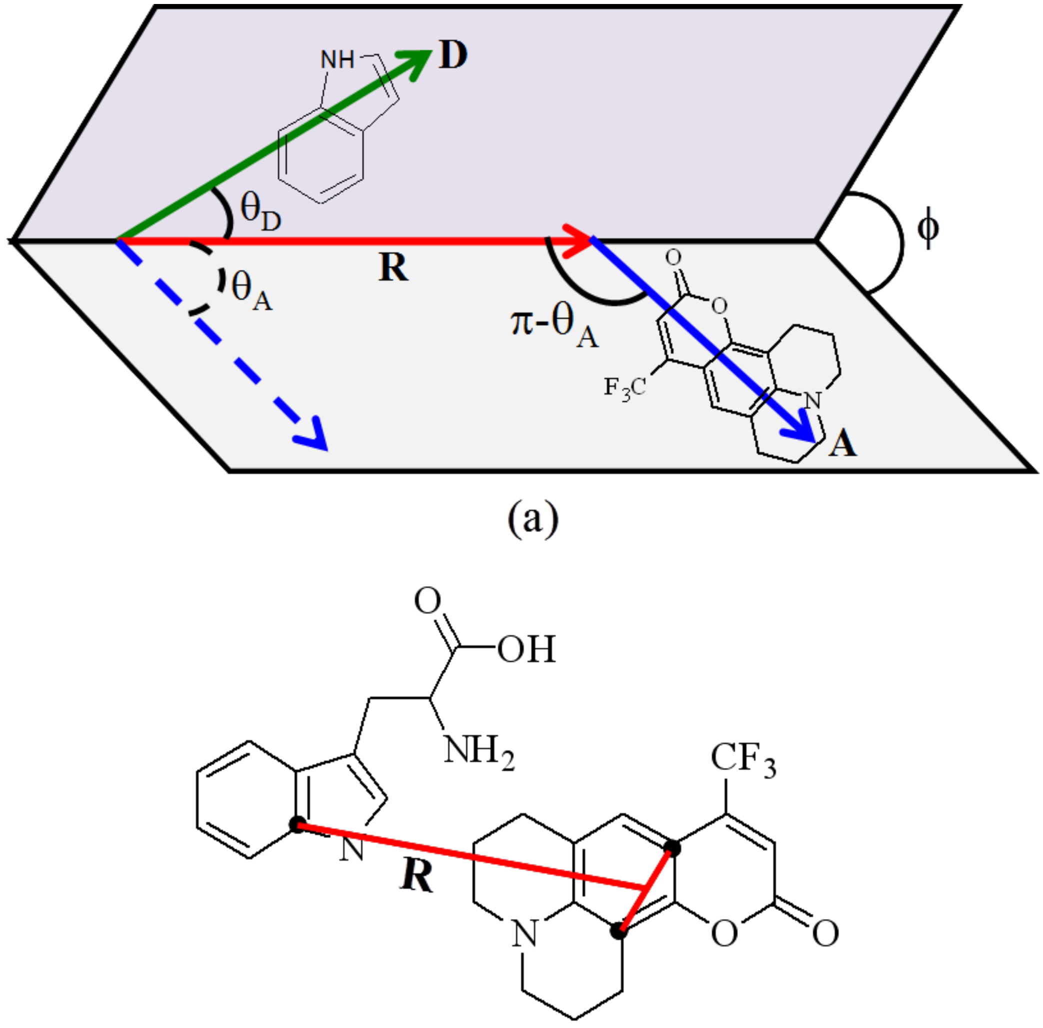

(a)

(b)

Figure 5.11. (a) Geometry used to calculate κ^2 for the determination of R_0 for the energy transfer between Trp and C153 in the complexes. The figure presents the mutual orientation of the donor transition dipole of Trp, θ_D, and the acceptor transition dipole of C153, θ_A. R is the separation vector between the donor and acceptor. κ^2 is calculated using eqn 6. θ_A is fixed at 21°, along the dipole moment of C153; and the donor is assumed to be isotropically oriented. The angles θ_D and ϕ are thus integrated over the range of $0–\pi$ and $0–2\pi$, respectively. This geometry gives $\kappa^2 = 5/4$. (b) The D–A distances from the equilibrated structures from the molecular dynamics simulations are computed with respect to the atoms illustrated. Distances obtained from energy transfer results and from simulations are summarized in **Table 5.4**.

A thorny problem in using energy transfer data to determine distances is obtaining an appropriate value for κ^2. Typically it is assumed that D and A can move freely and assume all orientations, in which case $\kappa^2 = 2/3$. This is clearly incorrect for the C153/apoMb system, where there is ample evidence suggesting that C153 is rigidly held in the heme pocket, at least for the wild type proteins. We have thus assumed that D is randomly orientated and that A is fixed at the angle θ_A with respect to the separation vector between the D and A, as shown in **Figure 5.11**. Various orientations between donor and acceptor have been discussed in detail by Dale and Eisinger.[98] For further simplicity, we assume that C153 is oriented along its transition dipole moment vector, θ_A=21°. [47] This is a reasonable and convenient assumption. The NMR data were not sufficient to permit the determination of the location of the coumarin's plane inside the heme pocket. If, however, the location of the C153 plane is undetermined to within a rotation about its transition dipole, κ^2 remains unchanged. Using the equation

$$\kappa^2 = \left[\sin\theta_D \sin\theta_A \cos\varphi - 2\cos\theta_D \cos\theta_A\right]^2 \tag{5.6}$$

we thus obtain $\kappa^2 = 5/4$. The overlap integral was calculated using the emission spectra of single Trp mutants of apoMb[99] and the absorption spectrum of C153 in WT apoMb. Finally, eqs 4 and 5 give R_0 as 25.5 and 27.0 Å for Trp14 and Trp7 in the HH-WT complex, using the quantum yields of Trp14 and Trp7 as 0.14 and 0.19, which were calculated from the ratio of the lifetimes of the individual Trps. [100] The distances, R, from Trp14 and Trp7 to C153 were thus determined to be 17.3 and 20.1 Å, respectively. For the SW-WT complex, the Trp-C153 distances were found to be 14.4 and 18.4 Å, which are significantly different from HH-WT complex. The distances obtained from energy transfer experiments have been compared with those in equilibrated simulation structures in **Table 5.4**. Unlike the case of the mutants, there is reasonably good agreement for the Trp–C153 distances determined by experiment and simulation in the wild type proteins. The differences in the location of C153 in the heme pockets of the two WT apoproteins, is also reflected in the reorganization energies and solvation correlation functions.

In concluding this section, it is well to note that other workers have studied the very efficient energy transfer from tryptophan to heme in myoglobin and to place our measurements and analysis in this context. Hochstrasser and Negus [101] provided a detailed analysis of energy transfer between Trps 7 and 14 to the heme in sperm whale myoglobin. They agree with our assessment that these two Trps are close to the exterior of the protein. They also conclude that the directions of the tryptophan transition moments are probably not a critical factor for the energy transfer. This conclusion is consistent with our assumption that the Trps are randomly distributed. They do, however, invoke anisotropy data to suggest that Trp 14 is restricted enough to transfer energy to the heme with a time constant of 30 ps. More recently, Zhong and coworkers [102] have extended these studies. They conclude that for ultrafast energy transfer, it is incorrect to assume that that the donor and acceptor are randomized.

We recognize that it is a gross approximation to assume that the Trps are completely randomly distributed. But we feel that it is a useful approximation and that it is unnecessary in the present case to assume that the Trps are not randomized. *The point of our energy transfer experiments is not to assay the rigidity of the tryptophans but to verify the location of the coumarin*, which is crucial for a proper comparison with simulations. The most important results of our experiments are that for the WT systems we clearly resolve two different energy transfer events and that the distances computed from these time constants are consistent with distances obtained from the simulations.

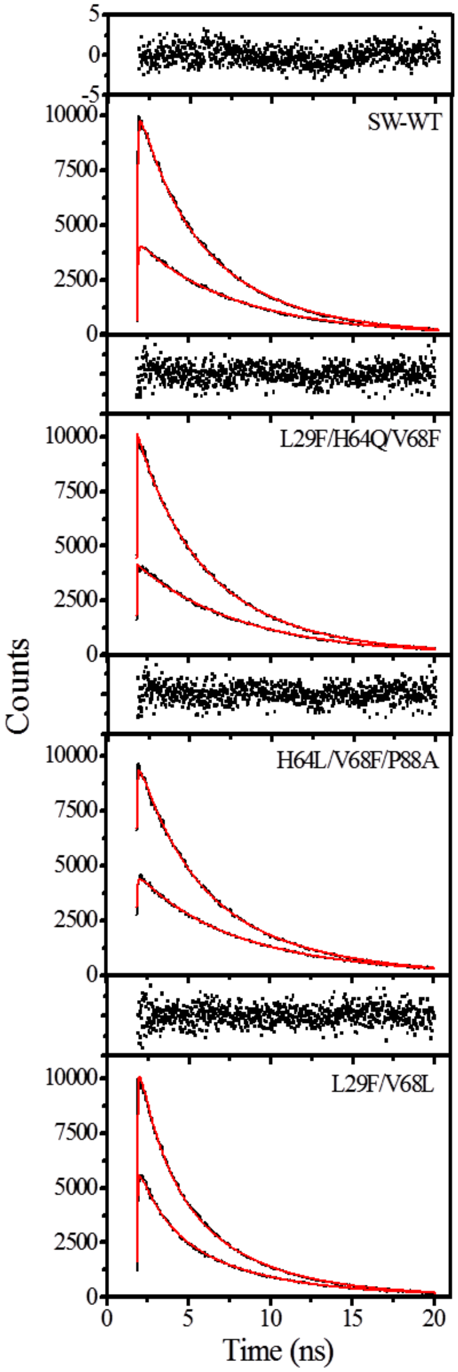

Figure 5.12. Polarized fluorescence decays of the complexes of C153 with wild type sperm whale apomyogobin and its mutants. λ_{ex} = 407nm; λ_{em} > 500 nm. A normalization factor was applied to the traces such that the maximum count was 10,000 owing to the requirements of the analysis software. The anisotropy measurements were repeated three times. The rotational reorientation times were obtained from simultaneous fitting[103] of parallel and perpendicular decays, and the results are summarized in **Table 5.2**. The top panels present the residuals from the fits (χ^2 ~1.2).

Fluorescence Anisotropy. Time-resolved fluorescence anisotropy data for C153/apoMb complexes are presented in **Figure 5.12**. The anisotropy decay of bound C153 in WT and the two triple mutants was single exponential with a rotational time of ~10 ns **(Table 5.2)**, which supports rigid binding of the probe in the heme pocket; because single-exponential decay would not be expected for a surface bound chromophore. [61,62] The r(0) values for these systems were found to be similar (~0.3). These results are consistent with our previous reports with HH-WT apoMb, which was single exponential with a rotational time of 9.2 ns. On the other hand, the double mutant L29F/V68L showed a much higher rotational time (>20 ns), with a significantly lower r(0) of ~0.2. These two values clearly impugn the structure integrity of the double mutant. The higher rotational diffusion time could arise from aggregation or improper folding of the protein. The reduced limiting anisotropy could arise from multiple binding sites of the C153.

Comparison of the Experimental and Simulated *C*(*t*)s

As suggested earlier, the origin of this discrepancy between the experimental and simulated *C*(*t*)s for the mutants may be found from structural studies of the complexes. From a comparison of the C153-Trp distances obtained from equilibrated simulation structures and energy transfer experiments (**Table 5.4**) and from the NMR measurements, it appears that the structural features for the C153/WT complex obtained from simulations and experimental measurements are in reasonable agreement. Again, this is not the case for the mutants.

TABLE 5.3

Steady-State parameters for C153/apoMb Complexes

System	$\nu_{em}^{max\ a}$ **cm^{-1}**	$\nu(''0'')^{max}$ ^{a} **cm^{-1}**	$\nu_{ex}^{max\ a}$ **cm^{-1}**	$\lambda(''0'')$ ^{b,c} **cm^{-1}**	$\lambda(\infty)$ ^{b,c} **cm^{-1}**	$\lambda(\infty)-\lambda(''0'')$ ^{c} **cm^{-1}**	$\lambda_{simul.}$ ^{c} **cm^{-1}**
HH WT	22940	20260	18730	1850	2450	600	888
SW WT	18970	20322	22910	1815	2453	638	715
L29F/H64Q/V68F	19160	20307	22840	1786	2355	569	1094
H64L/V68F/P88A	19690	20660	23360	1847	2450	603	1252
L29F/V68L	19360	20600	23090	1743	2390	647	755

[a] Peak maxima are obtained from log-normal fits of the spectra.

[b] λ values from experiments are calculated using eq. 1 and have an error of ± 5 cm^{-1} as determined from 3 different measurements.

[c] $\lambda(\infty)$ is the *total* Stokes shift including intramolecular and solvent contribution, whereas $\lambda(''0'')$ exclusively estimates the intramolecular vibrational contribution to the total Stokes shift. Their difference, $\lambda(\infty)-\lambda(''0'')$, is commensurate with that obtained from simulations, $\lambda_{simul.}$, calculated as $\lambda = <(\delta\Delta E)^2> / 2k_BT$ and which *only* accounts for the dynamic Stokes shift due to solvent contribution or relaxation.

The way in which the initial structures for the simulations are determined may provide a clue for understanding such discrepancies. For the wild type, the apo structure is obtained directly from protein data bank, presumably the same structure as the one used in the experimental measurements. On the other hand, the initial structures of the mutants are obtained from simple site mutations in the presence of the coumarin in the heme pocket.

This construction of the initial complex for the wild type proteins is different from those for the mutant complexes. More precisely, the construction of the mutant complexes for the simulations is not analogous to the preparation of the complexes for the experimental measurements. In the latter, the mutant protein is first expressed and the heme is removed, C153 diffuses into the heme pocket, and the heme pocket relaxes around the coumarin. In other words, the mutation and apoprotein formation and the subsequent introduction of the C153 correspond to two different equilibration steps in the molecular dynamics simulations. Indeed, the structures from simulations for the two wild type C153/apoMb complexes are in reasonable agreement with the experimental observations (**Table 5.4**), but the structures for the mutants are not.

TABLE 5.4

Distances from Trp7 and Trp14 to C153 in the Complexes

System	**Simulations**[a]		**FRET**			
			R_0[b]		**R**[c]	
	Trp7	**Trp14**	**Trp7**	**Trp14**	**Trp7**	**Trp14**
HH WT	21.1	17.0	26.9	25.5	20.1	17.3
SW WT	16.7	11.6	25.3	23.9	18.4	14.4
L29F/H64Q/V68F	17.8	13.8	25.2	23.8	16.8	16.7
H64L/V68F/P88A	17.2	12.9	25.5	24.1	15.9	15.9
L29F/V68L	18.1	12.1	25.9	24.4	17.3	17.2

All distances are in Angstroms.

[a] Distances between C153 and Trp are obtained from the equilibrated structures as shown in Figure 5.11b.

[b] R_0 is the so-called “critical distance” distance between donor and acceptor defined by eqs 5.4 and 5.5.

[c] R is the distance from the center of mass of donor (Trp) and acceptor (C153) as shown in Figure 5.11a.

One possible way to check this argument is to equilibrate the mutant apoprotein first and then insert the coumarin into the heme pocket with the initial structure being consistent with the energy transfer and NMR measurements. From such initial structures of the mutants the reorganization energies and solvation correlation functions from simulations could be tested against the experimental ones. Another possible way to test the reliability of the mutant complex structure is annealing, namely raising the simulation temperature to 500 K for some time, and then cooling the system down to 300 K to equilibrate for 10 ns. For the HH-WT/C153 complex, an annealing was done at 500 K for 3 ns and an equilibration at 300 K for 10 ns. There was no significant change for the structure of the complex.

Conclusion

We have continued to explore the use of the complex of C153 and apoMbs to study the protein dielectric response [30-33], which has proven to be extremely successful. Comparisons between experimental and simulated *C*(*t*)s for wild-type heme proteins, such as horse heart myoglobin,[32,33] leghemoglobin,[32,33] and sperm whale myoglobin range from very good to excellent. Furthermore, examination of these systems demonstrates the sensitivity of C153 to its environment and permits the observation of differences in the heme pockets among these three proteins. Perhaps most impressive is that we can detect changes in *C*(*t*) arising from only one change between the heme pockets of the horse heart and sperm whale myoglobins: Val67 in HH is replaced by Thr in SW (**Figure 5.3**).

Our success with the wild-type proteins encouraged us to study mutant sperm whale myoglobins. For the three mutants we investigated, however, agreement between experiment and simulation was considerably inferior to that for the wild-type systems. Our previous work suggests no reason to attribute such disagreement to the force fields used in the simulation but rather to question the structure of the complex used as the starting point for the simulation. Thus painstaking attention must be paid to structural details when comparisons are being made between theory and experiment for different proteins and, in particular, the same proteins with slight modifications. We consequently performed an NMR study of the complex of C153 with HH-WT apoMb, along with fluorescence energy transfer and anisotropy of all of the horse heart and sperm whale complexes to complement the NMR studies.

The NMR measurements provide important confirmation of our earlier conclusions [30-33] that the C153 lies in the heme pocket of the HH-WT apoMb. For the wild-type complexes, fluorescence energy transfer measurements provide two rise times, suggesting a definite spatial relationship between the two Trp donors and the C153 acceptor. On the other hand, the three mutants all provided single exponential rise times for the energy transfer. Such a result can be interpreted in at least three ways: R^6/κ^2 is the same for C153 and each of the two Trps (assuming a fixed dipole moment for C153); or the position and orientation of C153 only favors energy transfer from a single Trp residue; or the mutants proteins are not correctly folded and there are multiple C153 binding sites or the C153 is mobile on the time scale of the energy transfer giving rise to a averaged time constant. Fluorescence anisotropy studies suggest that the double mutant was not structurally intact.

It is important to stress that the rather poor agreement between simulation and experiment for, at least the triple mutants, is *not* a suggestion that it is not possible to identify the contribution of a single amino acid to the dielectric response. We reiterate that for HH-WT apoMb and apoLba, we have found excellent agreement between the $C(t)$ obtained from both experiments and simulations that the only difference between the heme pockets of the two WTs is that Val67 in HH is replaced by Thr in SW.[32,33] The mutant results point, rather, to the importance of the structural characterization of modified proteins used in studies of the dielectric response and suggest strategies for performing molecular dynamics simulations of modified proteins—i.e., starting perhaps with (limited) NMR data and employing more than one equilibration step. We believe that ours is the most thorough structural characterization to date of any system, whether it be based on nonnatural fluorescence probes or mutants, employed for the investigation of the dielectric response of proteins.

Acknowledgements

We thank Prof. John S. Olson at Rice University for providing the sperm holomyoglobin and its mutants. XS is grateful for financial support from NSF grant CHE-0809431.

References

(1) Nandi, N.; Bhattacharyya, K.; Bagchi, B. *Chem. Rev.* **2000**, *100*, 2013.

(2) Simon, J. D. *Acc. Chem. Res.* **1988**, *21*, 128.

(3) Fleming, G. R.; Wolynes, P. G. *Phys. Today* **1990**, *43*, 36.

(4) Barbara, P. F.; Jarzeba, W. Ultrafast Photochemical Intramolecular Charge Transfer and Excited State Solvation. In *Advances in Photochemistry*; Volman, D. H., Hammond, G. S., Gollnick, K., Eds.; John Wiley & Sons, 1990.

(5) Maroncelli, M. *J. Mol. Liq.* **1993**, *57*, 1.

(6) Hynes, J. T. Charge Transfer Reactions and Solvation Dynamics. In *Ultrafast Dynamics of Chemical Systems*, 1994; Vol. 7; pp 345.

(7) Fleming, G. R.; Cho, M. H. *Annu. Rev. Phys. Chem.* **1996**, *47*, 109.

(8) Stratt, R. M.; Maroncelli, M. *J. Phys. Chem.* **1996**, *100*, 12981.

(9) Castner, E. W., Jr.; Maroncelli, M. *J. Mol. Liq.* **1998**, *77*, 1.

(10) Mukamel, S. *Principles of Nonlinear Optical Spectroscopy*, First Edition ed.; Oxford University Press: New York, 1995.

(11) Hsu, C. P.; Song, X. Y.; Marcus, R. A. *J. Phys. Chem. B* **1997**, *101*, 2546.

(12) Song, X.; Chandler, D. *J. Chem. Phys.* **1998**, *108*, 2594.

(13) Marcus, R. A.; Sutin, N. *Biochim. Biophys. Acta* **1985**, *811*, 265.

(14) King, G.; Warshel, A. *J. Chem. Phys.* **1989**, *91*, 3647.

(15) Bader, J. S.; Kuharski, R. A.; Chandler, D. *Abstr. Paper Am. Chem. Soc.* **1990**, *199*, 65.

(16) Halder, M.; Headley, L. S.; Mukherjee, P.; Song, X.; Petrich, J. W. *J. Phys. Chem. A* **2006**, *110*, 8623.

(17) Lang, M. J.; Jordanides, X. J.; Song, X.; Fleming, G. R. *J. Chem. Phys.* **1999**, *110*, 5884.

(18) Perutz, M. F. *Science* **1978**, *210*, 1187.

(19) Moser, C. C.; Keske, J. M.; Warncke, K.; Farid, R. S.; Dutton, P. L. *Nature* **1992**, *355*, 796.

(20) Warshel, A.; Russel, S. T. *Q. Rev. Biol.* **1984**, *17*, 283.

(21) Sharp, K. A.; Honig, B. *Ann. Rev. Biophys. Chem.* **1990**, *19*, 301.

(22) Nakamura, H. *Q. Rev. Biophys.* **1996**, *29*, 1.

(23) King, G.; Lee, F. S.; Warshel, A. *J. Chem. Phys.* **1991**, *95*, 4366.

(24) Simonson, T.; Perahia, D.; Brünger, A. T. *Biophys. J.* **1991**, *59*, 670.

(25) Simonson, T.; Perahia, D. *Proc. Natl. Acad. Sci. U. S. A.* **1995**, *92*, 1082.

(26) Simonson, T.; Brooks, C. L. *J. Am. Chem. Soc.* **1996**, *118*, 8452.

(27) Simonson, T. *J. Am. Chem. Soc.* **1998**, *120*, 4875.

(28) Simonson, T.; Archontis, G.; Karplus, M. *J. Phys. Chem. B* **1999**, *103*, 6142.

(29) Warshel, A.; Sharma, P. K.; Kato, M.; Parson, W. W. *Biochimica et Biophysica Acta, Proteins and Proteomics* **2006**, *1764*, 1647.

(30) Chowdhury, P. K.; Halder, M.; Sanders, L.; Arnold, R. A.; Liu, Y.; Armstrong, D. W.; Kundu, S.; Hargrove, M. S.; Song, X.; Petrich, J. W. *Photochem. Photobiol.* **2004**, *79*, 440.

(31) Mukherjee, P.; Halder, M.; Hargrove, M.; Petrich, J. W. *Photochem. Photobiol.* **2006**, *82*, 1586.

(32) Halder, M.; Mukherjee, P.; Bose, S.; Hargrove, M. S.; Song, X.; Petrich, J. W. *J. Chem. Phys.* **2007**, *127*, 055101/1.

(33) Bose, S.; Adhikary, R.; Mukherjee, P.; Song, X.; Petrich, J. W. *J. Phys. Chem. B* **2009**, *113*, 11061.

(34) Cocco, M. J.; Lecomte, J. T. J. *Protein Sci.* **1994**, *3*, 267.

(35) Nemkovich, N. A.; Baumann, W.; Kruchenok, Y. V.; Reis, H.; Rubinov, A. N. *J. Appl. Spectrosc.* **1999**, *66*, 415.

(36) Pal, S. K.; Peon, J.; Bagchi, B.; Zewail, A. H. *J. Phys. Chem. B* **2002**, *106*, 12376.

(37) Pal, S. K.; Peon, J.; Zewail, A. H. *Proc. Natl. Acad. Sci. USA* **2002**, *99*, 1763.

(38) Peon, J.; Pal, S. K.; Zewail, A. H. *Proc. Natl. Acad. Sci. USA* **2002**, *99*, 10964.

(39) Shen, X.; Knutson, J. R. *J. Phys. Chem. B* **2001**, *105*, 6260.

(40) Jordanides, X. J.; Lang, M. J.; Song, X.; Fleming, G. R. *J. Phys. Chem. B* **1999**, *103*, 7995.

(41) Chowdhury, P. K.; Halder, M.; Sanders, L.; Calhoun, T.; Anderson, J. L.; Armstrong, D. W.; Song, X.; Petrich, J. W. *J. Phys. Chem. B* **2004**, *108*, 10245.

(42) Stryer, L. *J. Mol. Biol.* **1965**, *13*, 482.

(43) Pierce, D. W.; Boxer, S. G. *J. Phys. Chem.* **1992**, *96*, 5560.

(44) Macgregor, R. B.; Weber, G. *Nature* **1986**, *316*, 70.

(45) Bashkin, J. S.; Mclendon, G.; Mukamel, S.; Marohn, J. *J. Phys. Chem.* **1990**, *94*, 4757.

(46) Adhikary, R.; Barnes, C. A.; Petrich, J. W. *J. Phys. Chem. B* **2009**, *113*, 11999.

(47) Maroncelli, M.; Fleming, G. R. *J. Chem. Phys.* **1987**, *86*, 6221.

(48) Horng, M. L.; Gardecki, J. A.; Papazyan, A.; Maroncelli, M. *J. Phys. Chem.* **1995**, *99*, 17311.

(49) Lewis, J. E.; Maroncelli, M. *Chem. Phys. Lett.* **1998**, *282*, 197.

(50) Maroncelli, M.; Fee, R. S.; Chapman, C. F.; Fleming, G. R. *J. Phys. Chem.* **1991**, *95*, 1012.

(51) Kovalenko, S. A.; Ruthmann, J.; Ernsting, N. P. *Chem. Phys. Lett.* **1997**, *271*, 40.

(52) Muhlpfordt, A.; Schanz, R.; Ernsting, N. P.; Farztdinov, V.; Grimme, S. *Phys. Chem. Chem. Phys.* **1999**, *1*, 3209.

(53) Changenet-Barret, P.; Choma, C. T.; Gooding, E. F.; DeGrado, W. F.; Hochstrasser, R. M. *J. Phys. Chem. B* **2000**, *104*, 9322.

(54) Jiang, Y.; McCarthy, P. K.; Blanchard, D. J. *Chem. Phys.* **1994**, *183*, 249.

(55) Flory, W. C.; Blanchard, D. J. *Appl. Spectrosc.* **1998**, *52*, 82.

(56) Palmer, P. M.; Chen, Y.; Topp, M. R. *Chem. Phys. Lett.* **2000**, *318*, 440.

(57) Chen, Y.; Palmer, P. M.; Topp, M. R. *Int. J. Mass Spectrom* **2002**, *220*, 231.

(58) Agmon, N. *J. Phys. Chem.* **1990**, *94*, 2959.

(59) Chakrabarty, D.; Hazra, P.; Chakraborty, A.; Seth, D.; Sarkar, N. *Chem. Phys. Lett.* **2003**, *381*, 697.

(60) Tcherkasskaya, O.; Ptitsyn, O. B.; Knutson, J. R. *Biochemistry* **2000**, *39*, 1879.

(61) Petrich, J. W.; Martin, J. L.; Breton, J. *Springer Ser. Chem. Phys.* **1988**, *48*, 576.

(62) Das, K.; Smirnov, A. V.; Wen, J.; Miskovsky, P.; Petrich, J. W. *Photochem. Photobiol.* **1999**, *69*, 633.

(63) Song, X. *J. Chem. Phys.* **2002**, *116*, 9359.

(64) Cocco, M. J.; Kao, Y.-H.; Phillips, A. T.; Lecomte, J. T. J. *Biochemistry* **1992**, *31*, 6481.

(65) Alayash, A. I.; Ryan, B. A. B.; Eich, R. F.; Olson, J. S.; Cashon, R. E. *J. Biol. Chem.* **1999**, *274*, 2029.

(66) Nguyen, B. D.; Zhao, X.; Vyas, K.; La Mar, G. N.; Lile, R. A.; Brucker, E. A.; Phillips, G. N., Jr.; Olson, J. S.; Wittenberg, J. B. *J. Biol. Chem.* **1998**, *273*, 9517.

(67) Hargrove, M. S.; Singleton, E. W.; Quillin, M. L.; Ortiz, L. A.; Phillips, G. N.; Olson, J. S.; Mathews, A. J. *J. Biol. Chem.* **1994**, *269*, 4207.

(68) Headley, L. S.; Mukherjee, P.; Anderson, J. L.; Ding, R.; Halder, M.; Armstrong, D. W.; Song, X.; Petrich, J. W. *J. Phys. Chem. A* **2006**, *110*, 9549.

(69) Mukherjee, P.; Crank, J. A.; Halder, M.; Armstrong, D. W.; Petrich, J. W. *J. Phys. Chem. A* **2006**, *110*, 10725.

(70) Fee, R. S.; Maroncelli, M. *Chem. Phys.* **1994**, *183*, 235.

(71) Arzhantsev, S.; Ito, N.; Heitz, M.; Maroncelli, M. *Chem. Phys. Lett.* **2003**, *381*, 278.

(72) Ito, N.; Arzhantsev, S.; Heitz, M.; Maroncelli, M. *J. Phys. Chem. B* **2004**, *108*, 5771.

(73) Mukherjee, P.; Crank, J. A.; Sharma, P. S.; Wijeratne, A. B.; Adhikary, R.; Bose, S.; Armstrong, D. W.; Petrich, J. W. *J. Phys. Chem. B* **2008**, *112*, 3390.

(74) Zhong, D. P.; Pal, S. K.; Zhang, D. Q.; Chan, S. I.; Zewail, A. H. *Proc. Natl. Acad. Sci. USA* **2002**, *99*, 13.

(75) Lu, W.; Kim, J.; Qiu, W.; Zhong, D. *Chem. Phys. Lett.* **2004**, *388*, 120.

(76) Qiu, W.; Kao, Y.-T.; Zhang, L.; Yang, Y.; Wang, L.; Stites, W. E.; Zhong, D.; Zewail, A. H. *Proc. Natl. Acad. Sci. USA* **2006**, *103*, 13979.

(77) Qiu, W.; Zhang, L.; Okobiah, O.; Yang, Y.; Wang, L.; Zhong, D.; Zewail, A. H. *J. Phys. Chem. B.* **2006**, *110*, 10540.

(78) Zhang, L.; Wang, L.; Kao, Y.; Qiu, W.; Yang, Y.; Okobiah, O.; Zhong, D. *Proc. Natl. Acad. Sci. USA* **2007**, *104*, 18461.

(79) Zhang, L.; Yang, Y.; Kao, Y.-T.; Wang, L.; Zhong, D. *J. Am. Chem. Soc.* **2009**, *131*, 10677.

(80) Marchi, M.; Procacci, P. *J. Chem. Phys.* **1998**, *109*, 5194.

(81) Pearlman, D. A.; Case, D. A.; Caldwell, J. W.; Ross, W. S.; Cheatham, T. E., III; DeBolt, S.; Ferguson, D.; Seibel, S.; Kollman, P. *Comp. Phys. Commun.* **1995**, *91*, 1.

(82) Maroncelli, M.; Fleming, G. R. *J. Chem. Phys.* **1988**, *89*, 5044.

(83) Jimenez, R.; Fleming, G. R.; Kumar, P. V.; Maroncelli, M. *Nature* **1994**, *369*, 471.

(84) Li, T.; Hassanali, A. A.; Kao, Y.-T.; Zhong, D.; Singer, S. J. *J. Am. Chem. Soc.* **2007**, *129*, 3376.

(85) Nilsson, L.; Halle, B. *Proc. Natl. Acad. Sci. U. S. A.* **2005**, *102*, 13867.

(86) Abbyad, P.; Shi, X.; Childs, W.; McAnaney, T. B.; Cohen, B. E.; Boxer, S. G. *J. Phys. Chem. B* **2007**, *111*, 8269.

(87) Golosov, A. A.; Karplus, M. *J. Phys. Chem. B* **2007**, *111*, 1482.

(88) Kundu, S.; Snyder, B.; Das, K.; Chowdhury, P.; Park, J.; Petrich, J. W.; Hargrove, M. S. *Proteins: Struct. Funct. Genet.* **2002**, *46*, 268.

(89) Kundu, S.; Hargrove, M. S. *Proteins: Struct. Funct. Genet.* **2003**, *50*, 239.

(90) Lecomte, J. T. J.; Cocco, M. J. *Biochemistry* **1990**, *29*, 11057.

(91) Cocco, M. J.; Lecomte, J. T. J. *Biochemistry* **1990**, *29*, 11067.

(92) Cocco, M. J.; Barrick, D.; Taylor, S. V.; Lecomte, J. T. J. *J. Am. Chem. Soc.* **1990**, *114*, 11000.

(93) Kao, Y.-H.; Lecomte, J. T. J. *J. Am. Chem. Soc.* **1993**, *115*, 9754.

(94) Lecomte, J. T. J.; Kao, Y.-H.; Cocco, M. J. *Proteins: Struct. Funct. Genet.* **1996**, *25*, 267.

(95) Lecomte, J. T. J.; Sukits, S. F.; Bhattacharyya, S.; Falzone, C. *Protein Sci.* **1999**, *8*, 1484.

(96) Avouris, P.; Yang, L. L.; El-Bayoumi, M. A. *Photochem. Photobiol.* **1976**, *24*, 211.

(97) Rich, R. L.; Gai, F.; Lane, J. W.; Petrich, J. W.; Schwabacher, A. W. *J. Am. Chem. Soc.* **1995**, *117*, 733.

(98) Dale, R. E.; Eisinger, J. *Biopolymers* **1974**, *13*, 1573.

(99) Glandieres, J.-M.; Twist, C.; Haouz, A.; Zentz, C.; Alpert, B. *Photochem. Photobiol.* **2000**, *71*, 382.

(100) Sirangelo, I.; Malmo, C.; Casillo, M.; Irace, G. *Photochem. Photobiol.* **2002**, *76*, 381.

(101) Negus, D. K.; Hochstrasser, R. M. *Proc. Natl. Acad. Sci. U. S. A.* **1984**, *81*, 4399.

(102) Stevens, J. A.; Link, J. J.; Kao, Y.-T.; Zang, C.; Wang, L.; Zhong, D. *J. Phys. Chem. B* **2010**, *114*, 1498.

(103) Cross, A. J.; Fleming, G. R. *Biophys. J.* **1984**, *46*, 45.

CHAPTER 6: PHOTOINDUCED TRANS-TO-CIS ISOMERIZATION OF CYCLOCURCUMIN

A paper published in the *Journal of Physical Chemistry B*

R. Adhikary[1], CA Barnes[1], RL Trampel[1], SJ Wallace[2],
TW Kee[2],[*] and JW Petrich[1*]

Abstract

The photophysical properties of cyclocurcumin in various solvents are studied for the first time in order to shed light on the nonradiative processes of the parent compound, curcumin, which has a range of medicinal properties. Steady-state fluorescence and fluorescence-excitation spectra of cyclocurcumin in polar aprotic solvents are strongly dependent on excitation (λ_{ex}) and emission (λ_{em}) wavelength, respectively. The fluorescence quantum yield also depends on λ_{ex} and increases with the viscosity of the medium. Time-resolved studies show nonexponential fluorescence decay in all the solvents studied. The two fluorescence decay components of cyclocurcumin in alcohols exhibit a strong dependence on viscosity and temperature. NMR spectroscopy indicates that cyclocurcumin is entirely in the *trans* form with respect to the C6-C7 double bond in methanol, chloroform, and acetone. It is suggested that at least two

---

Reprinted with permission from *The Journal Physical Chemistry B* 2011, 115 (36), 10707-10714. Copyright (2009) American Chemical Society. [1]Department of Chemistry, Iowa State University, Ames, Iowa 50011-3111. [2]School of Chemistry and Physics, University of Adelaide, Adelaide, South Australia, 5005, Australia conformational isomers about another single bond (C5-C6 or C7-C1″ or both) and that *trans* to *cis* isomerization about the C6-C7 double bond of these isomers provide the most likely means of rationalizing the steady-state spectra and the nonradiative decay mechanisms in both protic and aprotic polar solvents.

Introduction

Turmeric, the rhizome of the plant *Curcuma longa L.*, has been used for centuries as a spice and as a food coloring in Asian countries.[1] Its yellow color is primarily caused by a group of structurally related polyphenols collectively known as curcuminoids, which are composed of curcumin (77%) (**Figure 6.1a**), as the major bioactive component, and two of its derivatives, demethoxycurcumin (17%) and bismethoxycurcumun (3%).[2] These three compounds only differ in methoxy substitution of their aromatic rings. In addition to these components, another curcuminoid, cyclocurcumin (**Figure 6.1b**), is present. Cyclocurcumin was first isolated from turmeric and characterized in 1993 by Kuchi et al.[3] Only a few biologically-active properties of cyclocurcumin have been reported.[4] The nematocidal activity of these curcuminoids increases remarkably when they are applied cooperatively whereas they were inactive when employed individually, which suggests a synergistic action between them.[3] A study of curcuminoids on the inhibitory effect on MCF-7 human-breast, tumor-cell proliferation shows that curcumin, demethoxycurcumin, and bismethoxycurcumin are potent inhibitors whereas cyclocurcumin is less inhibitory.[4] Comparisons of the molecular structures of these curcuminoids and their antiproliferative effects suggest that the diketone moiety of the curcuminoids appears to be essential for the inhibitory activity.[4]

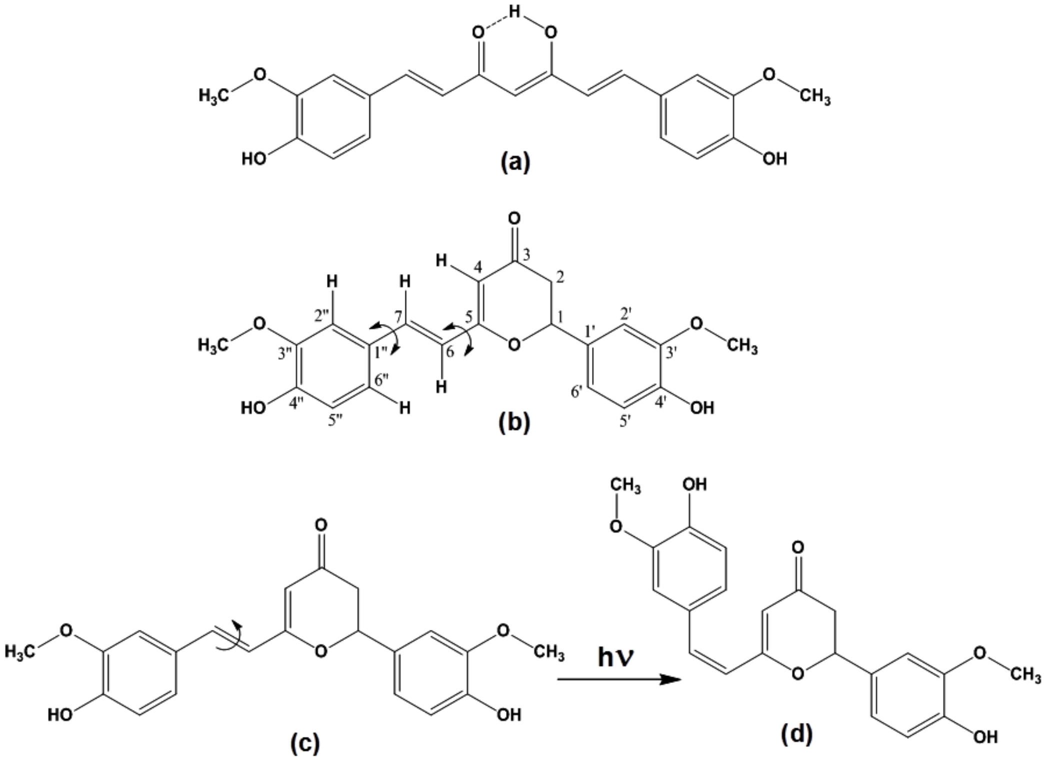

Figure 6.1. Chemical structures of (a) curcumin and (b) cyclocurcumin. Rotation around single bonds (C5-C6 or C7-C1″ or both) is suggested to produce rotamers that are involved in the excited-state photophysics investigated here. A rotation around the ethylenic double bond in the excited state of (c) the *trans*-isomer of cyclocurcumin generates (d) the *cis*-isomer.

The basis for studying cyclocurcumin is to shed light on curcumin itself. Curcumin has a variety of pharmacological activities including anti-inflammatory, anticancer and antioxidant properties.[5-9] Curcumin can also prevent protein aggregation in debilitating diseases such as Alzheimer’s and Parkinson’s.[10,11] It also shows photobiological and photosensitizating activity.[12,13] A number of studies have focused on understanding the medicinal properties of curcumin by developing insight into the molecular events that this compound undergoes. Our recent studies propose that excited-state intramolecular hydrogen atom transfer (ESIHT) is a major nonradiative process in curcumin.[14-16] Because cyclocurcumin cannot execute ESIHT, investigations of this compound may provide a powerful means to support the conclusions of our previous studies.[14-16] Furthermore, by suppressing ESIHT in cyclocurcumin, we are able to investigate in more detail other processes that curcumin itself may undergo.

Here we study the photophysical behavior of cyclocurcumin in various solvents using steady-state and time-resolved fluorescence spectroscopy. The data are surprisingly rich, and NMR spectroscopy was employed to provide additional structural information of the system in its ground state. We find that cyclocurcumin is entirely in the *trans* form (with respect to the C6-C7 double bond) in methanol, chloroform, and acetone. We suggest that at least two conformational isomers about another single bond (C5-C6 or C7-C1″ or both) and that *trans* to *cis* isomerization about the C6-C7 double bond of these isomers provide the most likely means of rationalizing the steady-state spectra and the nonradiative decay mechanisms in both protic and aprotic polar solvents.

Experimental Section

Materials. Cyclocurcumin (HPLC purity ≥ 98% and adjusted purity ≥ 95.6 %) was obtained from ChromaDex Inc. and was tested for purity by NMR and mass-spectroscopy (see supporting material). Coumarin 153 was purchased from Exciton Inc. (Dayton, OH). Cyclohexane (99.9%), chloroform (99.9%), acetone (99.7%), acetonitrile (99.9%), DMSO (99.9%) methanol (99.9%), ethanol (99.5%), ethylene glycol (99%) and glycerol (99.7%) were purchased from Fisher Chemical and used without further purification. 1-Propanol (> 99.9 %), 1-butanol (> 99%), 1-pentanol (> 99%), and 1-hexanol (> 99 %) were purchased from Sigma-Aldrich. Methanol-d_4 (> 99.8%), acetone-d_6 (> 99.8%), and chloroform-d (> 99.8%) were obtained from Cambridge Isotope Laboratories, Inc.

Sample Preparation. Dilute solutions (O.D. ≤ 0.08) of cyclocurcumin were prepared by adding a small amount of the solid to each solvent for the steady-state and time-resolved fluorescence measurements. Solutions of cyclocurcumin in cyclohexane and chloroform were sonicated and then kept in the dark overnight to ensure complete solubilization.

Steady-State Measurements. Steady-state UV-Vis absorption and emission spectra were recorded on a Hewlett Packard 8453 UV-visible spectrophotometer and Spex Fluoromax-4 with 1-nm resolution using a 5-mm path-length quartz cuvette. The emission spectra were corrected for lamp spectral intensity and detector response. The fluorescence quantum yields (ϕ_f) were determined using coumarin 153 as a standard ($\phi_f = 0.56$ in acetonitrile[17]) using:

$$\frac{\phi_S}{\phi_R} = \frac{1-10^{-OD_R}}{1-10^{-OD_S}} \times \frac{\int F_S(\tilde{\nu})d\tilde{\nu}}{\int F_R(\tilde{\nu})d\tilde{\nu}} \times \frac{n_S^2}{n_R^2} \qquad (6.1)$$

where ϕ, OD, F, and n represent fluorescence quantum yield, optical density, fluorescence spectrum on a wavenumber scale, and the index of refraction of the solvent, respectively. The subscripts S and R denote sample and reference, respectively.

Time-Resolved Measurements. Excited-state lifetime measurements were performed using the time-correlated single-photon counting (TCSPC) technique. A homebuilt mode-locked Ti:sapphire oscillator pumped by a 5-W Nd:VO$_4$ laser (Millennia, Spectra Physics) producing femtosecond pulses tunable from 780 to 900 nm with a repetition rate of 82 MHz was used as the laser source. Its fundamental wavelength at 814 nm (~500 mW) was modulated by a Pockels cell (Model 350-160, Conoptics Inc.) to reduce the repetition rate to approximately 8.8 MHz and was subsequently frequency doubled by using a harmonic generator (Model TP-2000B, U-Oplaz Technologies). The resulting blue light (407 nm) provided the excitation source. The fluorescence signals were collected in a 90^o geometry, and passed through an analyzer set at the magic angle (54.7^o) with respect to excitation polarization. Placing a half-wave plate before a vertical polarizer ensured the polarization of the excitation light. The appropriate filters were placed in front of a microchannel plate, MCP (Hamamatsu, R3809U-50) to block the excitation light and to select emission range from sample. The detector output was amplified and fed to a Becker & Hickl photon-counting module Model SPC-630. The full-width-at-half-maximum (FWHM) of the instrument response function was ~40–45 ps. A total of 65,000 counts were collected in the peak channel. The TCSPC cuvette holder was modified to allow temperature control. The temperature was modulated and maintained by a Polystat Cole-Parmer Refrigerated Cooler. Each sample was allowed to equilibrate for ~5-10 minutes at the desired temperature before collecting datae. A cuvette of 5-mm path-length was used for all the lifetime measurements except for isoviscous experiments where a 1-cm path-length cuvette for time-resolved lifetime experiments.

NMR Experiments. Samples of cyclocurcumin were prepared at a concentration of ~0.5-1 mM in freshly opened methanol-d_4, acetone-d_6, and chloroform-d. The chloroform-d solution was sonicated briefly to ensure complete solubilization of cyclocurcumin. Solutions were then placed in standard 5 mm NMR tubes (Wilmad). Standard 1D ^{1}H and 2D ^{1}H-COSY NMR spectra were obtained on a Bruker Avance 700 MHz spectrometer with an operational frequency of 700.13 MHz at 298 K. For the temperature dependent data, a Bruker Avance 400 MHz spectrometer, operating at 400.39 MHz was used to acquire spectra from 233 K – 298 K. Standard operating protocols were followed in the acquisition of spectra. In regards to 1D spectra, 32 scans for the 700 MHz and 400 MHz experiments were acquired using sweeping widths of 7692 Hz and 5630 Hz, respectively. For 2D ^{1}H-COSY spectra, 256 scans were accumulated with a two dimensional sweep width of 7702.28 Hz. NMR spectra were processed and analyzed with ACD/Labs NMR Processor Academic Edition (Version: 12.01). Chemical shifts are reported in δ values.

Results and Discussion.

***Absorption and Emission Spectroscopy*.** In order to investigate the influence of solvent polarity and proticity on spectral properties, steady-state absorption and fluorescence spectra of cyclocurcumin were obtained in a number of organic solvents: nonpolar, cyclohexane; polar aprotic, chloroform, acetone, and acetonitrile (ACN); and polar protic, methanol, ethanol, ethylene glycol (EG), and glycerol. Absorption spectra of cyclocurcumin in various solvents are presented in **Figure 6.2a**. The lowest energy absorption band of cyclocurcumin has peaks at ~355-377 nm in all the polar solvents studied. The absorption peak position in ethanol at 370 nm agrees with the previously reported value.[3] In addition, a shoulder or peak at ~330-336 nm is also found for cyclocurcumin in chloroform, acetone, acetonitrile, methanol and ethanol. In contrast, this shoulder is absent for cyclocurcumin in ethylene glycol and glycerol.

Figure 6.2b presents the fluorescence spectra (λ_{ex} = 370 nm) of cyclocurcumin in a range of solvents. There is a broad, structureless fluorescence spectrum in all the solvents. The Stokes shift increases with increasing solvent polarity. This indicates that the excited state dipole moment of cyclocurcumin is significantly larger than that of its ground state. The maximum of the fluorescence spectrum not only depends on solvent but also on the excitation wavelength (λ_{ex}). Representative fluorescence spectra of cyclocurcumin as a function of λ_{ex} in methanol and acetonitrile are shown in **Figure 6.3**. Cyclocurcumin in various solvents was excited at three wavelengths: 370, 330, and 407 nm. These wavelengths represent the maximum, and the blue and red wings, respectively, of the lowest energy absorption band. Interestingly, the fluorescence maxima of cyclocurcumin have similar values in protic solvents including methanol, ethanol, ethylene glycol, and glycerol. On the other hand, the wavelength of the maximum varies with the excitation wavelength in other solvents: namely chloroform, acetonitrile, and acetone. The excitation spectra of cyclocurcumin were also investigated and shown to vary as a function of emission wavelength (λ_{em}). It follows that distinct excitation spectra were obtained when emission was collected at the blue (450 nm) and red (550 nm) edges, and the maximum of the fluorescence spectrum (500 nm) for acetonitrile (see supporting information). On the other hand, no changes in excitation spectra with λ_{em} were observed in methanol, ethanol, ethylene glycol, and glycerol (see supporting information).

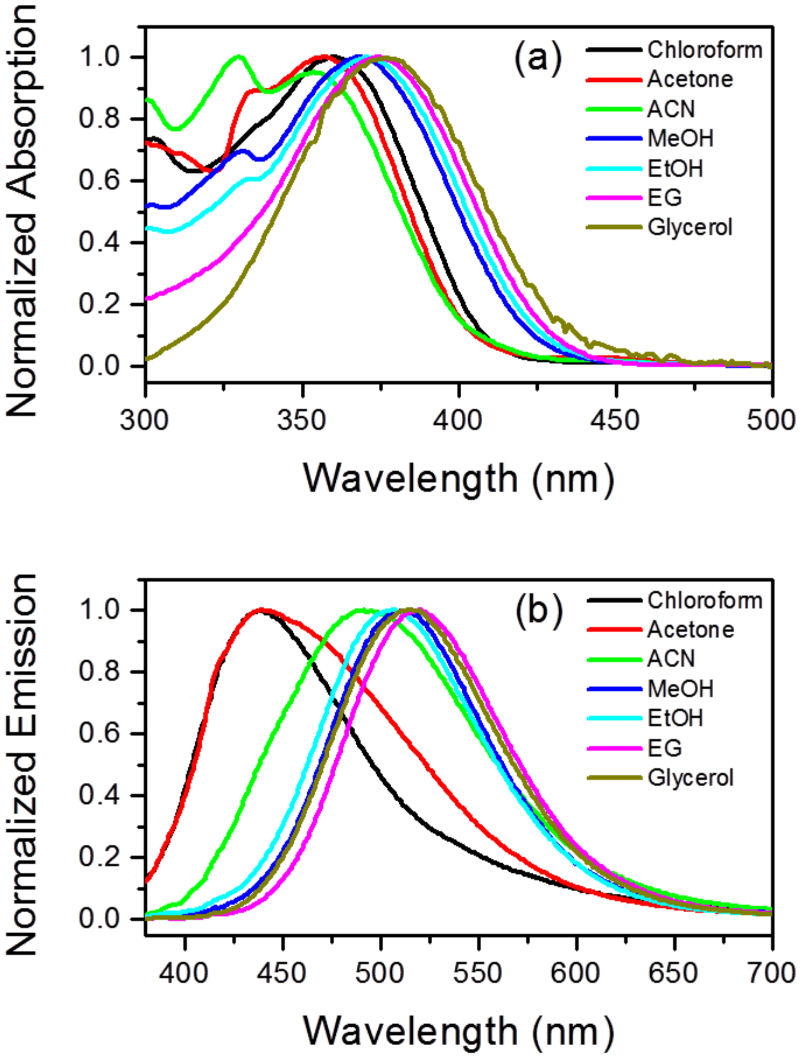

Figure 6.2. Normalized (a) absorption and (b) emission spectra of cyclocurcumin, exciting at 370 nm in chloroform, acetone, acetonitrile (ACN), methanol, ethanol, ethylene glycol (EG), and glycerol.

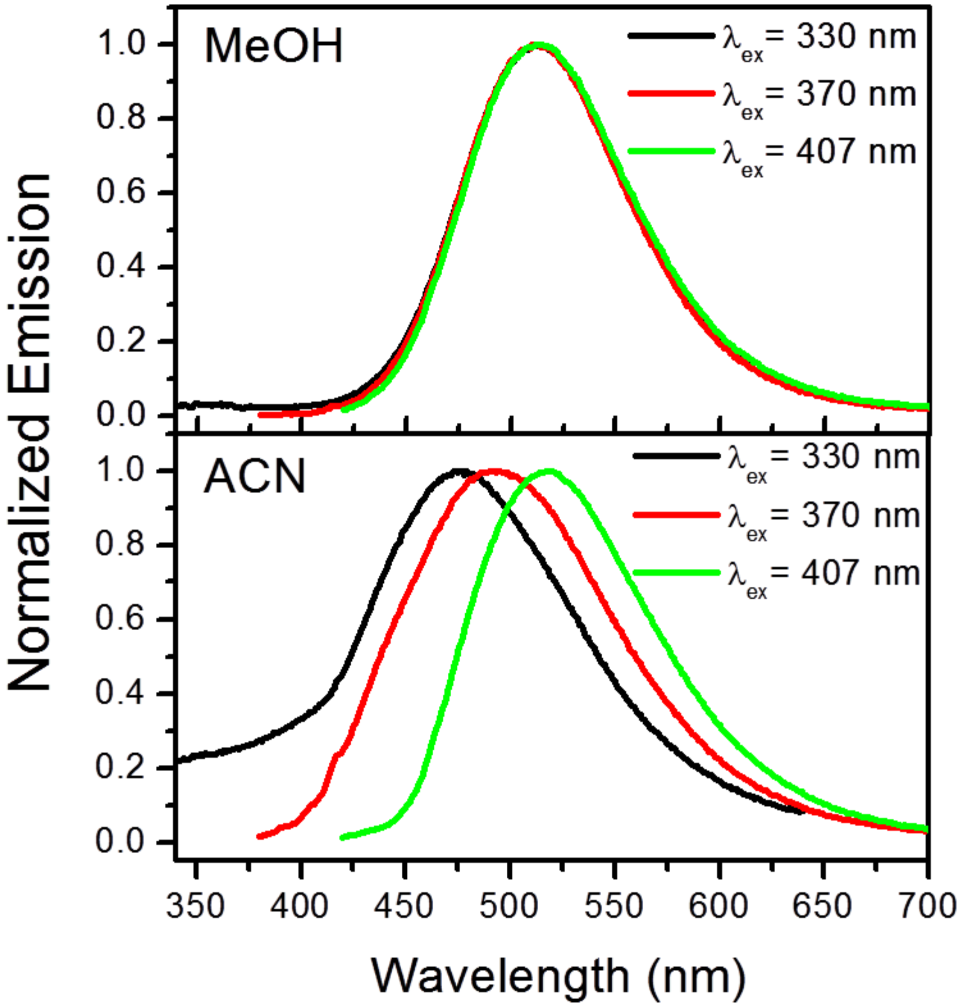

Figure 6.3. Representative excitation wavelength (λ_{ex}) dependent emission spectra of cyclocurcumin in methanol and acetonitrile (ACN). Emission spectra show a strong wavelength dependence in ACN.

The quantum yields of fluorescence (ϕ_f) in different solvents using λ_{ex} = 370 and 407 nm are listed in **Table 6.1**. The lowest and highest ϕ_f of cyclocurcumin were 0.02 in methanol and 0.23 in glycerol at λ_{ex} = 370 nm, respectively. Cyclocurcumin has ϕ_f = 0.13 at λ_{ex}= 370 nm in cyclohexane, which is higher than that in all the other aprotic polar and protic polar solvents, except glycerol. From **Table 6.1**, it is evident that ϕ_f is dependent on λ_{ex} and that it increases significantly with viscosity (η). Previous studies on curcumin and its nonsubstituted analog, dicinnamoylmethane (DCMeth), showed the lowest ϕ_f in cyclohexane (η = 0.98 cP).[18-22] The increase in the fluorescence of curcumin was attributed to the enhancement of nonradiative decay processes such as internal conversion (IC) and ESIHT.[14-16,19] In cyclocurcumin, however, due to the absence of intramolecular hydrogen bonding, ESIHT is impossible; and excited state isomerization about the C6-C7 double bond (**Figure 6.1c-1d),** in addition to IC, may be an important nonradiative deactivation process.

Table 6.1. Fluorescence quantum yield (ϕ_{fl}), lifetime components, radiative (k_r)[a] and non-radiative (k_{nr})[a] rate constants of cyclocurcumin in various solvents

Solvent	a_1	τ_1 (ps)	a_2	τ_2 (ps)	τ_3 (ps)	<τ> (ps)[b]	ϕ_{fl}[c]	ϕ_{fl}[d]	k_r ($\times 10^8 s^{-1}$)	k_{nr} ($\times 10^9 s^{-1}$)	η(cP)[e]
Cyclohexane	0.60	50	0.16	1100	5300	1500	0.13	0.05	0.34	0.64	0.898
Chlorofom	0.79	40	0.15	680	5000	430	0.09	0.04	0.93	2.2	0.542
Acetone	0.38	55	0.62	670	---	440	0.03	0.02	0.45	2.2	0.304
Acetonitrile	0.39	50	0.61	680	---	440	0.03	0.02	0.45	2.2	0.345
Methanol	0.77	55	0.23	140	---	75	0.02	0.01	1.3	13	0.544
Ethanol	0.80	85	0.20	320	---	130	0.02	0.01	0.77	7.6	1.07
Ethylene Glycol	0.39	130	0.61	380	---	280	0.07	0.04	1.4	3.4	16.1
Glycerol	0.34	200	0.63	1020	---	740	0.23	0.12	1.6	1.2	945

[a] k_r and k_{nr} were calculated from average fluorescence lifetime (τ_f^{av}) and quantum yield (ϕ_f) using the following equations $k_r = \phi_f / \tau_f^{av}$ and $k_{nr} = (1/\tau_f^{av}) - k_r$

[b] Fluorescence lifetime measurement were perform λ_{ex}= 407 nm and $\lambda_{em}\geq$ 500 nm and decay traces were fitted with $f(t)=\sum_{i=1}^{3}a_i e^{-t/\tau_i}$ and average lifetime were calculated using $\sum a_i\tau_i$

[c] ϕ_{fl} were calculated exciting at 370 nm

[d] ϕ_{fl} were calculated exciting at 407 nm

[e] All viscosities are at 25°C[69,70]

In order to test this idea, the fluorescence lifetime of cyclocurcumin was measured in various solvents. Representative fluorescence decay traces of cyclocurcumin are presented in **Figure 6.4**. In polar solvents, they are well fit to biexponential decay functions; while in nonpolar cyclohexane and polar aprotic chloroform, they require a triexponential decay function. Among all the solvents studied cyclocurcumin shows the highest average lifetime of ~1.5 ns in cyclohexane. In contrast, it has been previously reported that curcumin has the shortest lifetime of ~50 ps in cyclohexane.[19-21] The relatively long lifetime of cyclocurcumin in a nonpolar solvent is consistent with the absence of ESIHT as a major nonraditive process.

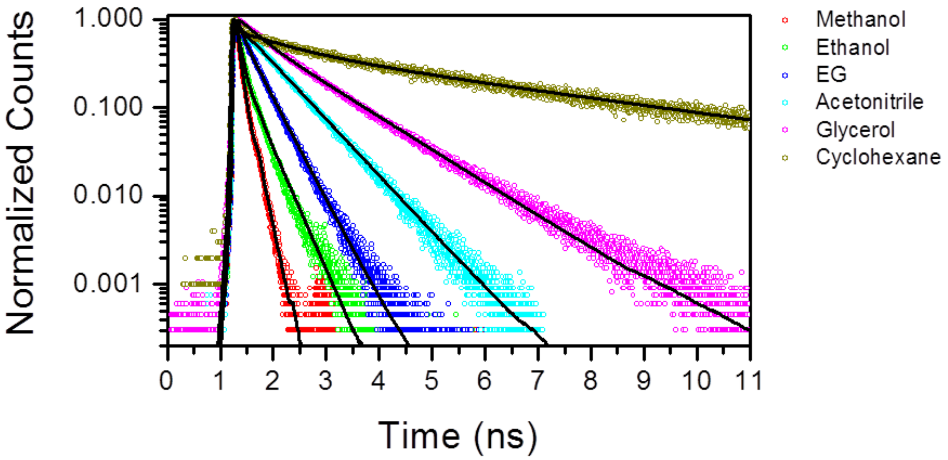

Figure 6.4. Fluorescence decay traces of cyclocurcumin in methanol, ethanol, ethylene glycol (EG), acetonitrile (ACN), glycerol, and cyclohexane at room temperature. The sample was excited at 407 nm and fluorescence was collected at wavelengths greater than 500 nm.

We originally surmised that the biexponential decay resulted from both *trans* and *cis* isomers about the C6-C7 double bond coexisting in the ground state and subsequently executing both *trans*-to-*cis* and *cis*-to-*trans* isomerization in the excited state. Further investigation proved this to be incorrect.

NMR Spectroscopy of Cyclocurcumin in Various Solvents. In order to obtain detailed information about the structure of cyclocurcumin in the ground state, we performed NMR experiments in various solvents. It is known that the vicinal coupling constants are always larger for *trans* (J_{HH} = 12-18 Hz, typical: 15 Hz) than for *cis* isomers (J_{HH} = 0-12 Hz, typical: 8 Hz).[23] We have performed 1D- NMR and 2D-NMR of cylcocurcumin in methanol-d_4, acetone-d_6, and chloroform-d after equilibration under room light. The NMR spectra and peak positions of cyclocurcumin are provided in the Supporting Information. Representative 2D-^{1}H-spectra of cyclocurcumin in chloroform-d are shown in **Figure 6.5**. Peaks at 6.46 ppm and 7.31 ppm are for the olefinic hydrogens (H-6 and H-7) of cyclocurcumin as indicated in **Figure 6.1b**. The coupling constants (J_{HH}) for both these proton are 15.5 Hz. The coupling constant is similar in acetone-d_6 and methanol-d_4, which indicates that cyclocurcumin completely exists in solution in the *trans* form in the ground state. This result is consistent with other systems[24] and is also qualitatively supported by a DFT calculation. For instance, the barriers to thermal isomerization are 48 kcal/mol for *trans*- and ~43 kcal/mol for *cis*-silbene in the ground state.[24] (The barrier is usually low in the excited-state.[24]) Our preliminary calculation of *cis*-*trans* isomerization of cyclocurmin in the ground state indicates that the activation barrier for *trans*-*cis* isomerization of cyclocurcumin is ~30 kcal/mol, and the *trans* form is 5.5 kcal/mol more stable than the *cis* form (see Supporting Information).

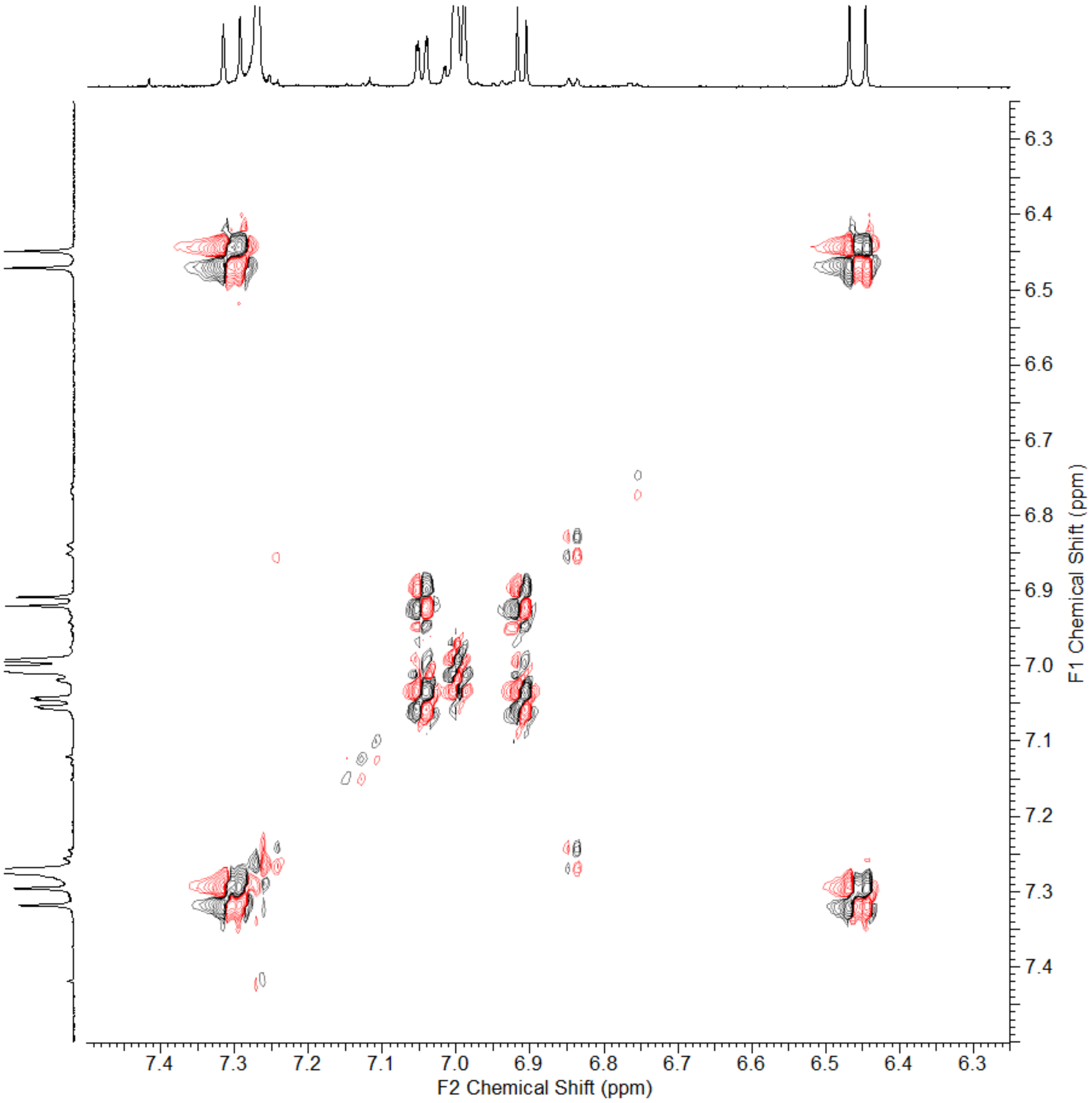

Figure 6.5. Representatative 2D ^{1}H-COSY, 700 MHz spectrum in chloroform-d. Coupling between the two olfenic protons H-6 (6.46 ppm) and H-7 (7.31 ppm) is 15.5 Hz, which indicates the presence of the *trans* conformation of cyclocurcumin in the ground state.

Given that there is only the *trans* isomer in the ground state, the dependence of the steady-state optical spectra on excitation and emission wavelength and the biexponential (or nonexponential) fluorescence decay is most reasonably explained by the existence of rotational isomers (rotamers) in the ground state that have different optical spectra and different rates of isomerization from the *trans* to *cis* isomer in the excited state. It is common for rotamers to display different absorption and emission properties owing to their slightly different energies, which arise from quasi-planner structures resulting from the interplay between the resonance stabilization of delocalized π-electron system and steric repulsion.[25] Unfortunately, the NMR spectra provided no evidence for such rotamers existing on the time scale of the NMR measurement. Thus, it must be concluded that if such rotamers exist, they interconvert rapidly on the NMR time scale. The rotational isomers most likely to be involved would arise from rotations about the C5-C6 or C7-C1″ bonds.

Origin of the Excitation Wavelength-Dependence and Nonexponential Decay. Cyclocurcumin bears a substituted ethylene, and the excited-state isomerization about the C6-C7 double bond of *trans*-cyclocurcumin can generate the *cis*-isomer, which is likely to have a different emission spectrum than that of the *trans*-isomer. (The *cis*- and *trans*-isomers of an analogous system, stilbene, have different absorption and emission spectra.[26-28]) NMR experiments show that cyclocurcumin is only in the *trans* form in the ground state. This indicates that the anomalous fluorescence is not a result of the presence of a mixture of *cis* and *trans* isomers in the ground state. The anomalous fluorescence properties of cyclocurcumin may, however, be rationalized by can be the presence of rotational isomers (rotamers) having slightly different absorption and emission properties. Solvents may affect the ground-state equilibrium of isomers by preferentially stabilizing selective conformations.[29-32] Internal rotation may substantially change the dipole moment of a molecule, and a change in solvent polarity may modify the relative stability of the isomers. Previous studies of 2-styrylquinoline demonstrated how solvents affect the equilibrium between two ground-state conformers.[32] Two conformers were found in aprotic solvents whereas only one conformer was found in protic solvents. Selective hydrogen bonding of alcohols to the nitrogen atom in the quinoline group was suggested to stabilize the so-called s-*trans* conformer. This phenomenon may be relevant for understanding cyclocurcumin: since no wavelength dependence on the emission and excitation spectra of cyclocurcumin in alcohols was observed, it is possible that either the spectral properties of the rotamers of cyclocurcumin are similar or that one of these rotamers is predominantly stabilized in alcohols.

The nonexponential decay of cyclocurcumin in all the solvents is consistent with the presence of rotational isomers. The excitation of these rotamers leads to (at least) a biexoponential decay if the rate of interconversion between them is slower than the rates of excited-state decay—and if each isomer has a different fluorescence lifetime. The difference in the fluorescence decay times of the rotamers can be attributed to a difference in their nonradiative decay rates. One of the most efficient nonradiative decay channels from the excited state for the cyclcocurcumin could be *trans*-to-*cis* isomerization via formation of a twisted intermediate, whose well established precedent is given by *trans*-to-*cis* isomerization of stilbene.

The excited-state relaxation of the two (or more) rotamers of cyclocurcumin due to *trans*-to-*cis* isomerization would necessarily need to be different in order for this explanation to be valid. There is precedent for this. For example, the drastic difference in fluorescence lifetime ($\tau_1/\tau_2 \sim 6$) of the two rotamers of 2-styrylnaphthalenes was first explained by a difference in the photoisomerization rate, which was proven in a later investigation.[33-37] *Trans*-2,3′-naphthylpyridylethylene also exists in the ground-state as a mixture of two rotamers.[38] The radiative rate constants for these rotamers are similar, but fluorescence lifetime of one rotamer is ~3 times greater than the other. The much higher nonradiative rate for one of the rotamer was attributed to the *trans*→perp internal rotation. It has also been reported that all-*trans*-1,4-diphenyl-1,3-butadiene exists in two conformations and exhibits biexponential decays with excited-state lifetimes of 0.6 and 9 ns.[39]

Excited-state relaxation kinetics can also be affected by solvent polarity. The photoisomerization of stilbene has been extensively studied for many years.[40-53] For the excited-state isomerization of *trans*-stilbene in *n*-alcohols, there is an enhancement of the rate accompanied by diminution of the fluorescence quantum yield as the barrier is lowered by increasing the solvent polarity.[54] Cyclocurcumin shows the shortest average fluorescence lifetime of 75 ps, with two time constants of 55 and 140 ps, in methanol compared with nonpolar and polar aprotic solvents. The low average lifetime in methanol could be due to an enhanced rate of excited-state *trans*- to *cis*-isomerization owing to stabilization of twisted intermediate in the low-viscosity polar protic solvent.

The fluorescence lifetime of cyclocurcumin changes significantly with solvent viscosity. While cyclocurcumin has a short lifetime of ~75 ps in methanol (η = 0.544 cP), the lifetime increases when a more viscous alcohol is used (**Figure 6.4** and **Table 6.1)**. The average lifetime of cyclocurcumin in ethanol (η = 1.07 cP), ethylene glycol (η = 16.1 cP) and glycerol (η = 945 cP) are 130, 280 and 740 ps at room temperature, respectively. It is important to note that the time constants of two decay components (τ_1 and τ_2) also increase with increasing solvent viscosity and that the magnitude of the increase of the two time constants is different. In the case of stilbene, a comparison of the ratio of the lifetimes of *cis*- and *trans*- stilbene shows a weaker viscosity dependence for *cis*-stilbene than for *trans*-stilbene.[52] Using the values of the fluorescence quantum yield and the average lifetime, the radiative rate constant (k_r) and nonradiative rate constant (k_nr) can be determined (see **Table 6.1,** caption). For cyclocurcumin in alcohols, k_r is similar, but k_{nr} changes significantly. k_{nr} decreases from 13×10^{9} s^{-1} for cyclocurcumin in methanol to 1.2×10^{9} s^{-1} in glycerol. This decrease in k_{nr} clearly indicates that viscosity plays a role in reducing the nonradiative rate of cyclocurcumin, and this is most likely an effect of reducing the rate of isomerization in the excited state because large amplitude motion is required for isomerization. For instance, the barrier height of *trans*-stilbene increases from 3.5 kcal/mol in cyclohexane to 9.7 kcal/mol in glycerol.[55] This effect of viscosity on the isomerization barrier of *trans*-stilbene reduces its nonradiative rate: at 25°C, the lifetime of *trans*-stilbene is 60 ps in cyclohexane.[55] Upon incorporation in a rigid environment, the lifetime increases to 1.7 ns.[55] Similarly, for cyclocurcumin, the activation barrier is expected to be high when the viscosity of the medium is large.

***Kinetics and Thermodynamics of Photo-Induced Isomerization*.** An excited-state relaxation process that involves photoinduced torsional motion about chemical bonds is manifested by a viscosity-dependent nonradiative rate constant, k_{nr}.[56-68] An increase in the lifetime and ϕ_f of cyclocurcumin in alcohols with increasing viscosity led us to study the temperature dependence in a viscous solvent, glycerol. Fluorescence lifetime measurements were performed at five different temperatures from 3 to 80 °C (**Table 6.2)**. All the fluorescence decays are well fitted to a biexponential function, whose origin can be explained by assuming an equilibrium between rotamers in the ground state, as we have discussed above.

Table 6.2. Temperature dependent fluorescence decay components of cyclocurcumin in glycerol

Temperature (^oC)	a_1	τ_1 (ps)	a_2	τ_2 (ps)	$<\tau>$ (ps)	a_1/a_2
3	0.28	250	0.72	1600	1200	0.39
20	0.34	200	0.66	1000	740	0.52
40	0.45	150	0.55	600	390	0.82
60	0.55	100	0.45	300	190	1.2
80	0.69	70	0.31	200	110	2.2

At 3^oC, the preexponential factors, a_1 and a_2, obtained from fitting the fluorescence decay of cyclocurcumin in glycerol are 0.28 and 0.72. The corresponding time constants, τ_1 and τ_2, are 250 ps and 1600 ps, respectively. The equilibrium constant (K_{eq}) between these two isomers can thus be estimated as the ratio of pre-exponential factors, i.e., a_1/a_2. Temperature dependent measurements can therefore be used to determine the standard enthalpy (ΔH^o), entropy (ΔS^o), and Gibbs free energy (ΔG^o) for inteconversion between the rotamers by applying the van't Hoff equation. A plot of $\ln K_{eq}$ against 1/T yields a straight line (**Figure 6.6)**, indicating that the enthalpy of the reaction is constant over the temperature range of interest. The ΔH^o and ΔS^o from the slope and intercept are 4.3 kcal/mol and 13.3 cal/mol/K, respectively. The ΔG^o at 25^oC is 0.34 kcal/mol obtained from ΔH^o and ΔS^o using $\Delta G^O = \Delta H^O - T\Delta S^O$. It is important to note that the a_1/a_2 ratios increases with increasing temperature indicating that there is a ground-state equilibrium between two rotamers in alcohols even though they do not show excitation wavelength dependence fluorescence or excitation spectra.

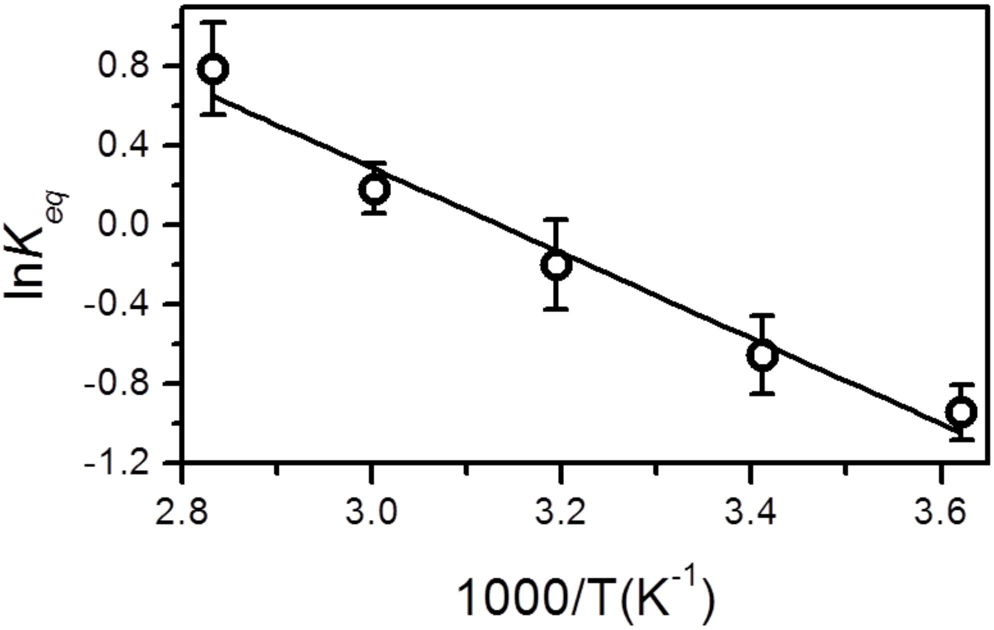

Figure 6.6. Plot of lnK_{eq} vs. 1/T for cyclocurcumin in glycerol. The data were fit to $\ln K_{eq} = -\Delta H^O / RT + \Delta S^O / T$, yielding $\Delta H^o = 4.3$ kcal/mol.

The radiationless decay rate owes part of its temperature dependence to changes in viscosity. The significant increase in τ_1 from 70 ps to 250 ps and in τ_2 from 110 ps to 1600 ps respectively were observed when viscosity is changed by varying the temperature from 80^o C to 3^o C. The activation energy for excited-state isomerization, E_a, can be obtained from the Arrhenius equation, $k_{nr} = A_{nr} \exp(-E_a / RT)$, where A_{nr} and T are the frequency factor and the absolute temperature, respectively. We assume that k_r is independent of temperature and compute k_{nr} for the two fluorescence lifetime components, τ_1 and $\tau_{2,}$ at different temperatures. As noted earlier, τ_1 and τ_2 are assigned to the excited state lifetimes two rotational isomers of curcumin. The Arrhenius plot (lnk_{nr} vs. 1/T) for cyclocurmin in glycerol obtained from τ_1 and τ_2

are displayed in **Figure 6.7a**. The activation energy, E_a, and the frequency factor, A_{nr}, are 3.3 kcal/mol and 1.5×10^{12} s^{-1} for one isomer and 5.4 kcal/mol and 10.6×10^{12} s^{-1} for the other.

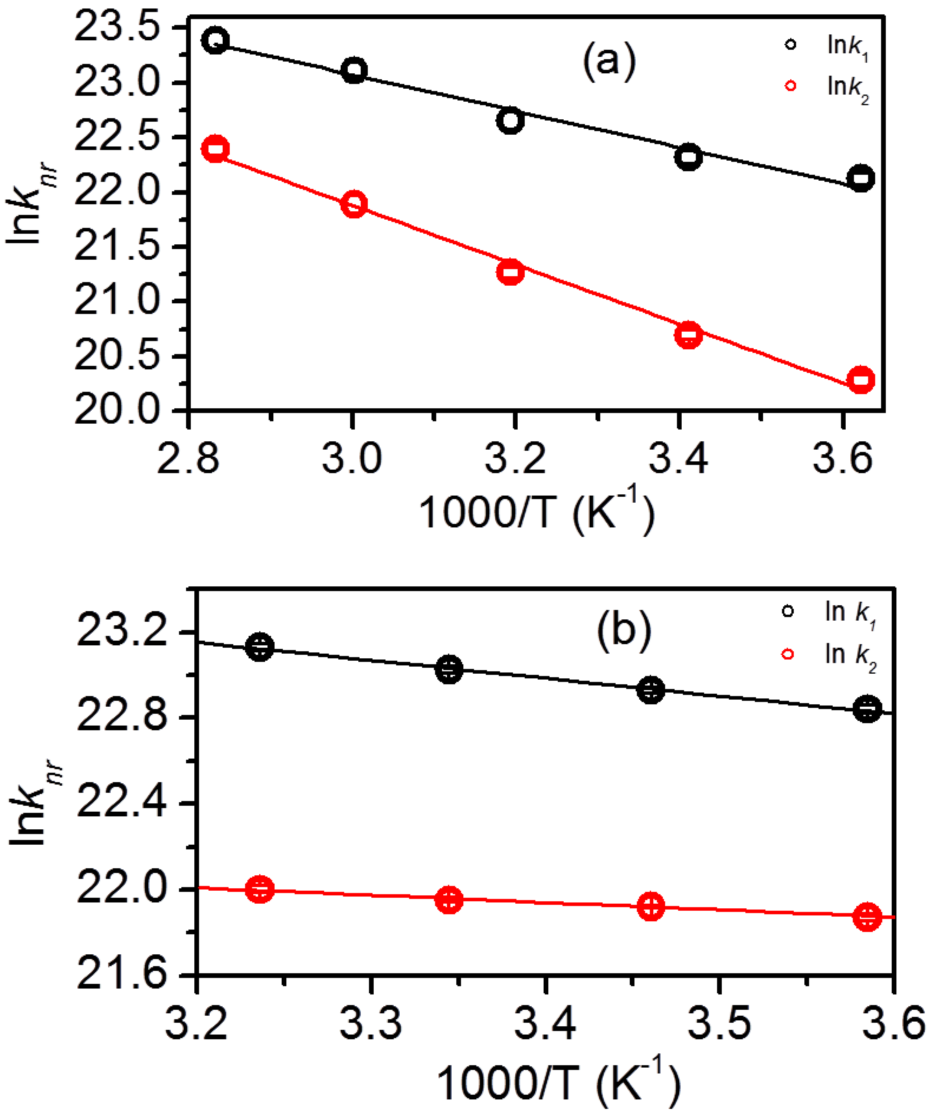

Figure 6.7. (a) Plot of ln(k_{nr}) vs. 1/T for cyclocurcumin from τ_1 and τ_2 in glycerol. The activation energy, E_a, and the frequency factor, A, are 3.3 kcal/mol and 1.5×10^{12} s^{-1} for τ_1 and 5.4 kcal/mol and 10.6×10^{12} s^{-1} for τ_2, respectively. (b) Plot of ln(k_{nr}) vs. 1/T from isoviscous experiment in a series of homologous alcohols. The activation energies are 1.65 and 0.68 kcal/mol for τ_1 and τ_2, respectively.

Since the solvent viscosity is dependent on temperature, the activation energy calculated in one solvent is not likely to yield the true internal barrier. In order to separate the effect of viscosity, an isoviscous (at 5 cP) experiment was performed using linear alcohols at different temperatures. The fluorescence decay parameters at 5 cP are given in **Table 6.3**. The activation energies (**Figure 6b**) are 1.65 kcal/mol and 0.68 kcal mol for τ_1 and $\tau_{2,}$ respectively. This indicates that the intrinsic barriers are lower than those evaluated from the temperature dependent experiment in glycerol.

Table 6.3. Fluorescence decay parameters of cyclocurcumin in a homologous series of alcohols at isoviscous (5 cP) temperature

Solvent	Temperature (°C)	a_1	τ_1 (ps)	a_2	τ_2 (ps)
1-Butanol	6	0.60	120	0.40	320
1-Pentanol	16	0.72	110	0.28	300
1-Hexanol	26	0.83	100	0.17	290
1-Heptanol	36	0.90	90	0.10	280

Conclusions

The spectral and photophysical properties of cyclocurcumin in various solvents are studied for the first time using steady-state and time-resolved spectroscopy. Steady-state absorption and fluorescence measurements illustrate that the spectral properties of cyclocurcumin are sensitive to the surrounding environment. The excitation wavelength dependent fluorescence studies indicate that in low-viscosity polar aprotic solvents there is ground-state heterogeneity due to the presence of rotational isomers of cyclocurcumin. The nonexopential fluorescence decay also supports the existence of ground-state rotamers having different relaxation rates. Temperature dependence of the ground state equilibrium constant obtained from pre-exponential factors provides the standard enthalpy and entropy change of 4.3 kcal/mol and 13.3 cal/mol/K, respectively for their interconversion in glycerol. Excited-state activation energies of these rotamers are 3.3 and 5.4 kcal/mol in glycerol, respectively. The true internal barriers for *trans*-to-*cis* excited-state isomerization for these rotamers are estimated from an isoviscosity plot and is determined to be 1.65 and 0.68 kcal/mol.

Acknowledgements. We thank Debabrata Mukherjee for performing and providing help in the analysis of 400 MHz NMR measurements, Dr. Kamel Harrata for performing the mass spectrometry measurements, Dr. Bruce Fulton (Department of Biochemistry, Biophysics, and Molecular Biology, Iowa State University) for performing and providing helpful suggestions in regards to the 700 MHz NMR measurements, and David Huang (University of Adelaide) for his suggestions on computational methods.

Supporting Materials. Mass, NMR, gas-phase calculation, excitation spectra, and fluorescence decays of cyclcurcumin. This material is available free of charge via the Internet at http://pubs.acs.org.

References

(1) Goel, A.; Kunnumakkara, A. B.; Aggarwal, B. B. *Biochem. Pharmacol.* **2008**, *75*, 787.

(2) Anand, P.; Thomas, S. G.; Kunnumakkara, A. B.; Sundaram, C.; Harikumar, K. B.; Sung, B.; Tharakan, S. T.; Misra, K.; Priyadarsini, I. K.; Rajasekharan, K. N.; Aggarwal, B. B. *Biochem. Pharmacol.* **2008**, *76*, 1590.

(3) Kiuchi, F.; Goto, Y.; Sugimoto, N.; Akao, N.; Kondo, K.; Tsuda, Y. *Chem. Pharm. Bull.* **1993**, *41*, 1640.

(4) Simon, A.; Allais, D. P.; Duroux, J. L.; Basly, J. P.; Durand-Fontanier, S.; Delage, C. *Cancer Lett.* **1998**, *129*, 111.

(5) Ruby, A. J.; Kuttan, G.; Babu, K. D.; Rajasekharan, K. N.; Kuttan, R. *Cancer Lett.* **1995**, *94*, 79.

(6) Lantz, R. C.; Chen, G. J.; Solyom, A. M.; Jolad, S. D.; Timmermann, B. N. *Phytomedicine* **2005**, *12*, 445.

(7) Aggarwal, B. B.; Kumar, A.; Bharti, A. C. *Anticancer Res.* **2003**, *23*, 363.

(8) Shi, M.; Cai, Q.; Yao, L.; Mao, Y.; Ming, Y.; Ouyang, G. *Cell Biol. Int.* **2006**, *30*, 221.

(9) Surh, Y.-J. *Food Chem. Toxicol.* **2002**, *40*, 1091.

(10) Yang, F.; Lim, G. P.; Begum, A. N.; Ubeda, O. J.; Simmons, M. R.; Ambegaokar, S. S.; Chen, P. P.; Kayed, R.; Glabe, C. G.; Frautschy, S. A.; Cole, G. M. *J. Biol. Chem.* **2005**, *280*, 5892.

(11) Masuda, M.; Suzuki, N.; Taniguchi, S.; Oikawa, T.; Nonaka, T.; Iwatsubo, T.; Hisanaga, S.-i.; Goedert, M.; Hasegawa, M. *Biochemistry* **2006**, *45*, 6085.

(12) Dahl, T. A.; Bilski, P.; Reszka, K. J.; Chignell, C. F. *Photochem. Photobiol.* **1994**, *59*, 290.

(13) Dahl, T. A.; McGowan, W. M.; Shand, M. A.; Srinivasan, V. S. *Arch. Microbiol.* **1989**, *151*, 183.

(14) Adhikary, R.; Mukherjee, P.; Kee, T. W.; Petrich, J. W. *J. Phys. Chem. B* **2009**, *113*, 5255.

(15) Adhikary, R.; Carlson, P. J.; Kee, T. W.; Petrich, J. W. *J. Phys. Chem. B* **2010**, *114*, 2997.

(16) Kee, T. W.; Adhikary, R.; Carlson, P. J.; Mukherjee, P.; Petrich, J. W. *Aust. J. Chem.* **2011**, *64*, 23.

(17) Guilford, J.; William, R. J.; Chol, Y. C.; William, R. B. *J. Phys. Chem.* **1985**, *89*, 294.

(18) Chignell, C. F.; Bilski, P.; Reszka, K. J.; Motten, A. G.; Sik, R. H.; Dahl, T. A. *Photochem. Photobiol.* **1994**, *59*, 295.

(19) Khopde, S. M.; Priyadarsini, K. I.; Palit, D. K.; Mukherjee, T. *Photochem. Photobiol.* **2000**, *72*, 625.

(20) Nardo, L.; Paderno, R.; Andreoni, A.; Masson, M.; Haukvik, T.; Toennesen, H. H. *Spectroscopy* **2008**, *22*, 187.

(21) Nardo, L.; Andreoni, A.; Bondani, M.; Masson, M.; Hjorth Tonnesen, H. *J. Photochem. Photobiol. B* **2009**, *97*, 77.

(22) Priyadarsini, K. I. *J. Photochem. Photobiol. C* **2009**, *10*, 81.

(23) Williams, H. D.; Fleming, I. *Spectroscopic Methods in Organic Chemistry*, 4th ed. revised ed.; McGraw-Hill Book Company (UK) Limited, 1989.

(24) Allen, M. T.; Whitten, D. G. *Chem. Rev.* **1989**, *89*, 1691.

(25) Mazzucato, U.; Momicchioli, F. *Chem. Rev.* **1991**, *91*, 1679.

(26) Saltiel, J.; Sun, Y. P. *Photochromism: Molecules and Systems*; Elsevier: Amsterdam, 1990.

(27) Saltiela, J.; Wallera, A. S.; Sears, D. F. J. *J. Photochem. and Photobiol. A* **1992**, *65*, 29.

(28) Fischer, G.; Seger, G.; Muszkat, K. A.; Fischer, E. *J. Chem. Soc., Perkin Trans. 2* **1975**, 1569.

(29) Marconi, G.; Orlandi, G.; Poggi, G. *J. Photochem.* **1982**, *19*, 329.

(30) Galiazzo, G.; Gennari, G.; Bortolus, P. *J. Photochem.* **1983**, *23*, 149.

(31) Galiazzo, G.; Gennari, G.; Bortolus, P. *J. Photochem.* **1986**, *35*, 177.

(32) Shim, S. C.; Kim, D. W.; Kim, M. S. *J. Photochem. Photobiol. A* **1991**, *56*, 227.

(33) Haas, E.; Fischer, G.; Fischer, E. *J. Phys. Chem.* **1978**, *82*, 1638.

(34) Ghiggino, K. P. *J. Photochem.* **1980**, *12*, 173.

(35) Matthews, A. C.; Sakurovs, R.; Ghiggino, K. P. *J. Photochem.* **1982**, *19*, 235.

(36) Bartocci, G.; Masetti, F.; Mazzucato, U.; Marconi, G. *J. Chem. Soc., Faraday Trans. 2* **1984**, *80*, 1093.

(37) Bartocci, G.; Mazzucato, U.; Masetti, F.; Aloisi, G. G. *Chem. Phys.* **1986**, *101*, 461.

(38) Bartocci, G.; Masetti, F.; Mazzucato, U.; Spalletti, A.; Cristina, M. B. *J. Chem. Soc., Faraday Trans. 2* **1986**, *82*, 775.

(39) Møller, S.; Yee, W. A.; Goldbeck, R. A.; Wallace-Williams, S. E.; Lewis, J. W.; Kliger, D. S. *Chem. Phys. Lett.* **1995**, *243*, 579.

(40) Saltiel, J.; D'Agostino, J.; Megarity, E. D.; Metts, L.; Neuberger, K. R.; Wrighton, M.; Zafiriou, O. C. *Org. Photochem.* **1973**, *3*, 1.

(41) Greene, B. I.; Hochstrasser, R. M.; Weisman, R. B. *J. Chem. Phys.* **1979**, *71*, 544.

(42) Greene, B. I.; Hochstrasser, R. M.; Weisman, R. B. *Chem. Phys.* **1980**, *48*, 289.

(43) Greene, B. I.; Hochstrasser, R. M.; Weisman, R. B. *Chem. Phys. Lett.* **1979**, *62*, 427.

(44) Doany, F. E.; Greene, B. I.; Hochstrasser, R. M. *Chem. Phys. Lett.* **1980**, *75*, 206.

(45) Doany, F. E.; Greene, B. I.; Liang, Y.; Negus, D. K.; Hochstrasser, R. M. *Springer Ser. Chem. Phys.* **1980**, *14*, 259.

(46) Hochstrasser, R. M. *Pure Appl. Chem.* **1980**, *52*, 2683.

(47) Courtney, S. H.; Fleming, G. R. *J. Chem. Phys.* **1985**, *83*, 215.

(48) Kim, S. K.; Fleming, G. R. *J. Phys. Chem.* **1988**, *92*, 2168.

(49) Courtney, S. H.; Balk, M. W.; Philips, L. A.; Webb, S. P.; Yang, D.; Levy, D. H.; Fleming, G. R. *J. Chem. Phys.* **1988**, *89*, 6697.

(50) Kim, S. K.; Courtney, S. H.; Fleming, G. R. *Chem. Phys. Lett.* **1989**, *159*, 543.

(51) Todd, D. C.; Fleming, G. R. *J. Chem. Phys.* **1993**, *98*, 269.

(52) Todd, D. C.; Jean, J. M.; Rosenthal, S. J.; Ruggiero, A. J.; Yang, D.; Fleming, G. R. *J. Chem. Phys.* **1990**, *93*, 8658.

(53) Todd, D. C.; Fleming, G. R.; Jean, J. M. *J. Chem. Phys.* **1992**, *97*, 8915.

(54) Sundström, V.; Gillbro, T. *Chem. Phys. Lett.* **1984**, *109*, 538.

(55) Saltiel, J.; D'Agostino, J. T. *J. Am. Chem. Soc.* **1972**, *94*, 6445.

(56) Fleming, G. R. *Chemical Applications of Ultrafast Spectroscopy*; Oxford University Press: London, 1986.

(57) Rothenberger, G.; Negus, D. K.; Hochstrasser, R. M. *J. Chem. Phys.* **1983**, *79*, 5360.

(58) Velsko, S. P.; Fleming, G. R. *J. Chem. Phys.* **1982**, *76*, 3553.

(59) Keery, K. M.; Fleming, G. R. *Chem. Phys. Lett.* **1982**, *93*, 322.

(60) Barbara, P. F.; Rand, S. D.; Rentzepis, P. M. *J. Am. Chem. Soc.* **1981**, *103*, 2156.

(61) Flom, S. R.; Nagarajan, V.; Barbara, P. F. *J. Phys. Chem.* **1986**, *90*, 2085.

(62) Brearley, A. M.; Flom, S. R.; Nagarajan, V.; Barbara, P. F. *J. Phys. Chem.* **1986**, *90*, 2092.

(63) Sundström, V.; Gillbro, T.; Bergstroem, H. *Chem. Phys.* **1982**, *73*, 439.

(64) Ben-Amotz, D.; Harris, C. B. *Chem. Phys. Lett.* **1985**, *119*, 305.

(65) Velsko, S. P.; Waldeck, D. H.; Fleming, G. R. *J. Chem. Phys.* **1983**, *78*, 249.

(66) Shank, C. V.; Ippen, E. P.; Teschke, O.; Eisenthal, K. B. *J. Chem. Phys.* **1977**, *67*, 5547.

(67) Tredwell, C. J.; Osborne, A. D. *J. Chem. Soc., Faraday Trans. 2* **1980**, *76*, 1627.

(68) Osborne, A. D. *J. Chem. Soc., Faraday Trans. 2* **1980**, *76*, 1638.

(69) Riddick, J. A.; Bunger, W. B. *Organic Solvents: Physical Properties and Methods of Purification.*, 3rd ed.; Wiley-Interscience: New York, 1970.

(70) Weast, R. C. In *CRC Handbook of Chemistry and Physics*; 53rd ed.; Weast, R. C., Ed.; CRC Press, The Chemical Rubber Co.: Cleaveland, Ohio, 1973.

CHAPTER 7: ENHANCED STABILITY AND ACTIVITY OF CELLULASE IN AN IONIC LIQUID AND THE EFFECT OF PRETREATMENT ON CELLULOSE HYDROLYSIS

A paper published in *Biotechnology and Bioengineering*

S. Bose[1], CA Barnes[2], and JW Petrich[1,2]*

Abstract

We discuss the hydrolysis of cellulose using a pure cellulase: endo-1,4-β-*D*-glucanase (EG) from the fungus, *Aspergillus niger,* in buffer, the pure ionic liquid (IL), tris-(2-hydroxyethyl)-methylammonium methylsulfate (HEMA), and various mixtures of the two at different temperatures. Steady–state fluorescence and absorbance studies were performed to monitor the stability and activity of EG using cellulose azure as the substrate. EG attains its highest activity at 45˚C in buffer and denatures at ~55˚C. On the other hand, HEMA imparts substantial stability to the enzyme, permitting the activity to peak at 75˚C. The relative roles of temperature, viscosity, pH, polarity, and the constituent ions of the ILs on the hydrolysis reaction are examined. It is demonstrated that pretreatment of cellulose with ILs such as BMIM Cl, MIM Cl, and HEMA results in more rapid conversion to glucose than hydrolysis with cellulose that is not pretreated. The percent conversion to glucose from pretreated cellulose is increased when the temperature is increased from 45 to 60°C. Two different ILs are used to increase the

---

Reprinted with permission from *Biotechnology and Bioengineering* 2012, 109 (2), 434-443. [1]U.S. Department of Energy Ames Laboratory, Iowa State University, Ames, Iowa 50011. [2]Department of Chemistry, Iowa State University, Ames, Iowa 50011.

efficiency of cellulose conversion to glucose. Cellulose is pretreated with BMIM Cl. Subsequent hydrolysis of the pretreated cellulose in 10–20% solutions of HEMA in buffer provides higher yields of glucose at 60°C. Finally, to our knowledge, this is the first study dealing with a pure endoglucanase from commercial *A. niger.* This enzyme not only shows higher tolerance to ILs, such as HEMA, but also has enhanced thermostability in the presence of the IL.

Introduction

Limited reserves of fossil fuels and global climate change have directed increasing attention to the use of renewable biomaterials for energy production. Ethanol produced by the fermentation of glucose is a promising fuel derived from biomass (Ragauskas et al. 2006). Its production, however, from edible agricultural feedstocks is problematic (Kumar et al. 2008). Research has thus focused on its production from cellulose, which is an abundant polymeric raw biomaterial. Consequently, during the past two decades, considerable effort has been devoted to the hydrolysis of cellulose for its ultimate conversion into fuel (Dadi et al. 2006; Ladisch et al. 1978; Lynd et al. 1991; Su et al. 2009; Xiang et al. 2003; Zhang and Lynd 2004; Zhao et al. 2007). There are, however, limitations to this process that are imposed mainly by the limited solubility of cellulose in water or other organic solvents. The common solvents used to dissolve cellulose may cause serious environmental problems (Reddy and Yang 2005; Swatloski et al. 2002; Wu et al. 2004).

These difficulties have been overcome by the introduction of room temperature ionic liquids (ILs), which have been reported to dissolve substantial amounts of cellulose. ILs are novel compounds that have great potential for replacing conventional, volatile, environmentally harmful organic solvents used in many catalytic and organic reactions (Adhikary et al. 2008; Bose et al. 2009). Rogers and coworkers (Fort et al. 2007; Remsing et al. 2006; Swatloski et al.

2002) have carried out comprehensive studies on cellulose dissolution and regeneration in ILs. They found that 1-butyl-3-methylimidazolium chloride (BMIM Cl) was the most effective in dissolving cellulose; and they attributed this effect to strong hydrogen bonding interactions of the hydroxyl groups of cellulose with the halide anions, consistent with the reports (Zhang et al. 2005) using 1-allyl-3-methylimidazolium chloride (AMIM Cl). It is reported (Doherty et al. 2010) that 1-butyl-3-methylimidazolium methylsulfate (BMIM $MeSO_4$) can dissolve lignin. The dissolution of cellulose and subsequent regeneration acts as a pretreatment step, which modifies the structure of complex cellulosic polymers (Hendriks and Zeeman 2009) making it more susceptible to enzyme hydrolysis.

Besides pretreating cellulose with ILs separately, studies have been done to explore the stability and activity of cellulolytic enzymes in ILs (Bose et al. 2010; Dadi et al. 2006; Lau et al. 2000; Park and Kazlauskas 2003; Sheldon et al. 2002; Turner et al. 2003). Enzymes have been reported to exhibit increased stability in certain ILs, as opposed to common organic solvents (Datta et al. 2010; Lozano et al. 2002; Wang et al. 2010). Furthermore, recycling and reusing enzymes in ILs (Feher et al. 2007; Itoh et al. 2001; Park and Kazlauskas 2001) is an additional advantage enabling continuous processing. The most thoroughly studied enzyme in ILs is *Candida antarctica* lipase B (Cal B), used to catalyze transesterification reactions (Lau et al. 2000; Lau et al. 2004; Park and Kazlauskas 2003; Sheldon et al. 2002). The presence of water is also found to be crucial for activity of enzymes; and thus there are also some reports of enzyme activity in mixtures of water and ILs, namely chloroperoxidase (CPO) from *C. fumago* was used to catalyze a sulfoxidation reaction in aqueous mixtures containing up to 70% of hydroxyethyltrimethylammonium ($HOEtMe_3N$) citrate IL. Recent reports (Datta et al. 2010) showed higher tolerance of purified endoglucanases from *T. maritima* and *P. horikoshii* towards 1-ethyl-3-methylimidazolium acetate (EMIM OAc), compared to that of the industrial benchmark, *Trichoderma viride* cellulase, in the same IL. A mixture of cellulases has been reported (Wang et al. 2010) to retain more than 60% of its activity after pre-incubating in 15–20% (w/v) EMIM OAc – buffer solutions at 50°C.

In this work, we discuss new studies made with a *pure* cellulase component, endo-1,4-β-*D*-glucanase (EG) from the fungus, *Aspergillus niger*, in buffer, in neat HEMA, and in various mixtures at different temperatures. Towards the goal of greener conversion of cellulose to glucose in IL media we have discussed two topics: the stability of cellulase in IL; and effects of pretreatment of cellulose with IL on subsequent hydrolysis kinetics to obtain glucose.

Experimental Section

Materials. A pure cellulase component, endo-1,4-β-*D*-glucanase (EG) (EC 3.2.1.4), from the fungus, *A. niger*, was purchased from Megazyme, Ireland. It was reported to show a single band on SDS PAGE, and was used without further purification. *A. niger* cellobiase (Novozyme 188) was purchased from Sigma. Citric acid monohydrate, also purchased from Sigma, was processed for use as 0.05 M citrate buffer, pH 4.8, adjusted with 1-M NaOH. Cellulose azure, used for enzyme activity studies, and Reichardt's dye and 4-nitroaniline (NA), for polarity measurements, were purchased from Sigma Aldrich. *N,N*-Diethyl-4-nitroaniline (DENA) was purchased from Frinton laboratories. The ILs (**Figure 7.1)** used in this study were obtained from Sigma Aldrich: HEMA, BMIM Cl and BMIM $MeSO_4$. The MIM Cl was synthesized as described elsewhere (Chowdhury et al. 2004). The sodium salt of methylsulfate (Sigma) was used as received. The hexokinase glucose assay was purchased from Sigma and dissolved in 50 mL of nanopure water.

Stability and Activity Measurements. The enzymes were equilibrated in pH 4.8 citrate buffer prior to any experiments. These aqueous enzymes were quantitatively added and were equilibrated for 15 minutes in the desired solvent systems before addition of the substrate. Cellulose azure is used as a substrate which upon hydrolysis releases the dye and its absorbance reports on the activity of the enzyme. Cellulose solubility and Kamlet–Taft solvent polarity measurements are described in details in the supplemental information.

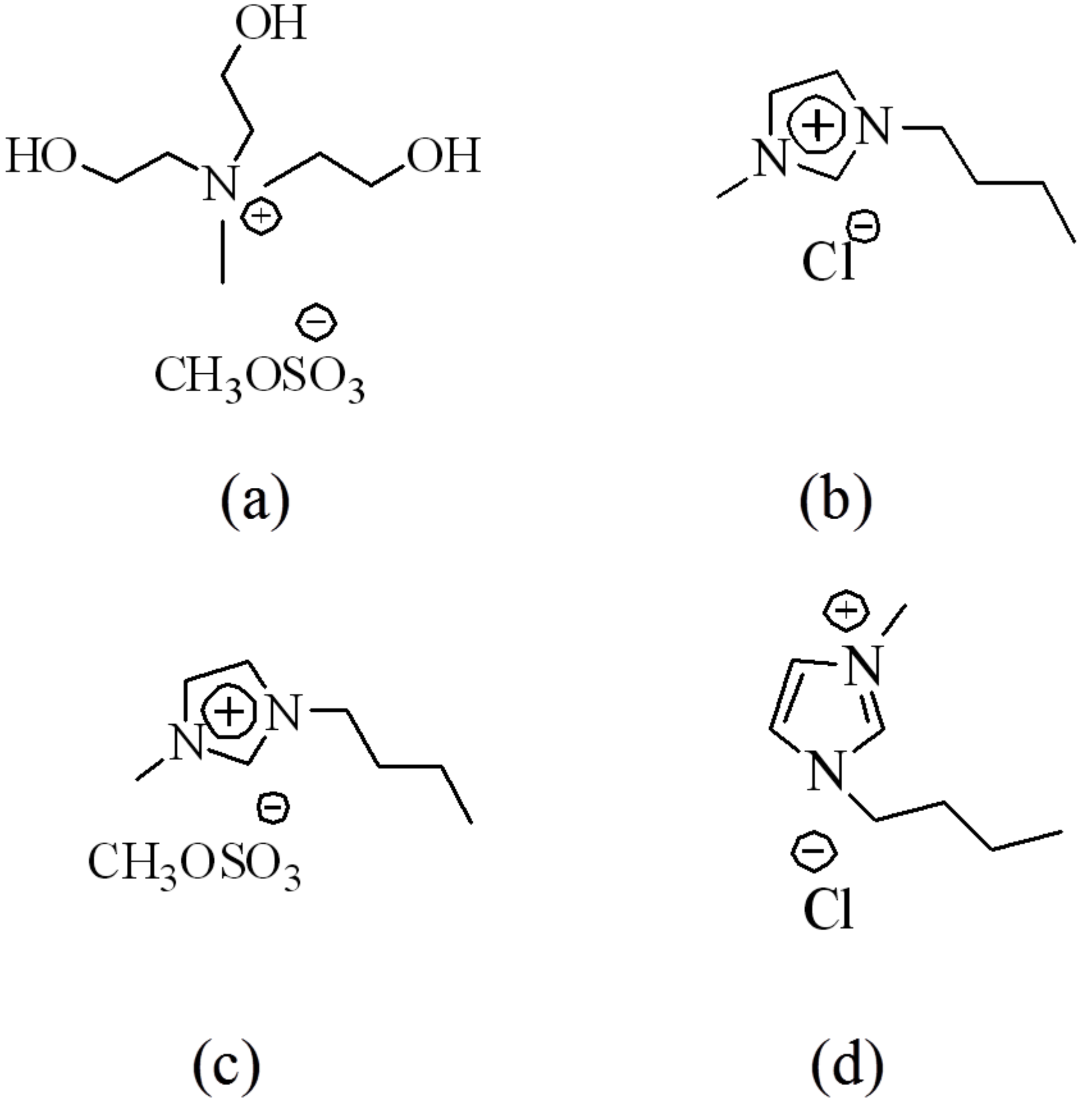

Figure 7.1. Structure of the ionic liquids studied: (a) tris-(2-hydroxyethyl)-methylammonium methylsulfate (HEMA), (b) 1-butyl-3-methylimidazolium chloride (BMIM Cl), (c) 1-butyl-3-methylimidazolium methylsulfate (BMIM $MeSO_4$) and (d) 1-methylimidazolium chloride (MIM Cl).

Differential Scanning Calorimetry Measurements. Differential heat flow curves were measured using a Q 10 Differential Scanning Calorimeter (TA Instruments.), attached to a liquid nitrogen cooling system (LNCS). The sample pans were loaded with 1 mg of dry native and IL-pretreated cellulose, while the reference pans are kept empty under nitrogen atmosphere. All the samples were scanned from 0 to 500^{o}C at 10^{o}C/minute.

Results and Discussions

Steady-state fluorescence from endo-1,4-β-*D*-glucanase (EG) obtained from *A. niger* was monitored in pH 4.8 citrate buffer and HEMA as a function of temperature from 20°C to 105°C. EG in HEMA had a higher fluorescence quantum yield at all temperatures compared to that in buffer. Quenching of fluorescence from tryptophan residues in EG was observed in both solvents. Significant fluorescence quenching at 50°C, accompanied by precipitation of the enzyme in buffer, indicated its denaturation. Such quenching did not occur until 75°C in HEMA, indicating that the IL imparts a higher thermal stability to EG. Precipitation of EG was not observed in HEMA, which speaks to the ability of the IL to solubilize the denatured protein. (It is important to note, as we have discussed in detail, (Bose et al. 2010) that *in itself*, fluorescence quenching is not necessarily a signature of denaturation. It is possible that there are nonradiative processes between the aromatic amino acid residues of the enzyme and the solvent that quench the fluorescence without perturbing the protein's structure or function.)

The fluorescence emission maximum of EG was monitored in buffer and HEMA (**Figure 7.2a**). At room temperature, it is 326 nm in buffer and 324 nm in HEMA. In buffer, the emission maximum undergoes a large red-shift (326 to 339 nm) at ~ 55°C; whereas a corresponding red shift (324 to 336 nm) is not observed until ~75°C in HEMA. This again indicates the higher thermal stability of EG in HEMA.

Reversibility of the unfolding process of the enzyme was studied in HEMA by gradual cooling, starting from different elevated temperatures as indicated by the arrows in **Figure 7.2b**. On cooling, a gradual blue-shift of the emission maxima was observed. The extent of the blue shift (i.e., the extent of the return to native conditions) depended on the starting temperature. Cooling from 95 and 105°C resulted in blue shifts from 336 to 333 nm, indicating irreversible denaturation of the protein, since the native conformation of the enzyme corresponds to λ_{max} = 324 nm in HEMA. Partially folded structures of the enzyme, with λ_{max} ~326 nm, were attained when cooled from 75–85 °C. The unfolding of EG started when the temperature was increased beyond 65°C. Although the fluorescence peak shifted slightly by ~2 nm at 65°C compared to that in room temperature, the enzyme was still active, as discussed later. The slight peak–shift might be due to small perturbations of the native conformation of the enzyme, which do not significantly affect its activity. In order to assess the stability of EG at different concentrations of HEMA in buffer, the emission maxima of tryptophan was monitored as shown in **Figure 7.2c**. There was no drastic shift of the fluorescence peak maxima at all concentrations of HEMA, indicating that EG does not denature, unlike what was observed in the temperature dependent study (discussed above). We also attempted to characterize the stability of EG in ILs using circular dichroism (CD) spectroscopy. The high absorbance of the ILs in the UV, however, completely masked the CD signals for the secondary and tertiary structures of the enzyme in the near and far UV regions. This prevented us from evaluating the structural features of EG in the ILs, which is consistent with earlier reports (Constatinescu et al. 2010; Wei and Danielson 2011).

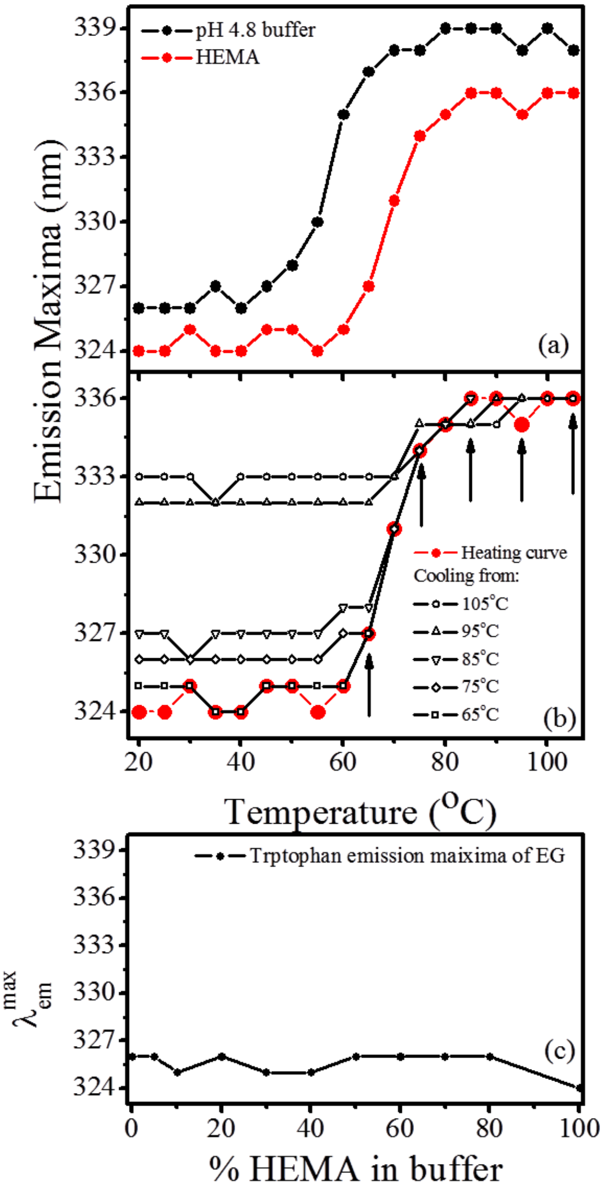

Figure 7.2. (a) Shift in the maximum of tryptophan fluorescence (λ_{ex}=295nm) from *A. niger* endoglucanase (EG) with temperature in pure pH 4.8 citrate buffer and HEMA. The red shift is associated with the unfolding of the enzyme. The transition temperature of EG in HEMA is higher than that in buffer, indicating greater thermal stability of the enzyme in the ionic liquid. (b) Cooling of the enzyme in HEMA, starting from temperatures 105, 95, 85, 75 and 65˚C (indicated by arrows), produces different blue shifts. The unfolding of EG was completely reversible up to 65˚C, whereas partial reversibility was observed at temperatures greater than 75˚C. (c) Trend of shift of tryptophyl emission maxima of EG with increasing concentrations of HEMA in buffer, at 25˚C. No significant shift of the peak maxima was observed indicating that EG retained its native structure. The EG concentration was maintained at $5x10^{-7}$ M. All cellulase samples were excited at 295 nm.

EG activity was studied at four different temperatures (45, 55, 65, and 75°C) different mixtures of HEMA and pH 4.8 citrate buffer, namely, 0, 10, 50, and 100% HEMA (more accurately 99%, since 1% water was introduced through addition of aqueous enzyme). The percent of maximum activity of EG in pure pH 4.8 buffer and in HEMA after 2 hours is shown in **Figure 7.3a**. In buffer, the activity peaked at 45°C, drastically dropped to 10% at 75°C, and finally decayed to zero at 85°C. On the other hand in HEMA, the activity was maximal at 75°C, and then dropped to 75% of this value at 85°C. The initial lower activity at low temperatures in HEMA is likely due to its high viscosity of 1460 cP at 20^{o}C (see below). **Figure 7.3b** presents a column graph of the relative activity of EG within 2 hours in different mixtures of buffer and HEMA at different temperatures, compared to that in pure buffer. The absorbance profiles as monitored with time are presented in the **Figure SI.2-3** in the supplemental information. The relative activity of EG in 10−50% HEMA—water mixture increased with temperature. Apart from studies at 45^{o}C, we observed equal or higher activity with addition of HEMA in water. To understand the effect of ILs on enzyme stability and its resulting activity, several factors need attention, such as the viscosity, pH, polarity of the ILs, and the effects of the individual ions and their concentrations constituting the IL. We discuss these factors explicitly below.

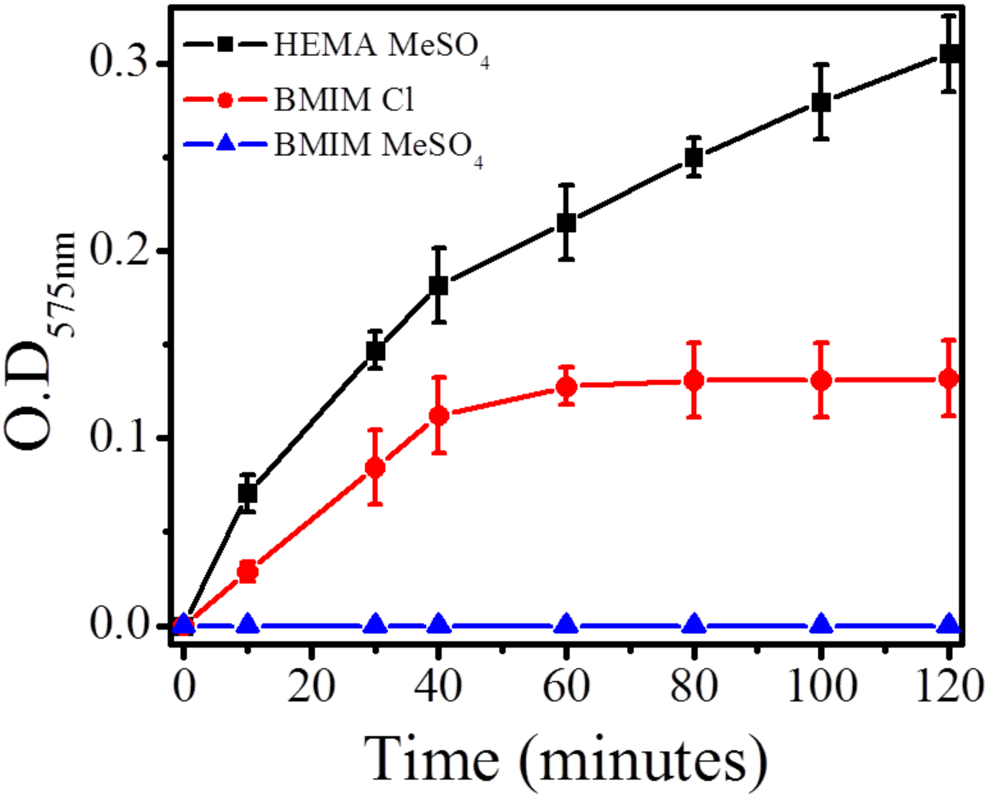

Figure 7.3. (a) The variation of the relative percent activity of endoglucanase (EG) in pH 4.8 citrate buffer (black) and HEMA (red) as a function of temperature (25 - 85°C) measured after 2 hours using cellulose azure as the enzyme assay. The activity of EG peaked (arbitrarily taken as 100% activity) at 45°C in buffer whereas in HEMA, the relative activity peaked at 75°C. (b) EG activity at 45, 55, 65°C (after 2 hours) and 75°C (after 3 hours) in different aqueous mixtures of HEMA. Relative activity was calculated with respect to the activity in citrate buffer (pH 4.8), where the activity of the latter is normalized to one, shown by a dashed line. The presence of HEMA enhances the EG activity, overcoming the viscosity barrier. EG concentration maintained at 4.76×10^{-6} M. EG-activity was monitored via the absorbance of the liberated dye from cellulose azure (1.5 mg/mL) at 572 nm. The absorbance values plotted here are the average of three measurements.

Effect of Solvent Viscosity

The kinetics of enzyme activity are strongly dependent on the viscosity of the medium (Bose et al. 2010; Hay et al. 2008). A higher viscosity obviously slows down the rate of diffusion of the enzyme to the substrate, resulting in a lower observed activity. In order to gain insight into the effect of viscosity on enzyme kinetics, viscosities of all the solvent systems were measured at different temperatures. The viscosity of pure HEMA is much higher than those of pure buffer and the binary mixtures at all temperatures. At 45°C, the activity of EG decreased upon addition of HEMA (**Figure 7.3b**), and this can be attributed to the increasing viscosity of the binary mixtures. It is significant that we did not observe this trend of decreasing activity with viscosity at the higher temperatures of 55, 65 and 75°C, where the EG-activity was either equal to, or higher than, that observed in pure buffer. This is owing to the stability that HEMA imparts to EG, which results in its higher activity, overcoming the effect of viscosity. Thus the resultant activity shown by EG is governed by both factors: the stability of the enzyme in the solvent and the inherent viscosity of the solvent. *It should be noted that lower activity should not be understood solely in terms of enzyme deactivation*, because viscosity itself can slow down the kinetics and quench the end-product formation. As we have substantial evidence of higher stability of EG in HEMA, the lesser activity can be attributed to the higher viscosity.

Effect of Ions

The stability and activity of enzymes are also governed by the effect of individual ions in ILs (Zhao 2005; Zhao 2010). Unlike organic solvents, ILs have exceptionally strong interactions with water molecules because they are comprised of ions, which, depending on their size and charge density, stabilize or destabilize the water structure around the enzyme (Cantone et al. 2007; Zhao 2006). This, in turn, influences the stability of the enzymes (Ru et al. 2000). But these effects vary from one enzyme to another. For example, whereas methylsulfate ($MeSO_4^-$) anion in HEMA imparted extreme stability to cellulase (Bose et al. 2010), it proved to be detrimental for other enzymes, such as penicillin G amidase (Cantone et al. 2007), Cal B (Lau et al. 2004), and β-galactosidase (Kaftzik et al. 2002).

In order to assess the increased stability of EG in HEMA, we studied its activity in two other ILs, BMIM Cl and BMIM $MeSO_4$ (**Figure 7.4)**. In our previous study, we observed that the activity of cellulase was comparable in HEMA and MIM Cl, whereas in our current study we found that the activity of EG in HEMA was significantly higher than that in BMIM Cl, which contains similar ions as MIM Cl. It is noteworthy here that unlike in HEMA, the activity of EG in BMIM Cl almost ceases within one hour from the start of the hydrolysis reaction of cellulose azure, which is indicated by the plateau in the absorbance curve in **Figure 7.4**. The plateau observed is not due to end product accumulation or exhaustion of substrate in the reaction medium, since visibly detectable amounts of unreacted solid cellulose azure remained in the reaction vessel. This is consistent with the reports of (Turner et al. 2003) who observed that high chloride concentration in BMIM Cl may interfere with the internal hydrogen bonding network of the enzyme and consequently cause denaturation. Comparison of the activity of EG in HEMA and BMIM $MeSO_4$ (which shares a common anion), gives the surprising result that complete loss of activity was observed in BMIM $MeSO_4$. The enzyme precipitated immediately on addition to BMIM $MeSO_4$. This observation of no activity towards cellulose azure is not a viscosity effect (since $\eta_{bmimMeSO_4} << \eta_{HEMA}$) but rather due to denaturation of the enzyme. This is in agreement with earlier reports on loss of appreciable activity of different enzymes in imidazolium alkylsulfates (Cantone et al. 2007; Kaftzik et al. 2004; Kaftzik et al. 2002; Lau et al. 2004). Thus comparison of the activity in HEMA and BMIM $MeSO_4$ (having equimolar $MeSO_4^-$ ions in the bulk ILs) indicates that the imidazolium moiety might also have a destabilizing effect on EG and in turn diminish its activity. This has been deduced as follows: 1) EG is more active in neat HEMA than in neat BMIM Cl; 2) EG has no activity in BMIM $MeSO_4$; 3) Both neat HEMA and neat BMIM $MeSO_4$ are 4.8 M in $MeSO_4$, yet EG is very active in HEMA and nonactive in BMIM $MeSO_4$; 4) Consequently, we conclude that the major factor contributing to the difference in the activities between HEMA and BMIM $MeSO_4$ arises from the cations of the two ILs. It is noteworthy that tetrakis-(2-hydroxyethyl)ammonium triflouromethanesulfonate, which has a similar cation as HEMA, was shown to improve the activity of *horseradish peroxidase* (HRP) (Das et al. 2007) compared to the conventional imidazolium ionic liquids.

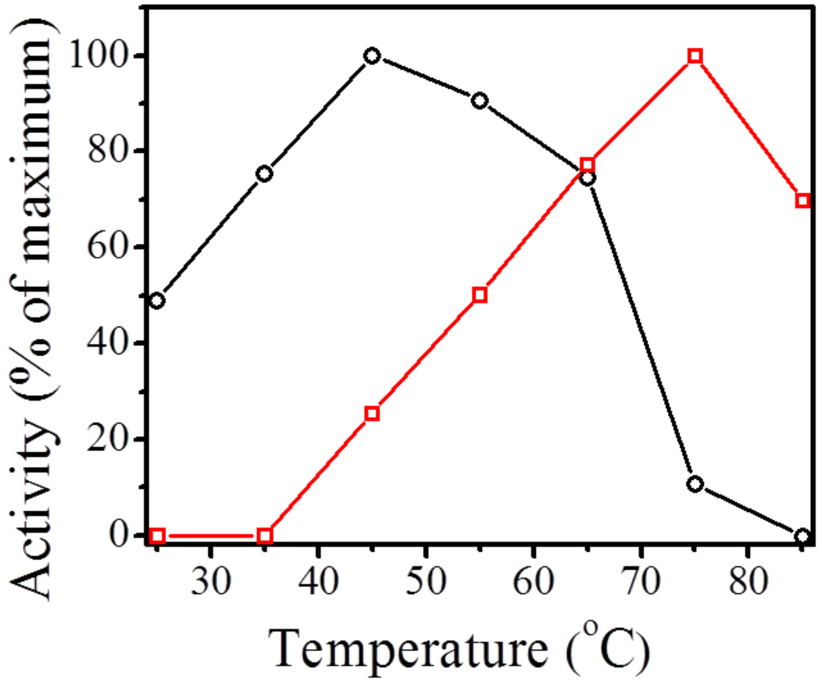

Figure 7.4. EG activity monitored via absorbance of the liberated dye from cellulose azure (1.5 mg/mL) at 575 nm in HEMA, BMIM Cl, and BMIM $MeSO_4$ at 70˚C. The EG concentration was maintained at $5x10^{-6}$ M. Absorbance values shown are multiplied by a factor of 10. Activity in three ILs was studied at the melting point of BMIM Cl. EG exhibited highest activity in HEMA. No activity was found in BMIM $MeSO_4$ at 70˚C or at lower temperatures. The error bars are calculated from three measurements.

The stability of enzymes is also governed by the pH (Yang and Pan 2005). The pH dependence of enzyme activity varies with the nature of the ions comprising the IL and water content. To understand the differential activity exhibited by EG in different ILs and the aqueous mixtures, we measured the pH of the medium as a function of increasing IL concentration

(**Figure 7.5)**. ILs were added to 0.05-M pH 4.8 citrate buffer, and the resultant pH was constant until [IL] = 1 M. A concentration larger than 1 M resulted in increased pH for the three ILs investigated, but the increase was the smallest for HEMA. Finally, we explored the effect of $MeSO_4^-$ on the pH. The opposite trend was observed. The pH *dropped* from 4.8 to 1.0 at 4 M of the sodium methylsulfate ($NaMeSO_4$) salt, which is probably due to the hydrolysis of $MeSO_4^-$ to methanol and hydrogensulfates (Wolfenden and Yuan 2007). This explained the decrease of activity of EG with increasing concentration of $NaMeSO_4$ as shown in **Figure 7.6**. The unfolding of EG was monitored as a function of fluorescence emission maximum of tryptophan in EG with respect to increasing concentration of $MeSO_4^-$ ion. Unlike in HEMA, red-shifted emission spectra (325 to 360 nm, data not shown) were observed with 1-M $NaMeSO_4$, indicating denaturation of the native structure of the enzyme. Thus the attempt to study the effect of $MeSO_4^-$ ions using $NaMeSO_4$ salt was not fruitful because of the drastic pH change it induces.

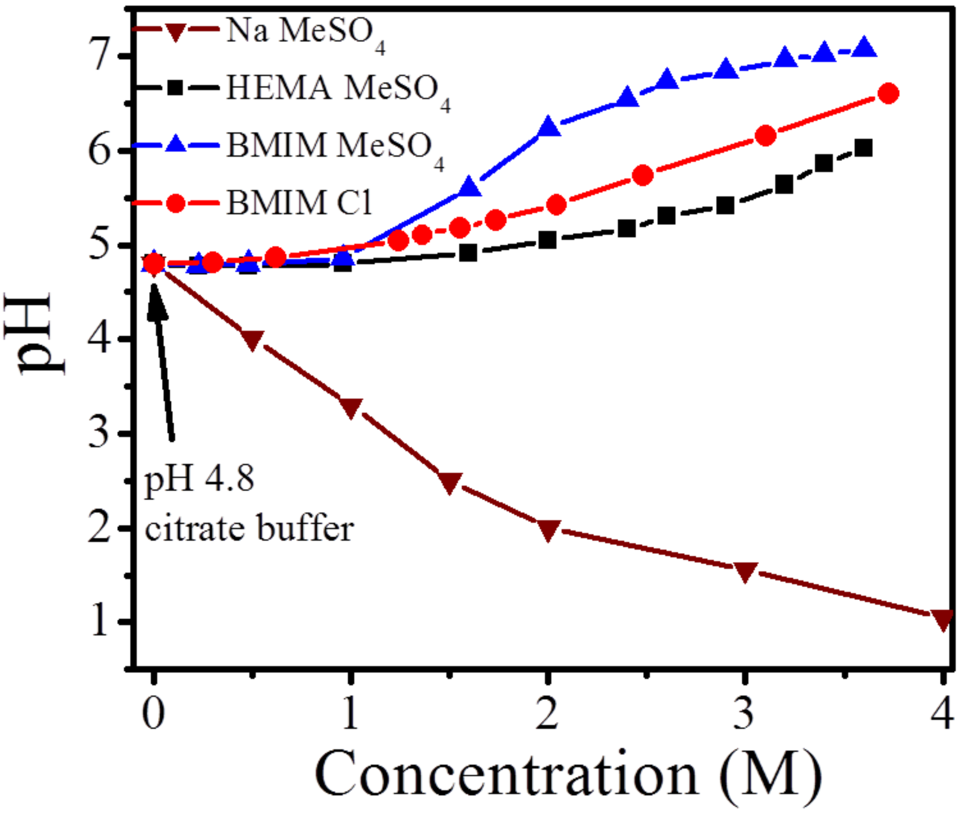

Figure 7.5. pH of water/IL mixtures and a sodium salt of methylsulfate as a function of IL concentration. The concentrations of the ILs were determined from the known added volumes and calculated densities. $NaMeSO_4$ drastically acidifies the solution, whereas the ILs gradually increase the pH. The buffer action holds until 1-M concentration of ILs.

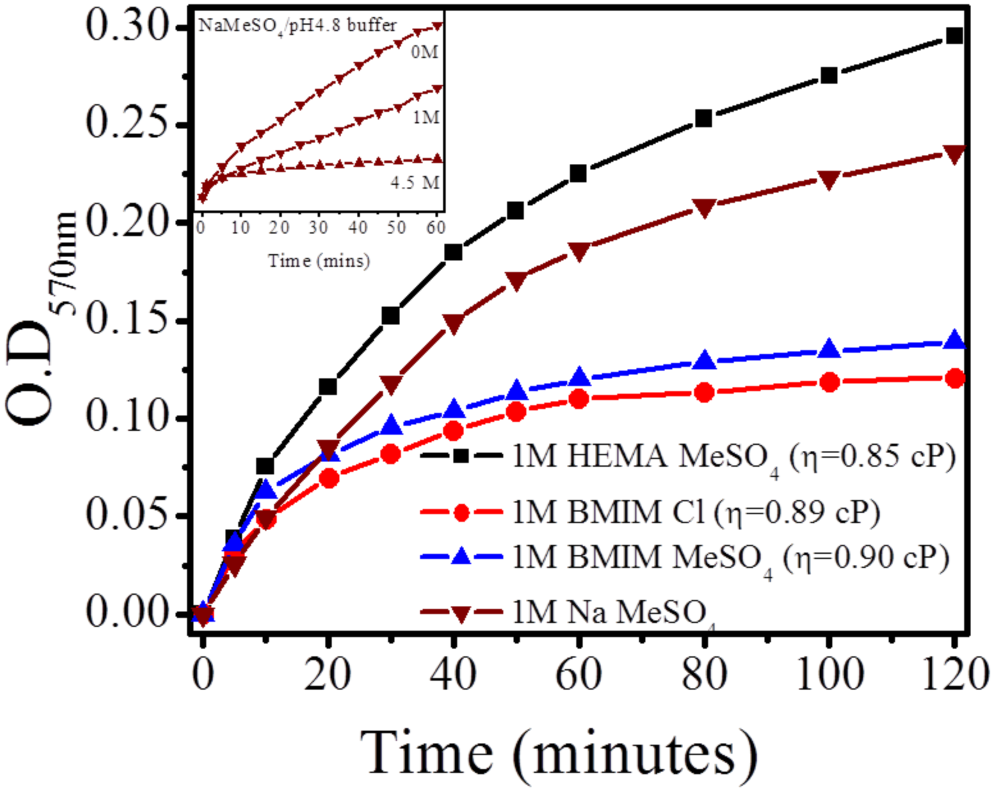

Figure 7.6. EG activity monitored via absorbance of the liberated dye from cellulose azure (1.5 mg/mL) at 570 nm in 1-M HEMA, BMIM Cl, BMIM $MeSO_4$ and $NaMeSO_4$ dissolved in pH 4.8 citrate buffer at 45˚C. The EG concentration was maintained at $5x10^{-6}$ M. The pH of the aqueous 1-M IL solutions was identical (~4.8). At 45˚C, these solutions were isoviscous; and the measured viscosities are given in the parentheses. The inset shows how the activity of EG decreases with increasing concentrations of $NaMeSO_4$ due to lowering of pH of the solution, causing the enzyme to denature.

From **Figure 7.5**, we see that the pHs of 1-M HEMA, BMIM Cl, and BMIM $MeSO_4$ in citrate buffer are almost identical. Thus we chose to study the EG activity using a concentration of 1-M for the three ILs to eliminate effect of pH as a variable in our consideration of the stability of the enzyme. In order to eliminate viscosity as a variable, activity studies were performed at 45°C, since 1-M solution of the ILs are isoviscous at that that temperature. As shown in **Figure 7.6**, EG activity in the ILs increased in the order: BMIM Cl < BMIM $MeSO_4$ << HEMA. The activity curve for 1-M $NaMeSO_4$ is also included, which showed lower activity than HEMA, but higher than two imidazolium ILs at 1-M. The lower activity at 1-M $NaMeSO_4$ was due to the partial denaturation of EG caused by the higher acidity of the solution. Even at isoviscous and identical pH conditions, the substantial decrease in the EG activity in the imidazolium ILs indicates that cationic species ($BMIM^+$) causes considerable alteration of the structural integrity of the native enzyme thereby decreasing its catalytic abilities. On the other hand, the higher activity in HEMA indicates that the tris(2-hydroxyethyl)methylammonium moiety imparts a certain stabilization to EG. The effect of polarity of the ionic liquids on the stability of the enzyme is discussed in the supplemental information.

Cellulose Solubility and Pretreatment before Hydrolysis

The solubility of cellulose was measured in various ILs (**Table 7.1**). The solubility in chloride based ILs was much higher than that in the $MeSO_4$-containing ILs. BMIM Cl dissolved ~10% (w/w) of cellulose, whereas the solubility was lesser in MIM Cl (~3%). The solubility of cellulose in HEMA and BMIM $MeSO_4$ is only ~1% (w/w). Based on a recent review (Mora-Pale et al. 2011), solubility studies in $MeSO_4$-based ILs are rare compared to those in chloride-based ILs. And chloride-based ILs have been reported (Swatloski et al. 2002) to dissolve up to ~10% (w/w) of cellulose. Dialkylimidazolium formates are reported to increase the solubility of cellulose up to 20% at 85°C (Fukaya et al. 2006).

Both the cation and anion of an IL can form a complex with the hydroxyl groups of cellulose, thereby disrupting the strong interchain hydrogen bonding network of cellulose polymers facilitating its dissolution (Vitz et al. 2009). The presence of oxygen atoms in the side chains of the cationic moiety in the IL is believed to interfere with the interchain hydrogen bonding network of cellulose, thereby decreasing its degree of polymerization and crystallinity, as reported for the alkoxy substituted imidazolium ILs (Zhao et al. 2008). But owing to the dispersion of negative charge among three oxygen atoms, it is likely that the hydrogen bonding ability is reduced with $MeSO_4^-$ compared to that with chloride ions. This may account for the much smaller solubility of cellulose in the presence of $MeSO_4^-$ ions. The tradeoff is that this same phenomenon would also aid to maintain the structural integrity of the enzymes, consequently making them more stable in HEMA.

The presence of water in the IL significantly decreases the solubility of cellulose. Cellulose was completely insoluble in the presence of 5% water (quantitatively added) in all of the ILs. Thus water was used as an anti-solvent to regenerate dissolved cellulose from ILs. All of the ILs studied here were dried prior to solubility measurements. The water content of the dried ILs was measured and is listed in **Table 7.1**. The dissolved cellulose in the ILs was regenerated as described in the *supplemental information*. Regeneration of cellulose from BMIM Cl was the most difficult since cellulose and BMIM Cl formed a fused gel-like substance. Thus purification of cellulose from BMIM Cl was also cumbersome compared to that of HEMA. There was a considerable loss of BMIM Cl, which is reflected from the percent recovery data collated in **Table 7.1**. Of all the ILs studied, the maximum recovery of cellulose and IL was obtained for HEMA. It is noteworthy that residual amounts of HEMA (if any) adsorbed on regenerated cellulose is not detrimental since it does not destabilize the cellulolytic enzymes, whereas this is not the case in BMIM Cl (Turner et al. 2003). Thus painstaking attention is required to ensure complete removal of BMIM Cl from regenerated cellulose prior to its hydrolysis

Table 7.1. Cellulose Solubility and Hydrolysis of Cellulose Pretreated with ILs

	Water Content[a] (%w/w)	**Solubility Measurements[b]**		**% recovery of IL**	**% cellulose regenerated**	**Cellulose Pretreatment**		
		% (w/w)	**Appearance after dissolution**			**% glucose converted[c]**	**T_d[e] (°C)**	**ΔH_d[e] (J/g)**
HEMA	0.03	1	clear	90-95	95	55	318	560
BMIM $MeSO_4$	0.08	<1	turbid	ND[f]	88	43	310	390
BMIM Cl	0.09	10	viscous gel	75-80	75	60	300	410
MIM Cl		3	clear			55		
Cellulose (untreated)						40	338	900

[a] Water content measured after purifying and drying the IL samples.

[b] Solubility of cellulose was measured at 100°C for 5 hours. The properties of regenerated cellulose were almost independent of the pretreatment time. Yellowish brown coloration was observed when heating with larger amounts of cellulose.

[c] The amount of glucose is determined by a glucose hexokinase assay. The percentage of glucose converted from cellulose is determined as the ratio of the mass of glucose produced to the initial mass of cellulose.

[e] T_d and ΔH_d are decomposition temperature and enthalpy change associated with the process, measured from DSC experiments.

[f] ND: not determined.

Hydrolysis of cellulose after IL pretreatment was faster than that for the untreated cellulose (**Figure 7.7**). Hydrolysis of cellulose performed at 45°C with a 1:1 ratio of EG and cellobiase from *A. niger* was monitored as a function of glucose formation with time. The initial kinetics of hydrolysis of regenerated cellulose from BMIM Cl, MIM Cl and HEMA were much faster than those regenerated from BMIM MeSO$_4$ and untreated cellulose. After 14 hours, all the regenerated cellulose from HEMA was completely converted into soluble sugars, leaving a clear solution, whereas, that regenerated from BMIM Cl was completely hydrolyzed within ~12 hours. Approximately 40% conversion to glucose was observed in the case of untreated cellulose after 14 hours. Dadi et. al. reported that the initial rates of hydrolysis of cellulose pretreated with BMIM Cl was much faster than those for the untreated cellulose (Dadi et al. 2006). Dordick and coworkers have studied the hydrolysis of wood flour pretreated in different ILs, namely EMIM acetate, 1-benzyl-3-methylimidazolium chloride (BZMIM Cl), and MMIM MeSO$_4$, and compared the reaction with that for untreated flour using *T. viride* cellulases (Lee et al. 2009). Conversion of samples pretreated by BZMIM Cl and MMIM MeSO$_4$ was slightly higher than that for the untreated ones, whereas 90% conversion to sugars was observed with EMIM acetate pretreated flour. Our observations are consistent with the above reports on IL-pretreated-cellulose hydrolysis.

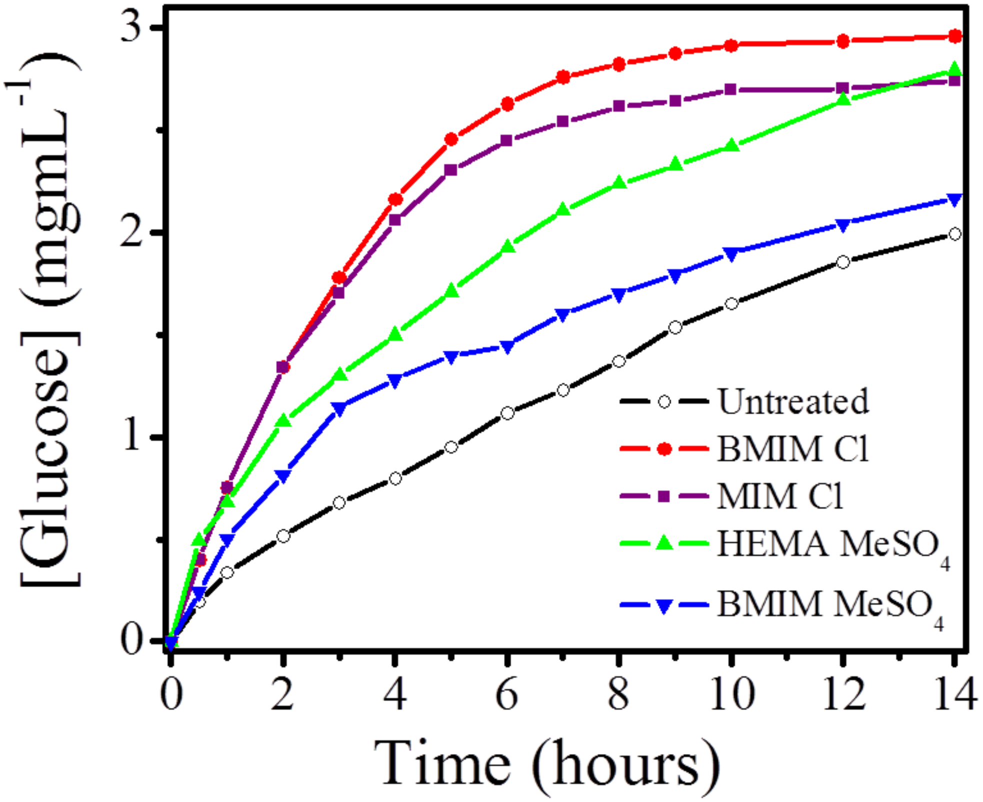

Figure 7.7. Hydrolysis of microcrystalline cellulose samples (5mg/mL) regenerated from the ILs, HEMA, BMIM Cl, and BMIM MeSO$_4$ and a comparison with untreated cellulose. All the cellulose samples were pretreated in the ILs for 3 hours and regenerated with water. A 1:1 ratio of EG to cellobiase from *A. niger* (3 mg/mL each) was added for hydrolysis. Glucose concentrations were measured with a glucose hexokinase assay using a standard calibration curve. All hydrolyses were carried in a peltier controlled temperature bath maintained at 45˚C. Hydrolysis of cellulose after IL pretreatment was faster than for the untreated cellulose.

Hydrolysis of untreated and of BMIM Cl pretreated cellulose was also carried out at higher temperatures, such as 60 and 70°C (**Figure 7.8**). Increasing the temperature of hydrolysis of untreated cellulose above 45°C resulted in a substantial decrease in the amount of glucose formation after 15 hours, indicating the deactivation of enzymes at higher temperatures. The concentration of glucose increased when BMIM Cl pretreated cellulose was hydrolyzed at 60°C, which is consistent with the previous reports of (Zhao et al. 2009). The authors argued that pretreated cellulose has more accessible surfaces for efficient adsorption of the enzymes on the substrate protecting it from thermal denaturation at 60°C. On the other hand hydrolysis of BMIM Cl pretreated cellulose was conducted in the presence of 10–20% HEMA in pH 4.8, citrate buffer. The glucose yield was higher in the presence in HEMA at 60°C, but the yield dropped on increasing the temperature to 70°C. The presence of HEMA stabilized the enzyme and prevented it from denaturation, which resulted in higher yields of glucose from cellulose at 60°C.

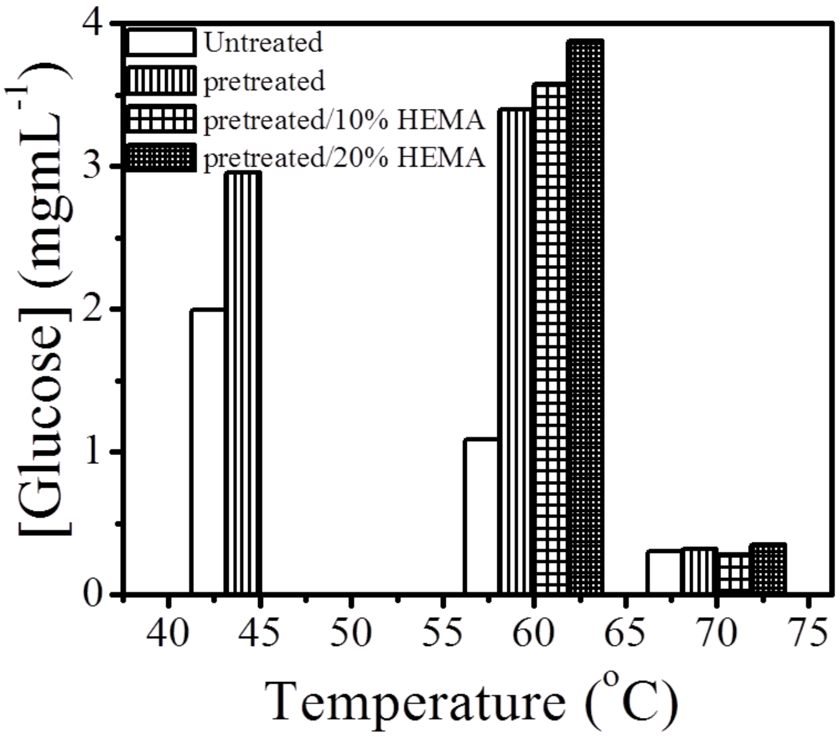

Figure 7.8. Glucose yields after 15 hours of enzymatic hydrolysis of BMIM Cl pretreated cellulose (5mg/mL) as a function of temperature (45, 60 and 70°C) was compared with that of untreated cellulose. Hydrolyses were carried out in pH 4.8 citrate buffer with 1:1 ratio of EG to cellobiase from *A. niger* (3 mg/mL each). Glucose yields from regenerated cellulose were maximized at 60°C. Effect of addition of HEMA (10 – 20%) in pH 4.8 citrate buffer on the glucose yields, was monitored at 60 and 70°C. Higher yields of glucose were obtained up to 20% addition of HEMA at 60°C.

Calorimetric and Other Characterization of Pretreated Cellulose

To gain insight into the differences in the observed kinetics of the hydrolysis reactions, calorimetric studies were done to characterize the cellulose obtained after regeneration from different ILs and to compare them with untreated cellulose. As shown in **Figure 7.9**, the “apparent melting” or decomposition of pretreated cellulose occurred at lower temperatures compared to that for untreated samples. The shape and position of the endothermic peak in the DSC profiles was dependent on the scan rate (data not shown), thus the endothermic transitions do not represent the actual thermodynamic melting points, but rather correspond to the decomposition of cellulose. In other words, because we are investigating an irreversible process leading to the decomposition of the cellulose, increasing the scan rate effectively increases the temperature-dependent rate constant for decomposition. The regenerated cellulose exhibited a lower onset temperature for decomposition. This can be attributed to partial unfolding or loss of crystallinity of the cellulose polymers after regeneration from the ILs. BMIM Cl pretreated cellulose showed the lowest decomposition temperature. The endothermic peaks for regenerated cellulose are broader than those of untreated samples. The enthalpy change associated in this process significantly decreased from that obtained in the untreated sample, as depicted in **Table 7.1**. The trend, however, of the decomposition temperatures of the pretreated cellulose samples is not exactly in accordance with the trend observed in the rates of their hydrolysis.

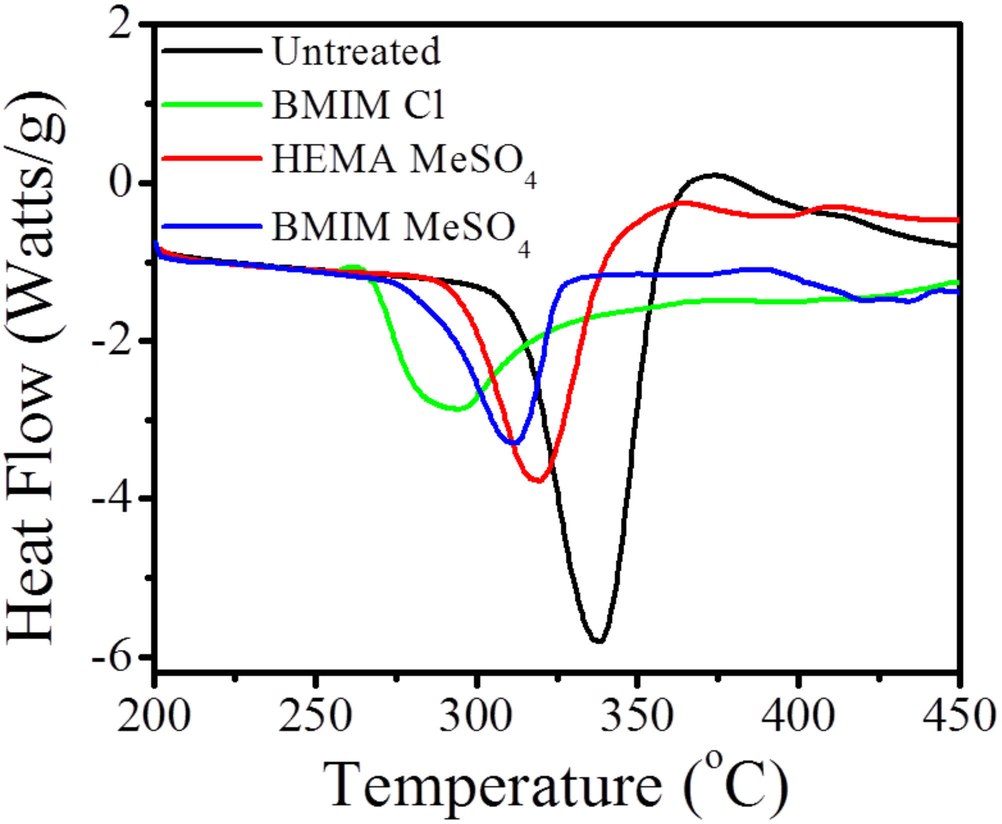

Figure 7.9. DSC scans of untreated cellulose and of cellulose pretreated with IL pretreated cellulose performed at 10˚C/minute from 0--500˚C. The endothermic transitions are associated with decomposition of cellulose. The decomposition temperature of pretreated cellulose was lower than that of the untreated cellulose, and the DSC parameters are listed in **Table 7.1**.

The effect of pretreatment with ILs on cellulose structure has been studied by acquiring SEM images of the morphology of the untreated and pretreated cellulose. Previous SEM studies (Swatloski et al. 2002) on BMIM Cl pretreated "paper" showed a rough and dented texture in which the fibers are fused into a relatively homogeneous macrostructure. As shown in the supplemental information **Figure SI.5**, the cellulose regenerated from ILs has certain changes in morphology compared to the original untreated cellulose. SEM images were taken at different magnifications from 25x to 3000x. The surface texture of the untreated cellulose was smooth, whereas that regenerated from ILs showed roughness with trenches and grooves. All the pretreated samples appeared to be fused and agglomerated, and these features are more prominent in cellulose regenerated from BMIM Cl and HEMA. The surface of the cellulose regenerated from BMIM $MeSO_4$ appeared brittle. Thus the modifications arising from pretreating cellulose are consistent with the calorimetric results discussed above. Less energy is required to decompose the partially modified cellulosic polymer, which is indicated by a premature decomposition temperature and a corresponding lower enthalpy change as compared to the untreated cellulose.

The different rates of hydrolysis of the pretreated cellulose can be attributed to different degrees of crystallinity achieved during the regeneration process with water (Zhao et al. 2009). The ions in the IL might affect this process to varying extents. Cellulose regenerated from ILs might be less crystalline with more rough and fractured surfaces (Dadi et al. 2006). The roughness on the surface of cellulose as seen in the SEM images indicates its amorphous nature, which increases the accessible surface area for the enzyme, thus resulting in its faster hydrolysis compared to untreated samples.

Kamlet-Taft Parameters

Kamlet-Taft parameters are determined (using the equations in the supplemental information) from the absorption maxima (ν^{max}) in kilokeyser (kK, 10^{-3} cm^{-1}) of the solvatochromic dyes NA and DENA. These parameters characterize the hydrogen bond basicity (β), hydrogen bond acidity (α) and polarizability (π^*) of the ILs, which together contribute to the overall polarity of the solvents. The hydrogen bond acceptor (HBA) capability of the ILs strongly affects their interaction with the cellulose and consequently alters its crystallinity upon pretreatment. A high HBA or β-value of an IL, for example, $\beta_{\text{BMIM Cl}}$ ~1.0 (Lungwitz et al. 2010) or $\beta_{\text{BMIM OAc}}$ ~ 1.2 (Doherty et al. 2010) indicates stronger hydrogen bonding interaction with cellulose, higher solubility, and substantial decrease in cystallinity after regeneration. As stated above, lesser crystallinity of the pretreated cellulose enhances its conversion to sugars. Thus slower hydrolysis of celluloses pretreated with BMIM $MeSO_4$ and HEMA $MeSO_4$ is consistent with their lower β-values as shown in the table and figure SI 6. Another method of determining the solubility and interactions of cellulose in ILs is by calculating the Hildebrand/Hansen solubility parameters (HSP). Dordick and coworkers discussed the solubility of cellulose in different ILs by comparing the HSP values of microcrystalline cellulose (as solute) with those of ILs (as solvents) and concluded that BMIM Cl has the highest potential of dissolving cellulose, since their HSP values are close (Mora-Pale et al. 2011).

Conclusions

This work provides a detailed study of EG stability and activity in buffer, HEMA, and their binary mixtures at different temperatures. From fluorescence studies, we conclude that the enzyme denatures and precipitates at ~55°C in buffer, whereas the transition temperature shifts to ~75°C in HEMA, which shows that the enzyme gains higher heat tolerance in the IL. EG activity was significantly enhanced in the presence of HEMA in buffer. The enzymatic activity rate is a compromise between both enzyme stability in a particular solvent and temperature and the viscosity of the medium. To our knowledge this is the first study dealing with a pure endoglucanase from commercial *A. niger*, which not only shows higher tolerance to ILs such as HEMA but also whose thermostability is markedly enhanced in the presence of the IL.

In addition to viscosity, we investigated other factors such as pH and polarity that could affect the activity of enzymes in ILs. By studying the activity of EG in different ILs with similar anions, it was concluded that imidazolium and HEMA cations have opposite effects towards the stability of EG. Imidazoliums destabilize, and HEMA cations stabilize.

Besides the inherent environmentally benign properties of ILs, their ability to dissolve cellulose and to enhance the kinetics of hydrolysis after regeneration proves to be a green aspect of the entire process of biofuel production. Pretreatment in ILs such as BMIM Cl, MIM Cl and HEMA resulted in much faster conversion to glucose compared to untreated cellulose. Higher yields of glucose were obtained from cellulose regenerated from these ILs. Cellulose regenerated from ILs has lower crystallinity with more rough and fractured surfaces which increases the accessible surface area for the enzyme, thus resulting in its faster hydrolysis compared to untreated samples. Interestingly glucose yields from pretreated cellulose are also affected by temperature of hydrolysis, and the yield is increased when the temperature is increased from 45 to 60°C.

As reported in the literature, it is very challenging to design an IL which will have both strong capabilities of dissolving cellulose and also stabilize the cellulolytic enzymes. Thus in this work, two different ILs were used in conjunction to increase the efficiency of cellulose conversion to glucose. In our studies, we found that the solubility of cellulose was highest in BMIM Cl, but the latter was also detrimental to the enzymes. Thus we chose to pretreat the cellulose with BMIM Cl and subsequently hydrolyze the pretreated cellulose in 10–20% solutions of HEMA in buffer. Addition of HEMA imparted extra stability to the enzymes and thus yielded higher amounts of glucose at 60°C. Thus the combination of two ILs turned out to be a fruitful strategy in enhancing the process of glucose production from cellulose.

Acknowledgements

We thank Zhongyuan Qian and Prof. Scott Chumbley for assistance in the SEM experiments. We thank Prof. Daniel W. Armstrong for synthesizing the ionic liquid MIM Cl. We also thank Debabrata Mukherjee for helping with the analytical separation process. S.B was supported by the U.S. Department of Energy, Office of Basic Energy Sciences, Division of Chemical Sciences, Geosciences, and Biosciences through the Ames Laboratory (S.B.). The Ames Laboratory is operated for the U.S. Department of Energy by Iowa State University under Contract No. DE-AC02-07CH11358.

References

Adhikary R, Bose S, Mukherjee P, Thite A, Kraus GA, Wijeratne AB, Sharma P, Armstrong DW, Petrich JW. 2008. Influence of Chiral Ionic Liquids on the Excited-State Properties of Naproxen Analogs. J. Phys. Chem. B 112(25):7555-7559.

Bose S, Armstrong DW, Petrich JW. 2010. Enzyme Catalyzed Hydrolysis of Cellulose in Ionic Liquids: A Green Approach Towards the Production of Biofuels. J. Phys. Chem. B 114(24):8221-8227.

Bose S, Wijeratne AB, Thite A, Kraus GA, Armstrong DW, Petrich JW. 2009. Influence of Chiral Ionic Liquids on Stereoselective Fluorescence Quenching by Photoinduced Electron Transfer in a Naproxen Dyad. J. Phys. Chem. B 113(31):10825–10829.

Cantone S, Hanefeld U, Basso A. 2007. Biocatalysis in non-conventional media—ionic liquids, supercritical fluids and the gas phase. Green Chem. 9(9):954–971.

Chowdhury PK, Halder M, Sanders L, Calhoun T, Anderson JL, Armstrong DW, Song X, Petrich JW. 2004. Dynamic Solvation in Room-Temperature Ionic Liquids. J. Phys. Chem. B 108(29):10245-10255.

Constatinescu D, Herrmanna C, Weingärtner H. 2010. Patterns of protein unfolding and protein aggregation in ionic liquids. Phys. Chem. Chem. Phys. 12(8):1756-1763.

Dadi AP, Varanasi S, Schall CA. 2006. Enhancement of Cellulose Saccharification Kinetics Using an Ionic Liquid Pretreatment Step. Biotechnol. Bioeng. 95(5):904-910.

Das D, Das Gupta A, Das PK. 2007. Improved activity of horseradish peroxidase (HRP) in 'specifically designed' ionic liquid. Tetrahedron Lett. 48(32):5635–5639.

Datta S, Holmes B, Park JI, Chen Z, Dibble DC, Hadi M, Blanch HW, Simmons BA, Sapra R. 2010. Ionic liquid tolerant hyperthermophilic cellulases for biomass pretreatment and hydrolysis. Green Chem. 12(2):338-345.

Doherty TV, Mora-Pale M, Foley SE, Linhardt RJ, Dordick JS. 2010. Ionic liquid solvent properties as predictors of lignocellulose pretreatment efficacy. Green Chem. 12(11):1967-1975.

Feher E, Major B, Belafi-bako K, Gubicza L. 2007. On the background of enhanced stability and reusability of enzymes in ionic liquids. Biochem. Soc. Trans. 35(6):1624-1627.

Fort DA, Remsing RC, Swatloski RP, Moyna P, Moyna G, Rogers RD. 2007. Can ionic liquids dissolve wood? Processing and analysis of lignocellulosic materials with 1-*n*-butyl-3-methylimidazolium chloride. Green Chem. 9(1):63-69.

Fukaya Y, Sugimoto A, Ohno H. 2006. Superior Solubility of Polysaccharides in Low Viscosity, Polar, and Halogen-Free 1,3-Dialkylimidazolium Formates. Biomacromol. Commun. 7(12):3295-3297.

Hay S, Pudney CR, Sutcliffe MJ, Scrutton NS. 2008. Are environmentally coupled enzymatic hydrogen tunneling reactions influenced by changes in solution viscosity? Angew. Chem. 47(3):537-540.

Hendriks ATWM, Zeeman G. 2009. Pretreatments to enhance the digestibility of lignocellulosic biomass. Biores. Tech. 100(1):10-18.

Itoh T, Akasaki E, Kudo K, Shirakami S. 2001. Lipase-Catalyzed Enantioselective Acylation in the Ionic Liquid Solvent System: Reaction of Enzyme Anchored to the Solvent. Chem. Lett. 30(3):262-263.

Kaftzik N, Kroutil W, Faber K, Kragl U. 2004. Mandelate racemase activity in ionic liquids: scopes and limitations. J. Mol. Catal. A: Chem. 214(1):107–112.

Kaftzik N, Wasserscheid P, Kragl U. 2002. Use of Ionic Liquids to Increase the Yield and Enzyme Stability in the beta -Galactosidase Catalyzed Synthesis of N-Acetyllactosamine. Org. Process Res. Dev. 6(4):553-557.

Kumar R, Singh S, Singh OV. 2008. Bioconversion of lignocellulosic biomass: biochemical and molecular perspectives. J. Ind. Microbiol. Biotechnol. 35(5):377-391.

Ladisch MR, Ladisch CM, Tsao GT. 1978. Cellulose to Sugars: New Path Gives Quantitative Yield. Science 201(4357):743-745.

Lau RM, Rantwijk Fv, Seddon KR, Sheldon RA. 2000. Lipase-catalysed Reactions in Ionic Liquids. Org. Lett. 2(26):4189-4191.

Lau RM, Sorgedrager MJ, Carrea G, Rantwijk Fv, Secundo F, Sheldon RA. 2004. Dissolution of Candida antarctica lipase B in ionic liquids: effects on structure and activity. Green Chem. 6(9):483-487.

Lee SH, Doherty TV, Linhardt RJ, Dordick JS. 2009. Ionic Liquid-Mediated Selective Extraction of Lignin From Wood Leading to Enhanced Enzymatic Cellulose Hydrolysis. Biotechnol. Bioeng. 102(5):1368-1376.

Lozano P, Diego Td, Carrié D, Vaultier M, Iborra JL. 2002. Continuous green biocatalytic processes using ionic liquids and supercritical carbon dioxide. Chem. Commun.(7):692 - 693.

Lungwitz R, Strehmel V, Spange S. 2010. The dipolarity/polarisability of 1-alkyl-3-methylimidazolium ionic liquids as function of anion structure and the alkyl chain lengthw. New J. Chem. 34(6):1135-1140.

Lynd LR, Cushman JH, Nichols RJ, Wyman CE. 1991. Fuel Ethanol from Cellulosic Biomass. Science 251(4999):1318-1323.

Mora-Pale M, Meli L, Doherty TV, Linhardt RJ, Dordick JS. 2011. Ionic Liquid Pretreatment of Cellulosic Biomass: Enzymatic Hydrolysis and Ionic Liquid Recycle. Biotechnol. Bioeng. 108(6):1229-1245.

Park S, Kazlauskas RJ. 2001. Improved Preparation and Use of Room-Temperature Ionic Liquids in Lipase-Catalyzed Enantio- and Regioselective Acylations. J. Org. Chem. 66(25):8395–8401.

Park S, Kazlauskas RJ. 2003. Biocatalysis in Ionic liquids - advatages beyond green techonology. Curr. Opin. Biotechnol. 14(4):432-437.

Ragauskas AJ, Williams CK, Davison BH, Britovsek G, Cairney J, Eckert CA, Frederick WJ, Jr., Hallett JP, Leak DJ, Liotta CL and others. 2006. The path forward for biofuels and biomaterials. Science 311(5760):484-489.

Reddy N, Yang Y. 2005. Properties and potential applications of natural cellulose fibers from cornhusks. Green Chem. 7(4):190-195.

Remsing RC, Swatloski RP, Rogers RD, Moyna G. 2006. Mechanism of cellulose dissolution in the ionic liquid 1-n-butyl-3-methylimidazolium chloride: a ^{13}C and $^{35/37}$Cl NMR relaxation study on model systems. Chem. Commun.(12):1271-1273.

Ru MT, Hirokane SY, Lo AS, Dordick JS, Reimer JA, Clark DS. 2000. On the Salt-Induced Activation of Lyophilized Enzymes in Organic Solvents: Effect of Salt Kosmotropicity on Enzyme Activity. J. Am. Chem. Soc. 122(8):1565-1571.

Sheldon RA, Lau RM, Sorgedrager MJ, Rantwijk Fv, Seddon KR. 2002. Biocatalysis in ionic liquids. Green Chem. 4(2):147-151.

Su Y, Brown HM, Huang X, Zhou X-d, Amonette JE, Zhang ZC. 2009. Single-step conversion of cellulose to 5-hydroxymethylfurfural (HMF), a versatile platform chemical. Appl. Catalysis A 361(1-2):117-122.

Swatloski RP, Spear SK, Holbrey JD, Rogers RD. 2002. Dissolution of Cellulose with Ionic Liquids. J. Am. Chem. Soc. 124(18):4974-4975.

Turner MB, Spear SK, Huddleston JG, Holbrey JD, Rogers RD. 2003. Ionic liquid salt-induced inactivation and unfolding of cellulase from *Trichoderma reesei*. Green Chem. 5(4):443–447.

Vitz J, Erdmenger T, Haensch C, Schubert US. 2009. Extended dissolution studies of cellulose in imidazolium based ionic liquids. Green Chem. 11(3):417–424.

Wang Y, Radosevich M, Hayes D, Labbé N. 2010. Compatible Ionic Liquid-Cellulases System for Hydrolysis of Lignocellulosic Biomass. Biotechnol. Bioeng. 108(5):1042–1048.

Wei W, Danielson ND. 2011. Fluorescence and Circular Dichroism Spectroscopy of Cytochrome c in Alkylammonium Formate Ionic Liquids. Biomacromolecules 12(2):290-297.

Wolfenden R, Yuan Y. 2007. Monoalkyl sulfates as alkylating agents in water, alkylsulfatase rate enhancements, and the ‘‘energy-rich’’ nature of sulfate half-esters. Proc. Natl. Acad. Sci. U. S. A. 104(1):83-86.

Wu J, Zhang J, Zhang H, He J, Ren Q, Guo M. 2004. Homogeneous acetylation of cellulose in a new ionic liquid. Biomacromol. 5(2):266-268.

Xiang Q, Lee YY, Pettersson PO, Torget RW. 2003. Heterogeneous Aspects of Acid Hydrolysis of α-Cellulose. Appl. Biochem. Biotechnol. 107(1-3):505-514.

Yang Z, Pan W. 2005. Ionic Liquids: Green Solvents for nonaqueous biocatalysis. Enzyme Microbial Technol. 37(1):19-28.

Zhang H, Wu J, Zhang J, He J. 2005. 1-Allyl-3-methylimidazolium Chloride Room Temperature Ionic Liquid: A New and Powerful Nonderivatizing Solvent for Cellulose. Macromol. 38(20):8272-8277.

Zhang Y-HP, Lynd LR. 2004. Toward an Aggregated Understanding of Enzymatic Hydrolysis of Cellulose: Noncomplexed Cellulase Systems. Biotechnol. Bioeng. 88(7):797–824.

Zhao H. 2005. Effect of ions and other compatible solutes on enzyme activity, and its implication for biocatalysis using ionic liquids. J. Mol. catal. B: Enzymatic 37(1-6):16–25.

Zhao H. 2006. Are ionic liquids kosmotropic or chaotropic? An evaluation of available thermodynamic parameters for quantifying the ion kosmotropicity of ionic liquids. J. Chem. Technol. Biotechnol. 81(10):877–891.

Zhao H. 2010. Methods for stabilizing and activating enzymes in ionic liquids – a review. J. Chem. Technol. Biotechnol. 85(7):891–907.

Zhao H, Baker GA, Song Z, Olubajo O, Crittlea T, Peters D. 2008. Designing enzyme-compatible ionic liquids that can dissolve carbohydrates. Green Chem. 10(6):696–705.

Zhao H, Holladay JE, Brown H, Zhang ZC. 2007. Metal Chlorides in Ionic Liquid Solvents Convert Sugars to 5-Hydroxymethylfurfural. Science 316(5831):1597-1600.

Zhao H, Jones CL, Baker GA, Xia S, Olubajo O, Person VN. 2009. Regenerating cellulose from ionic liquids for an accelerated enzymatic hydrolysis. J. Biotechnol. 139(1):47-54.

CHAPTER 8: GENERAL CONCLUSIONS

Chapter 3 demonstrated that animals consuming significant levels of green plant materials in their diets will excrete feces with amounts of pheophorbide a (php) and pyropheophorbide a (pyp) that are in excess of the levels (10-30 fold) reported to be inhibitory to bacterial efflux pumps (0.5 μg/mL). Even though pyp does not currently have evidence to support its EPI activity, the amount of php present and its properties as an EPI could force a microbial population to persist without efflux pump activity, thereby allowing antibiotics to reach their intended destinations. Inhibitors are also known to place an energy burden on the bacterial cell to produce more efflux pumps in order to compensate for the nonfunctional pumps. This energy costs may be too much and as a result there is a selection against antimicrobial resistant phenotypes. As such it is possible that the amount of antimicrobial resistance expressed in the GI tract could be dictated by the presence of php. Given these data, further research is warranted to determine if other EPIs exist and if feed components can modulate the antimicrobial resistance of bacteria in the gut.

The coexistence of different excited states with different excited state properties could negatively impact solvation dynamic studies in heterogeneous environments. Thus in **Chapter 4** we studied the solvation dynamics of the locally excited (LE) and charge transfer (CT) states of PRODAN within reverse micelles. As initially indicated by the work of Novaria et al, we found that the LE and CT states of PRODAN solvate on different time scales in reverse micelles (2 and ~0.4 ns, respectively). Based on these results we were able to offer an alternative hypothesis to the unusual protein solvation results reported in the literature. This study ultimately leads to questioning of the viability in using PRODAN-based chromophores or similar chromophores with complicated excited-state chemistry in solvation dynamic studies of heterogeneous types of environments such as proteins. This study proves that considerable caution must be used in selecting and characterizing a system before a full analysis of the results.

In **Chapter 5** we delved deeper into the exploration of a protein's dielectic response with the complex of C153 and apoMb. Previous solvation dynamic studies of C153 in the heme pockets of horse heart myoglobin (HH Mb), leghemoglobin a (LHba), and sperm whale myoglobin (SW Mb) resulted in very good to excellent agreement between the experimental and theorectical C(t). In addition the results showed that C153 is very sensitive to its surrounding environment with notable changes in the C(t) observed from just one amino acid change in the heme binding pockets of SW and HH apomyglobin (apoMb). Based on these results we additionally studied the solvation dynamics of three different mutants of SW myglobin.

The C(t) results of C153 in the binding pockets of these mutants failed to show agreement between experiment and simulation. Based on the previous studies we assumed that the error was related to the starting structure used in the simulations (which were based on the SW wild type complex). To test our hypothesis, we carried out substantial structural analysis of the C153 HH-WT complex using NMR along with fluorescence resonance energy transfer (FRET), and anisotropy of all C153 apoMb complexes (C153 HH-WT and mutant SW apoMbs).

Based on the NMR and FRET studies of the WT complex, our previous hypothesis of the C153 location within the heme binding pocket was confirmed. In contrast, the FRET and fluorescence anisotropy results of the three mutants indicate that the mutant protein structures were structurally dissimilar to those of the WT. From these results we concluded that the mutant structures in the simulations were probably in error. Although C153 is very sensitive to the environment and an excellent probe of a proteins dielectric response, the results of this study point to the importance of structurally characterizing modified proteins before comparing experimental and theoretical results. To our knowledge this was the most extensive structural analysis of a protein and solvochromatic probe complex at the time.

In **Chapter 6** we studied the photophysical and spectral properties of cyclocurcumin in several solvents for the first time using steady-state and time resolved spectroscopies in order to understand the nonradiative processes of the parent compound, curcumin, which reportedly has multiple medicinal benefits. Based on absorption and fluorescence steady state studies, cyclocurcumin demonstrates sensitivity to the surrounding environment. But the photophysics and spectral properties were complicated in low viscosity polar aprotic solvents. In these solvents, the steady state fluorescence and excitation spectra are strongly dependent on the excitation and emission wavelength, respectively. Also the fluorescence quantum yield is dependent on excitation wavelength and shows an increase with increasing viscosity of the solvent. These studies indicated that there is ground state heterogeneity possibly resulting from the existence of rotational isomers.

Time resolved fluorescence studies of cyclocurcumin were nonexponential in all the solvents studied indicating two different structural forms in the excited state with different rates of relaxation which further supports the hypothesis of rotational isomers. NMR studies revealed that the ground state structural form of cyclocurcumin is *trans* with respect to the C6-C7 double bond in acetone, methanol, and water. Using the preexponential constants of the exicited state decays from temperature dependent studies, the standard entropy and enthalpy changes were found to be 13.3 cal/mol/K and 4.3 kcal/mol, respectively for the interconversion between rotamers in glycerol. The excited state activation energies of these rotamers were 3.3 and 5.4 kcal/mol in glycerol. Based on the isoviscosity plot, the *trans*-to-*cis* internal barriers for exited-state isomerization were calculated to be 1.65 and 0.68 kcal/mol. From the results of this study, it is believed that at least two conformational isomers about a single bond (C5-C6 or C7-C1″ or both) and *cis*-to-*trans* excited state isomerization of each isomer can best explain the steady state spectral properties and nonexponential decay behavior in both polar protic and aprotic solvents observed for cyclocurcumin.

We have also we worked to further explore the possibility of using ionic liquids as an effective medium for the conversion of cellulose into glucose which can be used in the production of biofuels. Previous studies have provided evidence that ILs, specifically BMIM Cl, MIM Cl, and HEMA can dissolve significant amounts of cellulose. Out of these it was found that HEMA imparts additional stability to cellulase in the hydrolysis of cellulose, in comparison to buffer. Thus in **Chapter 7** we continued our study of the hydrolysis of cellulose by cellulase using a pure form of the enzyme (endo-1,4-β-*D*-glucanase (EG) from the fungus, *Aspergillus niger*) in both buffer and HEMA as well as different ratios of the two, at different temperatures. According to steady-state fluorescence and absorption studies the thermal stability of EG in HEMA is significantly better than buffer with an ~20 ˚C increase in peak activity. Also it was found that the pretreatment of cellulose with BMIM Cl, MIM Cl, and HEMA allowed for its faster hydrolysis by cellulase in buffer. Furthermore pretreatment of cellulose by BMIM Cl followed by dissolution in 10-20% HEMA solutions provided higher amounts of glucose from enzymatic hydrolysis in comparision to buffer. From these studies we feel that HEMA could be used as an ideal starting candidate in designing other ILs for biomass to biofuel conversion in efforts to make the process more economical and environmentally friendly.